

NASA/CR–2015-218704/Volume II



Subsonic Ultra Green Aircraft Research: Phase II – Volume II – Hybrid Electric Design Exploration

*Marty K. Bradley and Christopher K. Droney
Boeing Research and Technology, Huntington Beach, California*

April 2015

NASA STI Program . . . in Profile

Since its founding, NASA has been dedicated to the advancement of aeronautics and space science. The NASA scientific and technical information (STI) program plays a key part in helping NASA maintain this important role.

The NASA STI program operates under the auspices of the Agency Chief Information Officer. It collects, organizes, provides for archiving, and disseminates NASA's STI. The NASA STI program provides access to the NTRS Registered and its public interface, the NASA Technical Reports Server, thus providing one of the largest collections of aeronautical and space science STI in the world. Results are published in both non-NASA channels and by NASA in the NASA STI Report Series, which includes the following report types:

- **TECHNICAL PUBLICATION.** Reports of completed research or a major significant phase of research that present the results of NASA Programs and include extensive data or theoretical analysis. Includes compilations of significant scientific and technical data and information deemed to be of continuing reference value. NASA counter-part of peer-reviewed formal professional papers but has less stringent limitations on manuscript length and extent of graphic presentations.
- **TECHNICAL MEMORANDUM.** Scientific and technical findings that are preliminary or of specialized interest, e.g., quick release reports, working papers, and bibliographies that contain minimal annotation. Does not contain extensive analysis.
- **CONTRACTOR REPORT.** Scientific and technical findings by NASA-sponsored contractors and grantees.

- **CONFERENCE PUBLICATION.** Collected papers from scientific and technical conferences, symposia, seminars, or other meetings sponsored or co-sponsored by NASA.
- **SPECIAL PUBLICATION.** Scientific, technical, or historical information from NASA programs, projects, and missions, often concerned with subjects having substantial public interest.
- **TECHNICAL TRANSLATION.** English-language translations of foreign scientific and technical material pertinent to NASA's mission.

Specialized services also include organizing and publishing research results, distributing specialized research announcements and feeds, providing information desk and personal search support, and enabling data exchange services.

For more information about the NASA STI program, see the following:

- Access the NASA STI program home page at <http://www.sti.nasa.gov>
- E-mail your question to help@sti.nasa.gov
- Phone the NASA STI Information Desk at 757-864-9658
- Write to:
NASA STI Information Desk
Mail Stop 148
NASA Langley Research Center
Hampton, VA 23681-2199

NASA/CR–2015-218704/Volume II



Subsonic Ultra Green Aircraft Research: Phase II – Volume II Hybrid Electric Design Exploration

*Marty K. Bradley and Christopher K. Droney
Boeing Research and Technology, Huntington Beach, California*

National Aeronautics and
Space Administration

Langley Research Center
Hampton, Virginia 23681-2199

Prepared for Langley Research Center
under Contract NNL08AA16B

April 2015

The use of trademarks or names of manufacturers in this report is for accurate reporting and does not constitute an official endorsement, either expressed or implied, of such products or manufacturers by the National Aeronautics and Space Administration.

Available from:

NASA STI Program / Mail Stop 148
NASA Langley Research Center
Hampton, VA 23681-2199
Fax: 757-864-6500

Abstract

This Final Report summarizes the hybrid electric concept design, analysis, technology, and modeling work accomplished by the Boeing Subsonic Ultra Green Aircraft Research (SUGAR) team. The time period of the work was February 2012 through June 2014. This includes work that was part of Task 2.2 (Hybrid Electric Concept Studies and Exploration) and Task 3.3 (Hybrid Electric Modeling Environment). The team consisted of Boeing Research and Technology, Boeing Commercial Airplanes, General Electric, and Georgia Tech.

A variety of performance and sizing tasks were conducted including looking at hybrid electric versions of a conventional tube-and-wing aircraft and a hybrid wing body. Trends and results were similar to the high wing Truss Braced Wing (TBW) SUGAR Volt aircraft. The SUGAR Volt was updated based on results from the TBW work in Task 2.1 (documented in a separate report) and new engine performance models from team member GE.

Energy cost and acoustic analyses were conducted and technology roadmaps were updated for hybrid electric and battery technology. NO_x emissions were provided by GE for landing and takeoff (LTO) and cruise.

Georgia Tech developed detailed NPSS models for hybrid electric components and tested the modeling environment with an integrated analysis of superconducting and non-superconducting hybrid electric engines.

The hybrid electric SUGAR Volt was shown to produce significant additional emissions and fuel burn reductions beyond those levels achieved by the conventionally powered SUGAR High. The SUGAR Volt was able to meet the NASA goals for fuel burn. Total energy utilization was not decreased but reduced energy cost can be achieved for some cost scenarios. The team was not able to identify a technology development path to meet the noise goals established by NASA.

Acknowledgements

This project and report reflect the combined efforts of the SUGAR team. The team members are Boeing Research and Technology, Boeing Commercial Airplanes, GE Aviation, and the Georgia Institute of Technology. The coordinated effort of this team has produced this final report. In addition to the two primary authors from Boeing, a partial list of writers that contributed to this report includes Ronen Elkoby from Boeing, Jeff Hamel from GE, and Chris Perullo from Georgia Tech.

Funding for this effort is provided by the NASA Fundamental Aeronautics Program, through the Subsonic Fixed Wing organization. The contract number is NNL08AA16B task order NNL11AA00T.

The team would like to thank Erik Olson of the NASA Langley Research Center for his guidance as the NASA Contracting Officer Technical Representative (COTR), and the task technical advisors (TA's): Gerry Brown and Jim Felder. Gerry Brown and Jim Felder were important subject matter experts who contributed significantly to the team's efforts.

Table of Contents

Abstract.....	i
Acknowledgements.....	ii
Table of Contents.....	iii
List of Tables and Figures.....	v
Tables.....	v
Figures.....	vi
1.0 Introduction.....	1
2.0 Hybrid Electric Vehicle Concept Study.....	4
2.1 Configuration Basis, Design Trades, and Evolution.....	4
2.1.1 Hybrid Electric propulsion for a HWB and Conventional Tube and Wing.....	6
2.1.2 Propulsion System Development.....	8
2.2 Configuration Description.....	18
2.2.1 Integration.....	19
2.2.2 Battery Pods.....	21
2.2.3 Propulsion.....	22
2.3 Configuration Analysis and Final Performance.....	24
2.3.1 Aerodynamics.....	24
2.3.2 Mass Properties.....	25
2.3.3 Performance and Sizing.....	25
2.3.4 Acoustic Analysis.....	38
2.3.5 hFan+2: Emissions.....	56
2.3.6 Energy Cost Analysis.....	56
2.4 Technology Plans and Roadmaps.....	63
2.4.1 Hybrid Electric Engine.....	63
2.4.2 High Performance Batteries.....	68
3.0 Hybrid Electric Propulsion Modeling Environment & Sizing Studies.....	72
3.1 Hybrid Electric Modeling Environment.....	72
3.1.1 Electric Model.....	73
3.1.2 Fuel Cell Model.....	88
3.1.3 Battery Model.....	105
3.1.4 Cryocooler Model.....	113
3.1.5 Generating High Speed Propeller Performance Map.....	136
3.2 Hybrid Electric Sizing Studies.....	171
3.2.1 Modeling Methodology.....	171
3.2.2 Gas Turbine Modeling Considerations.....	172
3.2.3 Verification of the NPSS Hybrid Electric Model to GE Public Domain Data.....	176
3.2.4 Hybrid Electric Engine Sizing Studies.....	178

4.0	Summary	187
4.1	Performance and Sizing Analysis.....	187
4.2	Emissions Analysis	187
4.3	Noise analysis	187
4.4	Energy cost analysis	187
4.5	Technology Plans and Roadmaps.....	188
4.6	Hybrid Electric Propulsion Modeling Environment.....	188
4.7	Conclusions.....	188
4.8	Recommendations	188
	References	189
	Appendix A – Georgia Tech Propeller Performance Maps and Reference Sheets.....	A

List of Tables and Figures

Tables

Table 2.1 – hFan+ Key Characteristics	14
Table 2.2 – hFan+ LTO NOx Emissions	14
Table 2.3 – 765-095 Revision History	19
Table 2.4 – Principal Characteristics	21
Table 2.5 - hFan+2 Key Characteristics	24
Table 2.6 – Battery Aero Characteristics	24
Table 2.7 – 765-096-RA Group Weight Statement	25
Table 2.8 – 765-096 Rev A Mission Performance Comparison	30
Table 2.9 – 765-096 Rev A Core Shutdown Trade	31
Table 2.10 – Flight Performance Parameters for Noise Analysis	40
Table 2.11 – Main Gear & Nose Gear Noise Prediction Input Parameters	45
Table 2.12 – Slat Noise Prediction Input Parameters	46
Table 2.13 – Flap Noise Prediction Input Parameters at Approach	48
Table 2.14 – Flap Noise Prediction Input Parameters at Cutback	48
Table 2.15 – Flap Noise Prediction Input Parameters at Sideline	48
Table 2.16 – GE Noise Modeling Assumptions for the SUGAR HE Volt Engine	49
Table 2.17 – Parametric Noise Reduction & Stage 4 CUM Margins for SUGAR High.....	54
Table 2.18 – Parametric Noise Reduction & Stage 4 CUM Margins for SUGAR Volt	54
Table 2.19 – Potential Airframe Noise Reduction Technology.....	55
Table 2.20 – Potential Engine Noise Reduction Technology	55
Table 2.21 – 750 Balanced and Core Shutdown NOx Emissions	56
Table 2.22 – Cost Assumptions.....	58
Table 2.23 – Cost Results for Nominal Cost Assumptions	58
Table 2.24 – Cost Results for More Optimistic Battery Assumptions.....	60
Table 2.25 – Cost Results for Most Optimistic Battery Assumptions	61
Table 3.1 – NPSS HTS Motor Validation.....	80
Table 3.2 – Parameter Estimates	82
Table 3.3 – Validation data used for pressure variation tests.....	99
Table 3.4 – Validation inputs for composition variation tests.....	100
Table 3.5 – Inputs used for improved matching of composition tests.....	101
Table 3.6 – Inputs for temperature variation validation	103
Table 3.7 – Trend line parameters for YSZ resistances.....	105
Table 3.8 – Necessary values from discharge curve	108
Table 3.9 – Validation Inputs	111
Table 3.10 – Comparison of integration results	112

Table 3.11 – Sizing test inputs and results.....	113
Table 3.12 – Thermodynamic Cycle Summary.....	114
Table 3.13 – NPSS Model Independents and Dependents.....	119
Table 3.14 – Comparison NPSS inputs to Source Inputs First Validation	122
Table 3.15 – Comparison NPSS inputs to Source Inputs Second Validation	124
Table 3.16 – NPSS Off Design Dependent and Independent Setup	126
Table 3.17 – F7A7 Design and Operational Variable Values.....	138
Table 3.18 – Hamilton – Standard Performance Maps Design Variable Ranges.....	153
Table 3.19 – Hamilton – Standard Performance Maps Selected for F7A7 Performance Estimation	157
Table 3.20 – Conventional Power Code Definitions	173
Table 3.21 – Conventional NPSS Power Management Scheme	173
Table 3.22 – Electric Power Code Definitions.....	174
Table 3.23 – Georgia Tech hFan Calibration Point	176
Table 3.24 – NPSS Hybrid Electric Weight Assumptions.....	178
Table 3.25 – Core Sensitivity to Sizing With Motor (60 OPR, 2500R T41, FPR 1.45).....	182
Table 3.26 – All Fuel Penalties for Smaller Core	185

Figures

Figure 1.1 – SUGAR Phase II Tasks and Groupings	2
Figure 1.2 – SUGAR Phase II Team Structure.....	3
Figure 2.1 – Hybrid Electric Task Flow	5
Figure 2.2 – SUGAR Hybrid Electric Concepts.....	6
Figure 2.3 – Hybrid Electric Tube and Wing Sizing Results.....	7
Figure 2.4 – Hybrid Electric Aircraft Thrust Requirements.....	8
Figure 2.5 – Booster Stall Margin with Electric Fan Power Augmentation	9
Figure 2.6 – Fan Speed with Electric Power Augmentation	10
Figure 2.7 – Specific Fuel Consumption with Electric Power Augmentation	11
Figure 2.8 – SUGAR Volt Aircraft Sensitivities	12
Figure 2.9 – Hybrid Electric hFan+ Architecture.....	13
Figure 2.10 – Hybrid Electric Architecture with Conventional Electric Technology.....	15
Figure 2.11 – Conventional 8,000HP Electric System Efficiency Map	16
Figure 2.12 – Hybrid Electric Architecture with Superconducting Electric Technology.....	17
Figure 2.13 - Sample Trajectories for Continuous Descent and Descent Regeneration	17
Figure 2.14 – SUGAR Volt (765-096-RevA) General Arrangement	20
Figure 2.15 – 750 Balanced Thrust Requirements.....	23
Figure 2.16 – 750 Core Shutdown Thrust Requirements	23
Figure 2.17 - 765-096-RA 1380 HP sizing Plot.....	28

Figure 2.18 - 765-096-RA 1750 HP sizing Plot.....	28
Figure 2.19 - 765-096-RA 7150 HP sizing Plot.....	29
Figure 2.20 - Economic Mission Fuel and Energy Reduction.....	32
Figure 2.21 - Payload v. Range Chart for Hybrid Electric Aircraft.....	33
Figure 2.22 - Fuel Burn per Segment for Hybrid Electric Aircraft.....	34
Figure 2.23 - Energy Use per Segment for Hybrid Airplanes.....	34
Figure 2.24 - Specific Range (Energy) per Segment for Hybrid Airplanes.....	35
Figure 2.25 - Fuel Burn v. Range for Hybrid Aircraft.....	36
Figure 2.26 – Energy v. Range for Hybrid Aircraft.....	37
Figure 2.27 – Battery Weight v. Range for Hybrid Aircraft.....	37
Figure 2.28 – Modes of operation for hybrid airplanes.....	38
Figure 2.29 – Fleet Fuel and Energy Reduction as compared to NASA Goal.....	38
Figure 2.30 – Noise Levels & Stage 4 Margins for the SUGAR High & Volt.....	39
Figure 2.31 – FAR 36 Noise Profile.....	40
Figure 2.32 – Overall Noise Analysis Process.....	41
Figure 2.33 – SUGAR Geometry at Approach.....	42
Figure 2.34 – CFD++ Solution Convergence.....	43
Figure 2.35 – CFD++ Computed Mach Cuts.....	43
Figure 2.36 – Post-Processing of CFD++ Data for Computing Sectional Lift Coefficient.....	44
Figure 2.37 – Airframe Noise Analysis Process.....	45
Figure 2.38 – SUGAR Slat System Deployment for Approach/Cutback/Sideline.....	46
Figure 2.39 – SUGAR Slat System 3-Element Definition for Noise Analysis.....	46
Figure 2.40 – SUGAR Flap System Deployment at Approach.....	47
Figure 2.41 – SUGAR Flap System Deployment at Cutback/Sideline.....	47
Figure 2.42 – SUGAR Flap System Definition for Noise Analysis.....	47
Figure 2.43 – GE Noise-Power-Distance (NPD) Predictions for Hardwall Engine.....	49
Figure 2.44 – Process for Derivation of SUGAR HE Treated Engine Noise.....	50
Figure 2.45 – PNLT Contribution at AP from All Subcomponents for SUGAR Volt.....	51
Figure 2.46 – PNLT Contribution at CB from All Subcomponents for SUGAR Volt.....	52
Figure 2.47 – PNLT Contribution at SL from All Subcomponents for SUGAR Volt.....	52
Figure 2.48 – Comparison of Total Engine and Airframe Noise for the SUGAR Volt.....	53
Figure 2.49 – Energy + Battery Cost Results for Nominal Assumptions.....	59
Figure 2.50 – Total Cost Results for Nominal Assumptions.....	59
Figure 2.51 – Energy + Battery Cost Results for More Optimistic Battery Assumptions.....	60
Figure 2.52 – Total Cost Results for More Optimistic Battery Assumptions.....	61
Figure 2.53 – Energy + Battery Cost Results for Most Optimistic Battery Assumptions.....	62
Figure 2.54 – Total Cost Results for Most Optimistic Battery Assumptions.....	62
Figure 2.55 – Hybrid Electric Engine Technologies*.....	67
Figure 2.56 – High Performance Battery Technology Roadmap.....	71

Figure 3.1 – Half Wave Rectifier	76
Figure 3.2 – Solver layout diagram	78
Figure 3.3 – Motor Loss Buildup	83
Figure 3.4 – SRM Torque-Speed Characteristic	84
Figure 3.5 – Motor Off-Design Operation.....	88
Figure 3.6 – Diagram of SOFC	91
Figure 3.7 – SOFC Architectures	92
Figure 3.8 – Formation of the polarization curve	93
Figure 3.9 – Comparison of model pressure test output with output from (24)	99
Figure 3.10 – Comparison of model composition test outputs with results from (24).....	101
Figure 3.11 – Model output from improved composition matching with results from (24).....	101
Figure 3.12 – Initial comparison of model output with experimental data from (23).....	104
Figure 3.13 – Comparison of improved matching output with experimental data (23)	104
Figure 3.14 – Arrhenius plot of YSZ resistances.....	105
Figure 3.15 – Example battery discharge curve.....	108
Figure 3.16 – Data flow for Sizing algorithm.....	111
Figure 3.17 – Battery performance model validation plots.....	112
Figure 3.18 – Power Capacity vs Specific Mass Cryocooler Survey	115
Figure 3.19 – Power vs Mass for Cryocooler Types	115
Figure 3.20 – Power Capacity vs Percent Carnot for Cryocooler Types	116
Figure 3.21 – Closed Circuit Reverse Turbo Brayton Cycle.....	117
Figure 3.22 – Reverse Turbo Brayton Diagram (from Create Contract #NAS5-31281).....	118
Figure 3.23 – NPSS Block Schematic of Reverse Turbo Brayton Cycle	119
Figure 3.24 – setTotalSP workaround using Secant Solver	121
Figure 3.25 – NPSS Model Comparison to Actual Data First Validation	122
Figure 3.26 – First Validation H-S Diagram	123
Figure 3.27 – NPSS Model Comparison to Actual Data Second Validation	125
Figure 3.28 – Second Validation H-S Diagram	125
Figure 3.29 – Rejection Temperature	127
Figure 3.30 – Heat Rejection Load	127
Figure 3.31 – HPC Power.....	128
Figure 3.32 – HPT Power.....	128
Figure 3.33 – FS_2 Temperature.....	129
Figure 3.34 – FS_2 Pressure	129
Figure 3.35 – FS_2 Massflow	129
Figure 3.36 – FS_3 Temperature.....	130
Figure 3.37 – FS_3 Pressure	130
Figure 3.38 – FS_3 Massflow	130
Figure 3.39 – FS_5 Temperature.....	131

Figure 3.40 – FS_5 Pressure	131
Figure 3.41 – FS_5 Massflow	131
Figure 3.42 – FS_6 Temperature.....	132
Figure 3.43 – FS_6 Pressure.....	132
Figure 3.44 – FS_6 Massflow	132
Figure 3.45 – FS_7 Temperature.....	133
Figure 3.46 – FS_7 Pressure	133
Figure 3.47 – FS_7 Massflow	133
Figure 3.48 – RC_4 Temperature	134
Figure 3.49 – RC_4 Pressure	134
Figure 3.50 – RC_4 Massflow.....	134
Figure 3.51 – HX_1 at HEX	135
Figure 3.52 – CX_1 at CEX	135
Figure 3.53 – CX_3 Heat Absorption.....	135
Figure 3.54 – HX_1 Across HEX.....	135
Figure 3.55 – CX_1 Across CEX.....	136
Figure 3.56 – Turbine Pressure Ratio.....	136
Figure 3.57 – Compressor Pressure Ratio.....	136
Figure 3.58 – F7A7 C_{PQA} vs. Advance Ratio Map.....	138
Figure 3.59 – F7A7 Efficiency vs. C_{PQA} / J^3 Map.....	139
Figure 3.60 – F7A7 C_{PQA} vs. Advance Ratio for $2 \leq J \leq 3$	140
Figure 3.61 – F7A7 Efficiency vs. C_{PQA} / J^3 for $2 \leq J \leq 3$	140
Figure 3.62 – Constant Speed Propeller Operation.....	142
Figure 3.63 – NACA Method Correction for Blade Number and Geometry (39).....	143
Figure 3.64 – NACA Method Compressibility Correction (39).....	144
Figure 3.65 – NACA Method Counter-Rotation Correction (39).....	145
Figure 3.66 – SR-1 Peak Efficiency Points based on Pitch Angle	147
Figure 3.67 – SR-1 Peak Efficiency Points based on Advance Ratio	147
Figure 3.68 – Repopulated Compressibility Correction Chart based on SR-1 Data.....	148
Figure 3.69 – Blade Geometry Correction based on SR-1 Data.....	149
Figure 3.70 – Validation Test Efficiency vs. Advance Ratio for the Adjusted NACA Method at Mach 0.2	150
Figure 3.71 – Validation Test Efficiency Error for the Adjusted NACA Method at M=0.2.....	150
Figure 3.72 – Validation Test Efficiency vs. Advance Ratio for the Adjusted NACA Method at M=0.6.....	151
Figure 3.73 – Validation Test Efficiency Percent Error for the Adjusted NACA Method at M=0.6	151
Figure 3.74 – Validation Test Efficiency vs. Advance Ratio for the Adjusted NACA Method at M=0.75.....	152

Figure 3.75 – Validation Test Efficiency Percent Error for the Adjusted NACA Method at
 M=0.75 152

Figure 3.76 – Sample Hamilton – Standard Performance Map (40)..... 154

Figure 3.77 – Hamilton – Standard General Compressibility Correction (40) 155

Figure 3.78 – Hamilton – Standard Mach Number Adjustment for Blade Camber (40) 156

Figure 3.79 – Interpolated C_{PQA} vs. Advance Ratio Map for F7A7 158

Figure 3.80 – Interpolated Efficiency vs. Advance Ratio Map for F7A7 158

Figure 3.81 – Output Generation Steps for the Validation Test..... 159

Figure 3.82 – Efficiency vs. C_{PQA} / J^3 Validation Test at a Pitch Angle of 55.7° 160

Figure 3.83 – Validation Test Efficiency Percent Error at a Pitch Angle of 55.7° 160

Figure 3.84 – C_{PQA} vs. J Validation Test at a Pitch Angle of 55.7° 161

Figure 3.85 – Validation Test C_{PQA} Percent Error at a Pitch Angle of 55.7° 161

Figure 3.86 – Efficiency vs. C_{PQA} / J^3 Validation Test at a Pitch Angle of 56.9° 162

Figure 3.87 – Validation Test Efficiency Percent Error at a Pitch Angle of 56.9° 162

Figure 3.88 – C_{PQA} vs. Advance Ratio Validation Test at a Pitch Angle of 56.9° 163

Figure 3.89 – Validation Test C_{PQA} Percent Error at a Pitch Angle of 56.9° 163

Figure 3.90 – Efficiency vs. C_{PQA} / J^3 Validation Test at a Pitch Angle of 58.5° 164

Figure 3.91 – Validation Test Efficiency Percent Error at a Pitch Angle of 58.5° 165

Figure 3.92 – C_{PQA} vs. Advance Ratio Validation Test at a Pitch Angle of 58.5° 165

Figure 3.93 – Validation Test C_{PQA} Percent Error at a Pitch Angle of 58.5° 166

Figure 3.94 – Efficiency vs. C_{PQA} / J^3 Validation Test at a Pitch Angle of 60.2° 166

Figure 3.95 – Validation Test Efficiency Percent Error at a Pitch Angle of 60.2° 167

Figure 3.96 – C_{PQA} vs. Advance Ratio Validation Test at a Pitch Angle of 60.2° 167

Figure 3.97 – Validation Test C_{PQA} Percent Error at a Pitch Angle of 60.2° 168

Figure 3.98 – Efficiency vs. C_{PQA} / J^3 Validation Test at a Pitch Angle of 61.2° 169

Figure 3.99 – Validation Test Efficiency Percent Error at a Pitch Angle of 61.2° 169

Figure 3.100 – C_{PQA} vs. Advance Ratio Validation Test at a Pitch Angle of 61.2° 170

Figure 3.101 – Validation Test C_{PQA} Percent Efficiency at a Pitch Angle of 61.2° 170

Figure 3.102 – Hybrid Electric Engine Architecture (53)..... 172

Figure 3.103 – GE hFan Powerhook..... 176

Figure 3.104 – Georgia Tech Hybrid Electric Trends..... 177

Figure 3.105 – Georgia Tech Average Performance 177

Figure 3.106 – Motor Sized Non-Cryogenic Fan Sizing Breakdown..... 179

Figure 3.107 – Cryogenic Cycle Trades 180

Figure 3.108 – Cryogenic System Sizing..... 181

Figure 3.109 – FPR Electric and Sizing Trades..... 182

Figure 3.110 – OPR / T41 Trade Space..... 183

Figure 3.111 – OPR/T41 Electric and Sizing Trades 184

1.0 Introduction

In 2009-2010, Boeing conducted the Subsonic Ultra Green Aircraft Research (SUGAR) study for NASA. In this study, Boeing identified and analyzed advanced concepts and technologies for aircraft that would fly in the 2030-2035 timeframe. Large possible improvements in fuel burn, emissions, and noise were identified and roadmaps developed for key technologies. Specific recommendations were made in the Boeing Phase I Final Report (1):

- Conduct additional design and analysis of hybrid electric gas turbine propulsion
- Conduct a comprehensive study of high aspect ratio truss braced wings
- Consider additional noise technologies (partially addressed as part of hybrid electric tasks)
- Conduct a follow-on study to consider the synergistic benefits of methane and/or hydrogen fuel

Considering the recommendations of Boeing and the other contractor teams, as well as program objectives, NASA developed these Research Objectives for Phase II:

- Experimental and Higher-Fidelity Exploration of Key Technologies to investigate the prioritized technology challenges identified in Phase I and begin moving toward the realization of the proposed vehicle concept(s) capabilities that would enable an entry into service (EIS) in the 2030-2035 timeframe, market permitting
- N+3 Advanced Vehicle Concept Study to further explore, refine, and otherwise update the preferred N+3 advanced vehicle and component concept(s) identified and developed during Phase I
- N+4 Advanced Vehicle Concept Study to leverage the substantial investment of Phase I and study the effect of additional technology development time beyond that assumed in Phase I

Boeing structured the SUGAR Phase II program to address the recommendations from Phase I as well as the research objectives provided by NASA. Three major tasks, corresponding to the Research Objectives, are included in this Phase II effort. Subtasks are organized and grouped by technical area (Figure 1.1).

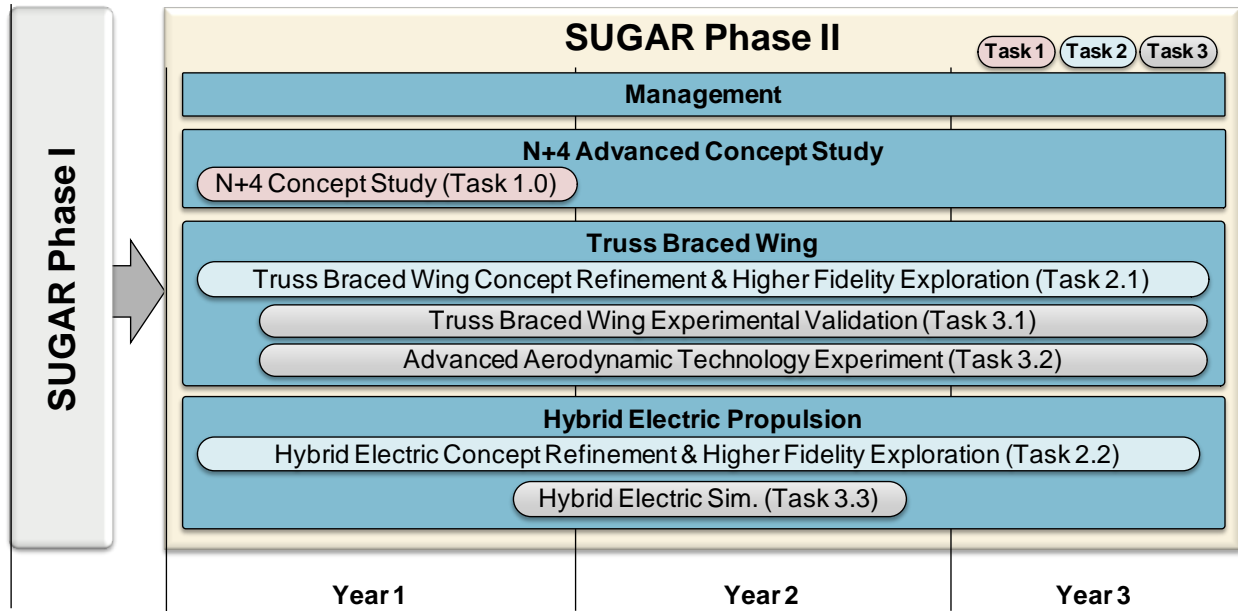


Figure 1.1 – SUGAR Phase II Tasks and Groupings

The SUGAR team from Phase I consisted of Boeing Research and Technology, Boeing Commercial Airplanes, General Electric, and Georgia Tech. In Phase II (depicted in Figure 1.2), the team was expanded to include Virginia Tech, NextGen Aeronautics, and Microcraft to enhance the technical capability and to build hardware to support the testing of the truss-braced wing tasks.

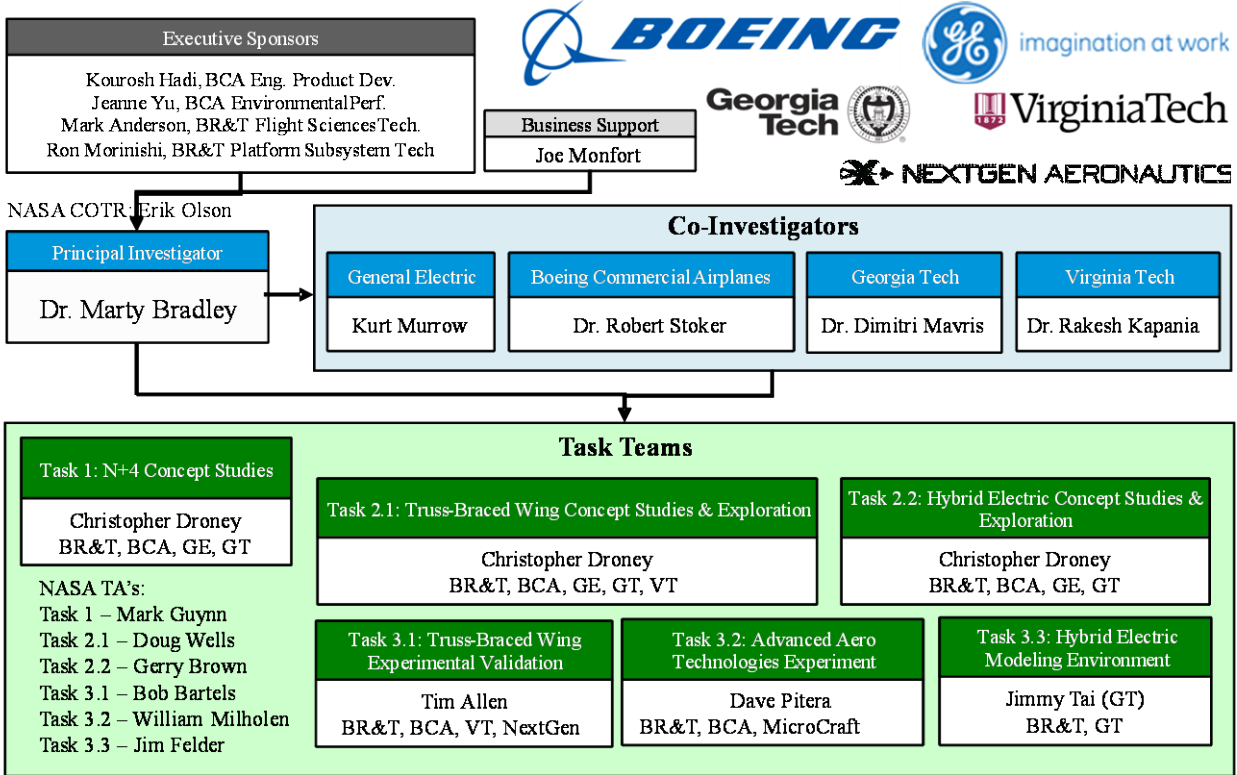


Figure 1.2 – SUGAR Phase II Team Structure

This is the Final Report for Tasks 2.2 and 3.3 only. Task 1 is fully documented in the Task 1 final report (2) and Truss Braced Wing Tasks 2.1, 3.1, and 3.2 are fully documented in a separate Final Report (Volume I – Truss Braced Wing Design Exploration) and Test Report (Volume III – Truss Braced Wing Aeroelastic Test Report). In 2012, additional resources were allocated to Task 3.3 to allow more integrated hybrid electric modeling by Georgia Tech and those results are documented in the report.

2.0 Hybrid Electric Vehicle Concept Study

As part of SUGAR Phase II, hybrid electric vehicles were analyzed. Due to the iterative nature of airplane development, trades are performed at various stages of development. For clarity, this document breaks the configuration development into three sections.

Section 2.1 – Configuration Basis, Design Trades, and Evolution, focuses on the trades and logic that lead to the air vehicle’s current embodiment. All data contained within is intended to document the mid-iteration trades and should not be correlated to the final configuration performance unless specifically noted.

Section 2.2 – Configuration Description, details the final configuration in detail. This section represents the vehicle as analyzed for vehicle performance.

Section 2.3 – Configuration Analysis and Final Performance contains the analysis results and performance data for the vehicle described in the previous section.

2.1 Configuration Basis, Design Trades, and Evolution

One recommendation from Phase I was to perform additional design and analysis of hybrid electric gas turbine propulsion. To address this, in Phase II the team was funded to perform the following design and analysis tasks:

- Refine the hybrid gas turbine/ battery powered (hFan) propulsion system concept arrived at in Phase I.
- Investigate conceptual layouts of the hybrid architecture.
- Generate propulsion data for the revised engine concept(s) across the mission flight envelope, gas generator power settings and battery-to-gas generator power splits.
- Update its integration, resizing the configuration and updating the performance assessment.
- Conduct a trade study on total energy cost by parametrically varying fuel cost, battery performance, battery life, battery cost, and electricity cost.
- Estimate the noise during takeoff and approach with combined electric-turbine operation.
- Integrate the hybrid gas turbine/ battery powered propulsion system on the Refined SUGAR (conventional low-wing tube-and-wing configuration) and SUGAR Ray (Hybrid Wing body), resize those configurations and assess their fuel burn, emissions, noise and takeoff performance compared to NASA’s Subsonic Fixed Wing N+3 goals.
- Update the technology roadmaps from Phase I.

This work has been organized into the tasks and task flow shown in Figure 2.1. The various new configuration nicknames are shown in Figure 2.2, with the Task 2.2 configurations highlighted.

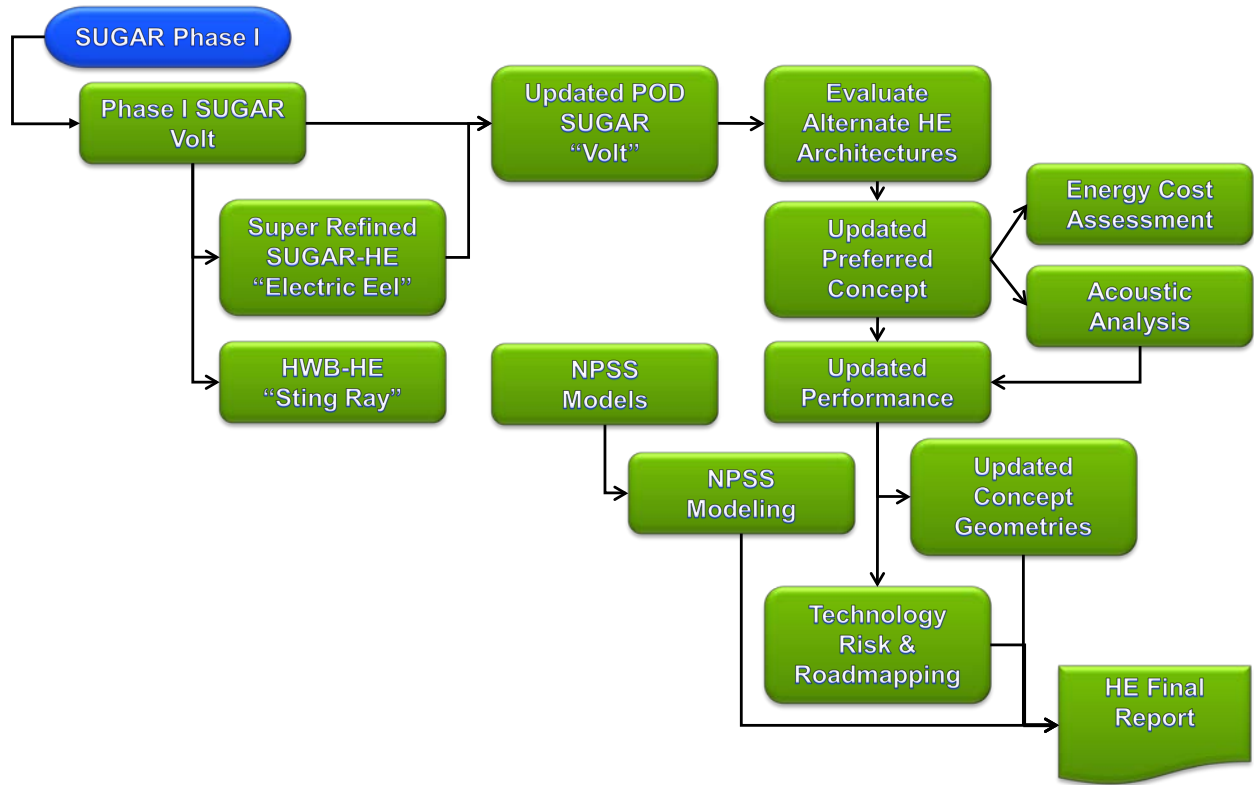


Figure 2.1 – Hybrid Electric Task Flow










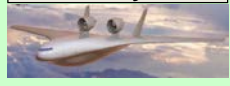
	N	N+3	N+3 Hybrid Electric	N+4
Conventional Tube & Wing	Baseline "SUGAR Free" 	Reference "Refined SUGAR" 		N+4 Reference "Super Refined SUGAR" 
Unconstrained* Conventional Tube & Wing * <i>Optimum span</i>		"Super Refined SUGAR" 	"SUGAR Electric Eel" 	
High Span Truss Braced Tube & Wing		TBW High L/D "SUGAR High" 	"SUGAR Volt" 	Advanced N+4 Technology "SUGAR Freeze" 
HWB		HWB "SUGAR Ray" 	"SUGAR Sting Ray" 	

Figure 2.2 – SUGAR Hybrid Electric Concepts

2.1.1 Hybrid Electric propulsion for a HWB and Conventional Tube and Wing

At the end of Phase I, since the SUGAR Volt was based on the high span truss-braced SUGAR High configuration, there was a question as to whether the benefits of hybrid electric propulsion would apply equally well to conventional tube-and-wing and Hybrid Wing Body configurations. At the beginning of Task 2.2, a sizing study was performed to investigate this question. Results showed nearly identical performance improvements. Additional information on these results is shown below.

Please note: the information contained within this section is not directly comparable to the results shown in Section 2.3. These results are produced with a different set of engine data, vehicle analysis methods, and performance tools and are more comparable to SUGAR Phase I results.

2.1.1.1 Hybrid Electric HWB "SUGAR Sting Ray"

The HE increment for the HE HWB was very similar to original SUGAR Volt. At the 900 nm average mission range, adding hybrid electric propulsion reduces fuel burn by:

- 25%-46% compared to original SUGAR Ray
- 57%-70% compared to SUGAR Free Baseline

Similar to the original SUGAR Volt from Phase I, the SUGAR Ray-HE (SUGAR Sting Ray) had a fuel burn advantage at ranges less than ~2,800 nm.

2.1.1.2 Hybrid Electric Tube & Wing “SUGAR Electric Eel”

The HE increment for the HE tube and wing configuration was very similar to original SUGAR Volt. The “Super Refined SUGAR” configuration, with the gFan+ engine and without wing span constraints, was used as a baseline. At the 900 nm average mission range, adding hybrid electric propulsion reduces fuel burn by:

- 33%-55% compared to conventional gFan+ propulsion
- 65%-79% compared to SUGAR Free Baseline

The SUGAR Electric Eel had a wingspan of approximately 162 ft. and a cruise L/D of approximately 24.5. It is likely that a span constrained version (118 ft.) would not have as significant a benefit for HE propulsion, as the heavy electrical components would carry a larger performance penalty due to the lower vehicle lift-to-drag ratio.

Similar to the original SUGAR Volt from Phase I, the Super Refined SUGAR-HE (SUGAR Electric Eel) had a fuel burn advantage at ranges less than 2,800-2,900 nm (Figure 2.3).

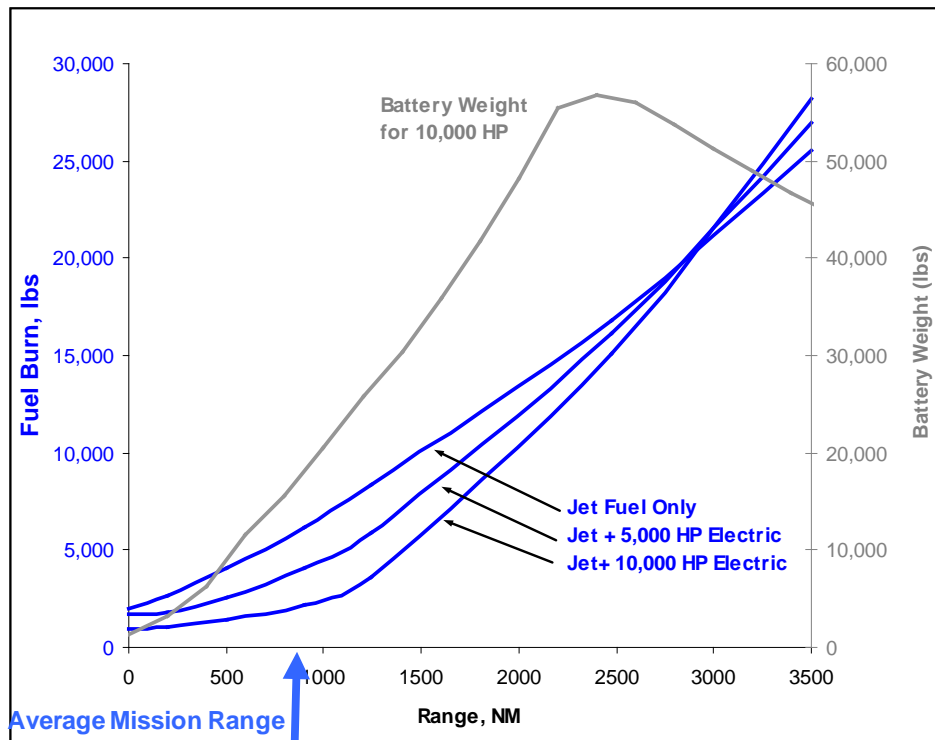


Figure 2.3 – Hybrid Electric Tube and Wing Sizing Results

2.1.2 Propulsion System Development

This study is focused on refining the hybrid gas turbine/electric powered propulsion system architecture developed in Phase I. The objectives are to decrease fuel burn, noise, and emissions while evolving a viable design. The hFan engine proposed in Phase I of the program was modeled as a mixed-flow hybrid electric turbofan and post processed to create a separate-flow representation of the propulsion system performance dataset based on program time constraints and funding.

For increased fidelity and functionality, the mixed-flow NPSS model used in Phase I was reworked for use in Phase II. The mixer was removed and a core nozzle was added to create a separate-flow NPSS model. The improved model maintains separate core and bypass streams. The separate-flow turbofan model enables accurate modeling of thrust bookkeeping and turbo machinery operating lines. In addition, the separate-flow model allows both variable fan and core nozzles. The variable area nozzles provide stability margin on the fan and booster when electric power is applied to the Low Pressure (LP) spool.

2.1.2.1 Hybrid Electric Aircraft Thrust Requirements

Boeing provided thrust requirements representative of the Hybrid Electric (HE) aircraft concept, termed the SUGAR Volt, for use in hybrid electric propulsion system studies. These requirements, along with the Boeing aircraft are shown in Figure 2.4. GE has provided scaling rules to resize the engine as the aircraft evolves, as well as for use with other single aisle aircraft.

SUGAR Volt



TOGW:	170,000 lbf
Top of Climb Thrust per engine:	3,500 lbf
Takeoff BET required per engine:	17,500 lbf
Takeoff SLST:	20,100 lbf

Figure 2.4 – Hybrid Electric Aircraft Thrust Requirements

2.1.2.2 Initial Hybrid Electric Turbo Machinery Modeling (hFan+)

Utilizing the separate-flow turbofan NPSS model, preliminary power sweeps have been executed to analyze the effects of adding electric power to the LP spool. Initial runs modeled electric fan power augmentation of up to 6,000HP in increments of 1,000HP. Power augmentation sweeps have been completed at takeoff and cruise flight conditions.

As electric power is added to the LP spool the booster stall margin drops toward the minimum acceptable level. The variable core nozzle closes to alleviate the booster operating line, but its authority is not sufficient to maintain the required booster stall margin. Thus, as electric power is added, variable bleed valve (VBV) doors open to direct flow from the booster into the fan stream. The VBV modulates to the minimum acceptable booster stall margin, as shown below in Figure 2.5. An innovative VBV design, capable of accepting large fractions of the booster airflow will be required for this architecture. The ability to efficiently mix the bleed flow with the core stream will play a strong role in establishing the transfer and propulsive efficiencies of the propulsion system, and will therefore be critical for efficient utilization of battery electric power. Alternative architectures alleviating this potential inefficiency have been identified for exploration.

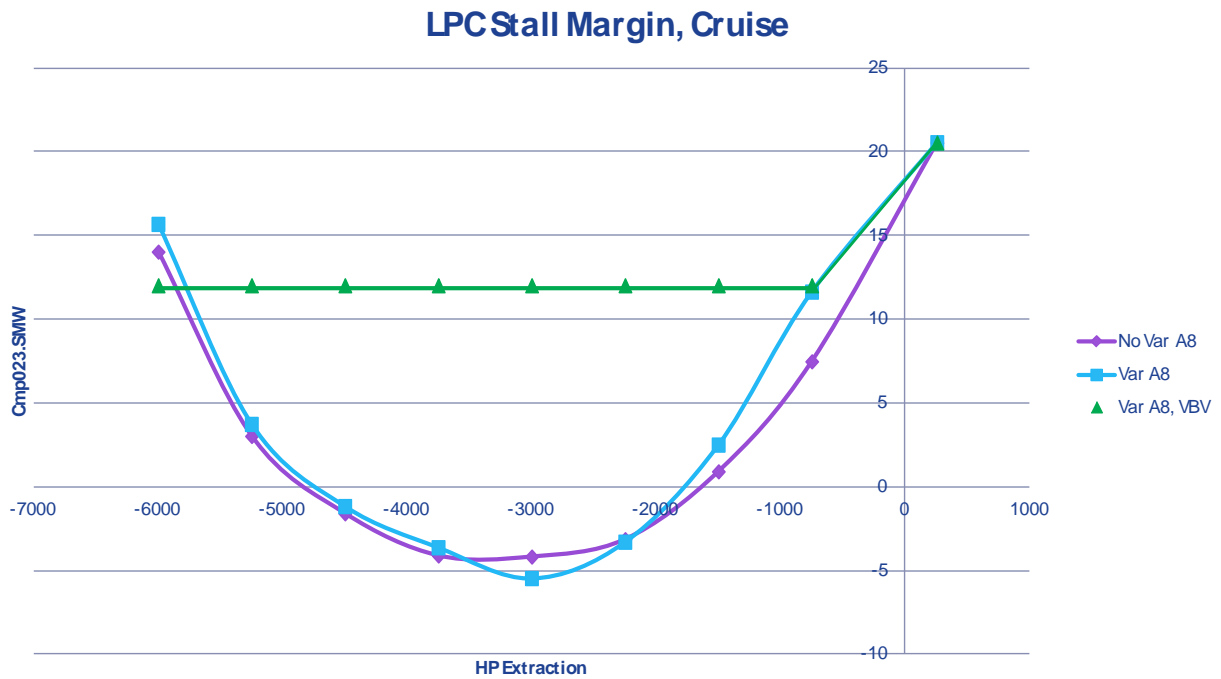


Figure 2.5 – Booster Stall Margin with Electric Fan Power Augmentation

For a fixed thrust setting, as electric power is added to the LP spool, the turbofan core will roll back, leading to a loss of core thrust. Consequently, a conventionally designed fan must overspeed to maintain the given thrust requirement. However, the excessive fan speed becomes

inefficient at this off-design operating condition, as well as possibly mechanically prohibitive. The fan speed increase trend can be seen below in Figure 2.6. To correct this condition, a larger fan must be designed, accounting for the deficit in core thrust while preserving the intended maximum electric augmented operating speed. Alternatively, electric augmentation could be reserved for cruise, in which case the unaugmented fan and core would be adequate to produce climb thrust. The interwoven nature of design and control philosophies for the hybrid propulsion system emphasizes the need for a highly integrated airframe/engine manufacturer design process.

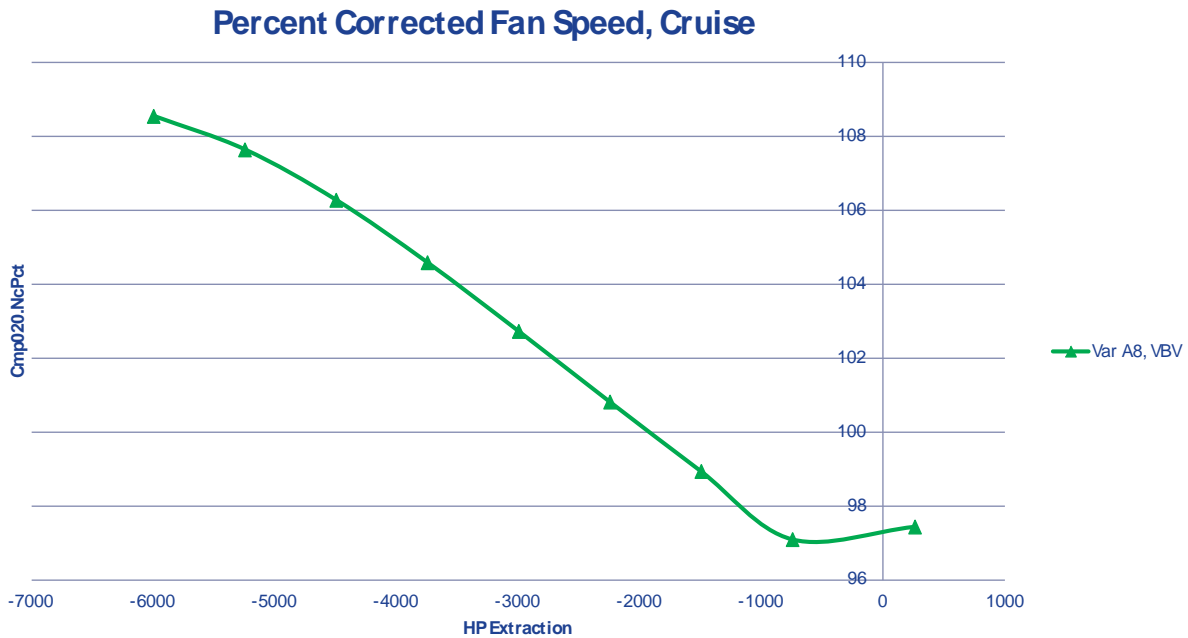


Figure 2.6 – Fan Speed with Electric Power Augmentation

The addition of electric power will decrease the fuel consumption of the propulsion system at a specified thrust level. Electric fan power augmentation causes the fuel flow to cut back, resulting in substantial improvements in SFC, as shown in Figure 2.7. At the cruise condition, a 6,000HP electric motor results in roughly a 75% SFC reduction.

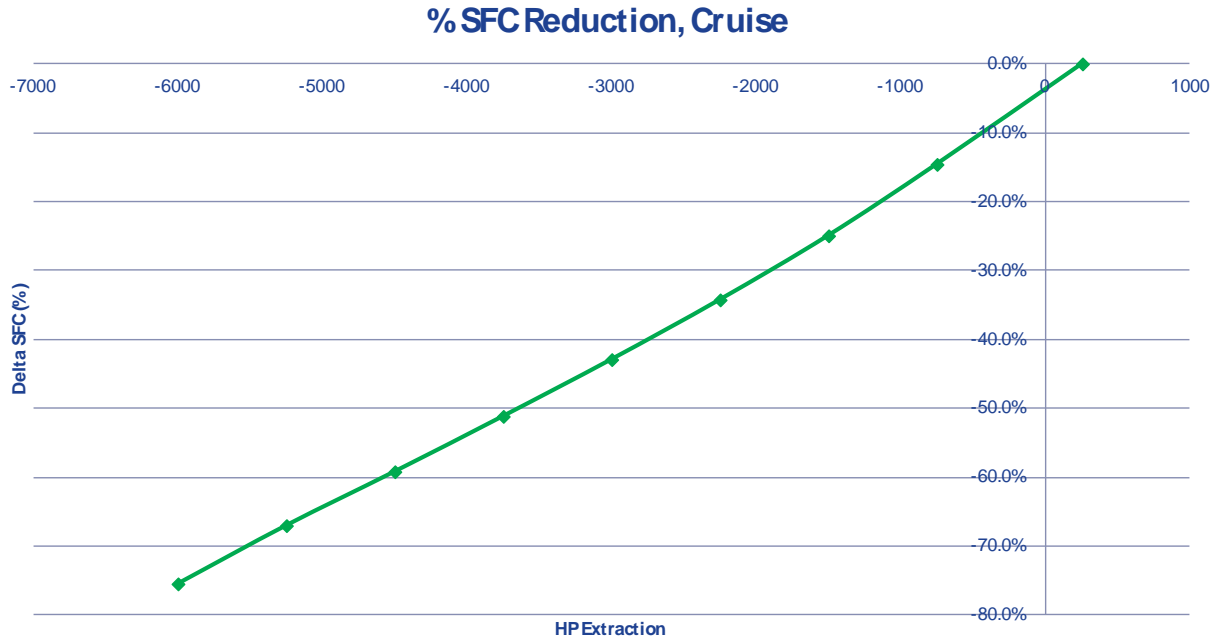


Figure 2.7 – Specific Fuel Consumption with Electric Power Augmentation

The electric fan augmentation allows for substantial improvements in SFC for the Hybrid Electric propulsion system. While this improvement in SFC does not necessarily represent a reduction in specific energy consumption, it does represent a shift from generating the mechanical power in flight to generating it on the ground, where there is significant flexibility and potential for cost and emissions reduction.

2.1.2.3 *hFan+ Advanced Hybrid Electric Turbofan*

The propulsion system for the SUGAR Volt airframe is a hybrid electric engine architecture that utilizes an electric motor to distribute power to the LP spool of the turbofan. The propulsion system is also required to satisfy the SUGAR Volt thrust requirements while operating strictly as an advanced turbofan, without aid of the electric motor. In SUGAR phase II, Boeing provided GE with aircraft fuel burn sensitivities to engine specific fuel consumption, weight, and drag for the SUGAR Volt aircraft. These sensitivities are summarized in Figure 2.8.

SUGAR Volt

- 1% SFC = 1.1% FB
- 1000 lbs Engine Wt = 12% FB
- 2.4 lbf Nacelle Drag = 0.10% FB
- 2.4 lbf Drag per inch of Fan Diameter
- 1 inch Fan Dia = 0.10% FB
- 1% Battery Weight = 1.02% FB

Figure 2.8 – SUGAR Volt Aircraft Sensitivities

The concept of utilizing batteries in conjunction with an electric motor to add power to the LP spool of a gas turbine for aviation use was explored in phase I of the SUGAR program. In Phase II, the concept was investigated with increased fidelity. For Concept 1, the hFan+, the team completed a parametric study utilizing derivatives from Boeing found above in Figure 2.8. The study's result is a direct-drive turbofan with a 1.45 fan pressure ratio. This selection yields a sacrifice in SFC to realize a lighter weight, lower drag engine. The resulting design minimizes fuel burn while meeting the thrust requirements of both a 3,500nm and 900nm mission. An electric motor translates energy from the batteries via a power conditioning unit to add power on the LP spool. In discussion with Boeing, the electrical system bookkeeping was divided into two sections separated at the pylon interface. GE is responsible for the electric motor, propulsion system line losses, and power conditioning, while Boeing will account for the batteries, aircraft line losses, and turnaround efficiency. An overview of the key characteristics of the hFan+ and the electrical system bookkeeping is shown below in Figure 2.9.

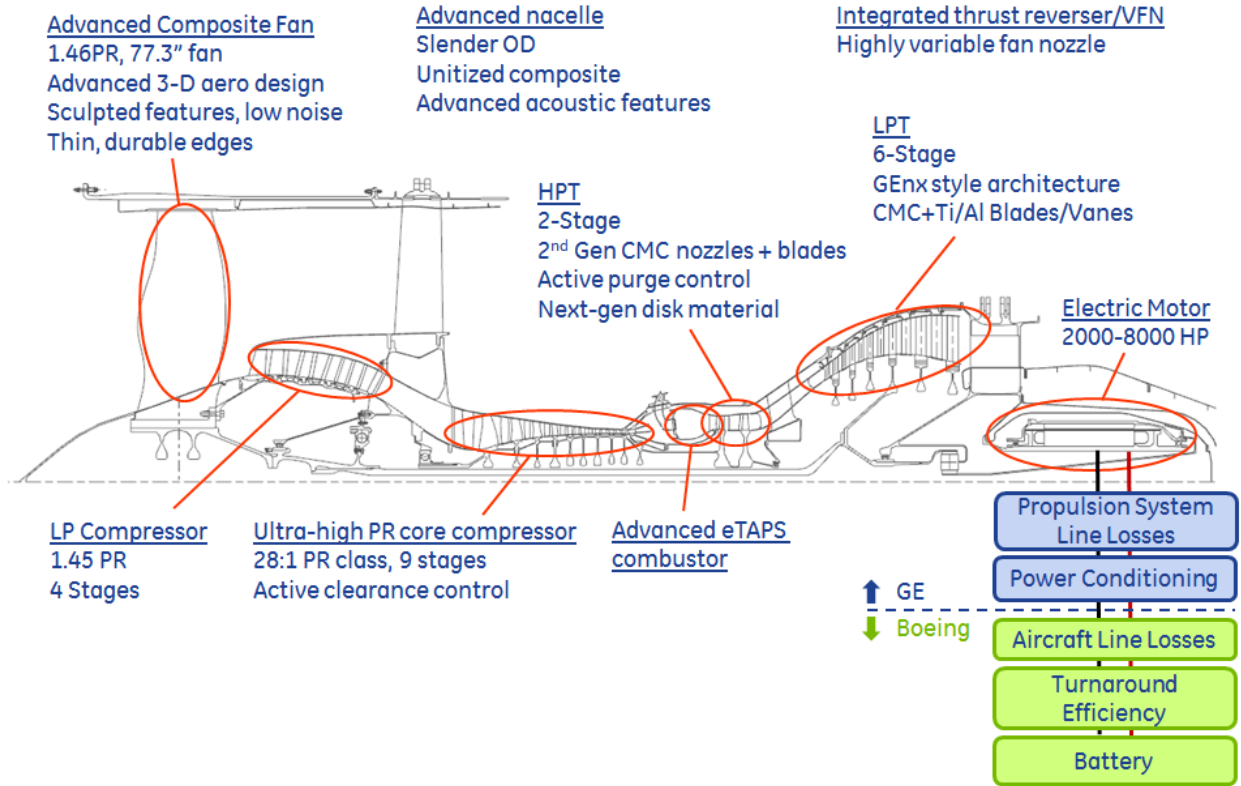


Figure 2.9 – Hybrid Electric hFan+ Architecture

As a result of discussions with Boeing, GE completed four electrical system layouts with design electric motor outputs of 2,000HP, 4,000HP, 6,000HP, and 8,000HP. This sweep in electrical power would provide Boeing the option to use electric power to partially or fully drive the LP spool. As a result, the core of the turbofan could be slowed to an idle or windmilling condition, if desired. A summary of the propulsion system key characteristics is provided in Table 2.1.

Table 2.1 – hFan+ Key Characteristics

hFan+ (2000HP Electric Motor)			hFan+ (4000HP Electric Motor)		
Fan Diameter	78.6"		Fan Diameter	78.6"	
Length	129"		Length	129"	
Propulsion System Weight	7572 lbf		Propulsion System Weight	8422 lbf	
	Thrust (lbf)	SFC (lbm/lbf/hr)		Thrust (lbf)	SFC (lbm/lbf/hr)
SLS	24048	0.180	SLS	24048	0.159
TKOF	18025	0.271	TKOF	18025	0.244
TOC	3605	0.320	TOC	3605	0.214
Cruise	2884	0.407	Cruise	2884	0.257
hFan+ (6000HP Electric Motor)			hFan+ (8000HP Electric Motor)		
Fan Diameter	78.6"		Fan Diameter	78.6"	
Length	129"		Length	129"	
Propulsion System Weight	9272 lbf		Propulsion System Weight	10122 lbf	
	Thrust (lbf)	SFC (lbm/lbf/hr)		Thrust (lbf)	SFC (lbm/lbf/hr)
SLS	24048	0.139	SLS	24048	0.120
TKOF	18025	0.218	TKOF	18025	0.192
TOC	3605	0.112	TOC	3605	0.000
Cruise	2884	0.000	Cruise	2884	0.000

2.1.2.4 Emissions

The LTO NOx emissions for the hFan+ propulsion system were assessed. The CAEP/6 requirements, characteristic LTO NOx, and margined estimates are listed below in Table 2.2. Calculations for the LTO NOx emissions were performed for both the non-electric and electric modes of operation.

Table 2.2 – hFan+ LTO NOx Emissions

LTO NOx Emissions - Round 1 hFan+		
	hFan Non-Electric	hFan Electric
CAEP/6, g/kN	66.2	66.2
Characteristic LTO NOx, g/kN	13.5	7.9
Margined Estimate, % CAEP/6	22.6%	13.2%

2.1.2.5 hFan+ Conventional Electrical System

In agreement with Boeing and NASA, the team decided to investigate both conventional and superconducting electrical systems for application on the SUGAR Volt. The hFan+ utilizes a conventional electrical system. On the propulsion side, the system requires a power conditioner, solid state circuit breaker, heat exchanger, and an electric motor. The conventional system utilizes a Switched Reluctance Motor (SRM). The motor sizing assumptions are based on a high power density SRM with liquid cooling for continuous peak electromagnetic power operation. Advanced composite materials are used for the shaft and motor case. The power

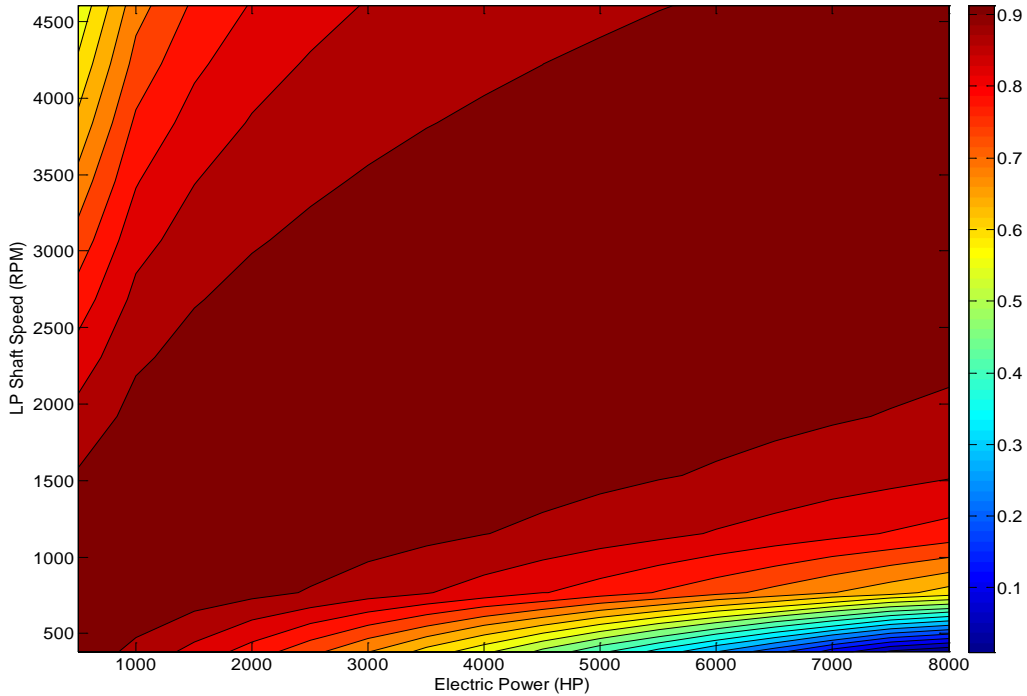


Figure 2.11 – Conventional 8,000HP Electric System Efficiency Map

2.1.2.6 *hFan+ Superconducting Electrical System*

A superconducting electrical system has also been analyzed. This system also requires a power conditioner, solid state circuit breaker, heat exchanger, and an electric motor. The electrical system utilizes a superconducting electric motor, wires, and power conditioner. The motor sizing assumptions are based on the availability of liquid natural gas to the system. The motor includes conductors that are held at LNG temperatures and are superconducting with alternating current. The motor requires high strength insulating structural materials and an evacuated ironless design. The power conditioning unit employs an advanced composite LNG cooled heat sink and high voltage SiC devices. It also takes advantage of advanced low loss inductors and advanced plastic film capacitors. The resulting superconducting electric system has a specific power in the class of 5-6 HP/lbm and an overall efficiency of ~0.99. An overview of the superconducting electrical system is displayed below in Figure 2.12. The superconducting architecture was used in Task 1 (reported separately) and was also modeled in Task 3.3, but was not part of the SUGAR Volt performance and sizing analysis that follows.

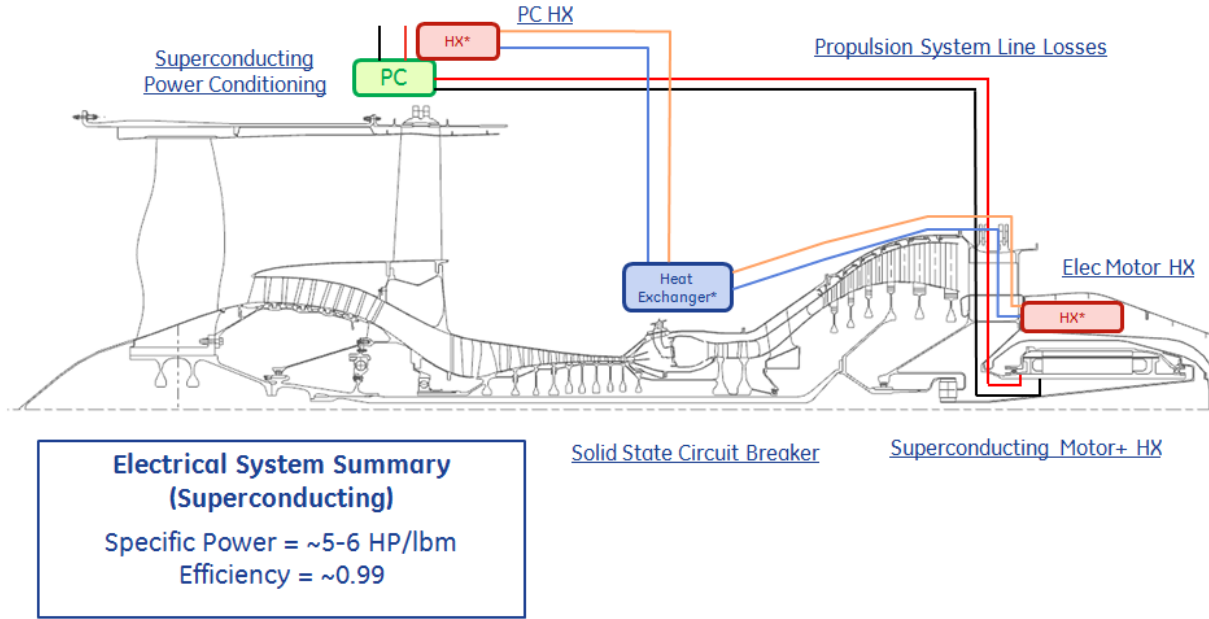


Figure 2.12 – Hybrid Electric Architecture with Superconducting Electric Technology

2.1.2.7 Regenerating Descent Energy into the Battery System

The best fuel burn is achieved when a continuous descent approach is utilized, with minimal energy expended during the descent and speed is varied to maintain a high L/D ratio throughout the descent. For the SUGAR N+3 timeframe, it is assumed that air traffic management is highly efficient and that continuous descent approaches are the norm. Extracting power during the descent will lower the aircraft L/D and steepen the descent angle. This requires the aircraft to have flown further in cruise and consume energy before the descent. This is illustrated in Figure 2.13.

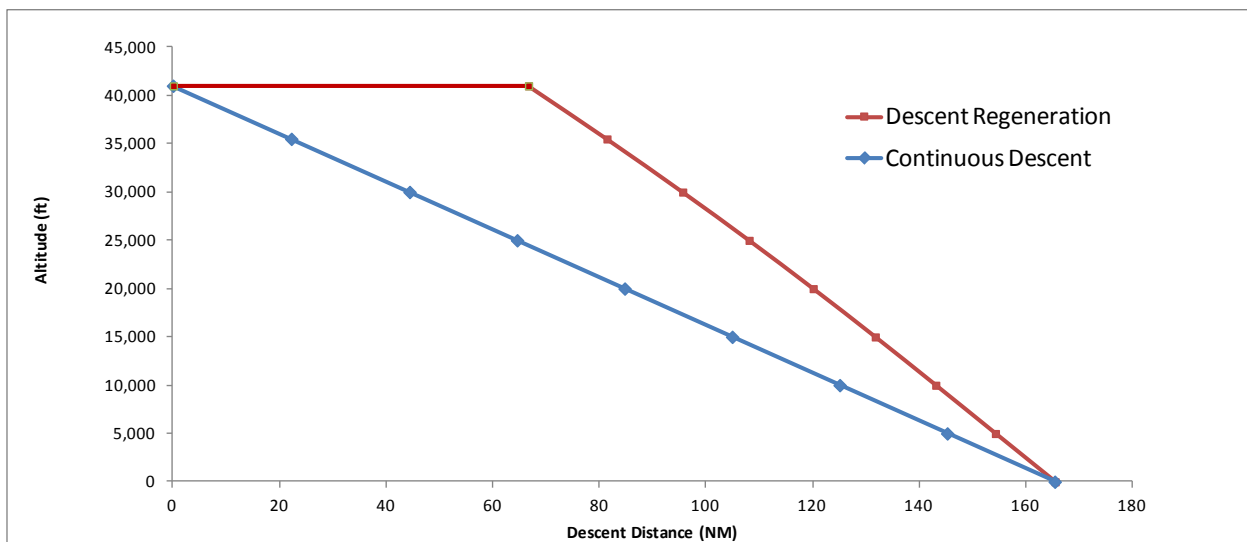


Figure 2.13 - Sample Trajectories for Continuous Descent and Descent Regeneration

Like many trades involving the hybrid electric propulsion system on the SUGAR Volt, the additional degrees of freedom that result from having an electric motor or motor/generator and energy storage create a complex situation to evaluate the benefits or optimize operation.

In this case, energy recovered during descent is stored in the battery, but additional fuel energy is expended during the extended cruise. So, generally, in an ideal case, there is nothing to be gained by extending the cruise and then recovering energy. As losses are included for using the fan for regeneration, the case for regeneration only gets worse.

The efficiency of the energy extraction from the fan also is lower than normal fan operation, as the fan needs to be designed to produce thrust at high efficiency and any compromise to the fan design for energy extraction comes at the expense of thrust efficiency. The fan efficiency on the hFan is high at cruise, when the fan airfoils are making lift the as-designed direction (low pressure on the side that's closer to the nose). Regeneration mode puts low pressure on the side that's closer to the tail, so the airfoils are operating upside down, while the fan is still turning the same direction. Also, there are the electrical system losses and charging losses to consider. If energy cost is considered, then the energy regenerated is displacing relatively low cost electricity at the airport recharging with additional relatively expensive jet fuel that is consumed during the extended cruise segment.

However, there are elements to complicate the assessment. If a non-continuous descent is needed, then there are inefficiencies (extra drag needed) that could benefit the regeneration case. The idle fuel flow of the engine has an impact on the fuel used in both cases.

If you did have recharging capability in the engine, it could be used for emergency power, unusually steep descents, or holding to the glide slope instead of using spoilers. However, these benefits are small.

For these reasons, the baseline SUGAR Volt hFan concept is not assumed to extract power from the air stream to charge the batteries during flight. Doing so could add some flexibility to the system, but will not benefit fuel burn or likely produce significant benefits to energy use or cost.

2.2 Configuration Description

The configuration for the SUGAR High aircraft (765-096 Rev A) is derived from the 765-095 Rev D configuration and should be considered the first revision from the Phase I (1) SUGAR effort (765-096). The primary difference between the 095 and 096 is the addition of hybrid electric systems and wing mounted battery pods.

Table 2.3 – 765-095 Revision History

Rev.	Description of Major Changes	Date
New	SUGAR Phase I Exit	6/4/2009
A	Configuration brought to SUGAR 765-095-RD layout	11/11/12

2.2.1 Integration

The aircraft general arrangement drawing and principal characteristics are shown in Figure 2.14 and Table 2.4 respectively. Airplane components for this configuration are identical to the 765-095-RevD SUGAR High configuration, thus, the Wing, Strut, Jury Strut, Vertical Fin, Horizontal Stabilizer, Fuselage, and Landing Gear will not be repeated in this volume of the final report. The engine configuration and battery pods are the only changes as compared to the SUGAR High.

Parameter	Units	Total Projected	Horizontal Stab.	Vertical Fin
Area	ft.^2	1477.11	296.24	297.69
Aspect Ratio		19.552	5.000	1.000
Span	in.	2039.301	461.833	207.043
Taper Ratio		0.346	0.350	1.000
Root Chord	in.	130.313	136.839	207.043
Tip Chord	in.	45.135	47.894	207.043
Sweep 25%	deg.	12.52	20.63	41.00
MAC	in.	110.286	99.504	207.043
Volume Coeff.			1.5631	0.687

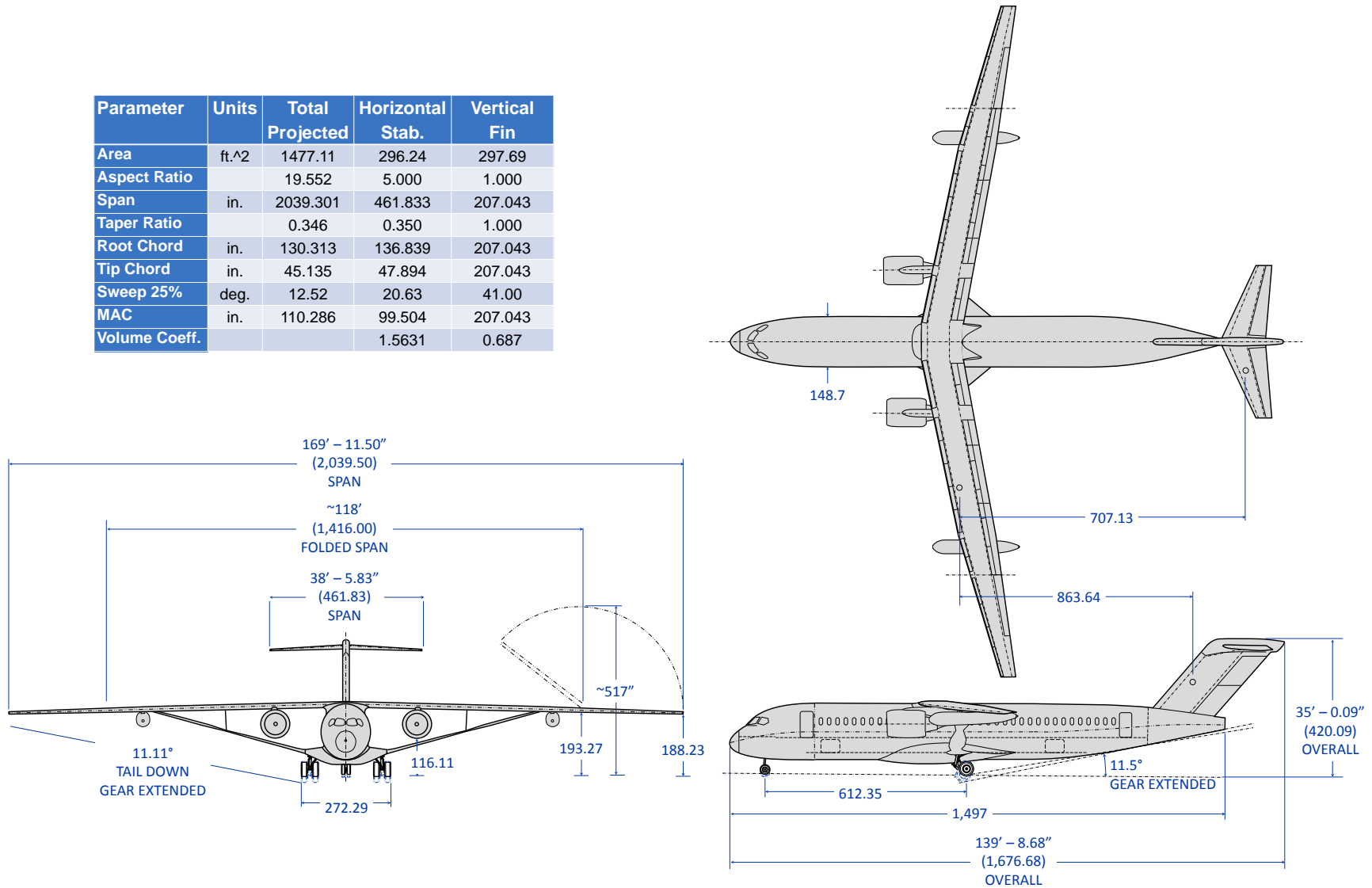


Figure 2.14 – SUGAR Volt (765-096-RevA) General Arrangement

Table 2.4 – Principal Characteristics

Model 765-095 Rev. D (As Drawn)	Balanced 1,380 Hp	Core Shutdown 7,150 Hp
Weights		
Maximum Takeoff Weight (MTOW)	150,000 lb	190,000 lb
Maximum Landing Weight (MLW)	143,300 lb	185,800 lb
Maximum Zero Fuel Weight (MZFW)	135,300 lb	177,800 lb
Maximum Battery Pod Weight (MBPW)	15,700 lb	47,900 lb
Operating Empty Weight (OEW)	88,800 lb	91,900 lb
Engine		
Engine Type	hFan+2	hFan+2
Rated Horse Power	1,380 hp	7,150 hp
Boeing Equivalent Thrust (no HP addition)	21,000 lbf	20,700 lbf
Fan Diameter	72.1 in	79.6 in
Overall Dimensions		
Length	139.7 ft	
Height	35 ft	
Fuselage Length	124.8 ft	
Fuselage Cross Section (Height x Width)	166.5 x 148.7 in	
Passenger Cabin Length	1127 in	
Wing		
Reference Area	1477.11 ft ²	
Span	169.3 ft	
Projected Sweep	12.52 deg	
Passenger, Baggage, Fuel Capacities		
Passenger Count (Dual Class)	154	
Class Distribution (FC / EC)	12 / 142	
Cargo Capacity	Bulk	
Fuel Capacity	5,416 USG	
Landing Gear		
Wheel Base	612.35	
Main Track	272.29	
Main Tire Size	45x17R21	
Nose Tire Size	30x10.5R15	

2.2.2 Battery Pods

Aside from the change to hFan engines, the SUGAR Volt is the same as SUGAR High. However, the SUGAR Volt has the addition of wing hard points for battery pod addition. Electric energy is inexpensive as compared to jet fuel however, batteries can be costly. It was decided that to minimize DOC, the SUGAR Volt would carry its battery pods as external components making

them rapidly exchangeable thus allowing slow charge rates and increasing battery life without interfering with conventional ground servicing operations or increasing aircraft turn time. In addition to the rapid change capability, the battery pod location helps spanload the configuration reducing the OEW penalty for carrying their weight. These benefits come with extra drag and possible lateral imbalance issues (depending on pod weight). It should be noted that the location of the batteries has not been traded. The pods could be palletized and contained within the cargo bay. This would increase the OEW because the configuration is less spanloaded and would require a palletized cargo handling system. The current design currently carries only bulk (non-palletized) cargo.

The battery pods are aerodynamically tailored for the wing to minimize interference. They contain a passive cooling system consisting of an inlet, ducting, and a nozzle. Depending on battery heat generation and atmospheric conditions, this passive system may be insufficient for some combinations of electrical system use. These constraints have not been analyzed and are most likely at high temperature, low speed, and/or low altitude. The batteries are not part of the base airplane and thus will not be reflected in the aero databases. The pod drag is booked as a delta f in the performance analysis.

2.2.3 Propulsion

Upon completion of the first round of SUGAR Volt sizing and economic analysis, two follow-on studies were conducted. Boeing developed two revised SUGAR Volt aircraft, the 750 Balanced and 750 Core Shutdown. “750” refers to the assumption of 750 Wh/kg battery technology. The objectives of these follow-on studies were to further reduce energy consumption and also to improve the propulsion system efficiency during core shutdown operation. The thrust requirements for the 750 Balanced and 750 Core Shutdown can be found in Figure 2.15 and Figure 2.16. The Balanced engine contained a 1,380 HP electric motor, while the Core Shutdown engine contained a 7,150 HP electric motor.

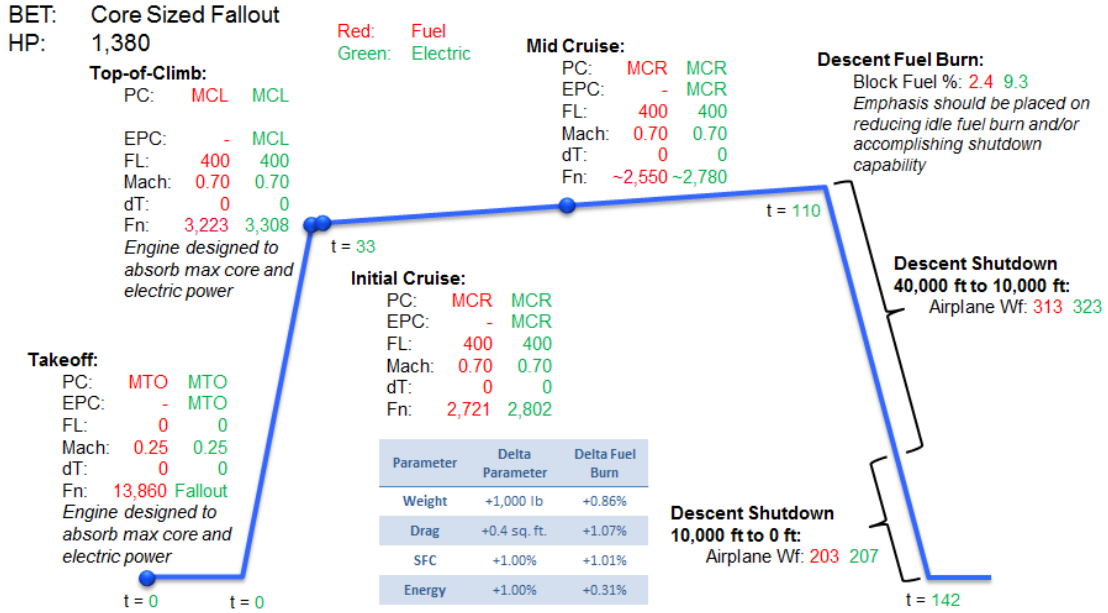


Figure 2.15 – 750 Balanced Thrust Requirements

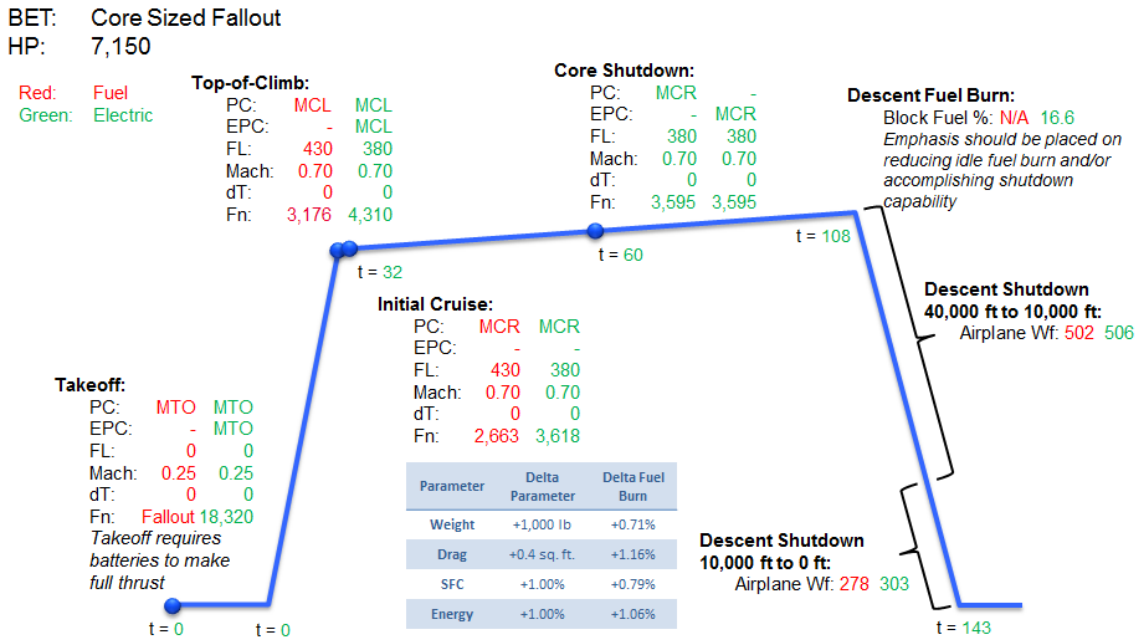


Figure 2.16 – 750 Core Shutdown Thrust Requirements

The thrust requirements and aircraft sensitivities were again used to conduct a parametric optimization study to size two hybrid electric advanced turbofan architectures. These “hFan+2” propulsion systems leverage the conventional electrical system and gas turbine technologies from the hFan+. Using weight, drag, SFC, and energy-to-fuel burn trades, the ideal fan pressure ratio and diameters of the 750 Balanced and 750 Core Shutdown engines were calculated. Propulsion system performance data was transmitted to Boeing for the two architectures.

Additionally, GE provided engine performance data for a 750 Balanced hFan+2 with an electric motor rated for 1,750HP. The supplementary 1,750 HP data set allowed Boeing to optimize the 750 Balanced aircraft and propulsion system through interpolation. A summary of the propulsion system key characteristics is provided in Table 2.5. The performance quotes include the respective electric motors running at full power throughout the flight envelope.

Table 2.5 - hFan+2 Key Characteristics

750 Balanced (hFan+2)			750 Core Shutdown (hFan+2)		
Fan Diameter		72.1"	Fan Diameter		79.6"
Length		129"	Length		129"
Propulsion System Weight		7030 lbf	Propulsion System Weight		10025 lbf
	Thrust (lbf)	SFC (lbm/lbf/hr)		Thrust (lbf)	SFC (lbm/lbf/hr)
SLS	17394	0.161	SLS	22992	0.113
TKOF	14276	0.251	TKOF	18320	0.186
TOC	3308	0.300	TOC	4310	0.080
Cruise	2780	0.272	Cruise	3595	0.000

2.3 Configuration Analysis and Final Performance

This section includes the discipline analyses of the configuration documented in Section 2.1.2.7 of this report and Section 2.2 of the Truss Braced Wing report. The results of the analysis are not used in the synthesis of the SUGAR Volt configuration but would be incorporated in the next configuration cycle.

2.3.1 Aerodynamics

The aerodynamic buildup of the SUGAR Volt (765-096-RA) is identical to the SUGAR Volt (765-095 Rev) D with the inclusion of a drag increment for battery pods mounted on the wings. The airplane delta f for a given battery pod size is shown in Table 2.6.

Table 2.6 – Battery Aero Characteristics

		Pod_1	Pod_2	Pod_3
Battery				
Energy Density	kWh/ft ³	34	34	34
Specific Energy	Wh/kg	750	750	750
Battery Energy	kWh	1,360	2,723	4,081
Pod Weight	lb	4,818	9,646	14,456
Airplane Delta F	ft ²	1.59	2.49	3.23

2.3.2 Mass Properties

The group weight statements for the 765-096-Rev A are shown in Table 2.7. These weights are generated starting with the 765-095-Rev D, changing the propulsion system to the hFan, including the hard points for the batteries, and adding electric systems. The weight data is generated at 150,000 pounds for the low horsepower aircraft and 190,000 pounds for the high horsepower aircraft.

Table 2.7 – 765-096-RA Group Weight Statement

GROUP	WEIGHT (LB)		
	1,380 HP	1,750 HP	7,150 HP
WING	16,986	17,011	18,808
TAIL	3,157	3,157	3,157
FUSELAGE	16,929	16,928	17,307
WING STRUT & MLG SUPT INSTL	5,077	5,077	6,584
LANDING GEAR	5,073	5,116	6,264
NACELLE & PYLON	3,682	3,682	3,682
PROPULSION	11,028	11,314	16,429
ENGINES	9,300	9,586	14,698
FUEL SYSTEM	1,728	1,728	1,731
FLIGHT CONTROLS	2,652	2,652	2,652
POWER SYSTEMS	4,068	4,068	4,068
AUXILIARY POWER UNIT	1,014	1,014	1,014
HYDRAULICS	758	758	758
ELECTRICAL	2,297	2,297	2,297
INSTRUMENTS	773	773	773
AVIONICS & AUTOPILOT	1,504	1,504	1,504
FURNISHINGS & EQUIPMENT	9,115	9,115	9,115
AIR CONDITIONING	1,441	1,441	1,441
ANTI-ICING	121	121	121
MANUFACTURER'S EMPTY WEIGHT (MEW)	81,607	81,960	91,907
OPERATIONAL ITEMS	7,207	7,207	7,207
OPERATIONAL EMPTY WEIGHT (OEW)	88,814	89,167	99,114
USABLE FUEL	14,716	13,298	12,178
MAX BATTERY POD	15,670	16,735	47,908
DESIGN PAYLOAD	30,800	30,800	30,800
TAKEOFF GROSS WEIGHT (TOGW)	150,000	150,000	190,000

2.3.3 Performance and Sizing

Performance and sizing analysis for a hybrid electric airplane is very complex as compared to a conventionally fueled configuration. Heritage performance routines have various levels of flexibility in their sizing capability however, neither of Boeings codes (there are two commercial transport performance routines at Boeing; Douglas heritage CASES and Boeing heritage BMAP) can directly accommodate electric aircraft. For this reason, a ModelCenter

environment was created that allows mission performance to be calculated. BMAP was selected for this environment for consistency with the fuel energy airplane performance analyses.

Performance is analyzed for two missions, the long range mission used for sizing, and the average range economic mission which is used for block fuel comparison. The long range sizing mission is run in BMAP conventionally with the mission defined and executed in one performance evaluation which assumes an all fuel energy source. Some aircraft (the core shutdown hybrid electric) are held at a Maximum Takeoff Weight (MTOW) of 190,000 lbs.

Calculating the performance for the hybrid average range mission is significantly more complicated. To accomplish this, BMAP was configured to analyze segments rather than an entire mission. The mission was broken into 8 segments:

- Taxi Out
- Takeoff & Climbout
- Climb
- Cruise (Two segments for core shutdown cases)
- Descend
- Approach and Land
- Taxi In
- Reserves

Engine data is generated for each of the mission segments based on a presumed electric power code (how much electric horsepower is applied to the low pressure spool) for that mission segment. The segment performance is then executed in isolation with care taken to ensure that final conditions are appropriately passed to the next segments initial conditions. Battery weight is booked with OEW and is assumed not to change over the mission duration (which may not necessarily be true for some potential future battery chemistries). After fuel burn performance is calculated, electric energy is integrated by looking up the power demand at each Mach, altitude, airspeed, thrust, and electric power code at each time step reported by BMAP. The battery energy required to fly the mission is then converged with the battery energy available. This requires resizing the long range mission because of the OEW change associated with a change in maximum battery pod weight (the short range mission is assumed to utilize the maximum available battery energy). The original intent was to optimize reference horsepower, wing area, thrust, MTOW, and each segments electric power code to minimize fuel burn. Unfortunately, due to tolerance of the performance convergence and the long runtime of the environment, the aircraft were hand optimized assuming maximum electric power code for takeoff, climb, and cruise. Core shutdown aircraft use hybrid mode with maximum electric

effort for takeoff and climb, then an all fuel cruise segment (to burn of gross weight), followed by the remaining cruise segment with the core shutdown. 3% of the battery energy is carried as fuel using a fuel energy conversion ratio of 18,580 BTU / LB and assuming that 50% of the heat energy is converted to thrust energy.

Three hybrid aircraft are sized at 1,380, 1,750, and 7,150 reference horsepower. A sizing plot is shown for each airplane in Figure 2.17, Figure 2.18, and Figure 2.19 respectively. Each response surface represents a wing area and takeoff parameter (wing loading divided by thrust to weight ratio) variation with an MTOW converged on the long range mission distance (or target MTOW for the heavy airplanes). These aircraft are constrained by takeoff field length and the ability to fly at optimum altitude (thrust initial cruise altitude capability (thrust ICAC)) for all missions. The plots are calculated for a fixed Maximum Battery Pod Weight (MBPW) making them valid only at the sizing point illustrated on the chart. If the MBPW were converged at all points on the chart, those points above the sizing point would get higher in fuel burn and those below would get lower in fuel burn. This effectively scales the charts about the sizing point and would not change the location of the minimum fuel burn. These plots verify the airplane is at the optimum conditions.

Table 2.8 shows the performance summary of the three hybrid electric aircraft in addition to the SUGAR High (fuel powered) and SUGAR Free configurations. It is shown that the low horsepower aircraft have lower fuel burn at the economic mission range and remain competitive from an energy use perspective. Inspection of the sizing chart (Figure 2.19) for the 7,150 HP configuration shows that the engine is sized by the power required to shut down the core at the cruise condition (labeled thrust). Table 2.9 shows additional sizing options: the “No Ele. Thrust Const.” column shows a hypothetical airplane that ignores the constraint and runs to the intersection of the short range ICAC constraint and the TOFL constraint. This is hypothetical because the energy use at cruise requires more horsepower than the one supplied with the GE engine data can absorb but should approximate the benefits of installing a larger motor on the configuration (balancing top of climb thrust with takeoff thrust). The final column, “No Shutdown”, is a trade showing the fuel burn without shutting down the core during the cruise segment. This shows that the fuel burn vs. throttle setting curve is quite flat as the vehicle is better than the current sizing point (primarily achieved by balancing TOFL with top of climb thrust without an electric cruise sizing requirement for shutdown).

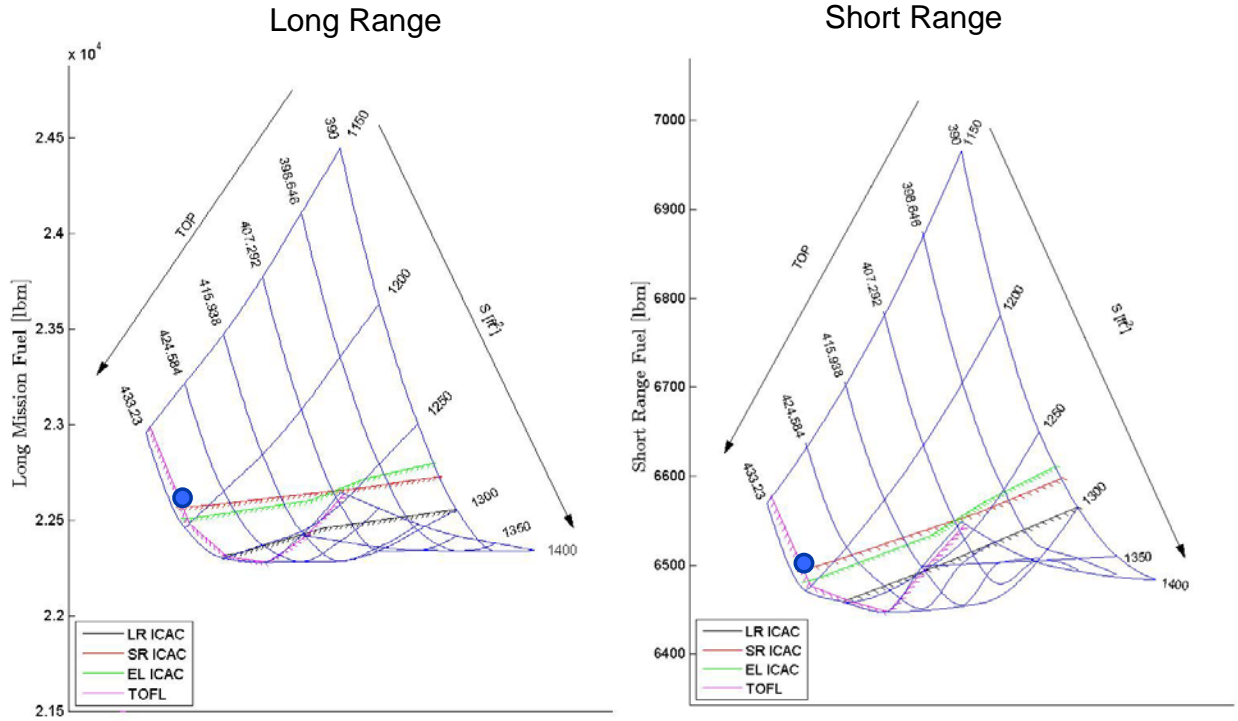


Figure 2.17 - 765-096-RA 1380 HP sizing Plot

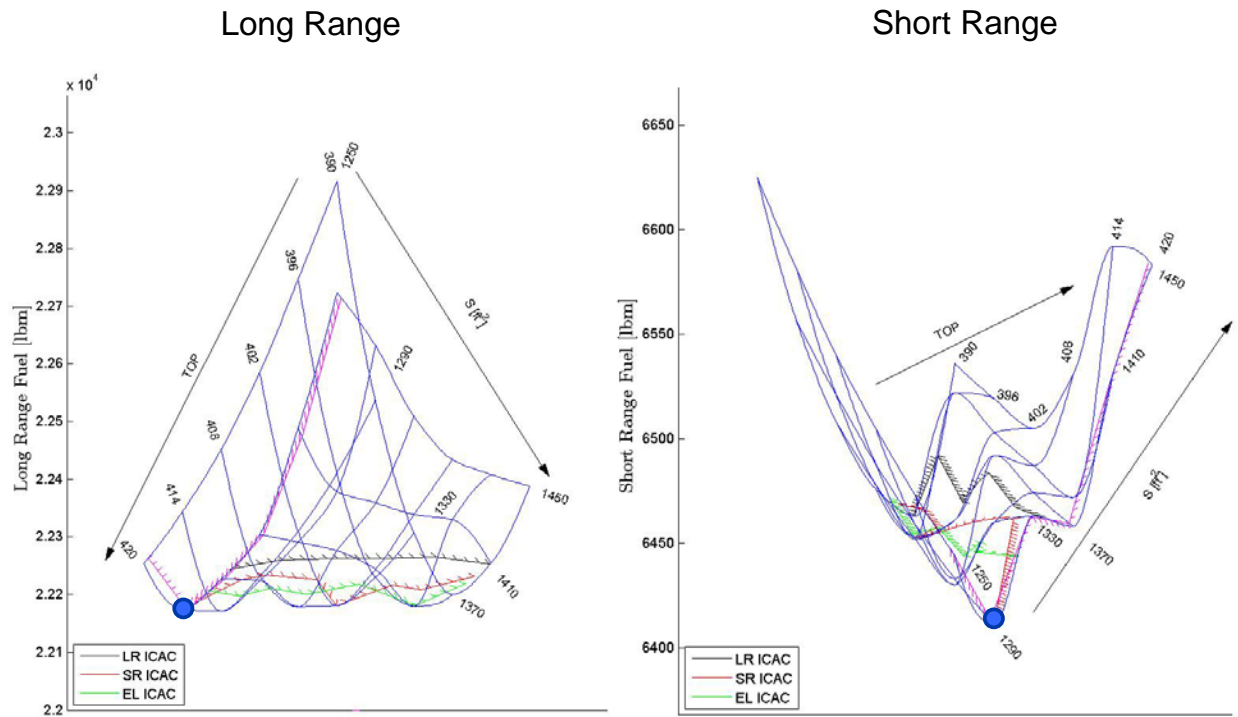


Figure 2.18 - 765-096-RA 1750 HP sizing Plot

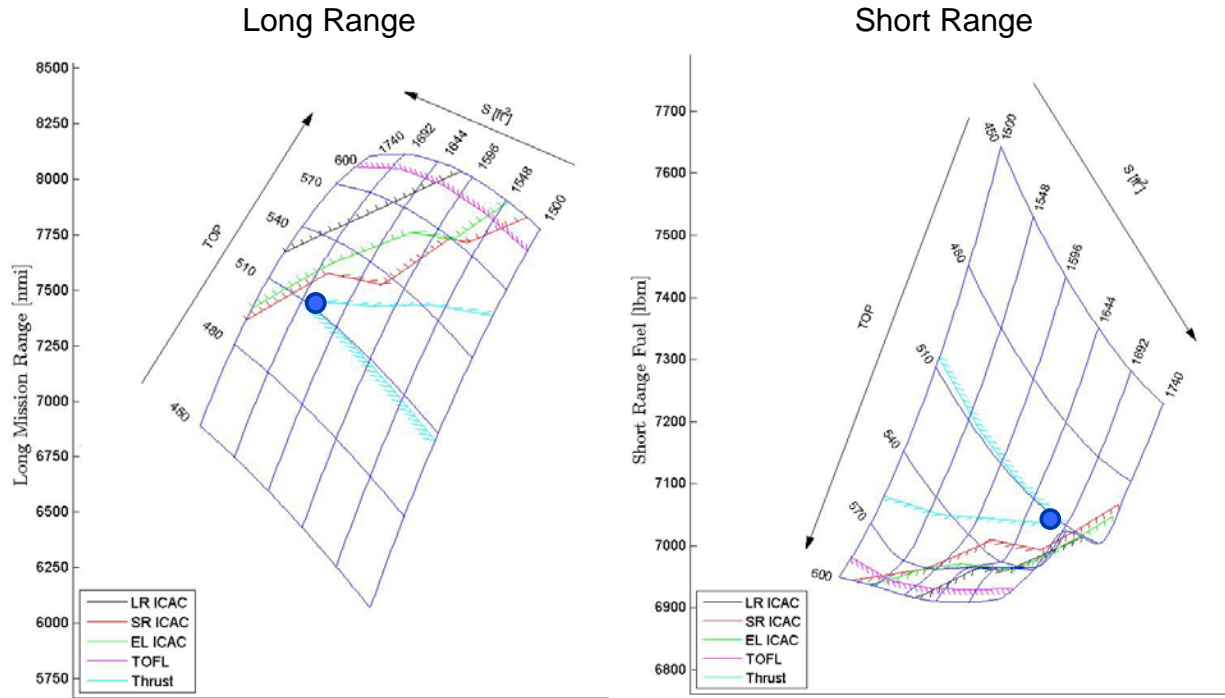


Figure 2.19 - 765-096-RA 7150 HP sizing Plot

NASA Contract NNL08AA16B – NNL11AA00T – Subsonic Ultra Green Aircraft Research – Phase II
 Volume II – Hybrid Electric Design Exploration

Table 2.8 – 765-096 Rev A Mission Performance Comparison

Model Sizing Level		765-093 FREE	765-095 SUGAR High	Balanced (Ref Hp 1,380)	Balanced (Ref Hp 1,750)	Core Shutdown (Ref Hp 7,150)
PASSENGERS / CLASS		154 / DUAL	154 / DUAL	154 / DUAL	154 / DUAL	154 / DUAL
MAX TAKEOFF WEIGHT	LB	182,600	138,300	140,700	139,700	190,000
MAX LANDING WEIGHT	LB	149,400	135,700	138,800	139,300	189,300
MAX ZERO FUEL WEIGHT	LB	140,400	127,700	130,800	131,300	181,300
MAX BATTERY WEIGHT	LB	-	-	15,700	16,700	47,900
OPERATING EMPTY WEIGHT	LB	94,400	81,700	84,300	83,800	102,600
FUEL CAPACITY REQ / AVIL	USG	9,633/9,633	4,213/4,213	4,185/4,194	4,121 / 4,605	4,426 / 6,340
ENGINE MODEL		CFM56	gFan+2	hFan+2	hFan+2	hFan+2
FAN DIAMETER	IN	62	66	69	67	79
HORSEPOWER	HP	-	-	1,260	1,502	7,053
BOEING EQUIVALENT THRUST (BET)	LB	27,900	19,400	19,200	18,000	20,700
WING AREA / SPAN	FT ² / FT	1,406 / 121	1,195 / 153	1,190 / 153	1,290 / 159	1,680 / 181
ASPECT RATIO (EFFECTIVE)		10.41	19.56	19.56	19.56	19.56
OPTIMUM CL (SR / LR)		0.584	0.759	0.769 / 0.798	0.728 / 0.730	0.730 / 0.733
CRUISE L/D @ OPT CL (SR / LR)		17.997	23.995	23.047 / 0.77	23.537 / 24.213	25.223 / 25.933
LONG MISSION RANGE	NM	3,680	3,500	3,499	3,500	3,500
PERFORMANCE CRUISE MACH		0.79	0.70	0.70	0.70	0.70
LONG RANGE CRUISE MACH (LRC)		0.79	0.70	0.70	0.70	0.70
THRUST ICAC (MTOW, ISA) (SR / LR)	FT	36,200	37,700	39,500 / 38,000	40,200 / 37,700	38,000 / 41,900
TIME/DIST (MTOW,35k FT,ISA)(SR/LR)	MIN / NM	23 / 148	23 / 147	(18/25)/(108/149)	(22/28)/(130/172)	(17/23)/(100/135)
OPT. ALTITUDE (MTOW, ISA)(SR/LR)	FT	34,900	37,700	37,700 / 37,600	38,200 / 38,400	37,200 / 41,100
BUFFET ICAC (MTOW, ISA) (SR / LR)	FT	36,200	43,000	42,700 / 42,600	44,300 / 44,400	43,300 / 47,000
TOFL (MTOW, SEA LEVEL, 86 DEG F)	FT	8,190	7,680	8,170	8,180	6,740
APPROACH SPEED (MLW)	KT	126	109	111	106	109
BLOCK FUEL / SEAT (900 NM)	LB	91.51 (0%)	42.46 (-53.6%)/(0%)	37.82 (-58.7% / -10.9%)	36.56 (-60% / -13.9%)	33.25 (-63.7% / -21.7%)
BLOCK ENERGY / SEAT (900 NM)	kBTU	1,700 (Base)	789 (-53.6%)	801 (-52.9%)	784 (-53.9%)	917 (-46.0%)
FUEL ENERGY FRACTION	%	100%	100%	87.8%	86.6%	67.3%

NASA Contract NNL08AA16B – NNL11AA00T – Subsonic Ultra Green Aircraft Research – Phase II
 Volume II – Hybrid Electric Design Exploration

Table 2.9 – 765-096 Rev A Core Shutdown Trade

Model Sizing Level		Core Shutdown (Ref Hp 7,150)	No Ele Thrust Const. (Ref Hp 8,080)	No Shutdown (Ref Hp 7,150)
PASSENGERS / CLASS		154 / DUAL	154 / DUAL	154 / DUAL
MAX TAKEOFF WEIGHT	LB	190,000	190,000	190,000
MAX LANDING WEIGHT	LB	189,300	189,500	189,400
MAX ZERO FUEL WEIGHT	LB	181,300	181,500	181,400
MAX BATTERY WEIGHT	LB	47,900	50,900	50,900
OPERATING EMPTY WEIGHT	LB	102,600	99,700	99,700
FUEL CAPACITY REQ / AVIL	USG	4,426 / 6,340	4,148 / 5,568	4,143 / 5,568
ENGINE MODEL		hFan+2	hFan+2	hFan+2
FAN DIAMETER	IN	79	Unk. (77+)	77
HORSEPOWER	HP	7,053	7,585	6,880
BOEING EQUIVALENT THRUST (BET)	LB	20,700	19,700	19,700
WING AREA / SPAN	FT ² / FT	1,680 / 181	1,511 / 172	1,516 / 172
ASPECT RATIO (EFFECTIVE)		19.56	19.56	19.56
OPTIMUM CL (SR / LR)		0.730 / 0.733	0.772 / 0.767	0.801 / 0.767
CRUISE L/D @ OPT CL (SR / LR)		25.223 / 25.933	24.496 / 25.737	24.463 / 25.766
LONG MISSION RANGE	NM	3,500	3,500	3,500
PERFORMANCE CRUISE MACH		0.70	0.70	0.70
LONG RANGE CRUISE MACH (LRC)		0.70	0.70	0.70
THRUST ICAC (MTOW, ISA) (SR / LR)	FT	38,000 / 41,900	36,200 / 37,200	38,700 / 37,200
TIME/DIST (MTOW,35k FT,ISA)(SR/LR)	MIN / NM	(17/23)/(100/135)	(19/34) / (114/203)	(20/34) / (119/205)
OPT. ALTITUDE (MTOW, ISA)(SR/LR)	FT	37,200 / 41,100	36,200 / 36,300	37,100 / 36,300
BUFFET ICAC (MTOW, ISA) (SR / LR)	FT	43,300 / 47,000	41,100 / 41,300	41,200 / 41,400
TOFL (MTOW, SEA LEVEL, 86 DEG F)	FT	6,740	8,180	8,180
APPROACH SPEED (MLW)	KT	109	115	115
BLOCK FUEL / SEAT (900 NM)	LB	33.25 (-63.7% / -21.7%)	32.12 (-64.9% / -24.4%)	32.69 (-64.3% / -23.0%)
BLOCK ENERGY / SEAT (900 NM)	kBTU	917 (-46.0%)	915 (-46.2%)	926 (-45.5%)
FUEL ENERGY FRACTION	%	67.3%	65.2%	65.6%

A summary of the fuel burn and energy reduction from the SUGAR Free configuration is shown in Figure 2.20. It is shown that the hybrid electric configurations do save fuel for the economic mission. The 1,750 Hp configuration is quite good and meets NASA’s goal for fuel burn but shows only a minor improvement in the energy use. The magnitude and sign of electric energy savings over an all fuel configuration has vacillated for hybrid solutions and, with the present understanding of the design, appears to be a push or a slight negative. Even with no energy advantage on the economic mission, the hybrid architecture may allow for a greener source of energy as many environmentally friendly ground charging options exist. It is also possible to alter where in the atmosphere emissions are being deposited (cruise altitude or ground power station).

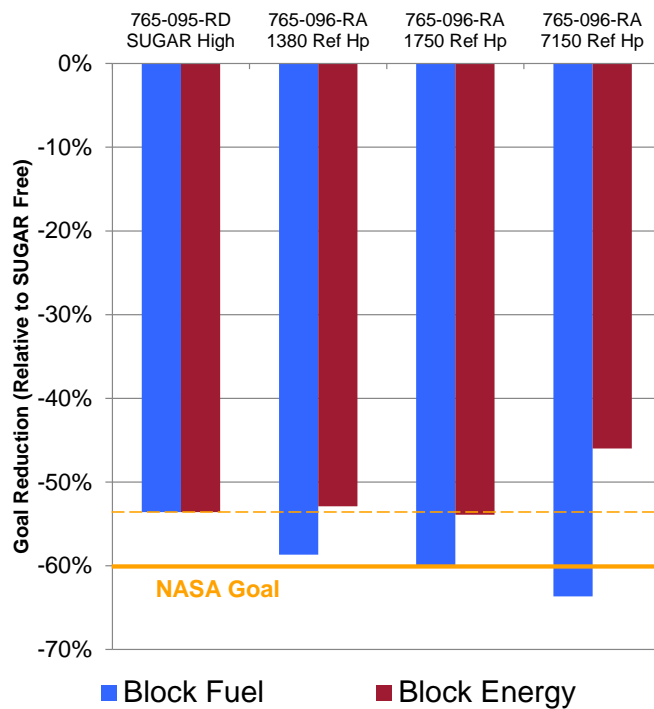


Figure 2.20 - Economic Mission Fuel and Energy Reduction

The payload range curves for each hybrid airplane are illustrated in Figure 2.21. This figure also shows the all fuel truss braced configuration (SUGAR High 765-095-RD) for comparison. The 7,150 Hp configuration is sized to 190,000 lb while the lower horsepower configurations are sized for the 3,500 nautical mile maximum range requirement. This is clearly depicted by the figure as the high horsepower configuration exceeds the range capability requirement and is fuel volume limited even without the 1,000 gallon body tank it carries (this curve is approximated). It should be noted that the payload range curves illustrated represent the all fuel capability of the airplane, thus, any mission under the payload range envelope can be performed in hybrid mode.

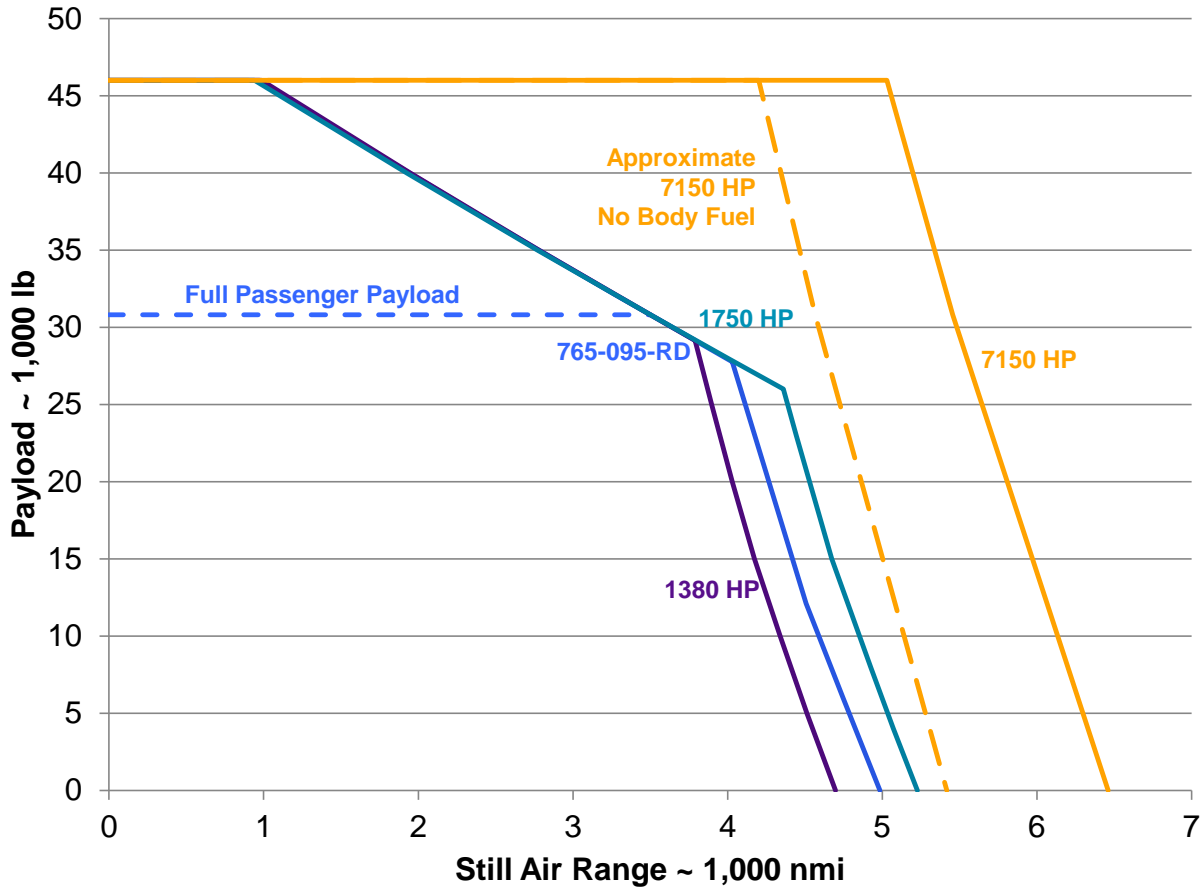


Figure 2.21 - Payload v. Range Chart for Hybrid Electric Aircraft

The fuel burn and energy use per segment for the hybrid electric airplanes is shown in Figure 2.22 and Figure 2.23 respectively for the 900 nautical mile economic mission. These metrics aren't particularly telling as the range of each segment varies from configuration to configuration. Figure 2.24 normalizes the energy use per segment by the range of the segment (specific range calculated with energy rather than fuel). This figure provides a metric to compare the efficiency of each airplane segment with respect to energy use. The 1,750 horsepower configuration shows equal cruise efficiency as compared to the SUGAR High UDF (UnDucted Fan). The fuel burn increment from the SUGAR High UDF and the SUGAR High (with the gFan+2 ducted fan) could be applied to any hybrid configuration.

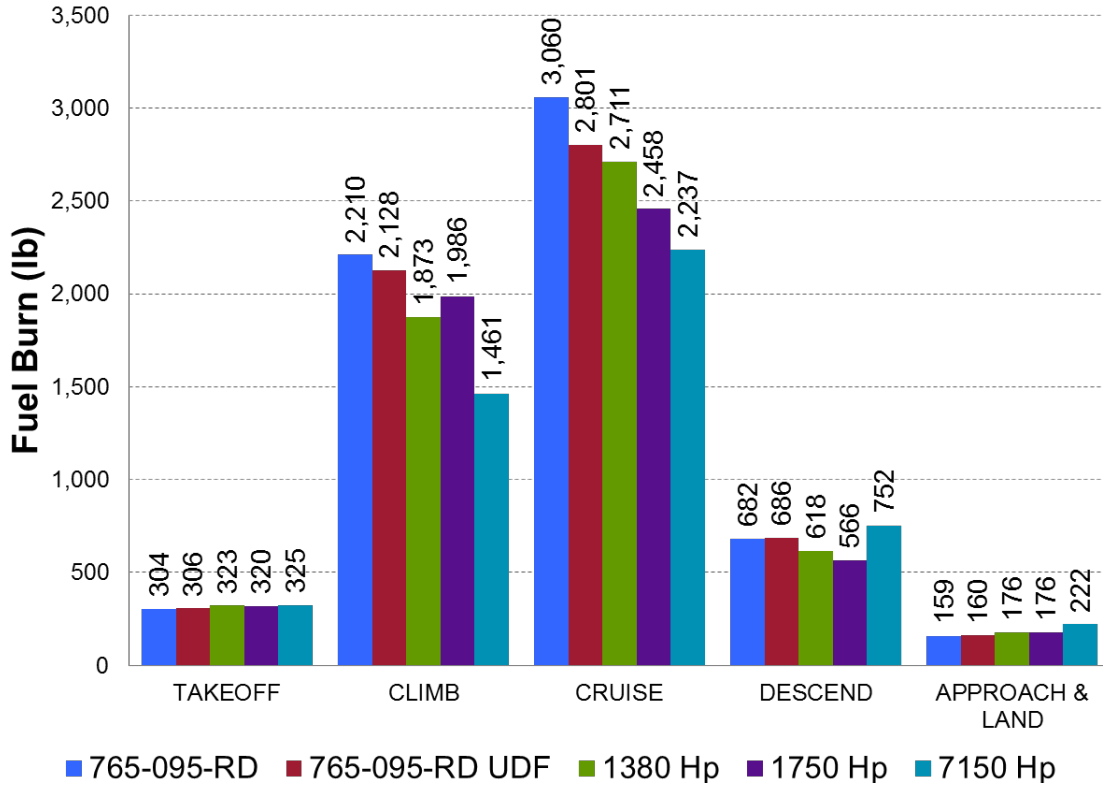


Figure 2.22 - Fuel Burn per Segment for Hybrid Electric Aircraft

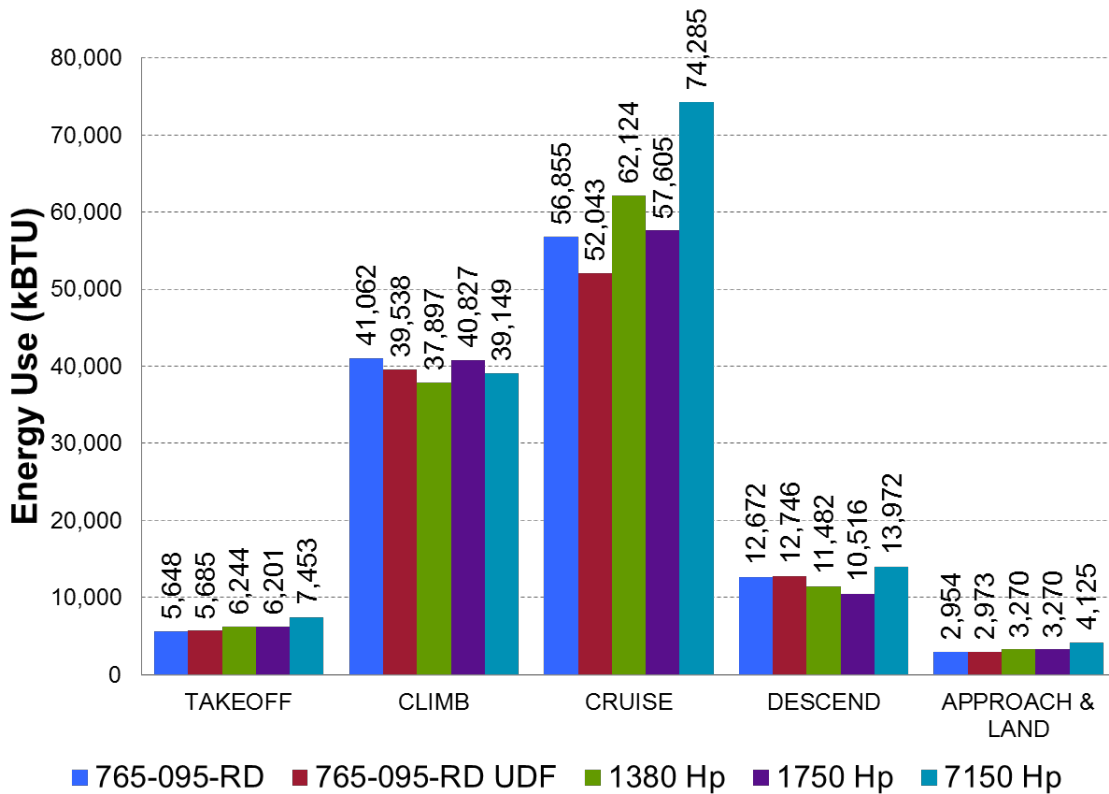


Figure 2.23 - Energy Use per Segment for Hybrid Airplanes

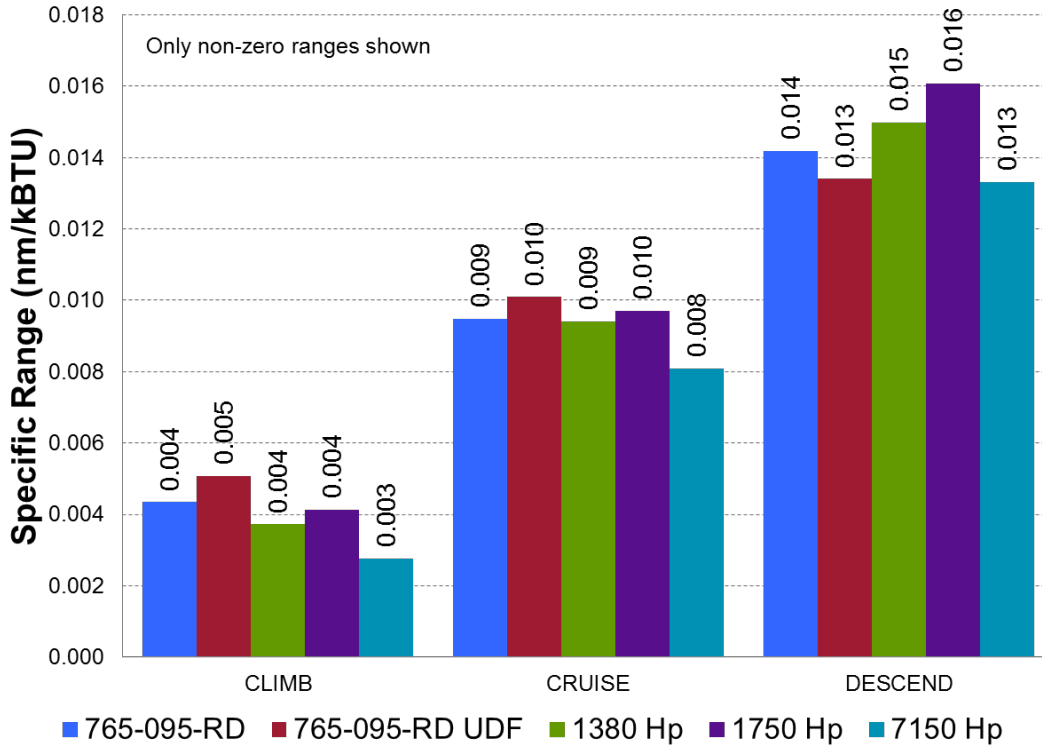


Figure 2.24 - Specific Range (Energy) per Segment for Hybrid Airplanes

Fuel burn as a function of range is illustrated by Figure 2.25. This shows the reduction of fuel burned at shorter ranges for hybrid electric airplanes. It should be noted that the hybrid electric 1,750 Hp engine has better performance than its all fuel counterpart even at the 3,500 maximum range. This shows that the airplane is favoring the cycle with a slightly larger fan than the baseline gFan+2 engine. Figure 2.26 shows energy verses range for the same aircraft. The large MTOW core shutdown airplane has similar energy use on a 400 nm mission but shows much worse energy use for a 900 nm mission. This becomes important later when fleet fuel burn is discussed. Figure 2.27 shows the optimum battery weight for fuel burn minimization for each hybrid airplane as a function of range. The aircraft operate in different modes depending on the size of the electric motor and the mount of battery that can be carried. Figure 2.28 illustrates what mode of operation each hybrid airplane is operating in as a function of range. The less than MTOW and less than max battery weight is a region where the airplane flies in hybrid mode but is at less than gross weight. This usually occurs because the electric motor cannot deplete the battery energy in the flight duration. The airplane operates at less than MTOW. This region followed by a region that can utilize MBPW but is not so long that the battery energy density is limiting range. Following this, a MTOW region is encountered. This region is where the battery energy density is traded for higher fuel energy density. The low MTOW airplanes (1,380 and 1,750 HP configurations) trade in this region from roughly the economic 900 nautical mile mission to the maximum range 3,500 nautical mile mission. The

7,150 HP, 190,000 pound configuration reaches a point where no battery energy is used. This region is a less than MTOW and non-hybrid. The cost of carrying the battery pod is outweighed by the drag penalty of carrying battery pods.

The average fleet frequencies verses range (previously reported (1)) can be used in coordination with these fuel and energy verses range charts to determine the fleet fuel burn and energy use (reported in Figure 2.29). This shows that, with the current concepts and engine architectures, the fleet energy use can be maintained at a fuel burn advantage. This can be a benefit in areas with a clean power grid or can be used to trade where the emissions are being deposited into the atmosphere.

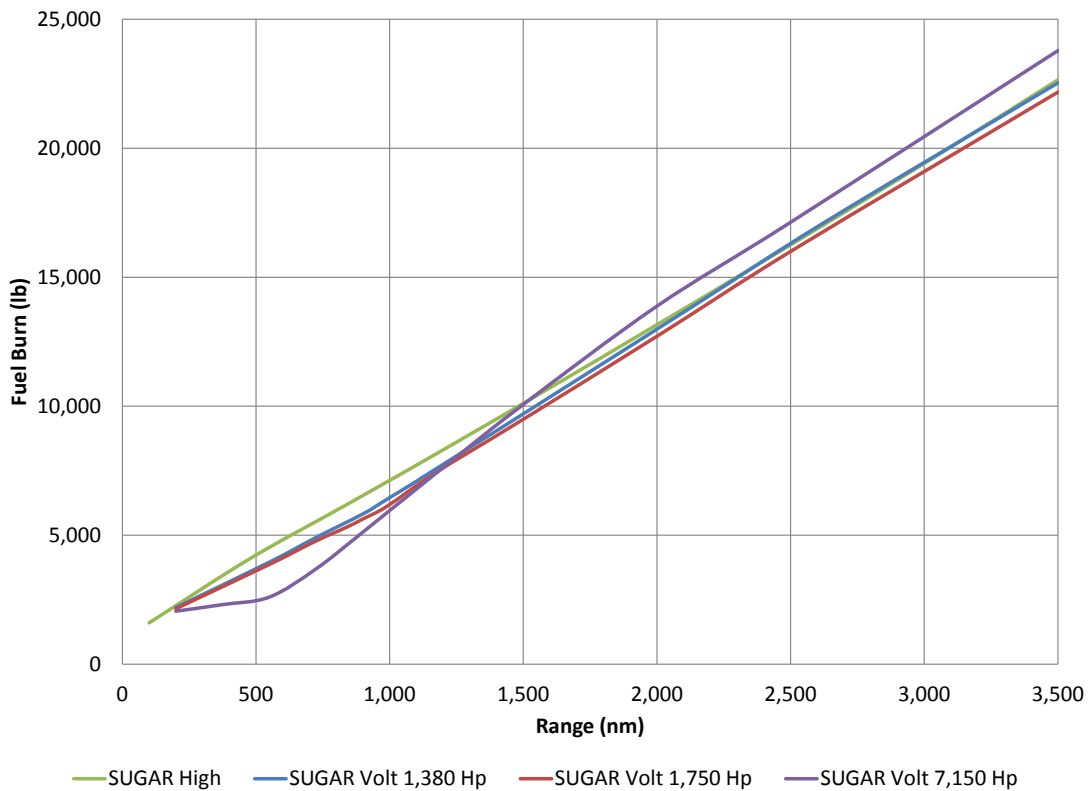


Figure 2.25 - Fuel Burn v. Range for Hybrid Aircraft

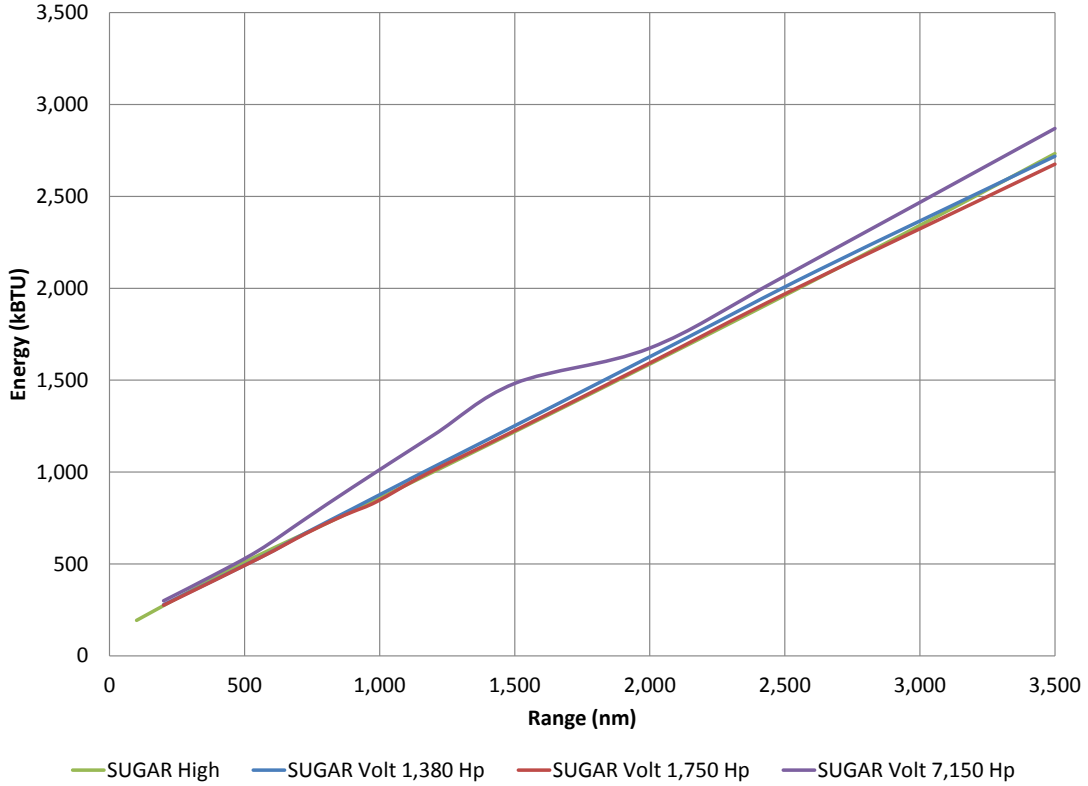


Figure 2.26 – Energy v. Range for Hybrid Aircraft

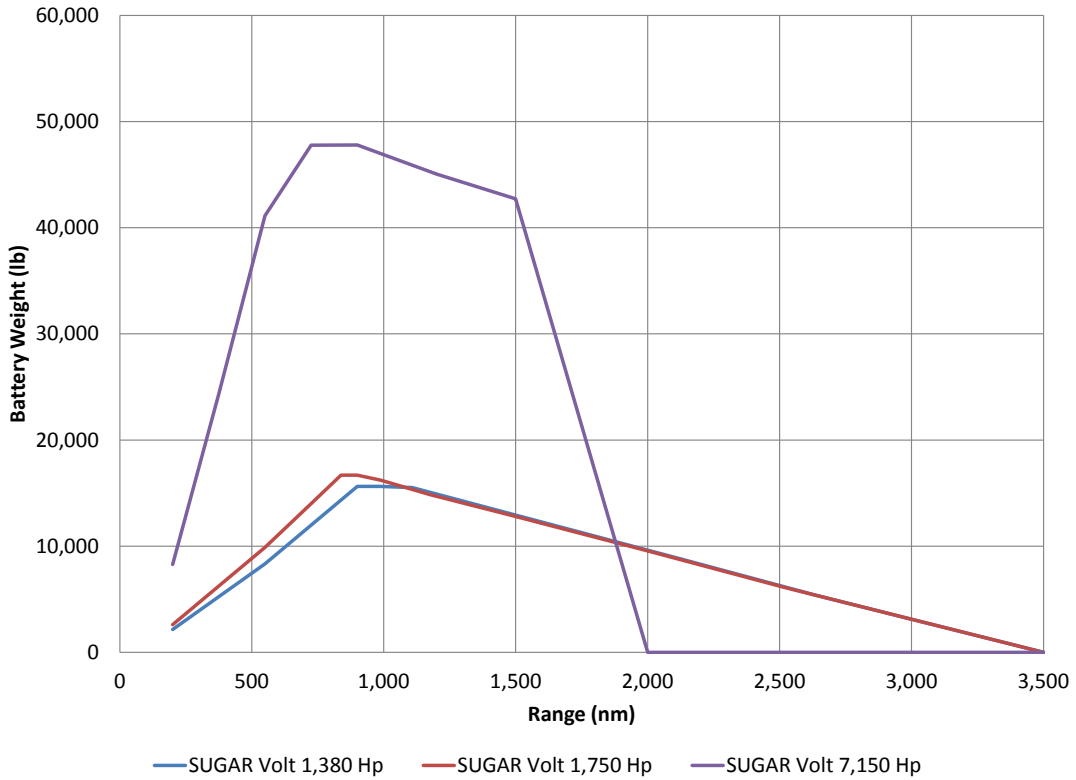


Figure 2.27 – Battery Weight v. Range for Hybrid Aircraft

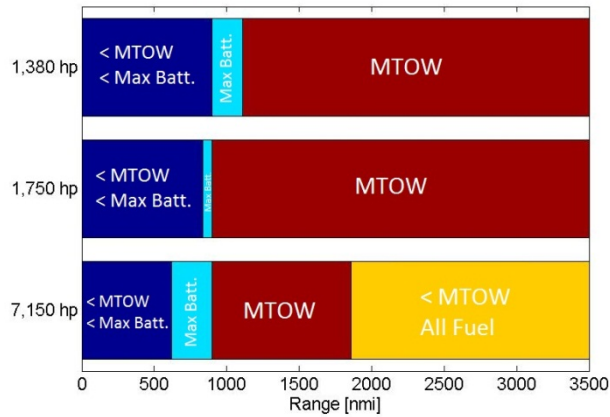


Figure 2.28 – Modes of operation for hybrid airplanes

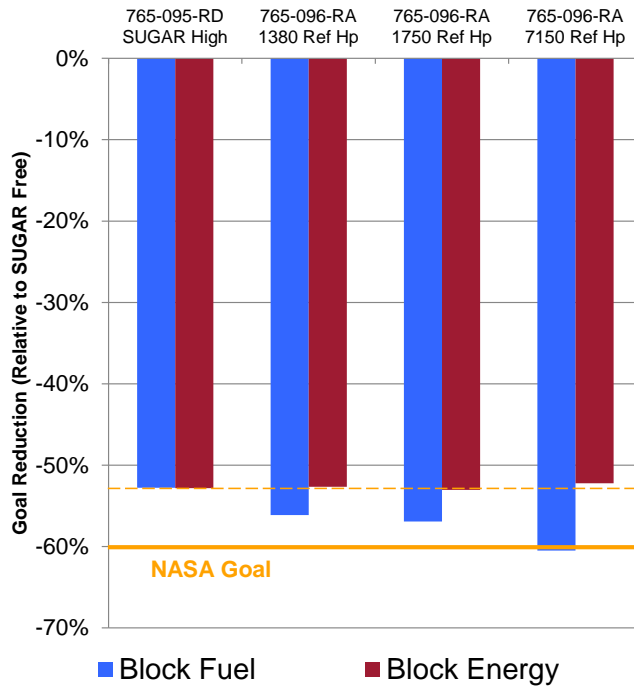


Figure 2.29 – Fleet Fuel and Energy Reduction as compared to NASA Goal

2.3.4 Acoustic Analysis

Acoustic analysis was completed for the SUGAR High (non-electric) and SUGAR Volt (HE) in order to benchmark the noise characteristics of the electric configuration and assess the potential for achieving NASA’s stated noise goal for a vehicle entering service in the 2030 time frame. The analysis methodology is similar to that used to conduct the noise analysis for the Environmentally Responsible Aviation (ERA) – Preferred System Concept (PSC) (3) study which strived to achieve a similar noise goal, although for a larger class aircraft. The results of the Boeing ERA study estimated the PSC vehicle could achieve the N+2 goal (-42 dB relative to Stage IV) by 2020, but would require some breakthrough technologies, as yet unidentified, if greater

noise reduction is needed. The SUGAR Hybrid Electric (HE) concept does have many features that are beneficial for noise reduction including advanced engine design, state of the art acoustic liner technology as well as excellent low speed aircraft performance.

2.3.4.1 Summary of Acoustic Results

The SUGAR High total aircraft noise at Approach (AP), Cutback (CB), and (SL) conditions is provided in Figure 2.30. The cumulative margin to Stage 4 of 22.8 EPNdB is noted as well. Similarly, Figure 2.30 also provides the total aircraft noise for the SUGAR Volt at 1,860 electric horsepower, yielding 24.3 EPNdB margin to Stage 4. Both airplanes have an acoustically treated engine, but do not have advanced noise reduction technology. The small differences in noise levels & margin is due to small differences in flight performance, and similarity in the engine noise between the non-electric and electric engine. With aggressive airframe and engine noise reduction technology, respectively, -3.0 EPNdB & -2.0 EPNdB, the SUGAR High achieves 30.1 EPNdB margin and SUGAR Volt achieves 31.4 EPNdB margin.

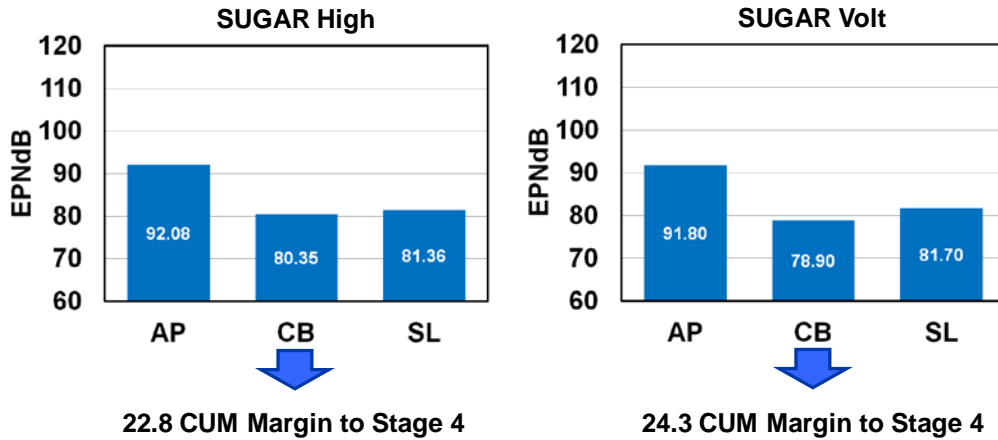


Figure 2.30 – Noise Levels & Stage 4 Margins for the SUGAR High & Volt

2.3.4.2 Configuration & Performance

The main geometric parameters of interest for noise calculation are the landing gear geometry (wheel diameter, strut diameter, etc.), and high-lift system geometry (chord, span, deflection, etc.). Details for the specific values will be provided below in the detailed analysis discussion.

Noise analysis was determined for a prescribed FAR 36 flight performance profile/condition, depicted in Figure 2.31. The standard parameters are: (a) SL 77 deg F, 77 RH, (b) climbout speed min = V_2+10 kts, (c) distance to the microphone = 21,325 ft from brake release, (d) start of engine cutback = 3,500 ft before the microphone and ending at 23,000 ft from brake release, (e) noise trajectory ending at 3,000 ft altitude, and (f) Sideline noise measured at 1,000 ft altitude

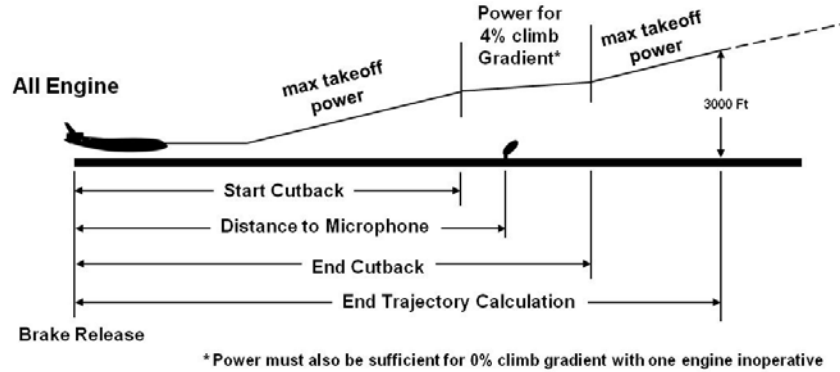


Figure 2.31 – FAR 36 Noise Profile

The relevant flight performance parameters and values for the Approach, Cutback, and Sideline noise profiles are provided below, in Table 2.10, for both the SUGAR High and Volt. The TOGW noted in the table was used to derive the Stage 3 noise limits.

Table 2.10 – Flight Performance Parameters for Noise Analysis

APPROACH	Altitude (FT)	Velocity (KTS)	Flight Path Angle (Deg)	Engine Pitch Angle (Deg)	Body Pitch (Deg)	Alpha (Deg)	Net Thrust / Engine (LBF)	TOGW
High	394	118.8	-3.00	3.70	3.70	6.70	1330	138,070
Volt	394	117.3	-3.00	3.66	3.66	6.66	1353	138,617

CUTBACK	Altitude (FT)	Velocity (KTS)	Flight Path Angle (Deg)	Engine Pitch Angle (Deg)	Body Pitch (Deg)	Alpha (Deg)	Net Thrust / Engine (LBF)	TOGW
High	1569	172.5	3.27	6.4	6.4	3.13	8313	138,070
Volt	1516	169.3	3.27	6.4	6.4	3.13	8328	138,617

SIDELINE	Altitude (FT)	Velocity (KTS)	Flight Path Angle (Deg)	Engine Pitch Angle (Deg)	Body Pitch (Deg)	Alpha (Deg)	Net Thrust / Engine (LBF)	TOGW
High	1000	171.2	7.41	10.5	10.5	3.09	13448	138,070
Volt	1000	168.1	7.10	10.1	10.1	3.00	13108	138,617

2.3.4.3 Overall Method of Analysis

The noise analysis was conducted in 3 major parts, namely, engine noise, airframe noise, and total aircraft (system noise). The overall noise analysis process is shown in Figure 2.32.

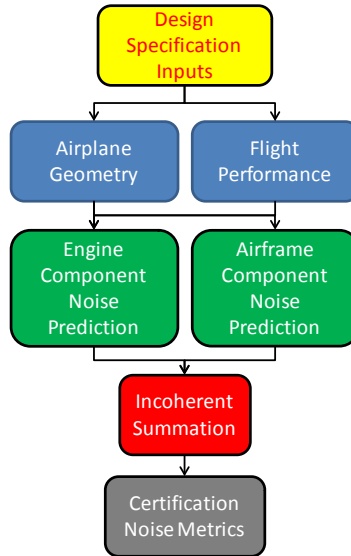


Figure 2.32 – Overall Noise Analysis Process

The design specification inputs entail the airframe design, flight profiles, engine type, and engine power conditions. These parameters served as the inputs for the engine and airframe noise predictions. They provided the specific geometry values for the subcomponents, such as chords, spans, deflections, etc., and also the flight operating conditions for the specific noise certification points, such as altitude, velocity, and others.

The engine noise was developed and provided by GE, using their in-house “GE Decomposition” method. Non-treated (hardwall) in-flight Noise-Power-Distance (NPD) engine noise data was provided for the baseline (non-electric) engine and for all electric power settings. It included subcomponent $1/3^{\text{rd}}$ octave spectral data for the Fan-Inlet, Fan-Exhaust, Jet, and Combustor.

Airframe noise was derived by Boeing’s component noise predictions which have been discussed and validated in References (4), (5), (6), and (7). Airframe noise included $1/3^{\text{rd}}$ octave spectral data for the nose gear, main gear, slat, and flap. Trailing edge noise was not analyzed.

Engine and airframe noise data was extrapolated from flight to 150 foot polar-arc condition and then back to certification SL/CB/AP flight conditions. The data was then log summed to yield the total aircraft noise, and system metrics of PNLT, PNL and EPNdB. The extrapolation from flight to 150 ft polar-arc, and then back to flight was done so that all the predicted data would be processed through a standard in-house extrapolation processes.

2.3.4.4 Detailed Acoustic Analysis

CFD Analysis for Noise

CFD analysis was performed for the SUGAR HE configuration using CFD++ with an unstructured grid. The analysis was conducted at the power-on, reference noise certification low-speed

conditions. The configuration geometry was modeled using CATIAv5. The approach condition geometry entailed: (a) extended main gear, (b) extended nose gear, (c) leading edge Krueger (slat) set to 40° , and (d) trailing edge (TE) flaps deflected to 35° . The take-off (cutback) and sideline configuration entailed: (a) retracted landing gear, (b) slat set at 40° , and (c) TE flaps set at 5° . The surface grids were generated using CATIAv5 Advanced Mesh Generation workbench tools. Care was taken to resolve all the TE surfaces as well as the flap and slat surfaces. High grid density was enforced using background source functions near the expected regions of large flow gradients. These regions included:

- Nacelle/pylon region to adequately resolve the powered flow field
- Around both the nose and main landing gears
- Around the wing and near LE Krueger, and TE flap

The Advancing Front Local Remeshing (AFLR) hybrid volume grid size grew to ~ 125 million cells. The unstructured grid geometry of the SUGAR configuration at approach is shown in Figure 2.33. The power-on boundary conditions were applied at the fan inlet, fan exit, and core exit faces. Finally, the CFD++ N-S analysis was performed at the appropriate flight conditions. The approach condition was set at $M = 0.2$, Altitude = 394ft, and $AOA = 6.859^\circ$. The sideline and takeoff (cutback) condition were set at $M = 0.268$, $AOA = 6.000^\circ$, and altitudes of 1,000 feet and 1,730 feet, respectively. The power-on boundary condition engine parameters (mass flow & temperature) for the inlet primary and bypass exhaust flows were interpolated from the engine cycle deck.

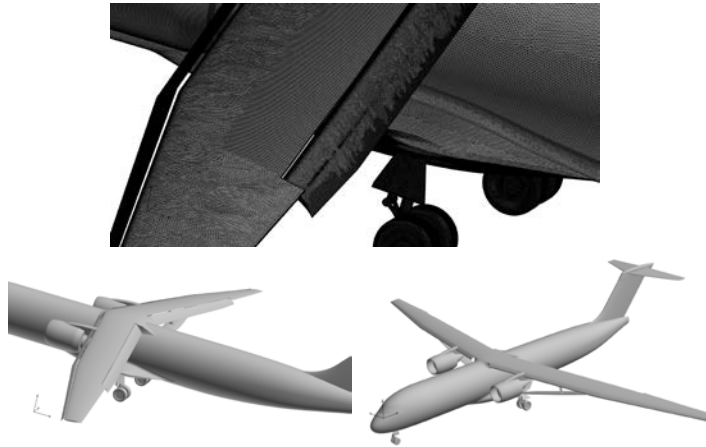


Figure 2.33 – SUGAR Geometry at Approach

Areas of high density gridding included the LE slat and TE flap. It is noted that, in the takeoff position, the leading edge of the flap is tucked under the wing such that the integrated lift of the flap alone had to be approximated. The solution iteration history for CL, CM, and CD parameters is shown in Figure 2.34. Note that the solution converged by ~ 600 iterations.

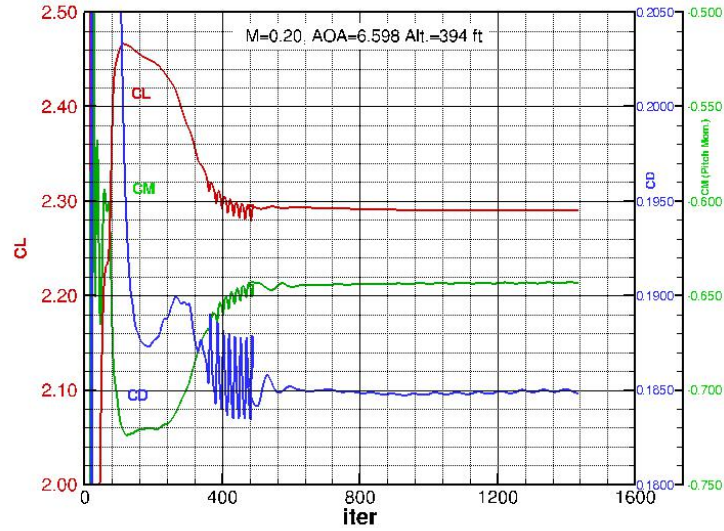


Figure 2.34 – CFD++ Solution Convergence

Flow parameter data was extracted from the CFD Q files for the airframe noise component prediction codes. These included total C_l , C_p , and Mach number. Figure 2.35 shows locations of streamwise and spanwise cuts used to calculate these parameters.

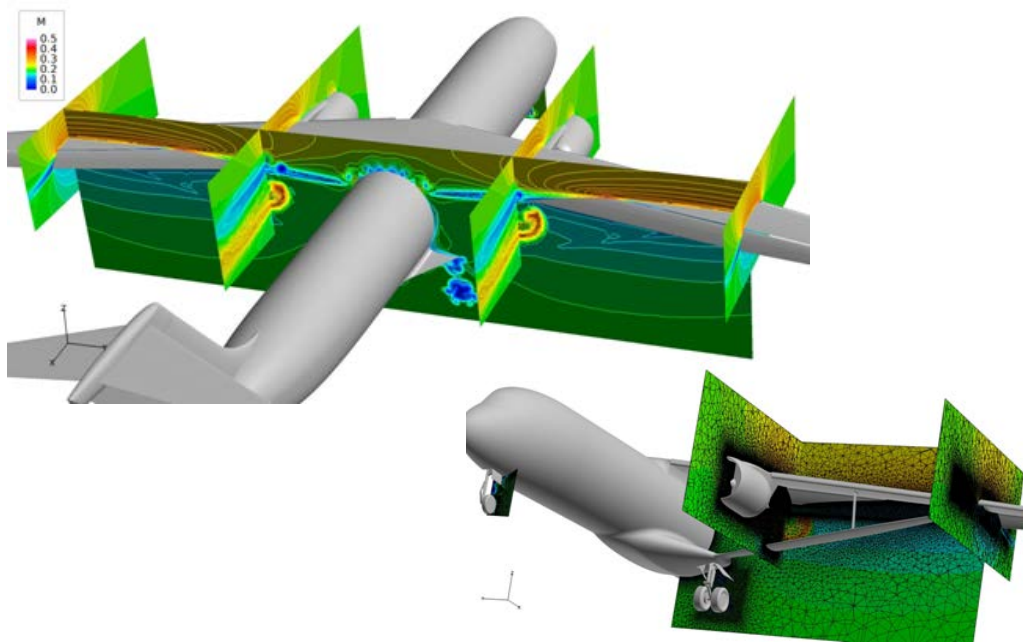


Figure 2.35 – CFD++ Computed Mach Cuts

For gear noise the flow field in front of the main and nose gears was used to calculate the local Mach which was an important parameter for the gear noise prediction.

Since CFD++ uses unstructured grids, sectional C_l was not directly available from the results. Hence, two Matlab routines were written, one to sort, filter, and smooth the CFD data, and

another to perform numerical integration, and then sum CPs to get sectional Cls. This process is illustrated in Figure 2.36.

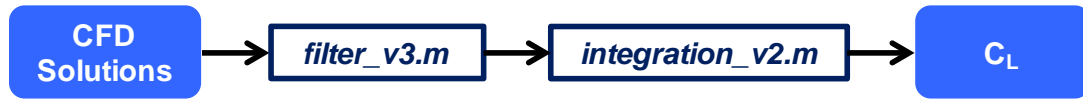


Figure 2.36 – Post-Processing of CFD++ Data for Computing Sectional Lift Coefficient

In the first Matlab routine, *filter_v3.m*, CFD results are filtered by C_p to separate wing upper surface and lower surface. The data points are then smoothed and *.int files are generated. The second Matlab routine, *integration_v2.m*, computes summations of C_p over the upper and lower surfaces. The magnitudes of ΣC_p are added to obtain total C_l . The sectional lift coefficient c_l is obtained by dividing C_l by chord length.

Airframe Noise Analysis

The airframe noise analysis included the nose gear, main gear, slat, and flap components. The trailing edge noise was not included. The approach condition included these four components, but the sideline and cutback conditions only included the slat and flap noise. It was assumed that the nose and main gear is stowed during cutback and sideline.

Both the SUGAR High & Volt are essentially a conventional tube-and-wing configuration other than the truss-braced wing aspect. Hence the methodologies developed for predicting the airframe components were relevant since they were validated for current generation aircraft. Moreover, the basis for the methods is aerodynamic sound generation theory, hence they are not limited to any particular aircraft type. Therefore, any effects specific to the SUGAR HE configuration were captured by the input parameters.

The airframe noise analysis process is depicted in Figure 2.37 below. In the first step, the airframe main-gear, nose-gear, flap, and slat subcomponents are predicted at in-flight condition for AP/CB/SL, using the “As-Drawn” airplane parameter inputs. The subcomponents are then merged (log summed) to yield the total airframe data at AP/CB/SL. This total airframe data is then extrapolated to 150 ft polar-arc condition at flight speed. This data is then scaled to the “Sized” airplane, using the scaling factor $SF = \text{SQRT}(\text{Wing Area Ratio}) = 0.923$, with Sized Area = 1260 ft² and As-Drawn Area = 1478 ft². The SPL correction is then $20\text{LOG}(SF) = -0.693$, which is a constant/fixed SPL adjustment for all angles and frequencies. The final step is extrapolation of the total airframe data to the AP, CB, and SL conditions noted in Table 2.10 above.

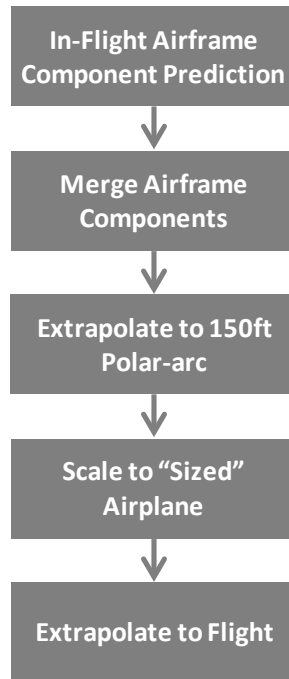


Figure 2.37 – Airframe Noise Analysis Process

The main & nose gear geometric input parameters for both the SUGAR High & Volt are provided in Table 2.11 below. The approach condition flight performance for the gear noise prediction is provided above, in Table 2.10. Aside from geometry, the most important input parameter for the gear noise prediction is the local Mach in proximity of the gear. This was derived, as noted above using CFD analysis with CFD++.

Table 2.11 – Main Gear & Nose Gear Noise Prediction Input Parameters

	Number of Wheels	Wheel Diam (in)	Wheel Width (in)	Wheel Track Angle (Deg)	Numer of Main Struts	Main Strut Length (in)	Main Strut Diam (in)	Main Strut Type
Main Gear	2	44	16	0	1	66	6	circular
Nose Gear	2	27	7.75	0	1	41	4	circular

The slat system is also the same for the SUGAR High and Volt, and consists of an inboard leading edge Krueger flap and several outboard elements which are all Krueger flaps. The deflection angle for the slat is the same for approach, cutback, and sideline, and is depicted in Figure 2.38 below. Note in Figure 2.38, that all the outboard elements deploy together. Effectively then, it can be considered as only 2 slat elements, an inboard and outboard element.

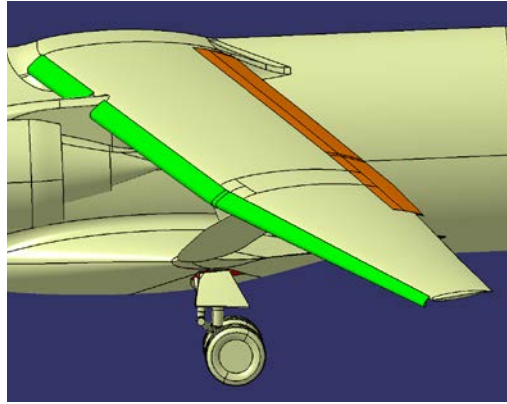


Figure 2.38 – SUGAR Slat System Deployment for Approach/Cutback/Sideline

However, because there is a large change in sweep and chord length from station 587.9, hence the slat was treated as 3 elements, namely, element 1 up to the engine centerline, element 2 from the engine center line to station 587.9 and element 3 from station 587.9 and onwards. This 3 element representation is illustrated in Figure 2.39 below.

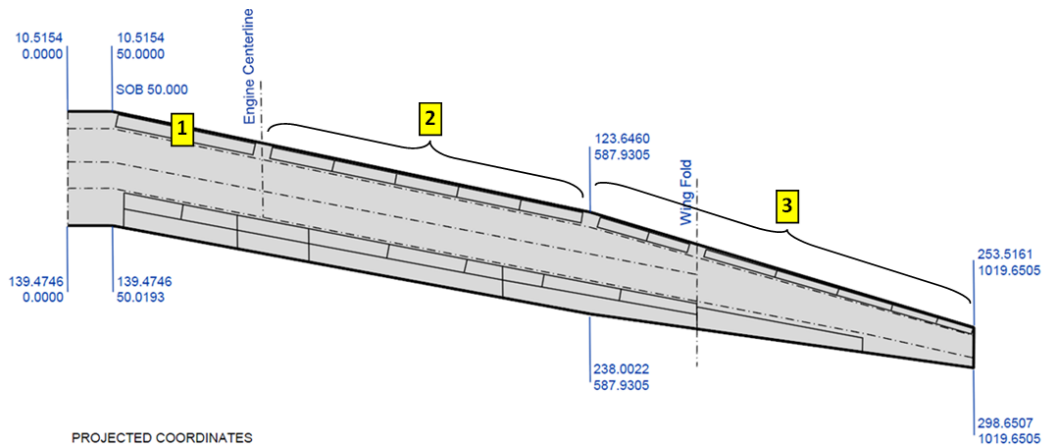


Figure 2.39 – SUGAR Slat System 3-Element Definition for Noise Analysis

The geometric input parameters for the slat system are provided in Table 2.12. The flight performance conditions for approach, cutback and sideline conditions for the slat noise prediction are provided in Table 2.10 above. The CFD++ analysis provided the slat lift coefficient data, and the total lift aerodynamic inputs required for the slat noise prediction.

Table 2.12 – Slat Noise Prediction Input Parameters

	Number of Slats per Wing	Slat Chord Lengths (in)	Slat Span Length (in)	Slat Deployment Angle (Deg)	Slat Sweep Angle (Deg)	Slat Gap (% of wing chord)
Slat	3	17.11	145.9	49.5	11.84	0.0197
		16.14	350.1	51.3	11.91	0.0225
		17.98	431.7	49.4	16.78	0.0189

The flap system is also the same for the SUGAR High and Volt, and consists of an inboard flap element, a flaperon, and 2 outboard flap elements. Both the inboard and outboard are single element fowler flaps. The flap system deflection for approach is illustrated in Figure 2.40. The deployment for cutback/sideline is depicted in Figure 2.41.

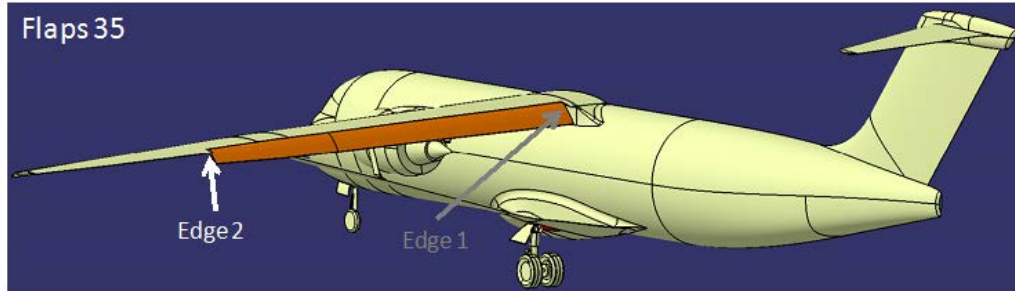


Figure 2.40 – SUGAR Flap System Deployment at Approach

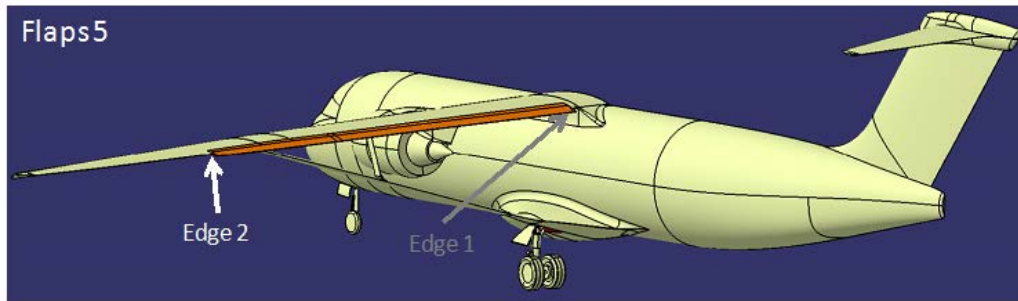


Figure 2.41 – SUGAR Flap System Deployment at Cutback/Sideline

Note in Figure 2.40 and Figure 2.41 that all the flap elements deploy together, which implies that there are only two edges, one edge between the body and inboard side of the inboard flap and one edge between the outboard edge of the outboard flap and the aileron. These 2 edges are schematically noted in Figure 2.42.

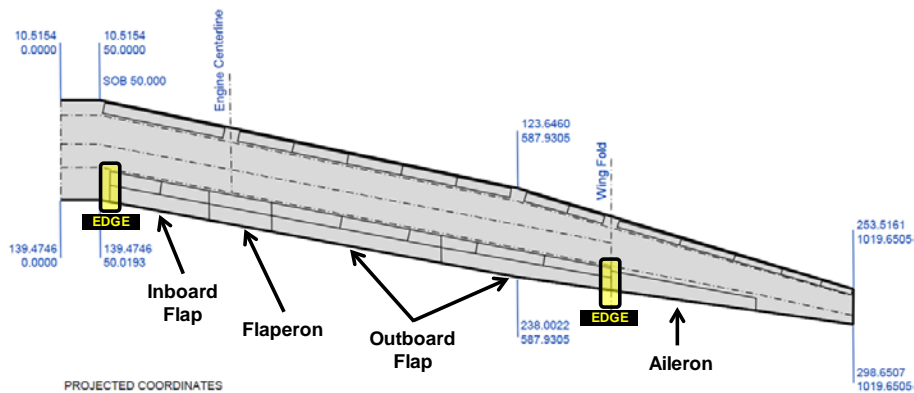


Figure 2.42 – SUGAR Flap System Definition for Noise Analysis

The SUGAR configuration geometric input parameters for the flap at approach are provided in Table 2.13 . The parameters for Cutback are provided in Table 2.14. Note that the only differences are in the deployment angle and CLs. The sideline parameters are provided in Table 2.15. Note that the cutback and sideline parameters are quite similar.

Table 2.13 – Flap Noise Prediction Input Parameters at Approach

	Number of Flap Side Edges	Flap Chord (in)	Flap Thickness (in)	Flap Span Length (in)	Flap Deployment Angle (Deg)	Flap Sweep Angle (Deg)	Flap Edge Type	Flap Lift Coefficient	Flap Sectional Lift
Flap - Approach	2	38.75	5.93	645.4	35	10.63	1	0.3539	1.63
		28.3	4.45	645.4	35	9.44	1	0.3539	1.23

Table 2.14 – Flap Noise Prediction Input Parameters at Cutback

	Number of Flap Side Edges	Flap Chord (in)	Flap Thickness (in)	Flap Span Length (in)	Flap Deployment Angle (Deg)	Flap Sweep Angle (Deg)	Flap Edge Type	Flap Lift Coefficient	Flap Sectional Lift
Flap - Cutback	2	38.75	5.93	645.4	5	10.63	3	0.141421	0.631
		28.3	4.45	645.4	5	9.44	3	0.141421	0.528

Table 2.15 – Flap Noise Prediction Input Parameters at Sideline

	Number of Flap Side Edges	Flap Chord (in)	Flap Thickness (in)	Flap Span Length (in)	Flap Deployment Angle (Deg)	Flap Sweep Angle (Deg)	Flap Edge Type	Flap Lift Coefficient	Flap Sectional Lift
Flap - Sideline	2	38.75	5.93	645.4	5	10.63	3	0.141454	0.626
		28.3	4.45	645.4	5	9.44	3	0.141454	0.599

The airframe noise levels will be shown later on in comparison to the engine noise levels.

Engine Noise Analysis

In this study, engine noise prediction and analysis was provided by GE. The data included spectral engine noise component predictions and final Noise-Power-Distance (NPD) EPNL levels at the noise certification conditions. All the data was at in-flight condition and for a Hardwall Engine. The methodology and technology assumptions GE used for their predictions are shown in Table 2.16. The engine noise was derived from a “parent” engine database using the most advanced engine technology that was applicable to this design, namely the GE GENX-1B engine. This acoustic database had to be scaled to the operating conditions of the SUGAR HE as well as account for any differences in the engine design.

Table 2.16 – GE Noise Modeling Assumptions for the SUGAR HE Volt Engine

Source Category	Methodology
Parent Engine Model	GENx-1B Hardwall – GE Decomposition
Lining Model & Airframe Noise	N/A – Boeing is adding both
Rotor Stator Spacing	Assume same as Genx-1B
Sweep and Lean OGV	Assume 30° sweep for benefit (-1.5 dB on Fan)
Shielding	1.5 dB on all components for SL due to fuselage
VFN	N/A
Electric Motor	Noise largely due to cooling fan – none assumed here
Core Chevron	Not included
Advanced Fan design	2dB benefit on Fan
Core & LPT	Core -3dB and no LPT shielding; Cutoff LPT
M-Factor	5 engine unified m-Factor
JIN	None assumed – built into m-Factor

Figure 2.43 below, gives the noise certification EPNL NPD levels at sideline, cutback and approach for the baseline (no electric motor) and for 2000 – 10,000 Hp electric motor / engine designs. The noise curves shown here are for total engine noise without the airframe noise and for hardwall engine (no acoustic liners). As noted in the figure, the addition of electric power at AP, CB and SL has very minimal impact or benefit on the noise levels.

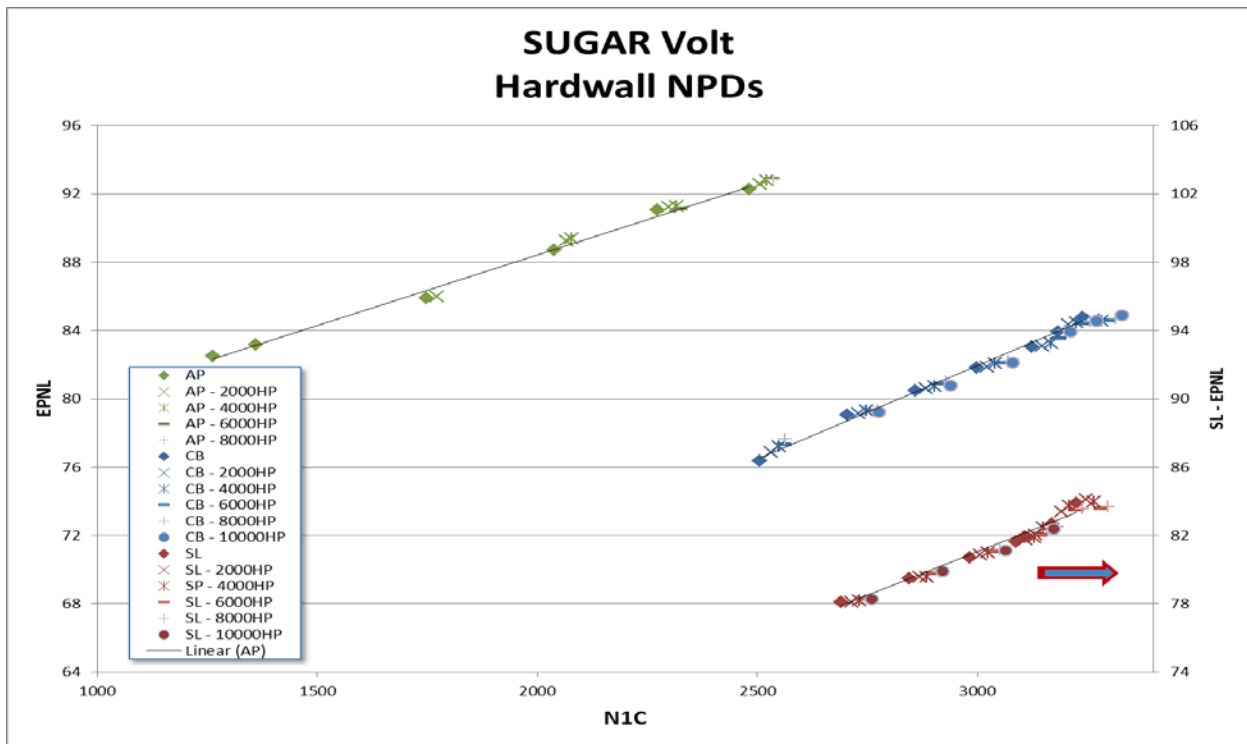


Figure 2.43 – GE Noise-Power-Distance (NPD) Predictions for Hardwall Engine

Engine treatment was defined and analyzed by Boeing. The GE supplied hardwall engine data was used as input. Detailed liner treatment analysis/design was out of scope for this study, hence a simpler approach was adopted, as illustrated in Figure 2.44.

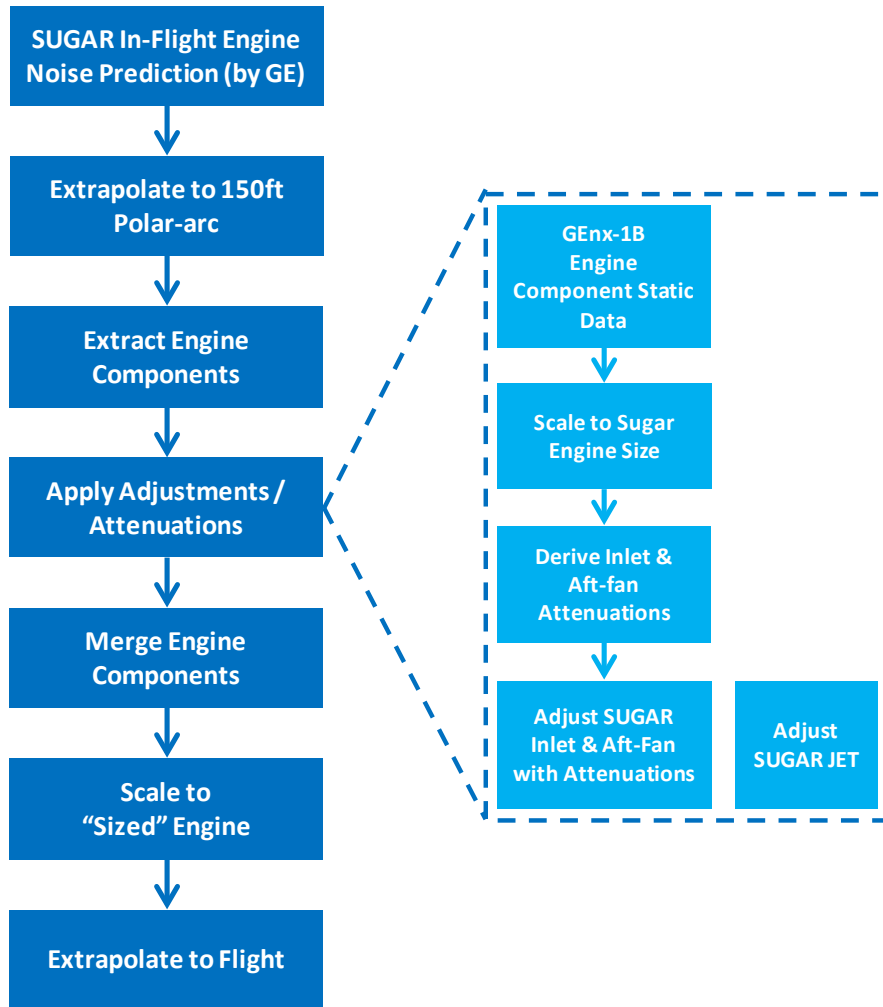


Figure 2.44 – Process for Derivation of SUGAR HE Treated Engine Noise

The first step is to extrapolate the SUGAR in-flight data to 150 ft polar-arc with speed and not for static condition since flight effects can't be undone. Then the inlet, aft-fan, jet and combustor engine subcomponents are extracted separately. Next the jet, inlet, and aft-fan are adjusted. The jet subcomponent adjustment is based on the Boeing database of HBR engines and is consistent with the standard system noise process. The fan-inlet and fan-exhaust are adjusted using the GENx-1B data. Similarity of engine treatment was assumed. This engine was chosen for derivation of attenuations since it was also the engine used as the starting point to define the hardwall SUGAR engine model provided by GE. The input is the GENx-1B engine component static test data. This data is scaled to the SUGAR engine size using the scale factor $SF = \text{Fan Diameter Ratio} = 0.64$, in which SUGAR = 71.2 in fan diameter and GENx-1B = 111.1 in.

The noise attenuations are then derived by subtracting the hardwall data minus the treated data for the aft-fan and inlet subcomponents. The derived spectral attenuations are then used to adjust the SUGAR aft-fan and inlet subcomponent data. Care was taken to align the correct power setting conditions between the scaled GENx-1B data and the SUGAR HE data so that tones aligned correctly when applying the attenuations. Next, the adjusted jet, inlet, and aft-fan subcomponents are remerged (log summed) with the combustor component to derive the adjusted (noise attenuated) total engine noise which includes lining effects. Next, the adjusted data is scaled by thrust to derive appropriate RPMS for AP/CB/SL. Finally, the selected RPM spectral data is extrapolated to AP/CB/SL flight conditions noted in Table 2.10 above.

Total Aircraft (System Noise)

With all the airframe and engine subcomponents properly scaled, adjusted, and projected to in-flight conditions, comparisons can now be made of the subcomponent noise levels relative to each other. Figure 2.45 shows the PNLT noise level contribution of each subcomponent for the SUGAR Volt at AP condition. Note that at AP, the main-gear is the dominant component. The next dominant component is the flap followed by the nose gear. Although not shown, the results are similar for the SUGAR High.

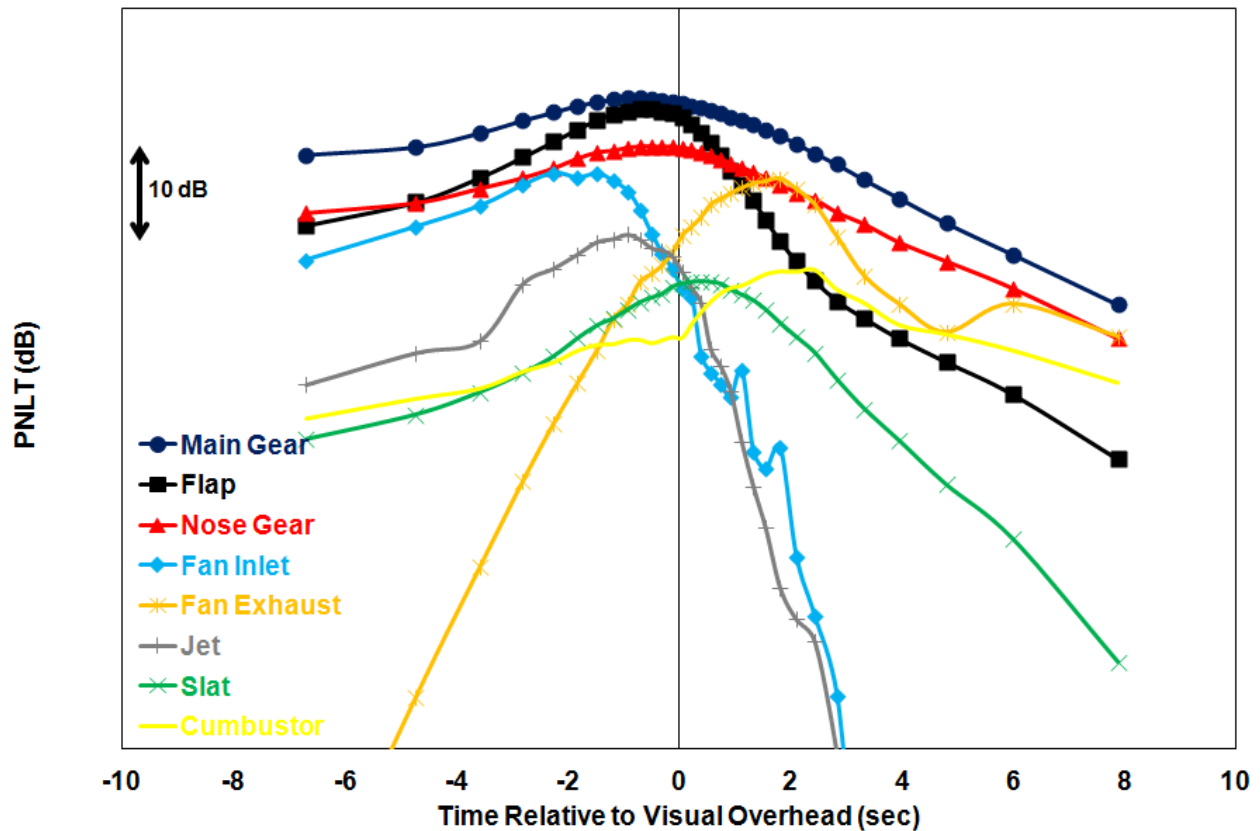


Figure 2.45 – PNLT Contribution at AP from All Subcomponents for SUGAR Volt

Similarly, Figure 2.46 shows the PNLT comparison at CB condition. Here the jet subcomponent dominates in the forward-arc (up to overhead). From overhead to about 16 sec after overhead, the aft-fan dominates, followed closely by jet. From then on the core noise becomes dominant. Again, similar results were noted for the SUGAR High.

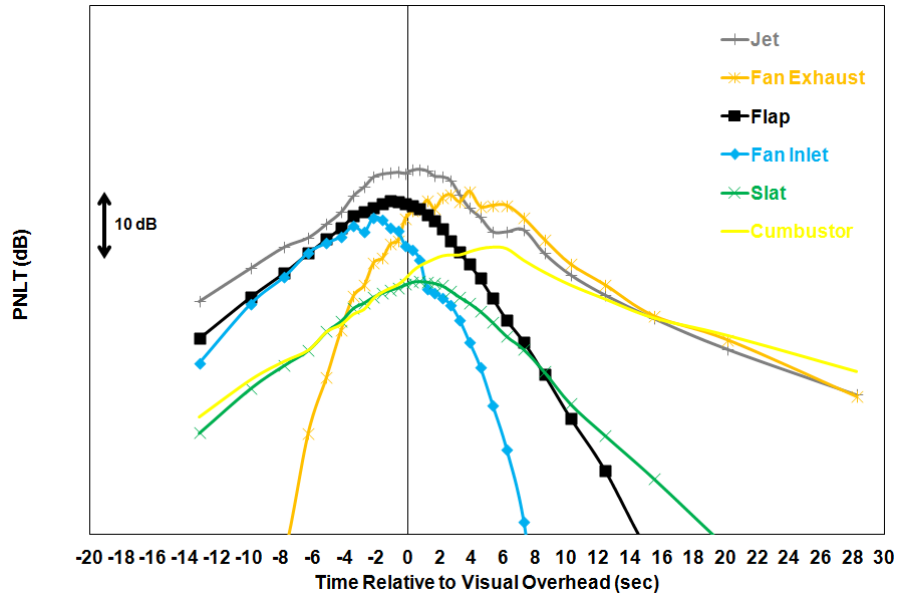


Figure 2.46 – PNLT Contribution at CB from All Subcomponents for SUGAR Volt

Finally, Figure 2.47 shows the PNLT comparison at SL condition. Here the jet subcomponent clearly dominates and by a far margin. After the jet subcomponent, the flap dominates up to overhead and the aft-fan dominates after overhead. Similar results noted for the SUGAR High

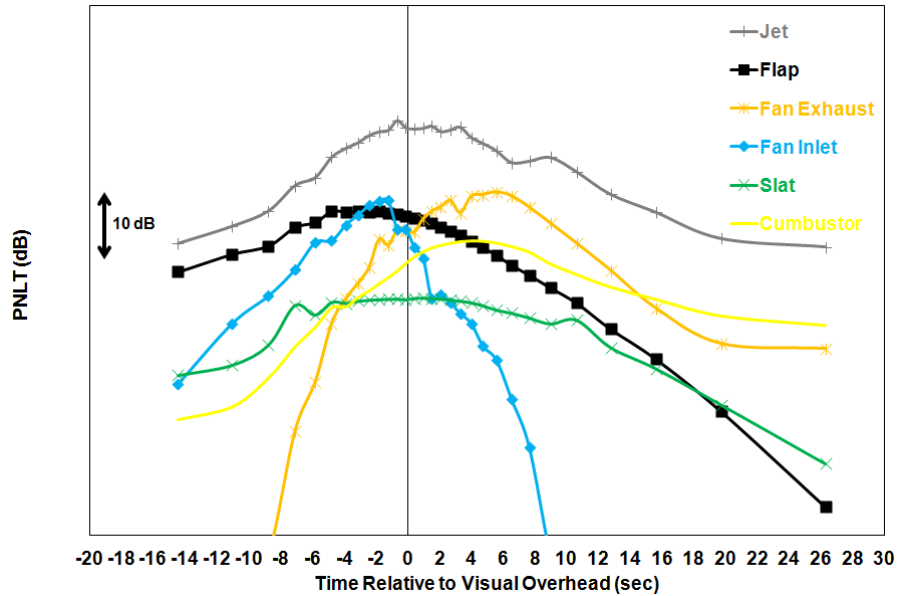


Figure 2.47 – PNLT Contribution at SL from All Subcomponents for SUGAR Volt

Having looked at the comparison of all the noise subcomponents on a PNLT basis, the total engine noise and total airframe noise are compared on an integrated EPNdB basis. Hence all the airframe subcomponents are merged (LOG summed) to derive total engine noise and all the engine subcomponents are merged to derive the total engine noise. Figure 2.48 provides the EPNdB comparison for the total engine and airframe noise at AP, CB, and SL for the SUGAR Volt. On a total basis, the airframe dominates at AP only and the engine dominates at CB and SL. Similar results were noted for the SUGAR High.

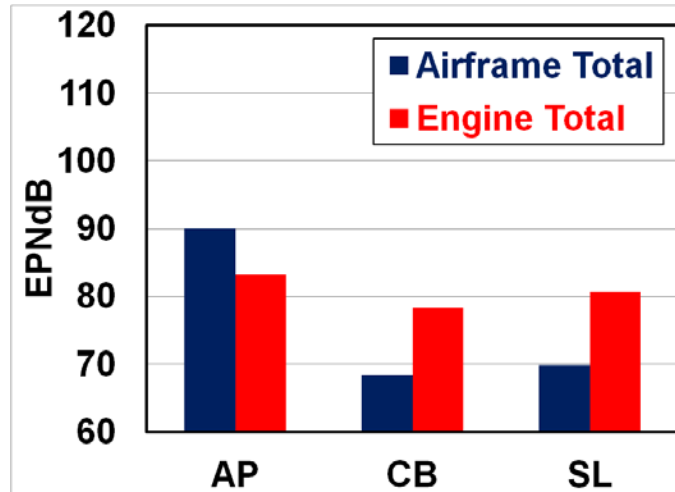


Figure 2.48 – Comparison of Total Engine and Airframe Noise for the SUGAR Volt

With the final subcomponent and total noise levels discussed so far, the SUGAR High and Volt yield the total aircraft (system) noise levels and margins shown in Figure 2.30. These noise levels and margins can be considered baseline. Recall, that the SUGAR High achieves a CUM margin to Stage 4 = 22.8 and the SUGAR Volt achieves a CUM margin = 24.3. The SUGAR High and Volt have similar noise levels and hence achieve similar CUM margins because of small differences in flight speeds, thrusts, and altitude at cutback between the airplanes, as well as similar engine noise between the electric and non-electric variants.

Parametric Noise Reduction

A conceptual level parametric noise reduction study was conducted to assess what further noise reduction can be achieved beyond the “baseline” noise levels and CUM margins. The engine and airframe components were considered separately and each was assigned a range of potential total component noise reduction that seemed reasonable and feasible to achieve in the future. However no detailed analysis was conducted to assess/identify which specific technology would account for the total component noise reduction, as this was outside the scope of the analysis. Thus the total component noise reduction levels were merely “placeholders” to then assess what would be the resultant reduction in the total system noise, and the gained reduction in the CUM noise margin. Table 2.17 provides the parametric study

results for the SUGAR High with a total airframe noise reduction from 0.0 to -3.0 EPNdB and a reduction in total engine noise from 0.0 to -2.0 EPNdB. Note that the 0.0 reduction in both the airframe and engine corresponds to the baseline 22.8 EPNdB CUM margin noted in Figure 2.30 and above. In contrast, looking at the highest potential reduction in airframe noise of -3.0 EPNdB and highest potential reduction in engine noise of -2.0 EPNdB, the maximum achievable CUM margin to Stage 4 is 30.1 EPNdB.

Table 2.17 – Parametric Noise Reduction & Stage 4 CUM Margins for SUGAR High

SUGAR High						
CUM Margins to Stage 4		Engine Noise Reduction (EPNdB)				
		0.0	-0.5	-1.0	-1.5	-2.0
Airframe Noise Reduction (EPNdB)	0.0	22.8	23.8	24.7	25.7	26.6
	-0.5	23.4	24.4	25.4	26.3	27.2
	-1.0	23.9	24.9	25.9	26.9	27.8
	-1.5	24.5	25.5	26.5	27.5	28.4
	-2.0	25.0	26.0	27.0	28.0	29.0
	-2.5	25.4	26.5	27.5	28.5	29.6
	-3.0	25.9	27.0	28.1	29.1	30.1

Similarly Table 2.18 provides the parametric study results for the SUGAR Volt. Note 24.3 EPNdB CUM that the 0.0 reduction in both the airframe and engine corresponds to the baseline 24.3 EPNdB baseline CUM margin for no reduction as noted in Figure 2.30 above. In contrast, at the highest reduction levels (airframe = -3.0, and engine = -2.0), the maximum achievable CUM margin to Stage 4 is 31.4 EPNdB.

Table 2.18 – Parametric Noise Reduction & Stage 4 CUM Margins for SUGAR Volt

SUGAR Volt 1860 (2000HP)						
CUM Margins to Stage 4		Engine Noise Reduction (EPNdB)				
		0.0	-0.5	-1.0	-1.5	-2.0
Airframe Noise Reduction (EPNdB)	0.0	24.3	25.4	26.3	27.3	28.4
	-0.5	24.8	25.8	26.9	27.9	28.9
	-1.0	25.3	26.4	27.3	28.4	29.4
	-1.5	25.7	26.8	27.9	29.0	30.0
	-2.0	26.3	27.2	28.3	29.5	30.6
	-2.5	26.6	27.8	28.9	29.8	31.0
	-3.0	27.0	28.1	29.3	30.4	31.4

With the margins identified for each potential airframe/engine noise reduction pairing, a brainstorming was conducted to identify some concepts that might help to achieve these component noise reductions. The gear, flap jet and fan were focused on since they were the dominant subcomponents. Table 2.19 provides the brainstormed noise reduction ideas for the airframe components. Table 2.20 provides the brainstormed noise reduction ideas for the engine components. This is by no means an exhaustive list but rather a sampling of potential ideas.

Table 2.19 – Potential Airframe Noise Reduction Technology

Gear Noise	Flap Noise
Lower Local Velocity	Porous Trailing Edges
“Cleaner” Design”	Side Edge Fences
Fairings	Continuous Mold-Line

Table 2.20 – Potential Engine Noise Reduction Technology

Jet Noise	Fan Noise
Chevrons	Scarf Inlet
Higher BPR / GTF	Advanced / Active Liners
Variable Area Fan Nozzle	Active Noise Control

2.3.4.5 Summary of Acoustic Analysis

Acoustic analysis was completed for the SUGAR High and SUGAR Volt. Engine Noise prediction and analysis was provided by GE. Airframe noise, and engine treatment noise prediction and analysis were conducted by Boeing. Final integration of engine and airframe noise and derivation of system noise was conducted by Boeing as well. With respect to the Phase 1 results and the preliminary Phase 2 results, the final results are drawn from higher fidelity noise analysis, and from use of flight performance and a refined more accurate baseline (reference). The SUGAR High & Volt were found to have similar noise levels and CUM margins due to similarity in flight performance and small influence on the engine noise due to use of electric power. The SUGAR High achieved a CUM margin to Stage 4 of 22.8 EPNdB, while the SUGAR Volt achieved 24.3 EPNdB CUM margin. With “placeholder” values for advanced airframe and engine noise reduction technology, the Sugar High achieved 30.1 EPNdB CUM margin to Stage 4 and the Sugar Volt achieved a CUM margin of 31.4 EPNdB. All results were far short of meeting the 52 EPNdB CUM margin goal.

2.3.5 hFan+2: Emissions

The LTO NOx emissions for the hFan+2 propulsion systems for the 750 Balanced and 750 Core Shutdown aircraft were assessed. The CAEP/6 requirements, characteristic LTO NOx, and margined estimates are listed below in Table 2.21. GE also provided estimates of cruise NOx emissions compared to a CFM-56. Propulsive and thermal efficiency gains in combination with improved thrust lapse characteristics have resulted in diminished LTO NOx emissions for the hFan+2 engine architectures. For LTO NOx, both the hFan+2 propulsion systems were better than the goal (20% of CAEP/6). For cruise NOx the 1380 and 1750 HP aircraft are close to the 80% reduction goal and the 7150 HP core shutdown aircraft has essentially no NOx emissions over approximately 50 percent of the cruise segment of the 900 nm mission.

Table 2.21 – 750 Balanced and Core Shutdown NOx Emissions

LTO NOx Emissions - 750 Balanced		
	Non-Hybrid Electric	Hybrid Electric
CAEP/6, g/kN	75.4	75.4
Characteristic LTO NOx, g/kN	13.1	7.4
Margined Estimate, % CAEP/6	19.2%	10.9%

LTO NOx Emissions - 750 Core Shutdown		
	Non-Hybrid Electric	Hybrid Electric
CAEP/6, g/kN	78.4	78.4
Characteristic LTO NOx, g/kN	11.6	5.2
Margined Estimate, % CAEP/6	16.3%	7.4%

Mid-Cruise Emissions (CFM56-7B Baseline)			
	1380 HP ICAC Constrained	1750HP ICAC Inactive	7150HP ICAC Inactive
Absolute NOx Reduction	73.5%	73.9%	99.3%

2.3.6 Energy Cost Analysis

The objective of the Energy Cost Study was to investigate the total energy cost of operating the SUGAR Volt by parametrically varying battery performance, fuel cost, battery life and cost, and electricity cost.

In addition to comparing the SUGAR Free and SUGAR High, two versions of the SUGAR Volt were analyzed: SUGAR Balanced (Ref HP 1,750) and SUGAR Core Shutdown. Both planes assumed a battery performance level of 750 Whr/kg. Each plane had a different design goal and approach:

- **Balanced (Ref HP 1,750) Design:**
 - MTOW Sized by 3,500 NM mission (assuming an all-fuel mission)
 - Net energy density (fuel + batteries) is traded for range while maintaining MTOW for missions longer than 900 nm
 - Ref HP 1,750 was chosen to fully discharge the 16,700 lb of batteries over the duration of the 900 nm mission
- **Core Shutdown Design:**
 - MTOW sized to 190,000 lb to maximize fuel burn savings on the 900 nm mission
 - Results in larger electric motors and greater battery size and weight capability
 - The electric horse power was sized (7,150 engine HP) to enable core shutdown at cruise.

An Excel-based tool was used to parametrically explore combinations of energy and battery cost. Electricity, fuel, and battery life assumptions do not change the aircraft weight and thus do not require the vehicles to be resized.

We evaluated the following costs:

- Fuel + electricity (“energy cost”)
- Fuel + electricity + battery replacement (“energy + batteries cost”)
- Fuel + electricity + battery replacement + other weight & complexity based costs (from public domain cost models) (8) (“total cost”)

To conduct the parametric analysis, we needed to establish a range of assumptions for the major drivers on aircraft costs. These included fuel cost, electricity cost, battery energy per mass, battery cost, and battery life. Based on expert judgment and historical trends, we established a range of values for each (low, middle, high), shown in Table 2.22. For battery specific energy, we used 750 Wh/kg (the reference N+3 level) where we have available sized aircraft configurations. It was our expectation, based on Phase I and Phase II Year 1-2 results that values below 750 Wh/kg would not yield any cost benefits due to the increased battery weight. Battery Life/Cost values were calculated by using the highest and lowest combinations of battery life and cost.

Table 2.22 – Cost Assumptions

Parameter	Units	Low Value	Middle Value	High Value	Nominal	More Optimistic	Most Optimistic
Fuel Cost	\$/gal	3.00	5.00	6.00	5.00	5.00	6.00
Electricity Cost	\$/kwh	0.03	0.07	0.10	0.07	0.07	0.03
Battery Energy	Wh/kg		750	1000	750	750	750
Battery Cost	\$/kg	44	88	220	88	44	44
Battery Life	Cycles	1,000	2,000	5,000	2,000	5,000	5,000
Battery Life/Cost	Cycles/kg/\$	4.5	23	114	23	114	114

2.3.6.1 Results for Nominal Assumptions

Using the nominal cost assumptions shown in Table 2.22, results were generated and are shown in Figure 2.49, Figure 2.50, and Table 2.23. These results indicate that the balanced SUGAR Volt (Ref HP 1750) is the better option. The percentages shown in Table 2.23 are computed as differences relative to SUGAR High. The balanced Volt has a 6% reduction in Energy Cost, a 1% reduction in Energy + Battery Cost, and a 2% increase in Total Cost compared to SUGAR High. The core shutdown plane shows a slight increase in Energy Cost, a 16% increase in Energy + Battery Cost, and a 15% increase in Total Cost. The core shutdown Volt, which had nearly triple the battery weight of the balanced Volt, clearly reflects this in the increased battery costs.

Table 2.23 – Cost Results for Nominal Cost Assumptions

Category	SUGAR Balanced 750 Wh/kg (Ref HP 1,750)	SUGAR Core Shutdown 750 Wh/kg
Energy Cost	-6.3%	0.1%
Energy + Batteries Cost	-0.8%	15.9%
Total Cost	1.8%	15.3%

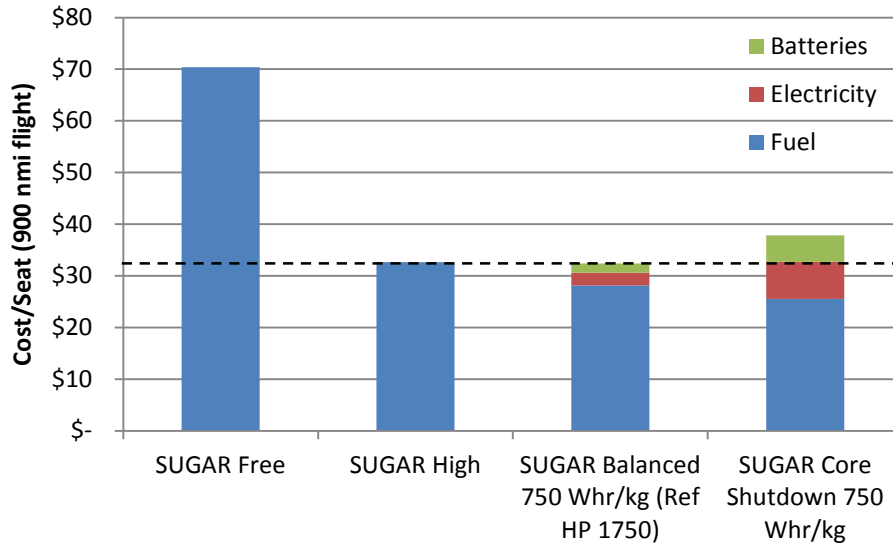


Figure 2.49 – Energy + Battery Cost Results for Nominal Assumptions

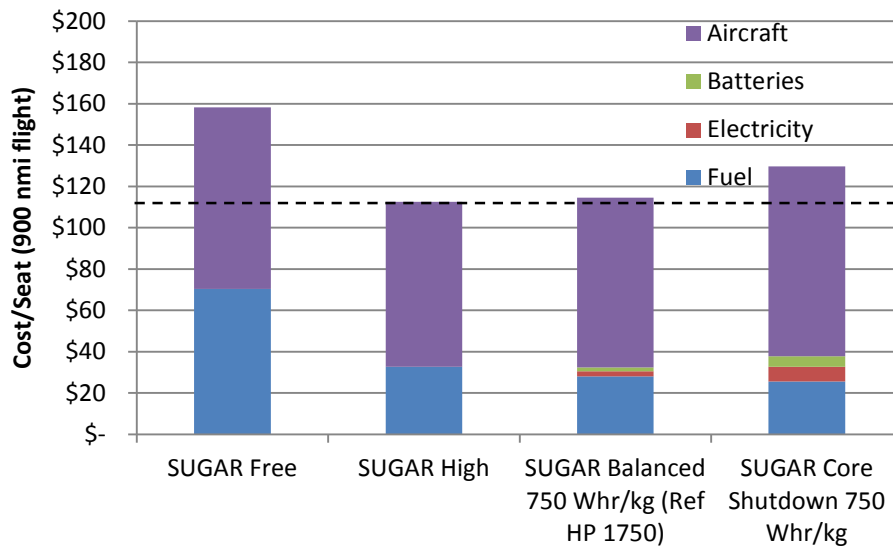


Figure 2.50 – Total Cost Results for Nominal Assumptions

2.3.6.2 Results for More Optimistic Battery Assumptions

Using the more optimistic battery cost and life assumptions shown in Table 2.22, results were computed and are shown in Figure 2.51, Figure 2.52, and Table 2.24. The percentages in Table 2.24 are taken relative to SUGAR High. Again, the balanced Volt looks best. The balanced airplane shows a 6% reduction in Energy Cost, a 5% decrease in Energy + Battery Cost, and a 1% Total Cost increase compared to SUGAR High. The core shutdown airplane has a slight increase in Energy Cost, a 3% increase in Energy + Battery Cost, and a 12% increase in Total Cost. The core shutdown airplane is heavily penalized for its significantly increased MTOW over SUGAR High.

Table 2.24 – Cost Results for More Optimistic Battery Assumptions

Category	SUGAR Balanced 750 Wh/kg (Ref HP 1,750)	SUGAR Core Shutdown 750 Wh/kg
Energy Cost	-6.3%	0.1%
Energy + Batteries Cost	-5.2%	3.3%
Total Cost	0.6%	11.6%

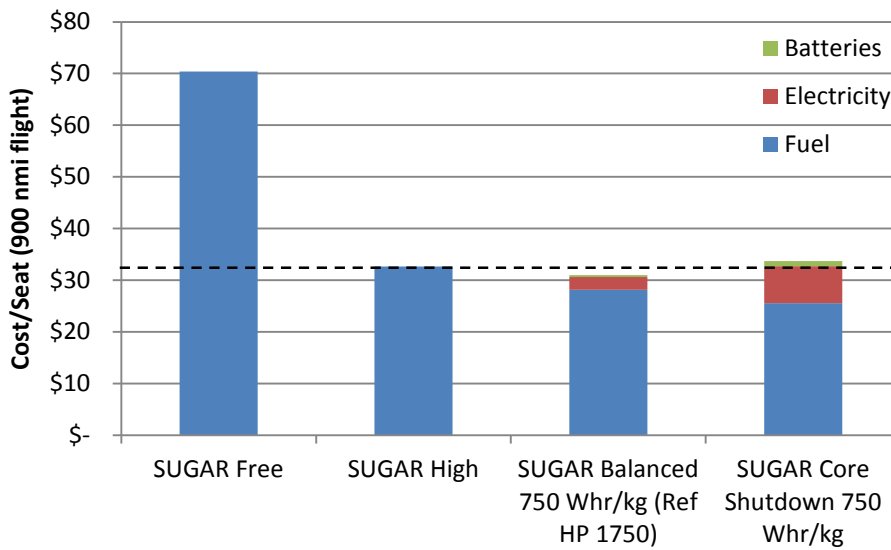


Figure 2.51 – Energy + Battery Cost Results for More Optimistic Battery Assumptions

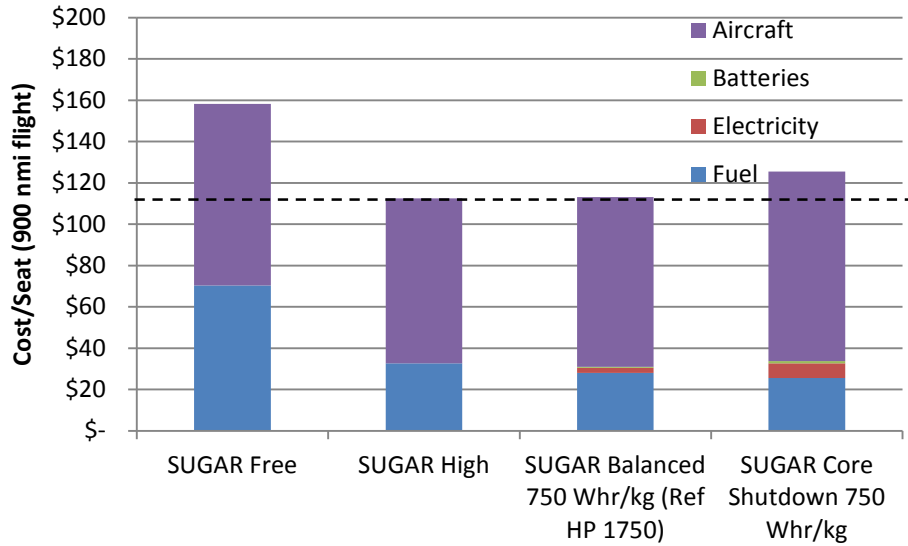


Figure 2.52 – Total Cost Results for More Optimistic Battery Assumptions

2.3.6.3 Results for Most Optimistic Assumptions for Electric Aircraft

Using the most optimistic battery cost and life assumptions, as well as a high fuel cost and a low electricity cost (see Table 2.22), the following results were generated and are shown in Figure 2.53, Figure 2.54, and Table 2.25 (relative to SUGAR High). The balanced airplane shows an 11% reduction in Energy Cost, a 10% decrease in Energy + Battery Cost, and a 1% reduction in Total Cost compared to SUGAR High. The core shutdown aircraft has a 14% reduction in Energy Cost, an 11% reduction in Energy + Battery Cost, and a 6% increase in Total Cost. Using the most optimistic assumptions, the balanced aircraft shows a lower Total Cost than SUGAR High.

Table 2.25 – Cost Results for Most Optimistic Battery Assumptions

Category	SUGAR Balanced 750 Wh/kg (Ref HP 1750)	SUGAR Core Shutdown 750 Wh/kg
Energy Cost	-11.2%	-13.9%
Energy + Batteries Cost	-10.3%	-11.3%
Total Cost	-1.4%	6.4%

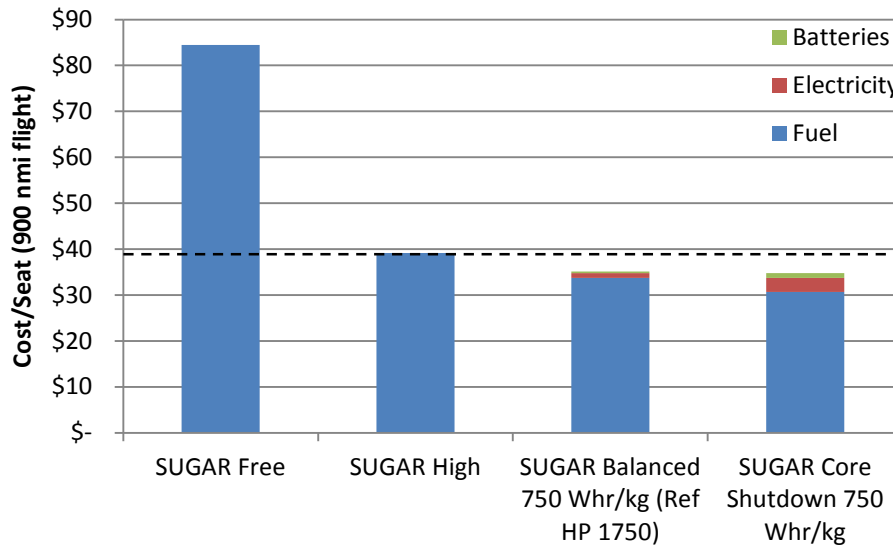


Figure 2.53 – Energy + Battery Cost Results for Most Optimistic Battery Assumptions

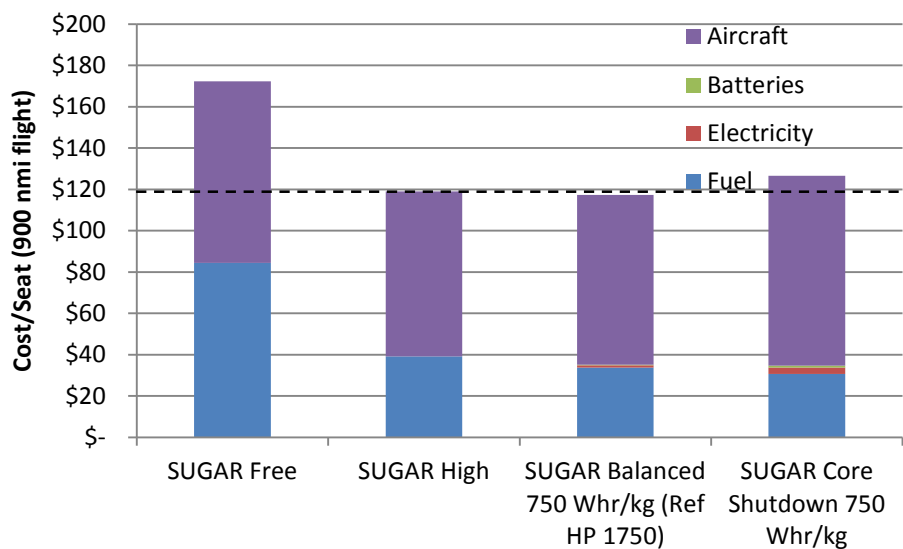


Figure 2.54 – Total Cost Results for Most Optimistic Battery Assumptions

2.3.6.4 Energy Cost Analysis Summary

These results are sensitive to fuel and electricity costs, battery energy density, battery cost, battery life, and weight.

SUGAR High reduces fuel and electricity cost by 54% and total cost by 29%, when compared to the SUGAR Free (current technology non-electric). SUGAR High includes all SUGAR N+3 technologies except the use of a hybrid electric battery gas turbine propulsion system. The SUGAR High is used as the reference for the hybrid electric SUGAR Volt aircraft results below.

The balanced SUGAR Volt shows a 6-11% reduced direct energy cost (fuel + electricity) and a 1-10% reduced energy (fuel + electricity + battery) cost relative to SUGAR High. However, including costs for increased aircraft weight and complexity reveals minimal cost difference (+2% to -2%) relative to SUGAR High. The balanced SUGAR Volt aircraft was found to be the best option of the two SUGAR Volt airplanes in this study.

The SUGAR Volt maintains an emissions advantage over the SUGAR High. NOx emissions are better because of reduced gas turbine throttle and reduced fuel use. Life cycle CO2 emissions can also be improved, but only if battery-charging electricity is from a clean, low-carbon source.

2.4 Technology Plans and Roadmaps

The team has updated some of the technology plans that were developed in Phase I. The following updated technology plans are included in this section:

- Hybrid Electric Engine
- High Performance Batteries

These plans are not included in this report but are included in Final Report Volume I Truss Braced Wing Design Exploration:

- NextGen Air Traffic Management
- Aerodynamic Technologies for Performance
- Airframe Acoustic Technologies
- Engine Acoustic Technologies
- Advanced Subsystems
- Structural Materials
- Structural Concepts
- Advanced Engine Technologies
- High Span TWB Technology Integration

2.4.1 Hybrid Electric Engine

Goals and Objectives:

Develop high performance, flight weight, and prime-reliable electric power components suitable for flight propulsion applications.

Performance Area and Impact:

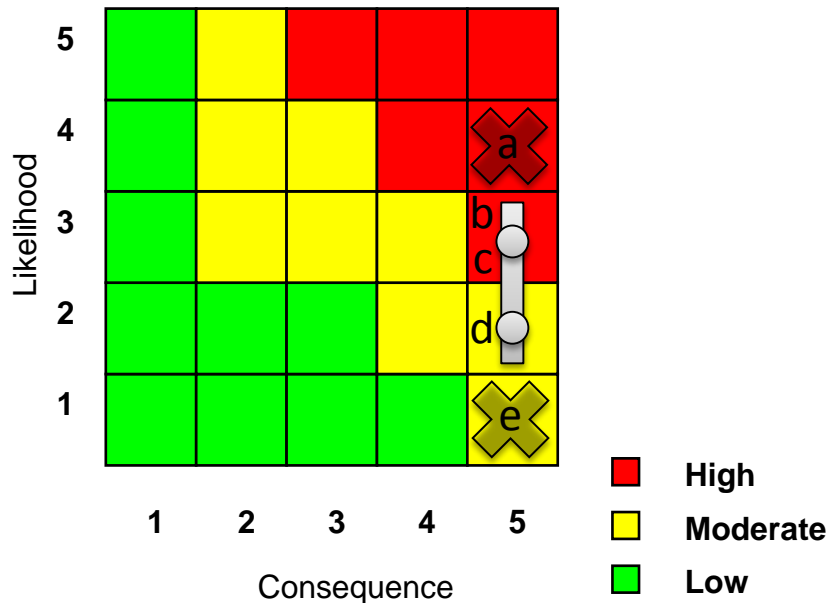
Fuel burn and emissions will be reduced by using energy stored in batteries that is generated from alternative energy sources, such as solar, wind, or nuclear. The battery energy will be leveraged to aid in hybrid turbo-electric propulsion of the aircraft.

Noise will be reduced by using stored battery energy to replace some of the energy generated by gas engines, thereby reducing the production of noise from the core of the engines. Hybrid electric systems also could enable distributed propulsion architectures which could enable BLI (Boundary Layer Ingestion) technology.

Technical Description:

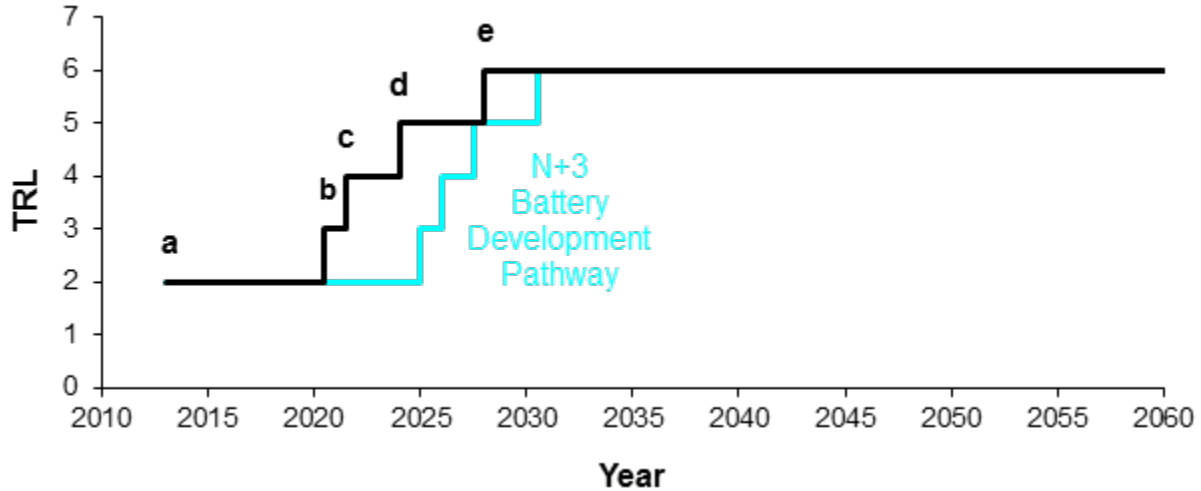
Hybrid turbo-electric propulsion enabled by energy stored in batteries has the potential to reduce fuel burn, emissions, and noise. Savings are dependent on battery energy density as well as the performance, efficiency, and weight of the electric power components. Efficient, high power, and light weight motors and motor controllers need to be developed. Light weight radiators and surface coolers are also needed to maintain the electric power components at temperatures conducive to high efficiency. A sustained program to develop high voltage conductors and insulators is also needed to support development of the necessary electric power components. A variable core nozzle needs to be developed to allow the engine to operate with more widely varying levels of load introduced by the option to switch to electric power. These components need to be integrated in a hybrid engine system that can be demonstrated in flight. Superconducting components should be considered as possible system enhancing technologies and this would require additional development, design, and testing of cryocooler systems for aircraft. Battery technology development is included in a separate technology plan.

Risk Assessment:



If hybrid engine performance and weight do not reach the levels assumed in the vehicle analysis, this technology will not contribute the projected benefits in fuel burn, emissions, and noise.

Major Milestones:



Maturation Plan:

TRL 2 (a) Current

- Some analysis of the engine system has been performed.
- Some mission and sizing analysis has been conducted to assess fuel burn, energy, and global life cycle emissions benefit.

TRL 3 (b)

- A life-cycle energy study will examine net benefit to fuel burn and emissions including generation of energy on the ground
- A study will assess the potential reductions in airport noise and emissions
- 3 motor design cycles
- 3 surface cooler/radiator design cycles
- 3 motor controller/power electronics design cycles
- Sustained program for lightweight high voltage conductors and insulators, with off-ramps every ~18 months
- Lightweight variable core exhaust nozzle design
- A design developed for a small-scale hybrid electric propulsion system

TRL 4 (c)

- 3 motor build, test, report-out cycles
- 3 surface cooler/radiator build, test, report out cycles
- 3 motor controller/power electronics build, test, report out cycles

- Sustained program for lightweight high voltage conductors and insulators, with off ramps every ~18 months
- Lightweight variable core exhaust nozzle build, test
- An integrated ground test of a small scale hybrid engine

TRL 5 (d)

- Integration of components into 1st full-scale demonstration engine
- 1st demonstration engine test
- Flight test of a small scale hybrid engine integrated into a small aircraft

TRL 6 (e)

- Integration of components into 2nd full-scale demonstration engine
- 2nd demonstration engine test
- Optional flight test

Dependency:

- High energy density battery technology is required to harness the benefit of hybrid engine technology.
- A suitable off-the-shelf engine asset is needed to support testing.

Success Criteria:

TRL	Success Criteria	Alternate Steps if Unsuccessful
3	Analysis shows hybrid engine system will have performance (fuel burn, emissions, noise) and weight consistent with meeting goals	Continue to optimize and improve design of system and components Consider application to smaller, shorter range aircraft
4	Tests of hybrid engine system components show performance (fuel burn, emissions, noise) and weight consistent with goals	Redesign components with shortfalls
5	Hybrid engine system components integrated and successfully tested Initial system performance (fuel burn, emissions, noise) and weight indicates goals can be met with some redesign	Redesign system to meet goals Accept meeting reduced goals
6	Hybrid engine system demonstrates performance (fuel burn, emissions, noise) and weight consistent with goals	Accept meeting reduced goals

NASA Contract NNL08AA16B – NNL11AA00T – Subsonic Ultra Green Aircraft Research – Phase II
 Volume II – Hybrid Electric Design Exploration

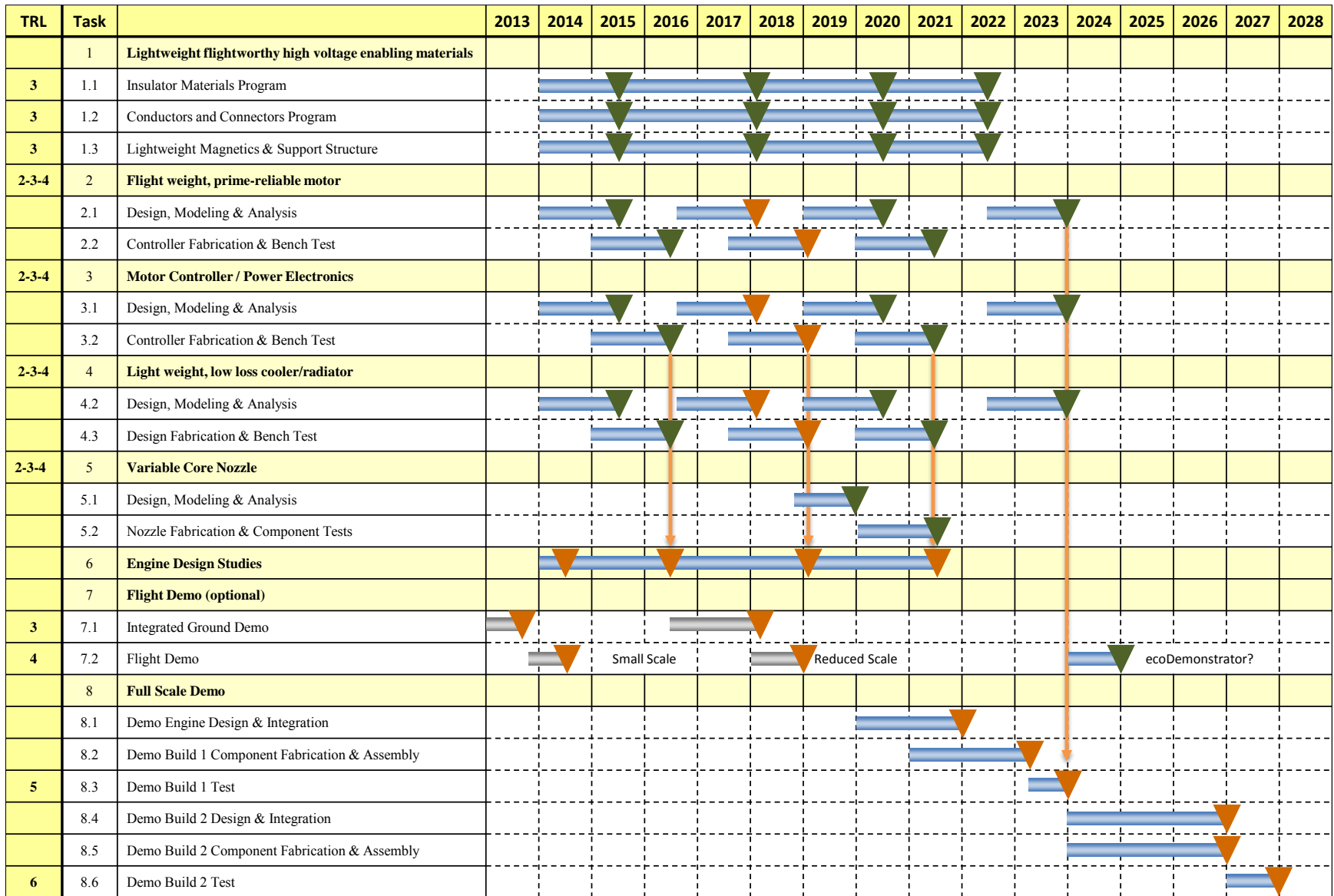


Figure 2.55 – Hybrid Electric Engine Technologies*

*The roadmap schedule shown is notional, suitable for overall program planning purposes only, with no implied guarantee or commitment on the part of GE Aviation 67

2.4.2 High Performance Batteries

Goals and Objectives:

Foster development of high energy density modular batteries. Work with one or more battery manufacturers to produce batteries that achieve aviation safety requirements and are tailored for aviation performance requirements and usage patterns. Integrate them in flight propulsion applications when the batteries are at an appropriate level of development.

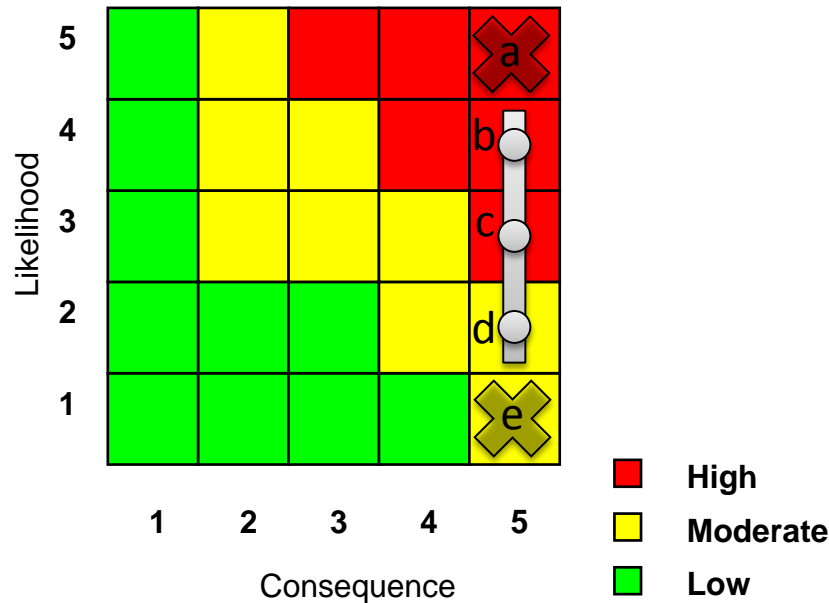
Performance Area and Impact:

Fuel burn and emissions will be reduced by using energy stored in batteries that is generated from alternative energy sources, such as solar, wind, or nuclear. High efficiency of electrical components may reduce total energy usage and emissions relative to conventional liquid fuels. Life cycle studies will be needed to confirm these savings.

Technical Description:

Multiple battery technologies have potential to produce the energy densities needed to reduce fuel burn and emissions in an aircraft application. Low-level studies are needed to produce requirements and data that can be provided to battery manufacturers to encourage the development of battery technology that can support such application. Once suitable batteries are available, a substantial development program will be required to integrate and test these batteries in combination with hybrid-electric engine technology and aviation specific requirements.

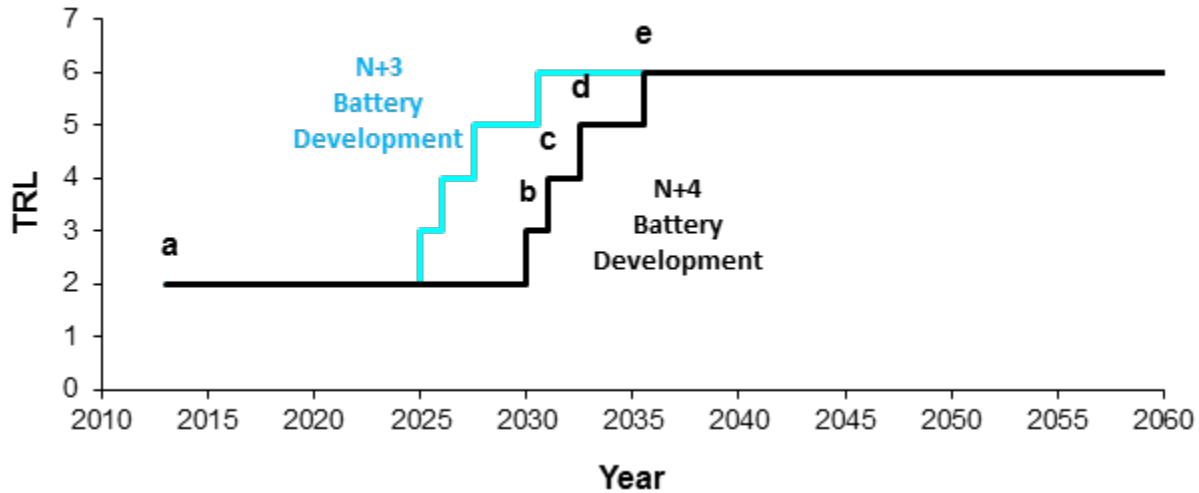
Risk Assessment:



If battery energy densities do not reach the levels assumed in the vehicle analysis, this technology will not contribute the projected benefits in fuel burn, emissions, and noise.

*The roadmap schedule shown is notional, suitable for overall program planning purposes only, with no implied guarantee or commitment on the part of GE Aviation 68

Major Milestones:



Maturation Plan:

TRL 2 (a) Current

- Theoretical estimates and some small-scale experiments indicate feasibility of reaching the needed energy density

TRL 3 (b)

- A life-cycle energy study will examine net benefit to fuel burn and emissions including generation of energy on the ground
- Aircraft system studies will define requirements for battery technology (including safety and charge/discharge rate)
- Battery manufacturers will develop the basic technology to achieve the required energy density. Develop approach to achieve aviation specific battery life, charge/discharge rate, and safety.

TRL 4 (c)

- Battery components will be tested for meeting aircraft power, life, charge/discharge rates, and safety requirements including operation in a relevant environment

TRL 5 (d)

- Battery components will be integrated and packaged for testing in flight
- A battery package of representative size will be tested in flight or simulated flight conditions

TRL 6 (e)

- A battery power system suitable for a demonstrator aircraft will be assembled
- The battery power system will be integrated with a hybrid-electric engine
- The combined hybrid-electric engine and battery power system will be tested in flight

Dependency:

Aviation batteries are dependent on dramatic improvements in battery technology for other applications such as ground transportation. Hybrid-electric or all-electric propulsion is required to harness the benefit of aviation battery technology.

Success Criteria:

TRL	Success Criteria	Alternate Steps if Unsuccessful
3	Analysis shows battery technology will result in fuel burn and emissions reductions through a complete energy life-cycle Battery energy density reaches required levels	Continue basic battery development Switch to alternative battery option* Switch to alternative technology option* Accept meeting reduced goals**
4	Component testing of batteries show suitability for aircraft application (including life, charge/discharge rate, and safety)	Resume basic battery development Switch to alternative battery option* Switch to alternative technology option*
5	Batteries successfully packaged for use in flight Battery package successfully tested in flight conditions	Redesign battery packaging Switch to alternative technology option*
6	Battery power system successfully tested with hybrid-electric engine in flight	Accept meeting reduced goals** Switch to alternative technology option*

* Baseline battery technology is assumed to be Lithium-Ion, but this chemistry may reach a plateau in performance before needed levels are reached. Alternative battery options include Zinc-Air, Lithium-Air, and liquid electrolyte slurries which would require additional systems. Alternative technology options include hybrid batteries (multiple chemistries), capacitors, hybrid battery capacitor, and flywheels. Zinc-Air and Lithium-air batteries require design of air induction and exhaust system which would require updated roadmap tasks to be added. Quick modular battery swap out or mechanically rechargeable components could be used if charge rates are not fast enough for quick gate turn requirements.

** Lower performance batteries could be suitable for smaller and especially shorter range aircraft

NASA Contract NNL08AA16B – NNL11AA00T – Subsonic Ultra Green Aircraft Research – Phase II
 Volume II – Hybrid Electric Design Exploration

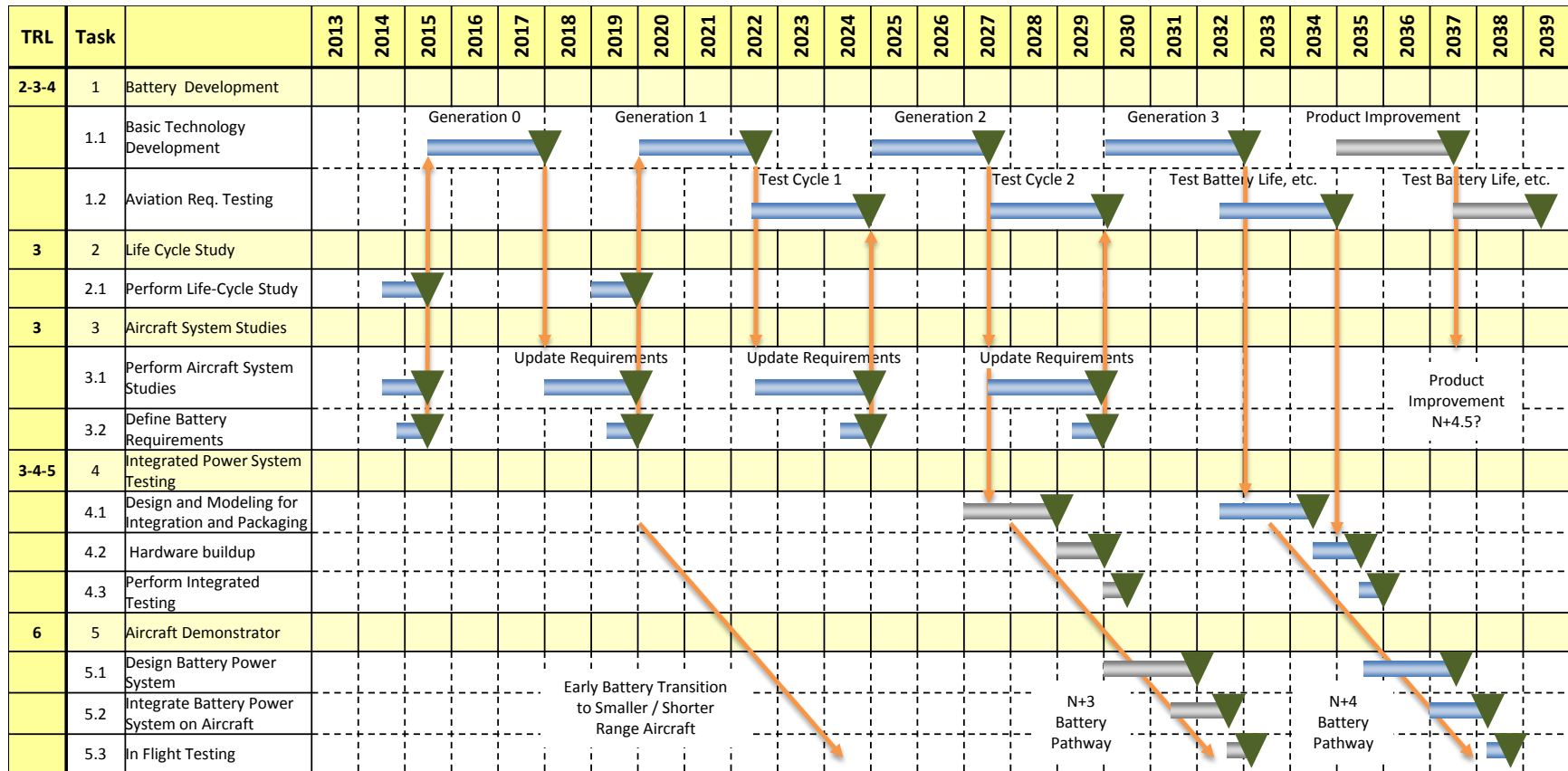


Figure 2.56 – High Performance Battery Technology Roadmap

3.0 Hybrid Electric Propulsion Modeling Environment & Sizing Studies

The modeling environment documentation is broken into two separate sections. The first section covers the modeling environment while the second covers sizing studies conducted within the environment.

3.1 Hybrid Electric Modeling Environment

In Task 3.3 Georgia Tech developed a set of generic NPSS elements that can be used to construct a modeling environment that will enable assessment of various electric and hybrid electric architectures, including batteries, fuel cells, and ducted and unducted fans.

The NPSS models were constructed using public domain methods in order to ensure their usability and traceability. When possible, the models were developed such that proprietary data or modeling algorithms could be easily implemented should that be required. After an initial period of discussion with Boeing and NASA, Georgia Tech finalized the list of modeling elements to be developed. The list of NPSS elements developed includes an SOFC fuel cell, generic battery, a suite of electrical distribution elements, motors, generators, and an augmentation to the base NPSS propeller performance element that allows for parametric generation of propeller performance maps for single and counter rotating applications.

Following the completion of the individual NPSS modeling elements, Georgia Tech completed Task 3.3.4 in 2013. Some of the individual elements were combined to construct a non-proprietary model similar to General Electric's hFan. This required construction of a parametric turbofan model within NPSS complete with appropriate power management logic. After noticeable performance differences were resolved between the GE and Georgia Tech NPSS models, Georgia Tech added detailed efficiency prediction capabilities to the motor, inverter, and battery elements in order to predict hybrid electric engine performance parametrically throughout the flight envelope. Finally, cycle trade studies were performed using Boeing generated aircraft trade factors to examine the influence of cryogenic and conventional components on engine cycle selection.

Individual element modeling has been completed and is described in more detail in the sections following the NPSS engine model description. Where further enhancements were made to model the hFan architecture, they are described in the NPSS Element sections 3.1.1.6 and 3.1.1.7. Additionally, each developed element contains reference sheets included in the Appendix A of this report.

The propeller performance element ran into some difficulty during the validation phase. An attempt was made to construct an algorithm that allows for parametric propeller maps to be generated as a function of basic design parameters suitable for high speed propellers. This

effort attempted several different routes, none of which yielded acceptable results. The corresponding section describes in detail the steps taken and why they were not successful.

3.1.1 Electric Model

The Electric Element set allows all electric or hybrid electric propulsion systems to be modeled in NPSS. The elements were constructed with relatively simple models which can be extended as needed, but form a complete set which interconnect as required to allow an aircraft to be modeled with any arbitrary number of power sources and sinks. The superconducting models were based on prior work by P. Masson, however the other models were constructed from first order models or approximations. This subtask first attempted a bottoms-up approach in which electrical elements such as inverters and rectifiers were modeled using their constituent components. This approach was somewhat successful but significant challenges regarding the complexity and setup of this approach were identified. As a result the approach was changed to a top-down approach which allows for generic elements consisting of an inverter, rectifier, connection cable, motor, and generator were constructed which make use of NPSS sockets to allow the modeler to use custom modeling routines as needed.

3.1.1.1 Nomenclature

Acronyms

NPSS – Numerical Propulsion System Simulation
AC – Alternating Current
DC – Direct Current

Equation Terms

f – Electrical Frequency
Kv– Motor Voltage constant
Kt– Motor Torque constant
I – Current
L– Inductance
Np – Number of Pole Pairs
P – Power
R – Resistance
T – Torque
V – Voltage

3.1.1.2 Introduction

A hybrid electric propulsion system for transport aircraft use several components which are not found in any conventional gas turbine based system. Before the hybrid system can be modeled in NPSS, elements representing each new component must be added to NPSS. These elements include the motors, generators, power cables, and power electronic converters. The elements must be connected electrically, using DataPorts for lack of native electric connections in NPSS, and must be arranged such that the solver can successfully converge on a solution. The

DataPorts are used to represent electrical ports which transfer voltage, current, frequency, and phase information between electrical elements.

3.1.1.3 Element Modeling

3.1.1.3.1 Electric Motor/Generator Modeling

The electric motor and generator were modeled in both superconducting and non-superconducting models. This allows use in both near term and cryogenically equipped propulsion systems. The conventional motor operation is based on several parameters including motor constant (Kv), motor Resistance (R), motor inductance (L) and the number of pole pairs in the motor (Np). The complete sequence from torque (T) and speed (w) to voltage (V), current (I), electrical frequency (f) and the phase between voltage and current (phase) is given in Equation 3.1 through Equation 3.8 below.

$$BackEmf = Kv * w$$

Equation 3.1

$$Kt = .73756214837/Kv$$

Equation 3.2

$$I = T * Kt$$

Equation 3.3

$$f = w * Np$$

Equation 3.4

$$Vimaginary = I * L$$

Equation 3.5

$$Vreal = BackEmf + I * R$$

Equation 3.6

$$V = Sqrt(Vreal^2 + Vimaginary^2)$$

Equation 3.7

$$Phase = arctan(Vimaginary, Vreal)$$

Equation 3.8

The generator is essentially a motor run ‘backwards’ at this level of abstraction and is identical except for the Vreal formula and the sign on Vimaginary

$$V_{real} = BackEmf - I * R$$

Equation 3.9

$$V_{imaginary} = -I * L$$

Equation 3.10

The cryogenic variants are adapted from Matlab models of a High Temperature Superconductor (HTS) motor developed by P. Masson (9). Unlike the conventional motor model, the HTS motor model begins by specifying the geometry of the motor and works out its operation as a physics based model. The motor can be scaled geometrically to increase or decrease its performance during the sizing phase of the simulation. The HTS generator is an adaptation of the HTS motor to convert torque into electricity, similar to the reversal of the conventional motor.

3.1.1.3.2 Power Cable

The power cables considered in the DC distribution system are either superconducting cables, which are lossless below their associated max current and temperature limits, or conventional cables, which in DC are simply resistances. The current entering the cable is as the exit current and the voltage drop is given by Ohm's Law, shown in Equation 3.11.

$$\Delta V = I * R$$

Equation 3.11

The resistance of the cable is heavily dependent on its length, and requires the layout of the system to be known to estimate the length of relevant cables. In the test cases modeled, the length of the cables carrying AC between motors/generators and their power electronics is considered small compared to the DC cabling connecting the motors to the generators, as the electronics is assumed to be mounted near the motors.

3.1.1.3.3 Power Electronics Modeling

The power electronics devices in the system convert power from one voltage to another and from AC to DC or back if necessary. An inverter converts DC into AC, for example to drive a motor. A rectifier converts AC into DC; for example to charge a DC bus from an AC generator. A DC transformer converts one voltage of DC into another. This would be used with battery systems or fuel cells. The following paragraphs describe the original approach to model these elements which was later abandoned for a more simplified approach. Please see the reference sheets for a complete listing of the inputs and outputs of each element.

The original approach to power electronics modeling was to construct them from the same basic electronic elements- transistors, diodes, inductors, capacitors and resistors. Each of these elements pass current through themselves based on the voltage at each of their nodes and

their internal state, which can be a function of their history or of time. Accordingly the circuits were constructed as a set of nodes with voltages as independent variables, connected by elements which calculated their currents from the node voltages. The currents were summed at the junction points between the subelements where the NPSS solver was used to drive the net current to zero at every node by varying the voltage at each node. The voltages and currents were passed between elements using DataInputPorts and DataOutputPorts. To manage the execution order the nodes were split into voltage and current nodes, with voltage nodes executing first and containing the independents, while current nodes contained the dependents. This required protection measures to make sure that the components were properly attached to each pair of voltage/current nodes, accomplished by adding a node identifier to the array passed between data ports. For transient simulations the system increments the time and repeats the entire process after it converges. The transistor was approximated as a two terminal device with internal logic to determine if it should turn on or off, based on the simulation time and a predetermined switching waveform.

Each of the circuit elements are relatively simple, so the first attempt at modeling the power electronics was to take models of the individual circuit elements and assemble them into the required circuits to make inverters rectifiers and DC transformers. These circuits do not operate with a steady state current flow, instead having transistors switch on and off and AC waveforms oscillating. To calculate the overall currents into and out of the devices their operation would have to be simulated over several periods of the AC waveforms and switching cycles and the performance averaged to find total energy into and out of the system at each voltage and frequency. Accordingly transient models were constructed of notional inverters, rectifiers, and DC transformers. An example circuit model of a rectifier and a graph of its operation are shown in Figure 3.1. The results are as expected. The sinusoidal AC current, represented in blue, is converted correctly to a stable DC current, represented in red.

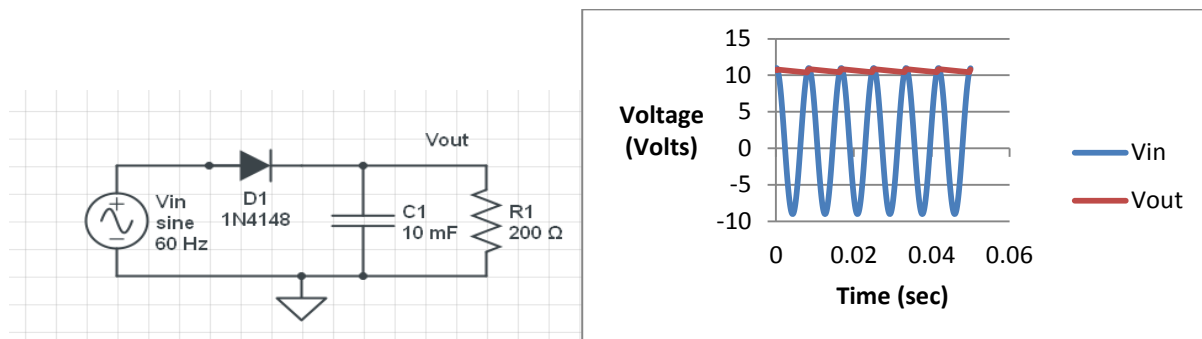


Figure 3.1 – Half Wave Rectifier

This approach was abandoned as a result of two problems that were discovered when constructing other circuits. First, every time a transistor turned on or off, this created a

discontinuity that the NPSS solver struggled to adapt to. These discontinuities also occur in the physical system so they had to be accurately modeled. Attempts to solve this problem exacerbated the second problem: the execution time of the transient model was on the order of minutes. This is required since the time steps necessary to solve a transient circuit are on the order of microseconds. This meant that for every pass of the overall model (trying to find the fuel flow in the gas turbine to meet a thrust requirement for example) each inverter would take minutes, making the overall convergence time unacceptable.

An alternative approach was adopted, modeling each piece of power electronics from the top down. Each was first modeled as a black box with a fixed efficiency, where power went in and flowed out at the appropriate frequencies and voltages. After these had successfully been integrated with the other electrical elements refinements were added in the form of sockets to calculate efficiency depending on the design power, and further refinements can similarly be added to meet whatever modeling fidelity is desired.

3.1.1.3.4 Electrical Bus

The only element which has more than two electrical connections, both in and out, is the bus. It can receive and send multiple currents at a constant DC voltage. The bus is essentially a model of the junction point where multiple power cables combine and allows the currents to be divided in any user defined manner; the only constraint being a net current of zero. As the bus is a model of a single connection point it currently contains no losses and is primarily a way for the solver to distribute currents.

3.1.1.4 Model Integration and Solver

NPSS contains a vast library of gas turbine and rocket engine components, and many ports with which to interconnect them. However, there is currently no electrical port available for one component to pass an electrical signal to another. To overcome this DataPorts were adapted as these allow a single object to be passed between elements. Data ports have two significant drawbacks compared to fluid or other ports- first there is no error when a DataOutputPort is not connected to a DataInputPort. In the electrical case this could allow a motor to run without drawing power from the bus if it isn't properly connected. The second drawback is that DataPorts only pass a single object. This was overcome by passing an array of voltage, current, phase, and frequency. A DC current can be represented by the voltage and current, while an AC additionally has a phase and a potential phase difference between the current and voltage waveforms, therefore a four element array was used with a frequency of zero signifying a DC current.

The solver layout is done such that there is a flow of information from the devices using power to the sources to minimize solver loops. Furthermore, the elements have been set up in a manner that the autosolver should automatically adjust to the number of elements within the

system without too much user modification. A notional system with one motor, one battery and one generator is shown below in Figure 3.2. In this example the speed of the constant speed generator, the voltage of the DC bus, and the speed and torque load on the motor are all specified as inputs. The motor executes, calculating its AC voltage and current, which are passed to the inverter. The Inverter calculates the efficiency loss and guesses what its DC input voltage is, not knowing the bus voltage or how much voltage will be lost in the power cable. It passes the DC voltage and current to the cable, which passes the entire current and a voltage updated due to the resistance to the bus. The bus checks if the passed voltage is equal to its own voltage, a dependent to match the independent in the inverter, before splitting the current and sending it up cables to the DC transformer and the rectifier. The independent torque in the generator is chosen and it sends its electric power to the rectifier, which compares the input and output powers to its efficiency. The battery current and DC transformer dependent evaluate simultaneously to complete the execution.

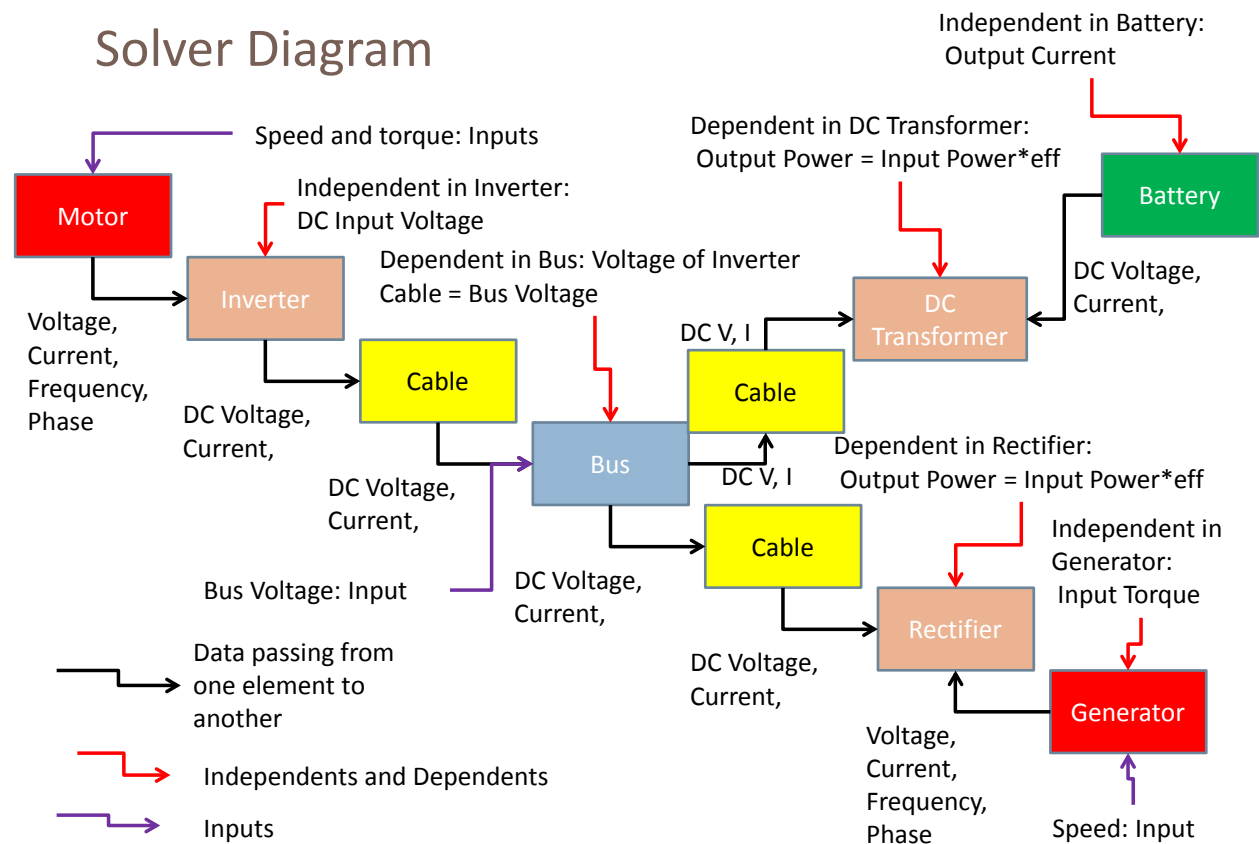


Figure 3.2 – Solver layout diagram

3.1.1.5 Verification

The majority of the models included here is based on very simple equations or black box efficiencies, and can be easily demonstrated to match Ohm's Law or the motor equations

detailed above for the conventional motor. However the HTS models were adapted into NPSS from Matlab models by P. Masson which were complex enough to warrant a detailed check to ensure that the calculations were identical to the original. Below are two of the sample cases where the same inputs were put into the original and the NPSS model to confirm that they had the same output in every category. The resulting NPSS model showed an exact match, indicating no error resulting from the conversion to NPSS.

Table 3.1 – NPSS HTS Motor Validation

Inputs	Case1 (Default)			Case2		
Machine Power (W)	8000000			8000000		
Machine Speed (RPM)	13000			8000		
Machine Shape Factor	5			4		
N pole Pairs	2			2		
Stat Ave Rad (m)	0.12			0.2		
Stat Elec Load (A/m)	500000			600000		
Stat Op Fac	0.6			0.6		
Stat AcLossDim (m)	0.00002			0.00002		
HTS Temp (K)	20			20		
BkFe Field Density (T)	1.9			2		
Cryostat Wall Thick (m)	0.004			0.004		
EMShield Thick (m)	0.002			0.002		
Cryocooler Carnot eff (%)	20			20		
Outputs	Matlab	NPSS	%error	Matlab	NPSS	%error
TotBearWeight (kg)	31.49	31.49	0	212.96	212.96	0
EMShield Weight (kg)	2.916	2.916	0	6.8788	6.8788	0
Shaft Weight (kg)	6.9999	6.9999	0	13.4588	13.4588	0
Rotor Sup Weight (kg)	8.7184	8.7184	0	33.2	33.2	0
rotor HTS weight (kg)	0.9548	0.9548	0	0.627	0.627	0
Stator ClPrWeight (kg)	2.0466	2.0466	0	5.4405	5.4405	0
Rotor ClPrWeight (kg)	4.7402	4.7402	0	24.8334	24.8334	0
Cryostat weight (kg)	26.4791	26.4791	0	59.4239	59.4239	0
Stator Torq T weight (kg)	117.856	117.856	0	384.753	384.753	0
Stator Sup Weight (kg)	3.45	3.45	0	12.5318	12.5318	0
Stator HTS Weight (kg)	1.39	1.39	0	3.315	3.315	0
BkFe Weight (kg)	96.85	96.85	0	377.243	377.243	0
Total Machine Weight (kg)	303.902	303.902	0	1134.7	1134.7	0
Machine T.Tube HL (W)	3342.9	3342.9	0	10563	10563	0
Stator CL Tot Loss (W)	98.3546	98.3546	0	118.025	118.025	0
Rotor CL Tot Loss (W)	115.158	115.158	0	153.218	153.218	0
Machine Ac loss op temp (W)	21792	21792	0	7786.6	7786.6	0
Total Machine losses (W)	25349	25349	0	18621	18621	0

3.1.1.6 Inverter Efficiency Subelement Development

In order to capture the effect of motor speed and power load on the inverter, a parametric model was constructed that allows for inverter efficiency to be predicted as a function of these parameters. The inverter efficiency is implemented via the efficiency socket in the developed inverter element. In addition to predicting inverter efficiency, the element converts the DC current coming from the battery into AC current that the motor element can then use to produce torque. The following sections describe the efficiency prediction algorithm. Parameters used to simulate cryogenic and conventional components. References used to determine the parameters in Table 3.2 are marked with reference in parentheses.

3.1.1.6.1 Model Inputs:

- Inverter max current
- Motor speed (voltage frequency)
- Voltage
- Input power
- Inverter rated power

3.1.1.6.2 Converter Parameters:

Some characteristics of the inverter must be known for the loss calculation. The variables that must be set are:

- Switch turn-off fall-time (t_f)
- Link capacitance (C)
- Switching frequency (f_s)
- Power factor (pf) (Estimated using polynomial regression)
- Switch voltage drop (V_t)
- Diode voltage drop (V_d)
- Switch on-resistance (R_s)
- Diode resistance (R_d)

Table 3.2 – Parameter Estimates

Parameter	Room-Temperature	Cryogenic
Switch turn-off fall time	$2 \cdot 10^{-7}$ (10)	$18.2 \cdot 10^{-9}$ (11)
Link capacitance	$\frac{\text{bus voltage}}{105.6 \cdot f_s^2 \cdot \text{source inductance}}$ (12)	$\frac{\text{bus voltage}}{105.6 \cdot f_s^2 \cdot \text{source inductance}}$ (12)
Switching frequency	10000 – 20000 (Hz) (13)	10000 – 20000 (Hz) (13)
Switch voltage drop	5.3 (V) (14)	n/a
Diode voltage drop	3.75 (V) (15)	n/a
Switch on-resistance	.11 (14)	n/a
Diode resistance	.02 (15)	n/a
Power Factor (16)	$-1.782 \cdot \% \text{ load}^2 + 1.9898$ $\cdot \% \text{ load}$ $+ 0.1571$	$-1.782 \cdot \% \text{ load}^2 + 1.9898$ $\cdot \% \text{ load}$ $+ 0.1571$

% load is the percentage is power/rated power

3.1.1.6.3 Efficiency Calculation:

There are two main types of losses in the converter: conduction losses and switching losses. Conduction losses are caused by the resistance of the switches and diodes in the converter. Switching losses are caused by the transient effect of rapid changes in the voltage and current profile across the switch.

Conduction losses (room-temperature) (13):

$$P_{c-sw} = \frac{1}{2} I_m V_s \left(\frac{1}{\pi} + \frac{m}{4} pf \right) + I_m^2 R_s \left(\frac{\sqrt{3}}{8\pi} + \frac{m}{3\pi} pf \right)$$

$$P_{c-d} = \frac{1}{2} I_m V_d \left(\frac{1}{\pi} + \frac{m}{4} pf \right) + I_m^2 R_d \left(\frac{\sqrt{3}}{8\pi} + \frac{m}{3\pi} pf \right)$$

For cryogenic conduction losses just divide each equation by 10 (11).

Where m is the modulation index, which is:

$$m = \frac{\text{voltage frequency}}{\text{switching frequency}}$$

Switching losses (13):

$$P_{sw} = \frac{1}{2} \frac{(I_m t_f^2)}{24C} f_s$$

Assuming the converter has 6 switches and 6 diodes, total losses are (13):

$$P_{loss} = 6(P_{c-sw} + P_{c-d} + P_{sw})$$

The efficiency of the inverter is then:

$$\eta = \frac{\text{power input} - P_{\text{loss}}}{\text{power input}}$$

3.1.1.7 Motor Efficiency Subelement Development

The basic motor element is fairly simple. The incoming AC power is combined with an efficiency number to predict the total torque on the output shaft, given a rotational speed. In order to add realism and the ability to perform parametric studies a detailed efficiency loss buildup is needed. This buildup allows the motor efficiency to change realistically throughout the operational envelope and across different rated motor sizes. Furthermore, a loss buildup model is desired that can be easily switched between a conventional and cryogenic operational mode. The modeling framework described in the following sections is based primarily on section 3.3 of (17) with elements incorporated from (18), (19), (20), (21) and (22). A switched reluctance motor type was chosen since that type is consistent with what GE assumed for the hFan configuration.

3.1.1.7.1 Motor Loss Definitions

Figure 3.3 shows a summary of major losses present in an electric motor. The major losses can be broken down into three groups, windage, copper, and iron losses. Windage loss results from the friction associated with cooling air flowing between the gap between the motor rotor and stator. Copper losses are a result of resistance within the wiring and coils. Iron losses results from eddy currents formed in the motor core as a result of moving magnetic fields.

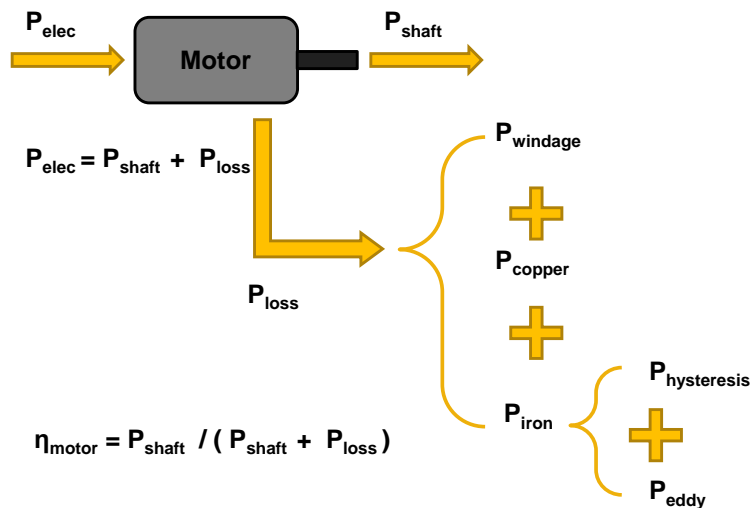


Figure 3.3 – Motor Loss Buildup

3.1.1.7.2 Motor Sizing Process

Since the modeling of the loss mechanisms in switched reluctance machines is well documented, the focus of this section will be on modeling elements specific to the NPSS implementation and verification of the resulting element. The primary consideration is how to size the motor. Sizing the motor is essential to predicting the individual losses. To understand the sizing process, one must first understand the operational behavior of a switched reluctance motor (SRM). For those not familiar with electrical devices, torque is proportional to current and voltage is proportional to speed. The torque-speed relationship is notionally shown in Figure 3.4. Starting from low rotational speed, the current is at a maximum (indicated by the red line), limited by the heat removal capability and wire gauge used in the motor coils. As speed increases, the current, and therefore torque is held constant. Since voltage and speed are increasing, the motor's power increases linearly up until the point that the maximum power is reached (indicated by the green line). The maximum motor power is a function of both the maximum current capability of the motor, and the ability of the upstream inverter to deliver power. As speed continues to increase, the torque, and therefore current must decrease in order to limit the motor to its maximum power. Eventually the point of maximum voltage, dictated by upstream conversion equipment is reached, and torque falls off rapidly beyond this point. Of course the motor may also operate at intermediate speeds below rated torque and power.

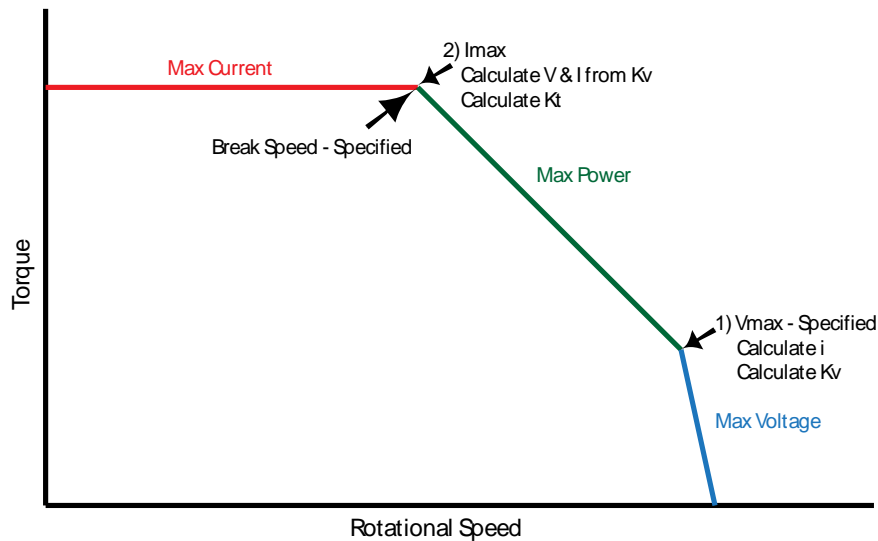


Figure 3.4 – SRM Torque-Speed Characteristic

This understanding of the SRM torque-speed characteristic is important because the loss models require operating current and voltage as inputs. Fortunately, the motor current and voltage can be estimated using K_t and K_v coefficients, shown in Equation 3.12 and Equation 3.13. K_t and K_v can be assumed constant for a given motor design.

$$Kv = \frac{(V - i * R0)}{\omega}$$

Equation 3.12 – Kv Definition

$$Kt = \frac{T}{i}$$

Equation 3.13 – Kt Definition

Using the Kt and Kv definitions it is not hard to see how, given an operating current and voltage that torque (and therefore power) can be determined. The question now becomes how to determine Kv and Kt for a given SRM. The first step is to parameterize the curve shown in Figure 3.4. It is assumed the maximum power will come from the user as a design parameter and the maximum speed can also be calculated from the fan shaft in this application. If it is further assumed that operating in the blue region where torque rapidly falls off is undesirable then point (1) in Figure 3.4 can be defined. Since power, speed, and therefore torque are all known at this point, the operating current can be calculated using a specified maximum operating voltage. With these parameters defined Kv can be calculated using Equation 3.14, where R0 is an assumed motor winding resistance.

$$Kv = \frac{(V_{max} - i * R0)}{\omega_{max}}$$

Equation 3.14 – Kv Calculation

To predict Kt, it is first necessary to define a parameter, named ω_{base} , as the ratio of the break speed (intersection of maximum power and torque) to ω_{max} . This is a user specified parameter which will depend on the specifics of the problem. Then, a system of equations consisting of Kv, the maximum specified voltage, V_{max} , ω_{base} , ω_{max} , and the maximum power can be solved to estimate the current at point (2) in Figure 3.4. First the voltage at point (2) is solved using Equation 3.15. Then the torque is calculated using the break speed and maximum power. Finally Kt can be calculated using i_{max} and the torque at point (2) in Figure 3.4.

$$i_{max} = 0.5 * \frac{\sqrt{Kv^2 * \omega_{base}^2 + 1.63299 * P_{max} * R0} - Kv * \omega_{base}}{R0}$$

Equation 3.15 – Solution for Voltage at Point 2

Now that Kv and Kt are defined for a ‘sized’ motor, voltage and torque can be estimated for any required speed and torque the motor is commanded to provide. Current and voltage are the primary inputs into the individual loss models listed in Figure 3.3.

3.1.1.7.3 Motor loss prediction

Once the motor is ‘sized’ (i.e. K_t and K_v calculated), the windage, copper, and iron losses can be estimated. This is done every time the motor element is executed within NPSS since K_v and K_t are held constant. While full details of the loss estimation process are provided in the aforementioned references, the following equations offer a brief summary of the final loss estimation algorithm.

In order to estimate the copper losses, the motor diameter and length is needed. These two parameters are determined using Equation 3.16 and Equation 3.17. The diameter equation was generated by iterating through the sizing process to estimate power as a function of diameter. The equation was then solved for diameter. Length is estimated by holding a constant length to diameter ratio based on the published GE hFan drawings.

$$Diameter = 0.0713950 * \log(P_{max}) - 0.1572667$$

Equation 3.16 – Motor Sized Diameter

$$Length = \frac{0.4}{0.48} * Diameter$$

Equation 3.17 – Motor Sized Length

Once motor dimensions are determined, the number of turns of coil are estimated using Equation 3.18. The resistance per turn is estimated using the regression shown in Equation 3.19 which is based off of AWG wire sizing charts.

$$T_{ph} = \frac{As * \pi * Diameter}{i_{max} n_{phase} * 2.0}$$

Equation 3.18 – Estimated Number of Coil Turns

$$r_{per,turn} = 48.83 * i_{max}^{-1.001259}$$

Equation 3.19 – Resistance Per Turn

Finally, total resistance is calculated by calculating total wire length, shown in Equation 3.20. Current power losses are then estimated using Equation 3.21 and the model’s operating current.

$$R = \frac{Diameter * \pi * r_{per,turn}}{1000}$$

Equation 3.20 – Wire Resistance

$$P_{copper} = I^2 * R * T_{ph}$$

Equation 3.21 – Copper Power Losses

Once the copper power losses are estimated, the iron losses are calculated as follows. First the motor operating frequency is estimated via Equation 3.22, and then the motor weight is estimated using Equation 3.23 assuming the core is manufactured from laminated steel. Note that this weight is suitable for predicting changes in efficiency since motor iron losses are proportional to weight/volume; however, it is not indicative of the entire motor installed weight.

$$Frequency = \frac{RPM * 2 * n_{phase} * 2}{120}$$

Equation 3.22 – Motor Operating Frequency

$$weight = 7650.0 * Length * \left(\frac{Diameter}{2}\right)^2$$

Equation 3.23 – Motor Core Loss Weight Estimation

Finally iron losses are estimated using the method from (21), replicated in Equation 3.24. B_p represents the peak magnetic flux. Georgia Tech found a value of 1.5 T worked well for motors applicable to the SUGAR requirements.

$$\begin{aligned} K_h &= 0.0275 \\ K_c &= 0.0000183 \\ K_e &= 0.0000277 \\ P_{iron} &= \left(K_h * B_p^2 * Frequency + K_c(B_p * Frequency)^2 \right. \\ &\quad \left. + K_e(B_p * Frequency)^{1.5} \right) \left(\frac{weight}{176} \right) \end{aligned}$$

Equation 3.24 – Motor Iron Losses

Finally, the windage loss is estimated using Equation 3.25 where the coefficient of friction is estimated from (20).

$$P_{windage} = c_{friction} * \pi * \omega^2 * \left(P_{max}^{0.3} * \frac{Diameter}{2} \right)^3$$

Equation 3.25 – Windage Loss Estimation

Once the loss model is defined, the motor efficiency is calculated using Equation 3.26.

$$eff = \frac{P_{mech}}{P_{mech} + P_{iron} + P_{copper} + P_{windage}}$$

Equation 3.26 – Motor Efficiency Definition

Examples of the motor performance for three different sized motors, with ω_{base} set to 0.6 are shown in Figure 3.5.

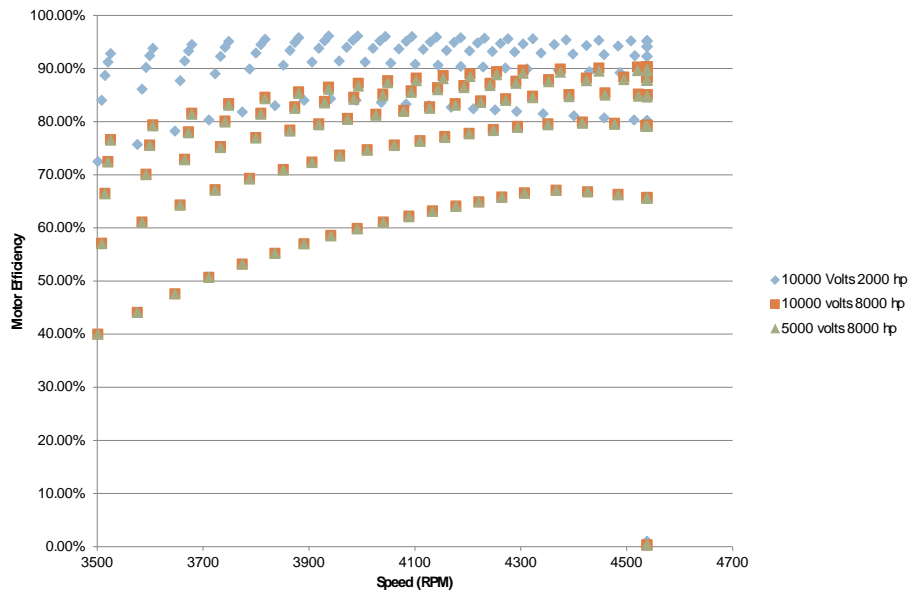


Figure 3.5 – Motor Off-Design Operation

3.1.2 Fuel Cell Model

3.1.2.1 Nomenclature

Abbreviations

- ASR – Area Specific Resistance
- FC – Fuel Cell
- GT – Gas Turbine
- SOFC – Solid Oxide Fuel Cell

Equation Terms

A – Area
Deff – Effective diffusivity
E – Reversible voltage, Energy
F – Faraday’s constant
H – Enthalpy
h – Plank’s constant
i – Current
j – Current density
k – Boltzman’s constant, installation factor, pre-exponent factor
N – Number
n – Number of electrons exchanged per molecule
P – Power
p – Pressure
Q – Heat
R – Universal gas constant
T – Temperature
t – Thickness
U – Fuel Utilization
V – Voltage
Vol – Volume
W – Weight
x – Mole fraction
 α – Reaction transfer coefficient
 ΔG – Change in Gibb’s free energy
 $\Delta \hat{h}$ – Enthalpy of reaction
 λ – stoichiometric coefficient
 η – efficiency
 v – molar flow rate
 ρ – Density
 σ – Conductivity
Superscripts
0 – Standard state, bulk fluid property
* – Component interface property

Subscripts

0 – Exchange
a – Anode property
act – Activation
c – Cathode property
cell – Cell property
conc – Concentration
design – Design point property
e – Electrolyte property
f – Formation
flow – pertaining to the anode and cathode flows
gen – Generated
i – For component
L – Limiting
op – Property while in operation
stack – Stack property
total – System property
volt – voltaic

3.1.2.2 Introduction

One of the advanced technologies that are considered in this study is a solid-oxide fuel cell (SOFC), an electrochemical device that produces electricity from hydrogen and oxygen, producing water as a byproduct. Many models exist for analyzing fuel cells, but they focus on varying aspects of the cell. Severson describes an SOFC model based on first principles used to parametrically analyze the electrochemical performance of a fuel cell in (23). Many papers have also been found documenting design and off-design analysis of a hybrid SOFC/gas turbine systems performed using parametric models (24; 25; 26; 27). Tornabene's model also performs a mass and volume calculation, important for aerospace applications (27). Lastly (28) provides a detailed description of a spreadsheet model used to analyze the electrical and heat performance of a fuel cell/gas turbine system.

The SOFC was chosen over other fuel cells because it operates at a high temperature (500 to 1000 °C), which can be used to preheat air for the combustor and it can use many different compounds, including hydro-carbons, as fuel. The fuel cell is able to use such a range of fuels either indirectly, using a fuel reformer, or directly, as the SOFC is able to use internal reforming to produce the hydrogen-rich gas necessary to function inside the anode (29). The model is developed in the NPSS which allows it to use the Chemical Equilibrium with Applications (CEA) code and JANAF thermodynamic data built-in to the system (30). The model is developed using the electrochemical equations from (23; 24; 31), heat equations from (29), and mass and volume equations from (27). Though the mass and volume equations are not explicitly stated in the paper, it is possible to ascertain them by comparing the numbers presented for densities, cell geometry, and the numbers given as the mass and volume results. In the following sections,

background information on solid oxide fuel cells is covered, and then the model development and finally the validation of the model using published data are described.

3.1.2.3 Background

3.1.2.3.1 Electrochemistry

A fuel cell consists of three main components, the anode, cathode, and electrolyte. A SOFC is so called because the electrolyte is a solid ceramic, as opposed to an aqueous solution (29). In an SOFC the most common chemical reaction used is the combustion of hydrogen and oxygen to produce water. In the fuel cell the total chemical reaction can be split into two half reactions that occur at each electrode. The oxidation of the hydrogen occurs at the anode, while the reduction of oxidizer, commonly air, occurs at the cathode. The electrons then travel from the cathode, through the load to the anode where the reaction is completed (Figure 3.6).

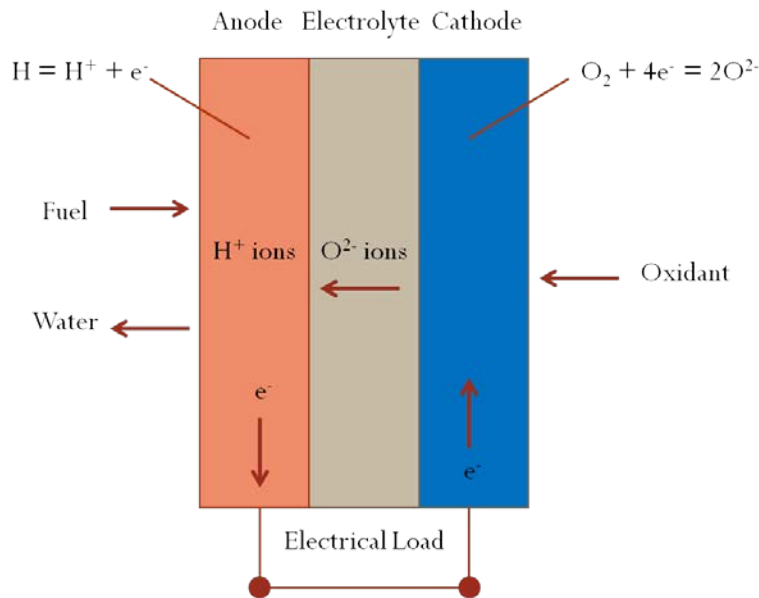


Figure 3.6 – Diagram of SOFC

3.1.2.3.2 Architectures

The literature shows three different manners in which the three components of a fuel cell can be combined, with benefits and detriments to each. The cross sections of all three are shown in Figure 3.7, with the anode in yellow, the cathode in blue, and the electrolyte in green.

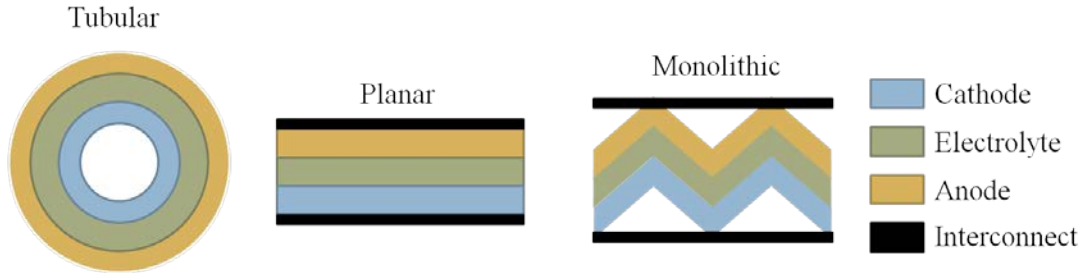


Figure 3.7 – SOFC Architectures

The tubular design is known for its ease of manufacturing, and for less thermal cracking from thermal properties mismatching. Another benefit is that there is no need for sealing to prevent the fuel gases from combining with the oxidant. However, the tubular design does yield a lower power density than the others and current collection from one tube to the next is complex to organize. The planar design increases the power density and there are lower fabrication costs than the tubular and monolithic, but it does require sealing between the anode and cathode inputs to create separate flows. The planar design also requires strict matching between the thermal expansion coefficients in order to prevent cracking and delamination. The monolithic design has the highest power density potential of all three architectures, and the flow arrangement of the anode and cathode gases is simple because of the natural gaps that form between the electrodes and the interconnect. However, like the planar design, the monolithic architecture requires strict matching of the thermal properties of the materials and sealing to prevent the anode and cathode gases from mixing. It also requires a difficult fabrication process to produce the honeycomb shape (32).

3.1.2.3.3 Losses

There are three primary losses in a fuel cell. These losses occur as functions of the current density of the cell and each loss is prominent in a specific region of current density. The first type of loss is activation loss. This occurs as the result of energizing the fuel at the anode and the oxidizer at the cathode, enabling the two half reactions to take place. This type of loss is prominent at low current densities. The second type is ohmic or resistance losses. This occurs because an electromotive force (voltage difference) needs to exist to move the electrons and the ions. Resistance losses are important in the middle region of current densities. The final type of losses, concentration or mass transfer losses, give an upper limit to the current density that can be present in a fuel cell. They come about when current density is high enough to deplete the hydrogen or oxygen, leaving no source for further current. The voltage of a fuel cell is determined by calculating the ideal voltage of the cell, and subtracting the sum of all of the losses as shown in Figure 3.8. This final curve that gives the voltage as a function of current density is known as the polarization curve of a fuel cell. The polarization curve is the main metric of fuel cell performance (31).

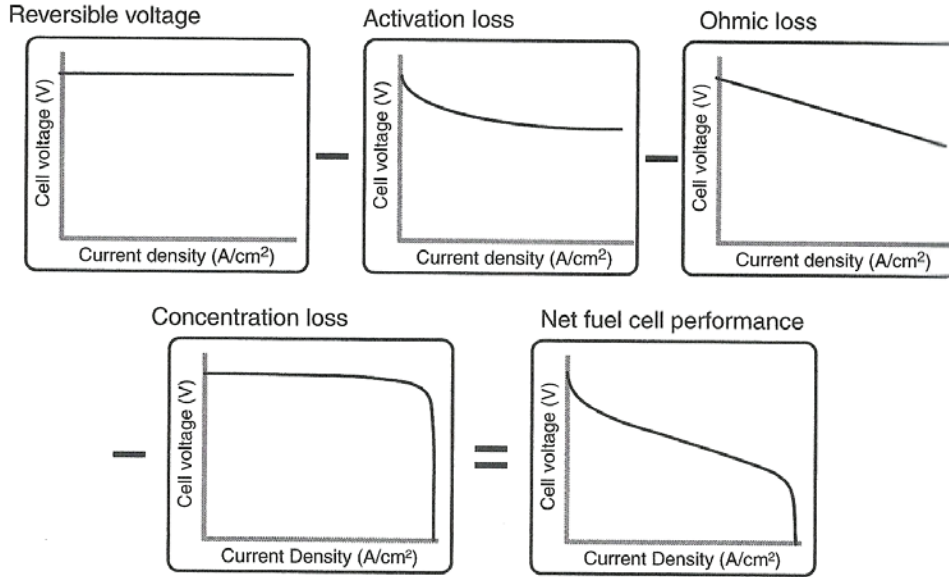


Figure 3.8 – Formation of the polarization curve

3.1.2.4 Model

The NPSS fuel cell model is a 1-D performance model that computes the electrical output of the fuel cell based on the desired current density. The performance model is wrapped into a sizing algorithm to output the size of a stack of fuel cells given a design current density and a design power load. Once a stack is sized, the model can output the performance of the cell over varying current densities, operating pressures, temperatures, and utilization rates based either on constant stoichiometry, where the fuel cell is fed the fuel and oxidizer in a set ratio, or constant fuel flow. The model is not dependent upon the architecture of the fuel cell, and the only calculation in the model that is absolutely dependent upon the geometry is the weight and volume calculation, which assumes a planar architecture.

3.1.2.4.1 Assumptions

In order to enable the parameterization of the model, the following assumptions were made:

- Only 1-dimensional flow across fuel cell is considered implying that any gradients across a cross section of the fuel cell are ignored
- Convective transport intricacies are ignored this assumption eliminates the consideration of any flow structures in the electrodes. Only the diffusion across the electrodes and electrolyte are analyzed (31).
- H₂O only exists as water vapor simplifies the analysis to a single phase product which eliminates the higher heating value from the analysis (31).
- Fuel reforming has already taken place and no internal reforming happens or anode recycling occurs (24).

3.1.2.4.2 Model Calculations

The model calculates the performance of the fuel cell based on the cell temperature, pressure, and the current density. During design analysis, a specified current density and operating conditions are used to determine the performance of a single cell, which is subsequently used to calculate the number of cells necessary to meet a power output requirement. Once the cell size is determined, the weight and the volume of the stack can be calculated using the density of the materials for each component, and the component thickness.

3.1.2.4.3 Electrochemistry

To analyze the electrochemical performance of a fuel cell, the ideal voltage is calculated using Equation 3.27, called the Nernst equation. This voltage is also known as the reversible voltage or the Nernst voltage. It is the highest voltage that can be produced by a fuel cell for a given reaction. There is some debate in the literature on what values to use for the partial pressures since they change across an electrode in a fuel cell (24; 29). This is important because partial pressures taken at the inlet will give a higher ideal voltage, and pressures taken at the outlet will give a lower ideal voltage (23).

$$V_{Ideal} = \frac{\Delta G_f^0}{nF} + \frac{RT}{nF} \ln \left(\frac{p_{H_2} p_{O_2}^{1/2}}{p_{H_2O}} \right)$$

Equation 3.27

Once the ideal voltage is calculated, the values for each of the losses need to be determined. Equation 3.28 through Equation 3.30 gives the voltage losses related to activation, resistance, and mass transfer (23). The operating voltage (Equation 3.31) is calculated by subtracting the losses from the ideal voltage.

$$V_{act} = \frac{RT}{\alpha nF} \ln \left(\frac{j}{2j_0} + \sqrt{\left(\frac{j}{2j_0} \right)^2 + 1} \right)$$

Equation 3.28

$$V_{ohmic} = j * ASR$$

Equation 3.29

$$V_{conc} = \frac{RT}{nF} \ln \left(1 - \frac{j}{j_L} \right)$$

Equation 3.30

$$V_{op} = V_{ideal} - (V_{act} + V_{ohmic} + V_{conc})$$

Equation 3.31

Previously, the activation loss was calculated using Equation 3.32. The natural logarithm in this equation caused inaccuracies below the exchange current density. During testing and validation this proved problematic as the voltage at lower current densities was consistently higher than the value in literature. After further investigation, Equation 3.28 was used in the model for the activation losses, and the model performed significantly better.

$$V_{act} = \frac{RT}{\alpha n F} \ln \left(\frac{j}{j_0} \right)$$

Equation 3.32

Once the operational voltage is known, the fuel cell is sized based on a design power load and an active area of the cell. The total area necessary to produce the required power is calculated using the current density and the operational voltage of the cell at the specified current density (Equation 3.33). The number of cells required to achieve the design power is the total area necessary divided by the area of a single cell (Equation 3.34).

$$A_{total} = \frac{P_{design}}{(V_{op} * j)}$$

Equation 3.33

$$N_{total} = \frac{A_{total}}{A_{cell}}$$

Equation 3.34

If the detailed material properties are known, such as diffusion of the reactants and products across the electrodes, the thicknesses of each component, and the conductivity of each component, Equation 3.35 through Equation 3.38 can be used to calculate the values needed for Equation 3.28 through Equation 3.30. The exchange current density can be calculated using Equation 3.35 and Equation 3.36 (23). For Equation 3.35 and Equation 3.36, the constants m and n are typically 1 and 0.25, respectively. The pre-exponent factor k and the activation energy can be found in literature (23) and the reference pressure can be set to 1 atmosphere for simplicity of calculation. Since the equations used for the exchange current density calculate it at each of the electrodes, then activation overpotentials also need to be calculated separately at each of the electrodes and summed to determine the total activation loss.

$$j_{0,a} = k_a \left(\frac{P_{H_2}}{P_{ref}} \right) \left(\frac{P_{H_2O}}{P_{ref}} \right)^m e^{-E_{act,a}/(RT)}$$

Equation 3.35

$$j_{0,c} = k_c \left(\frac{P_{O_2}}{P_{ref}} \right)^n e^{-E_{act,c}/(RT)}$$

Equation 3.36

Area specific resistance is calculated as the sum of the resistances of each of the components, the electrodes and the electrolyte. For a stack of cells, the interconnect would also need to be included in the calculation. The resistivity of the cell is equivalent to the inverse of the conductivity, σ , and t in Equation 3.37 is the thickness of the component (23).

$$ASR = \sum_{components} \frac{t}{\sigma}$$

Equation 3.37

The limiting current density, j_L is found using Equation 3.38, which uses the bulk mole fraction that is the most constraining, the effective diffusivity and the thickness of the electrode to determine the maximum current density possible at an electrode. This calculation should be performed at each electrode, and the lowest current density found should be used for j_L .

$$j_L = \frac{nFD^{eff}}{RT} \cdot \frac{px_i^0}{t}$$

Equation 3.38

The hydrogen molar flow is dependent on the amount of current output by the fuel cell and the fuel utilization, as shown by Equation 3.39. The oxygen molar flow is determined by the stoichiometric ratio between oxygen and hydrogen as shown by Equation 3.40. The water molar flow is only dependent on the amount of current, shown in Equation 3.41 (31).

$$v_{H_2} = \frac{i_{total}}{nF} \cdot \frac{1}{U_{H_2}}$$

Equation 3.39

$$v_{O_2} = \frac{i_{total}}{nF} \cdot \frac{\lambda_{O_2}}{U_{H_2}} = v_{H_2} \cdot \lambda_{O_2}$$

Equation 3.40

$$v_{H_2O} = \frac{i_{total}}{nF}$$

Equation 3.41

For a fuel cell, there are a few different measures of efficiency. The voltaic efficiency is measured as the voltage equivalent to the total available energy of the reaction divided by the operating voltage (Equation 3.42). The enthalpy of reaction of water vapor is used for the total

available energy as one of the assumptions states that only water vapor is produced. Another measure of efficiency is the fuel efficiency or utilization. This is defined as the ratio of fuel input to the cell to fuel used by the cell (Equation 3.43). The overall efficiency of the fuel cell is the product of the fuel efficiency and the voltaic efficiency (Equation 3.44) (29).

$$\eta_{volt} = \frac{V_{op}}{\Delta \bar{h}_f / nF}$$

Equation 3.42

$$\eta_{fuel} = U_{H_2} = \frac{i_{total} / nF}{\nu_{H_2}}$$

Equation 3.43

$$\eta_{fc} = \eta_{fuel} \eta_{volt}$$

Equation 3.44

3.1.2.4.4 Heat

The heat generated by the fuel cell is calculated using the voltaic efficiency as that gives the amount of energy from the reaction that is not used to generate the cell voltage (Equation 3.45). The heat transfer that occurs by the flow of reactants and products is calculated based on the enthalpy of the flows into and out of the electrodes (Equation 3.46). In this specific model, this calculation is enabled by the chemical equilibrium analysis (CEA) which is part of NPSS. The net heat out of the fuel cell is the heat generated less the heat absorbed by the cathode and anode flows (Equation 3.47) (29).

$$Q_{gen,total} = \left(\frac{V_{op}}{\eta_{volt}} - V_{op} \right) i_{total}$$

Equation 3.45

$$Q_{flow} = \sum_{out} x_i H_i - \sum_{in} x_j H_j$$

Equation 3.46

$$Q_{net} = Q_{gen} - Q_{flow}$$

Equation 3.47

3.1.2.4.5 Weight and Volume

The weight and volume are calculated by “building up” the fuel cell, component by component. First the weight is determined by adding up the weight of each of the components, calculated using the density, thickness and area of each (Equation 3.48). The total number of cells could be

split up into multiple stacks of cells. These stacks would be wired together to achieve the desired electrical output. The weight of one stack is the number of cells multiplied by the weight of a single cell, and an installation factor (Equation 3.49). The total weight is the number of stacks multiplied by the weight of a single stack and another installation factor (Equation 3.50). The volume of the fuel cells is calculated in the same manner, first with a buildup of the volume of a single cell using the thickness and area of each of the components (Equation 3.51); then the calculation of the volume of a stack using an installation factor and the number of cells (Equation 3.52). Finally, the total volume is the product of the volume of a stack, the number of stacks, and an installation factor (Equation 3.53) (27).

$$W_{cell} = \sum_{components} \rho_i t_i A_{cell}$$

Equation 3.48

$$W_{stack} = k_{cell,W} * N_{cell} * W_{cell}$$

Equation 3.49

$$W_{total} = k_{stack,W} * N_{stack} * W_{stack}$$

Equation 3.50

$$V_{cell} = \sum_{components} t_i A_{cell}$$

Equation 3.51

$$V_{stack} = k_{cell,Vol} * N_{cell} * V_{cell}$$

Equation 3.52

$$V_{total} = k_{stack,Vol} * N_{stack} * V_{stack}$$

Equation 3.53

3.1.2.5 Validation

To validate the model, data from (23) and (24) was used. Three tests were performed focusing on varying different inputs to the model. The first was to determine the effect of pressure on the performance, the second is a test to analyze the effect of varying the fuel composition, and the last test measures the effect of varying temperature. The first test was performed using inputs from (24), shown in Table 3.3. The cell pressure was varied between 1 and 15 atmospheres for the test, with the model results for 1 atmosphere and 15 atmospheres shown here. Some values are not present in the literature and had to be inferred. These are denoted by an asterisk (*) in the table. These parameters were used to match the outcome of the model to the published data. The values used in to fill in the missing information were also verified

against typical values for those parameters from other literature sources (23; 24; 28). The final validation plot is shown in Figure 3.9. For the validation, the average partial pressures of the fuel and air were used to calculate the Nernst voltage.

Table 3.3 – Validation data used for pressure variation tests

Description	Inputs Used		Inputs from Literature	
	1atm	15atm	1atm	15atm
P_op (atm)	1	15	1	15
T_op (K)	1273		1273	
iL (A/cm ²)	0.65	1.677	0.65	1.677
i0 (A/cm ²)	0.15		*	
Alpha	0.5		*	
ASR (ohm-cm ²)	0.3		*	
xH2	0.89		0.89	
xH2O	0.11		0.11	
xO2	0.21		0.21	
Utilization	0.85		0.85	
Stoichiometric Ratio of Air	6		6	

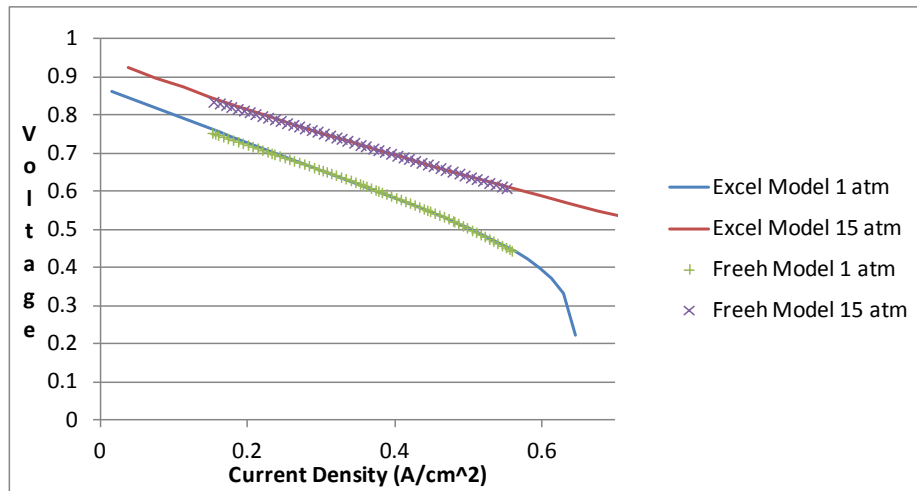


Figure 3.9 – Comparison of model pressure test output with output from (24)

The composition test used the inputs present in Table 3.4. The excel model indicates the NPSS algorithm results. The Freeh model indicates the validation data from the literature. Based on tests, pressure raises the voltage of the cell uniformly across all current densities. i_0 raises and lowers the voltage, but also affects the slope in the middle region of the graph. As the exchange current density is raised, the slope becomes closer to a constant across all current densities.

The transfer coefficient, alpha, also affects the slope of the plot, but does not change the curvature of the plot. Using only the data in the literature, the best match to the validation data is shown in Figure 3.11. Tests were also performed to determine if other combinations provided a closer match. The best result occurred with the values in Table 3.5. Different partial pressures for the Nernst voltage were also used to increase the fit of the data. The data at 10% H2 uses the output partial pressure, while the data at 97% H2 uses the average partial pressure for the ideal voltage calculation.

Table 3.4 – Validation inputs for composition variation tests

Description	Inputs Used		Inputs from Literature	
	10% H2	97% H2	10% H2	97% H2
P_op (atm)	1		*	
T_op (K)	1023		1023	
iL (A/cm ²)	0.325	7	0.325	7
i0 (A/cm ²)	0.25	0.25	*	
Alpha	0.3	0.3	*	
ASR (ohm-cm ²)	A*exp(E/T)		A*exp(E/T)	
A (ohm-cm ²)	2.1*10 ⁽⁻⁶⁾		2.1*10 ⁽⁻⁶⁾	
E (K)	10000		10000	
xH2	0.1	0.97	0.1	0.97
xH2O	0.03		0.03	
xN2	0.87	0.0	0.87	0.0
xO2	0.21		0.21	
Utilization	0.9		*	
Stoichiometric Ratio of Air	6		*	

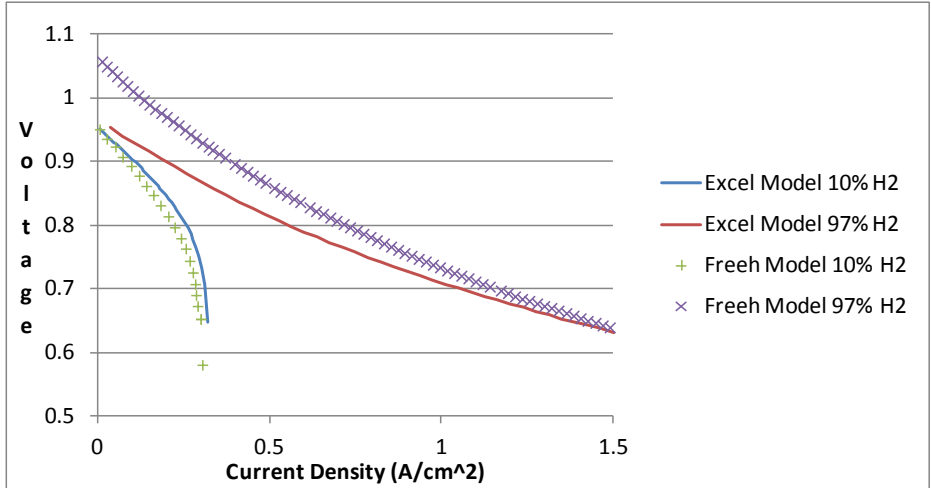


Figure 3.10 – Comparison of model composition test outputs with results from (24)

Table 3.5 – Inputs used for improved matching of composition tests

Inputs Used		
Description	10% H2	97% H2
iL (A/cm ²)	0.31	7
i0 (A/cm ²)	0.15	0.15
Alpha	0.41	0.41
ASR (ohm-cm ²)	$A \cdot \exp(E/T)$	$A \cdot \exp(E/T)$
A (ohm-cm ²)	$7.0 \cdot 10^{-6}$	$7.0 \cdot 10^{-6}$
E (K)	10000	10000

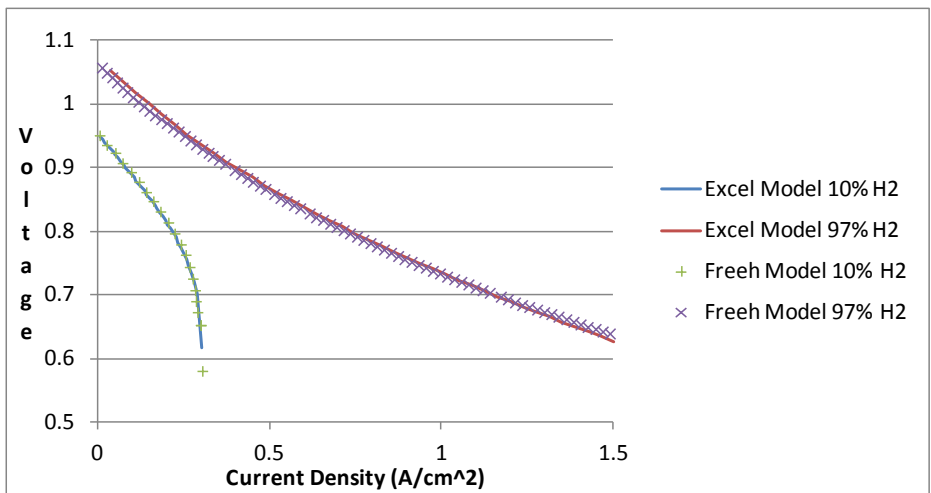


Figure 3.11 – Model output from improved composition matching with results from (24)

The temperature variation tests were performed at 600, 700, and 800C. The input data is taken from (23) and is shown in Table 3.6. ASR was calculated as the sum of the resistances of the components. Equation 3.54 through Equation 3.56 is the equations given in the literature to calculate the resistance of each component as a function of temperature. The only value not present in the literature is the limiting current density, i_L . The value used is the same as the value from the composition tests in (23) because the data in (23) comes from the same authors as that data. For the analysis, Equation 3.35 and Equation 3.36 are used for the exchange current density since they coordinate with inputs given in the literature. As a result, the activation voltage was initially calculated for each of the electrodes and summed to determine the total activation losses.

Figure 3.12 shows the initial model output with the published data. The resistance is determined to be the main source of error as it has a large effect on the slope of the polarization curve. The published equation for the resistances comes from a different source than the other inputs, so there is the possibility that it is not completely accurate to the tested fuel cell. Since the electrolyte resistance is the main source of resistance losses in fuel cells, according to the literature (29), this was adjusted to better match the experimental data. For the plot shown in Figure 3.13, Equation 3.57 was used for the resistance of the electrolyte. To be sure the matching was not just mathematical, but also validated conceptually, typical values for the resistance of the electrolyte material, yttria-stabilized zirconia (YSZ) were researched and plotted in an arrhenius plot with the updated resistance equation in Figure 3.14. Linear trend lines were fit to the data and compared to the changed equation which seems to fit in the same area as the other resistances. A more detailed legend is located in Table 3.7 and gives the properties of the trend lines for comparison. The other source of error is the Nernst voltage. The ideal voltage calculated by the model is less than the published data. One source of error could be the usage of partial pressures. For this test, average partial pressures were used in the Nernst voltage calculation. The actual partial pressures would change across the electrodes, but in the literature there is nothing pointing to using the partial pressures at one point as opposed to another.

Table 3.6 – Inputs for temperature variation validation

Description	Inputs Used			Inputs from Literature		
	600 C	700 C	800 C	600 C	700 C	800 C
P_op (atm)		1			1	
T_op (K)	873	973	1073	873	973	1073
iL (A/cm ²)		7			*	
Alpha		0.5			0.5	
k (A/cm ²)		5.5*10 ⁴			5.5*10 ⁴	
Eact (J/mol)		1*10 ⁵			1*10 ⁵	
ta (cm)		0.102			0.102	
tc (cm)		0.007			0.007	
te (cm)		0.0008			0.0008	
xH ₂		0.97			0.97	
xH ₂ O		0.03			0.03	
xO ₂		0.21			0.21	
Utilization		0.5			0.5	
Stoichiometric Ratio of Air		10			10	

$$\rho_a = 1 / \left[\frac{95 \times 10^4}{T} \exp \left(\frac{-1150}{T} \right) \right]$$

Equation 3.54

$$\rho_c = 1 / \left[\frac{42 \times 10^4}{T} \exp \left(\frac{-1250}{T} \right) \right]$$

Equation 3.55

$$\rho_e = 1 / \left[\frac{3.34 \times 10^2}{T} \exp \left(\frac{-10300}{T} \right) \right]$$

Equation 3.56

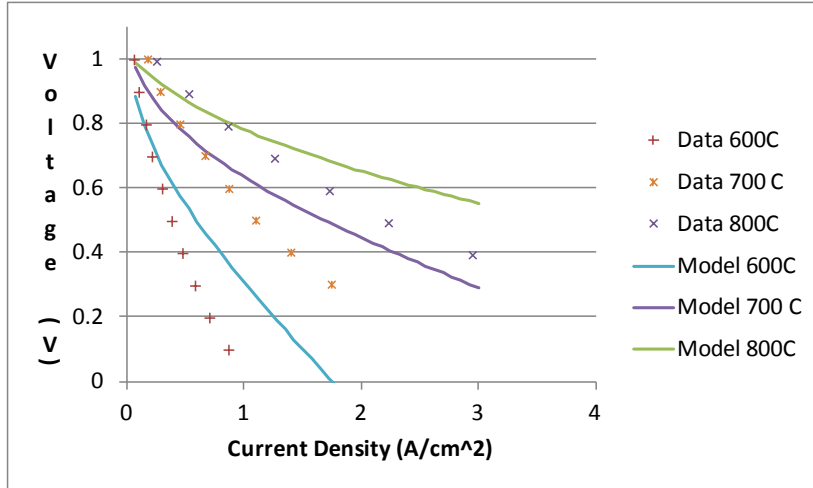


Figure 3.12 – Initial comparison of model output with experimental data from (23)

$$\rho_e = 1 / \left[\frac{2.5 \times 10^2}{T} \exp \left(\frac{-10700}{T} \right) \right]$$

Equation 3.57

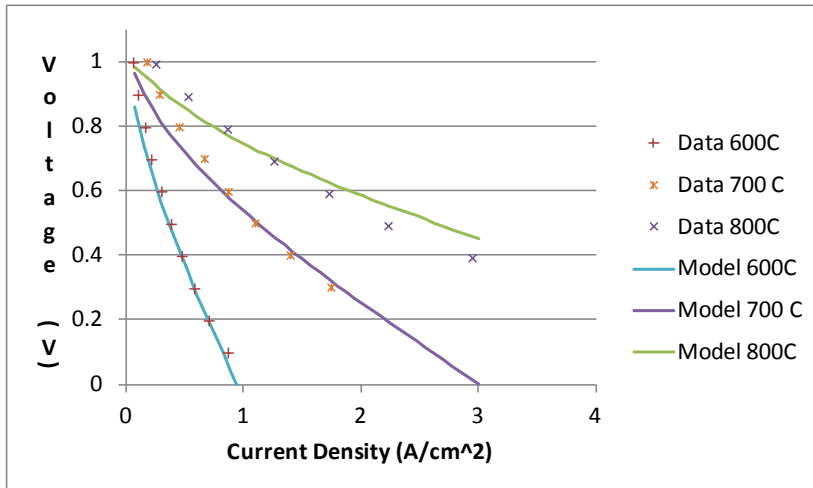


Figure 3.13 – Comparison of improved matching output with experimental data (23)

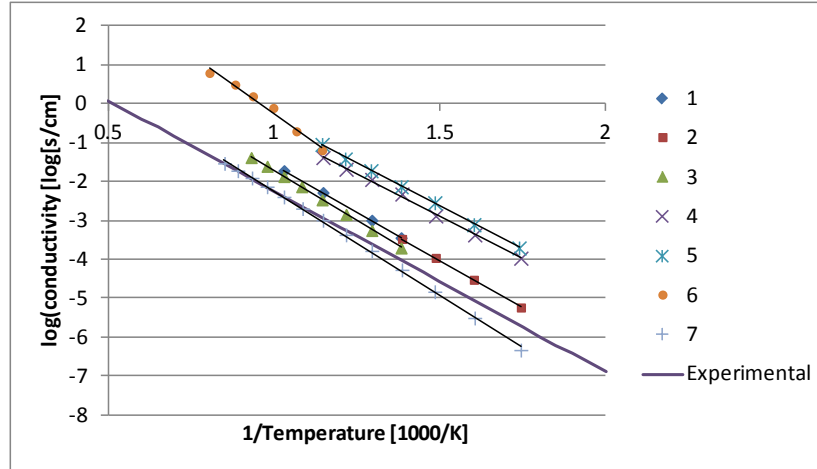


Figure 3.14 – Arrhenius plot of YSZ resistances

Table 3.7 – Trend line parameters for YSZ resistances

Number	Description	Slope	Y-intercept
1	Bulk YSZ	-4.87	3.30
2	Thin film YSZ on Pt (across plane)	-4.91	3.33
3	Thin film YSZ on Sapphire	-5.18	3.5
4	Thin film YSZ on Al ₂ O ₃ (in-plane) 200nm grains	-4.38	3.68
5	Thin film YSZ on Al-2O ₃ (in-plane) 20nm grains	-4.43	3.99
6	Thin film YSZ on Si (in-plane)	-5.98	5.73
7	Thin film on Sapphire (in-plane)	-5.35	3.10
Experimental		-4.65	2.40

3.1.3 Battery Model

The battery model is an NPSS element that calculates the size, layout, and performance of a battery stack. This calculation is based on the performance, which is given by a parameterized discharge curve. The discharge curve is determined by published data, but can also be modified to fit projections for future battery performance. To determine the size and layout of the stack, an operating profile and power load are used as the sizing criteria. Once the stack is sized, the model calculates the weight and volume of the stack, and can also determine the stack voltage and heat output at off-design points if given a state of charge and current load.

3.1.3.1 Nomenclature

Equation Terms

A – Exponential zone amplitude
B – Exponential zone time constant inverse
E – Voltage
i – Current
K – Polarization voltage
k – Technology factor
N – Number
P – Power
Q – Battery Charge, Heat
R – Internal resistance
SOC – State of Charge
t – Time
V – Voltage
W – Weight
 η – Voltaic efficiency
 ρ_{energy} – Specific energy
 ρ_{power} – Power density

Subscripts

batt – For a single Battery
dis – Discharge
exp – At end of exponential zone
L – Discharge limit
N – Nominal, as declared in literature
nom – At end of nominal zone
P – At power design point
parallel – For parallel batteries

3.1.3.2 Introduction

In a hybrid electric configuration, batteries can serve two roles. The first is as a power source connected to the power systems in order to provide electricity while discharging. The other is as a load-leveling device which would charge using any excess current from the system at low load times, and then discharge when the load on the system requires more energy than the primary power generation equipment can produce (33). In either case, it is necessary that the battery is sized properly to be able to provide the proper amount of power at the correct time without being over-designed and thereby too heavy. This model serves to determine the battery's performance and sizes the battery stack accordingly. The model also provides the capability to determine the weight and volume of the battery stack in addition to the heat produced and the electric performance characteristics of the battery.

3.1.3.3 Model Development

The main metric of battery performance is the discharge curve. This gives the voltage of the battery as a function of the state of charge and the current load. A functional model not based on first principles is desired as that simplifies the calculations of the model in addition to making the model usable without requiring intimate knowledge of the battery to be modeled. Using an empirically derived method also allows the NPSS model to easily accommodate varying battery chemistries. As the purpose of the project is to analyze future technologies, the model must also provide the ability to modify the battery attributes to predict future performance characteristics. Since these characteristics are not known currently, modifiers can be used to change the performance of current batteries to provide an estimate of future capabilities. These modifiers are essentially the technology factors. Using technology factors requires a general equation for the discharge curve that can be parameterized, but is still based on current capabilities. Reference (33) offers a generic equation that uses published data to determine parametric performance characteristics of a battery and can easily be modified by technology factors.

3.1.3.3.1 Assumptions

The model has some assumptions and limitations to its operation and results (33):

- The internal resistance is assumed to be constant and is independent of the amplitude of the current
- The parameters used in the model are determined by the discharge performance and are assumed to be the same for the charging performance
- The capacity of the battery is independent of the amplitude of the current
- The performance of the battery is independent of temperature
- The self-discharge of the battery is not taken into account
- The battery has no memory effect

This model outputs the point performance of the battery. It does not model battery degradation over time, or degradation due to over-charging or deep-discharge. The performance is assumed to be the same over all charge/discharge cycles.

3.1.3.3.2 Generic Performance curve

To model the performance of a battery as it discharges, a generalized discharge curve formulation in (33) is used. The curve models battery voltage as a function of SOC and current load on the battery. A discharge curve from a commercial data sheet or research literature can be generalized into the equation to be used in the model. Three points on the curve are needed to calculate the parameters for the generalized equation: the battery voltage at full charge, the battery voltage and charge at the end of the exponential zone, and the battery voltage and charge at the end of the nominal zone. The end of the exponential zone is determined by the point where the slope of the curve changes from a highly negative slope to close to constant.

There is no mathematical formulation to calculate the end of the exponential zone, but through iterative comparison to the original discharge curve, this value can be tested and changed to achieve better accuracy. The end of the nominal zone is the point where the discharge curve crosses the nominal voltage given by the battery documentation. An example curve is shown in Figure 3.15 with the three points identified. The values necessary to calculate the parameters for the generic equation are shown in Table 3.8.

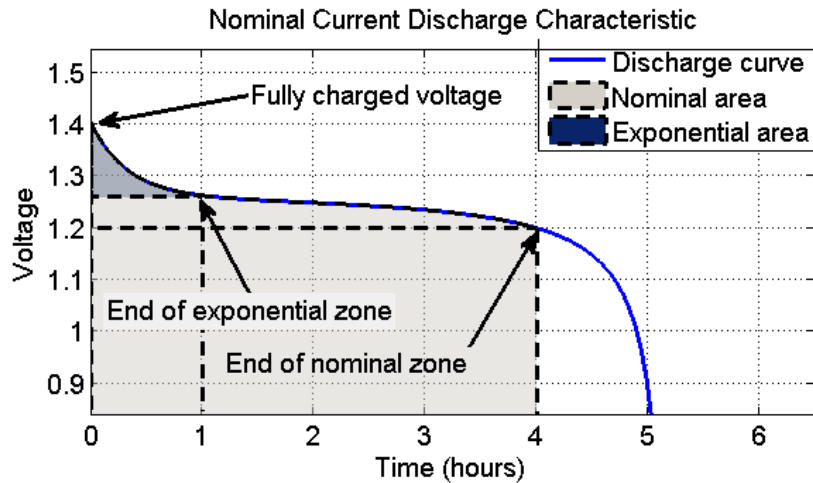


Figure 3.15 – Example battery discharge curve

Table 3.8 – Necessary values from discharge curve

Description	Voltage	Charge
Fully Charged Voltage	E_{full}	
End of Exponential Zone	E_{exp}	$Q_{exp} = i * t_{exp}$
End of Nominal Zone	E_{nom}	$Q_{nom} = i * t_{nom}$

To calculate the equation parameters, Equation 3.58 through Equation 3.62 is used with the values extracted from the discharge curve. First the voltage drop over the exponential zone and the time constant of the exponential zone are determined:

$$A = E_{full} - E_{exp}$$

Equation 3.58

$$B = \frac{3}{Q_{exp}}$$

Equation 3.59

Next, using the first two parameters and the point at the end of the nominal zone from the discharge curve, the polarization voltage is calculated.

$$K = \{E_{full} - E_{nom} + A[\exp(-B * Q_{nom}) - 1]\} * (Q_N - Q_{nom})$$

Equation 3.60

Q_N in Equation 3.60 is the nominal capacity stated by the manufacturer. The value for the internal resistance of the battery can be used to match the calculated curve to the curve given by the battery manufacturer. If there is a value available in the manufacturer's literature, it can be used as a starting value for this process, or one can be calculated using Equation 3.61:

$$R = V_N \cdot \frac{1 - \eta}{i_N}$$

Equation 3.61

Equation 3.61 uses an assumed value of 99.5% for the efficiency (33), and the current used to determine the discharge curve in the manufacturer's documentation. To calculate E_0 , the no-load constant voltage of the battery, the previous parameters are used:

$$E_0 = E_{full} + K + Ri - A$$

Equation 3.62

The final equation for the battery discharge curve uses the parameters and the amount of charge already lost to give the voltage output of the battery:

$$V = E_0 - K \frac{Q}{Q - it} + A \exp(-B * it) - Ri$$

Equation 3.63

The charge already lost is formulated as current multiplied by time if a constant current is used. If the current is not constant this value can also be calculated as the integral over time of the current. The parameters used represent physical characteristics of the battery and the materials from which it is composed. Adding in technology factors on the parameters allows the user to adjust for advances in battery technology projected to occur in the future. This results in Equation 3.64:

$$V = k_1 \cdot E_0 - k_2 \cdot K \frac{k_3 \cdot Q}{k_3 \cdot Q - it} + k_4 \cdot A \exp(-k_5 \cdot B * it) - k_6 \cdot Ri$$

Equation 3.64

The performance model also outputs the heat generated by the cell, which is equivalent to the power output of the internal resistance, given by Equation 3.65.

$$Q_{out} = i^2 \cdot R$$

Equation 3.65

3.1.3.4 Sizing Algorithm

The performance model is wrapped up into a sizing procedure to calculate the size and layout of a battery stack necessary to produce the required power over a given operating profile. The algorithm uses a design power load and current operating profile input by the user. Figure 3.16 shows the flow of information and calculations.

First, the number of parallel cells required in the stack is determined based on the current capacity calculated from the current load profile. The profile is integrated using the trapezoidal method to determine the total energy discharge over the profile. The model then calculates the current load on each cell using the number of parallel cells. The current at the design power load is found in the operating profile at the time of the design power load. The capacity discharged before the design power load is calculated as the integral of the load profile from the start to the time of the design power load. Again, the integration is done using the trapezoidal method. The performance model described previously calculates the voltage output based on the energy depleted, the current load, and the parameters input by the user. The voltage output multiplied by the current load gives the power output of the battery. The design power load divided by the power output of a single battery gives the entire size of the battery stack. To find the number of cells in series, the total number of cells is divided by the number of cells in parallel which is then rounded up. To form the complete stack as a full array of cells, the number of cells in series is multiplied by the number of cells in parallel. This gives the final number of total cells in the stack.

Once the battery stack is sized by the performance algorithm, the volume and weight of the battery stack are determined by the specific energy and the power density. The volume and weight calculations are performed in a subelement in NPSS. The final results of the sizing are the number of cells in the battery stack, the number of cells in parallel, and the weight and volume of the stack.

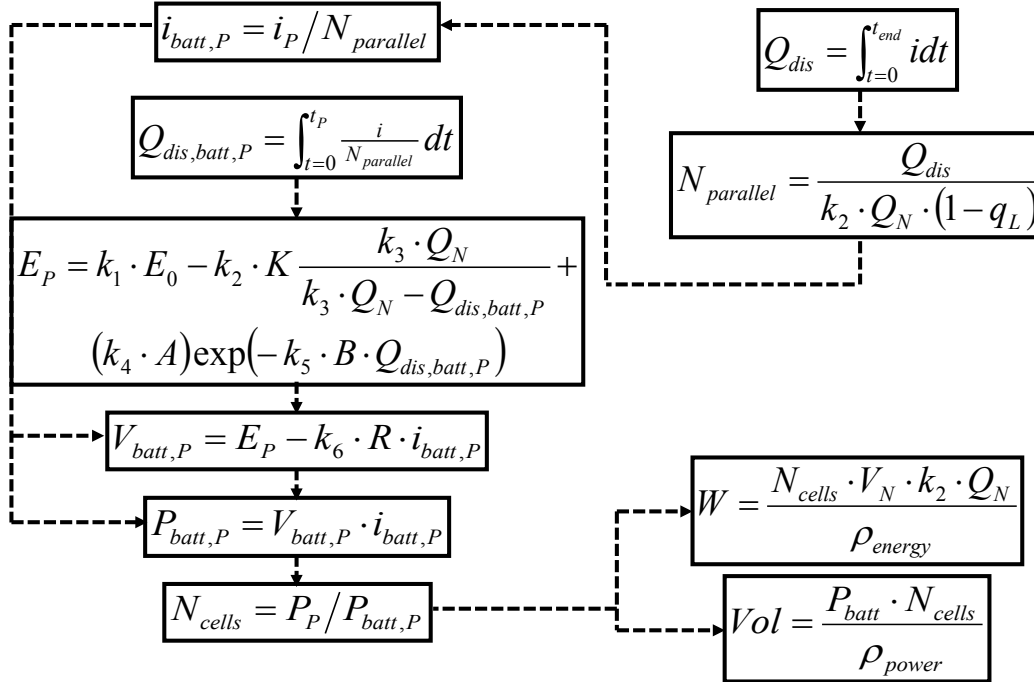


Figure 3.16 – Data flow for Sizing algorithm

3.1.3.5 Validation

For validation, data from (33) is input to the performance model and the discharge plots are compared with published results. The inputs to the model taken from the literature are shown in Table 3.9. These inputs represent the Panasonic HHR650D3, a 6.5 amp-hour, 1.2 volt nickel metal-hydride battery. The nominal current capacity of the battery tested is 6.5 Amp-hours, but the data sheet for the battery gives the average capacity as 6.8 Amp-hours. On the data sheet the internal resistance is given as 2 mΩ, but (33) found that a value of 4.6 mΩ matches the model to the manufacturer’s plots better.

Table 3.9 – Validation Inputs

Parameter	Value
E0 (Volts)	1.2848
R (Ohms)	0.0046
K (Volts)	0.01875
A (volts)	0.144
B (Ah) ⁻¹	2.3077

Figure 3.17 shows the output plots from the model with the literature plots overlaid. For the currents tested the model matches the published results exactly, validating the model.

To test the sizing algorithm, small stacks were sized using the inputs from the validation. An operating profile was generated in MATLAB to test the integration calculation in addition to the algorithm’s functionality. The results from the integration of the profile are displayed in Figure

3.17. Compared to the trapezoidal integration function in MATAB, the trapezoidal integration in the battery model obtains the same answer, proving its accuracy.

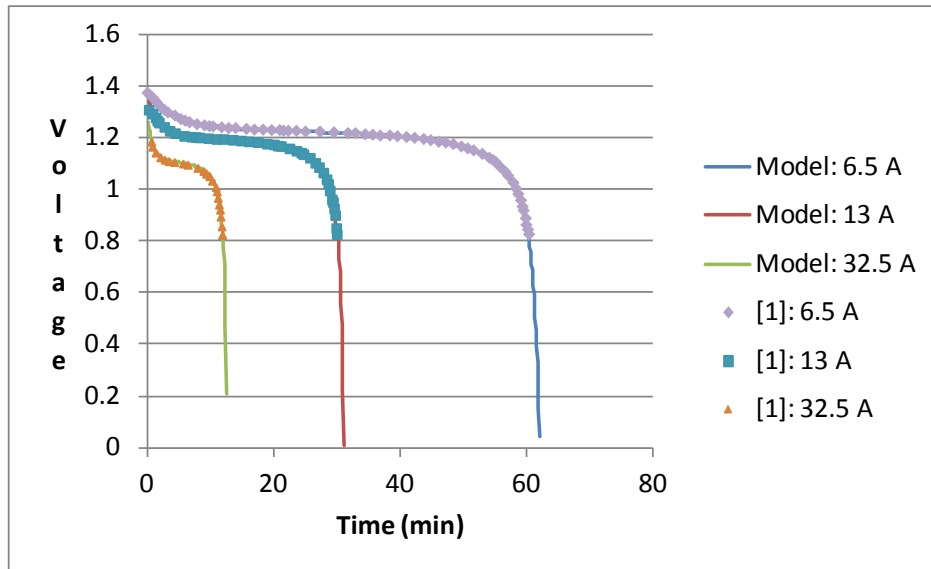


Figure 3.17 – Battery performance model validation plots.

Table 3.10 – Comparison of integration results

Description	MATLAB	Battery Element
Energy discharged before design power load (Amp-hrs)	5.139	5.139
Total energy discharged (Amp-hrs)	10.10	10.10

The model also correctly sized the battery stack to the design power load and the operating profile as shown in Table 3.11. The number of cells in parallel multiplied by the capacity is greater than the total energy discharged divided by the usable capacity of the battery (1 – % reserves). Also the nominal power output multiplied by the number of total cells is greater than the design power load. The most demanding requirement is the total capacity necessary, for which the stack is sized.

Table 3.11 – Sizing test inputs and results

Input	Value
Discharge Duration (Hours)	2
Design Power Load (Watts)	7
Nominal Battery Power (Watts)	7.8
Nominal Voltage (Volts)	1.2
Capacity	6.8
Charge Reserves (%)	10
Time of Design Power (Hours)	1
Specific Energy (Watt-hours/kg)	300
Power Density (W/m ³)	150
Output	Value
Cells in Parallel	1
Cells in Series	2
Total Cells	2
Stack Mass (kg)	0.052
Stack Volume (m ³)	0.104

3.1.4 Cryocooler Model

3.1.4.1 Introduction

One of the major components needed to model the hybrid electric engine is a cryogenic cooler or cryocooler. The cryocooler is used to reject excess heat from electrical components and reduce their temperature to cryogenic levels in order to attain superconductivity. To accomplish this, a specific variant of cryocooler was chosen. More specifically, the reverse turbo brayton cycle was chosen due to the ease of modeling in NPSS as well as the simplicity of being a steady state analysis along with its potential for high cooling capacity to weight ratios. With the model built in NPSS, it was validated using two different fluids, neon and helium. Following the validation, it was tested for off design conditions.

3.1.4.2 Problem Definition

There exist many variants of cryocooler systems. Each is based on a different thermodynamic cycle. In the beginning of this effort all the cycle types were surveyed. It was found that the main types were regenerative cycles and recuperative cycles. Within the regenerative types existed Stirling cycle, Pulse Tubes, and Gifford McMahon. For the Recuperative type there was the Joule Thomson and Reverse Turbo Brayton cycle. A summary of the cycle types can be seen in the table below.

Table 3.12 – Thermodynamic Cycle Summary

Type	Process 1-2	Process 2-3	Process 3-4	Process 4-1
Stirling	Isothermal	Isochoric	Isothermal	Isochoric
Pulse Tube	Isothermal	Isobaric	Isothermal	Isobaric
Gifford McMahon	Isothermal	Isobaric	Isothermal	Isobaric
Joule Thomson	Adiabatic	Isobaric	Adiabatic	Isobaric
Reverse Turbo Brayton	Adiabatic	Isobaric	Adiabatic	Isobaric

In general, many of the cryocoolers used today are designed for low power applications, used sensors and space for example. Each of the options offer particular advantages. The Stirling cryocooler, which works off of the Stirling cycle was one of the first cryogenic cycle discovered and used. One of its main advantages is compactness; however this advantage quickly disappears when applications require multiple components cooled simultaneously. Another solution frequently used, is the Gifford-McMahon cryocooler which is a variant of the Stirling type. It uses extra valves to isolate compression and expansion unit in order to increase compression ratio. This solution is more robust, allows separation of compressor from cold section, and allows ease of multi-staging. However the system suffers issues related to being a source of vibration, heat loss due to the shuttle, and lower efficiency. Another more recent type of cryocooler is the Pulse Tube. The Pulse Tube works by using pressure waves, within the system, to shuttle heat back and forward to create cool conditions. A big advantage of this system is that no moving parts are used in the cold region. However, this system cannot be scaled while maintaining efficiency. Also, extra space is required for the pulse tube. The last type, which is among the recuperative cycles, is the Reverse Turbo Brayton Cryocooler. This type of system is analogous to turbojet systems, except heat is removed where the combustor would be in a conventional heat engine. One of the particular benefits which is of interest to aerospace applications is the lower specific weight as seen in the figure below.

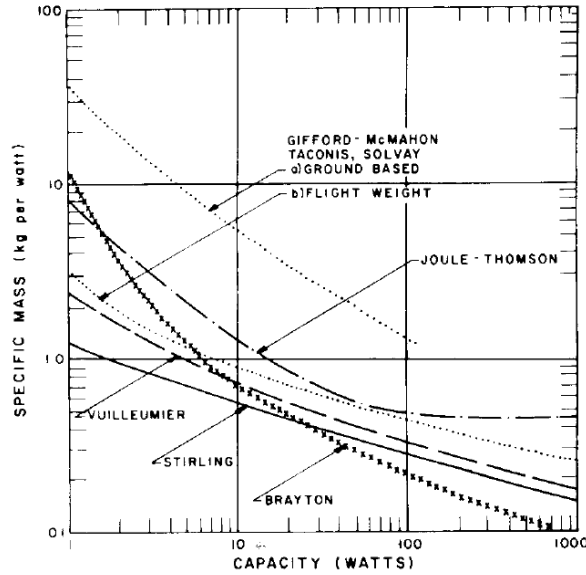


Figure 3.18 – Power Capacity vs Specific Mass Cryocooler Survey

While it has poor specific mass in the lower regimes, as capacity increases the system quickly becomes the lightest option available. This is also the reason few reverse Brayton cryocoolers are seen today; most cryo applications are relatively low power. In a SUGAR application the amount of heat that must be rejected is two or more orders of magnitude larger than current cryo cooler applications.

So far, the types of cryocoolers available have been shown and each offer specific advantages and disadvantages given specific requirements. But in order to narrow down, it is important to assess the impact of these systems given the aerospace application of interest. It is expected that heat rejection on the order of 100s of kW will be required.

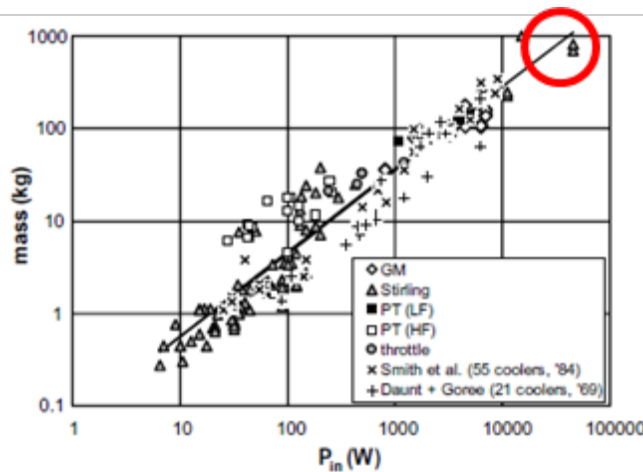


Figure 3.19 – Power vs Mass for Cryocooler Types

In the above figure, SUGARs application is indicated by the red circle. While it is seen the only current solutions offered are Stirling types, these units can be bulky due to reasons described earlier.

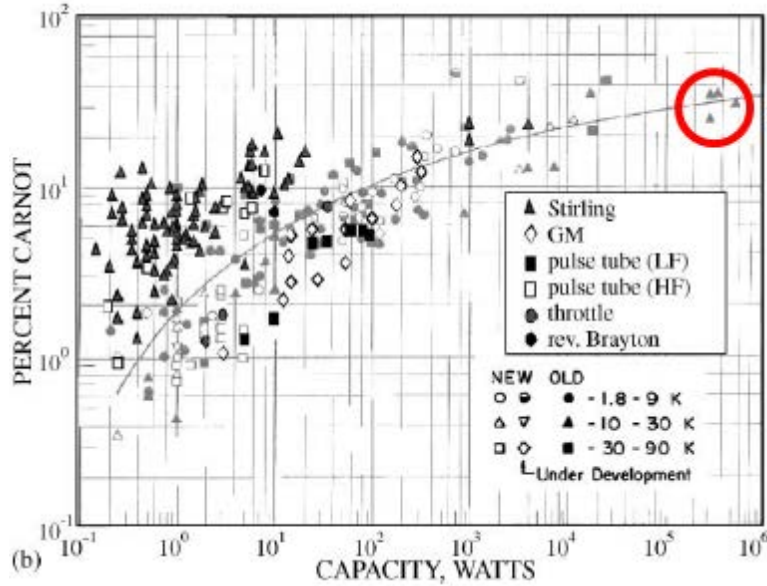


Figure 3.20 – Power Capacity vs Percent Carnot for Cryocooler Types

Similarly, in the figure above, SUGARs application is indicated with red circle showing options only available for Stirling cycles. While currently Reverse Turbo Brayton Cycles do not exist for the current application in mind, it is expected that options would become available for the N+4 timeframe.

In further evaluating each of the selections, it was found that the Regenerative types would require a transient analysis while Recuperative only required steady state. Along with only needing steady state analysis, the recuperative type offered the advantage of being able to use elements prebuilt in NPSS (compressor, duct, flowstart, etc.)

Among this survey, it was also found that typically Helium, Hydrogen, Nitrogen, Neon, and Methane were used as the working fluid. Helium was used for applications requiring 7 R, Hydrogen for 36 R, Neon for 135 R, Nitrogen for 144 R, and Methane for 216 R.

3.1.4.3 On Design Approach

In order to begin modeling, all the major inputs and outputs were needed. Along with these variables, it is also important to determine how such a system is thermodynamically sized, because the thermodynamic size will eventually be related to the physical size and mass of the system. Also, how do the characteristics vary at different conditions? This is important because the initial sizing represents the ideal case; however the system is more likely to experience off

design conditions. Then the system must be validated in order to prove the results coming out of the system to be reasonable. To determine the inputs/outputs a representative model was defined and can be seen below.

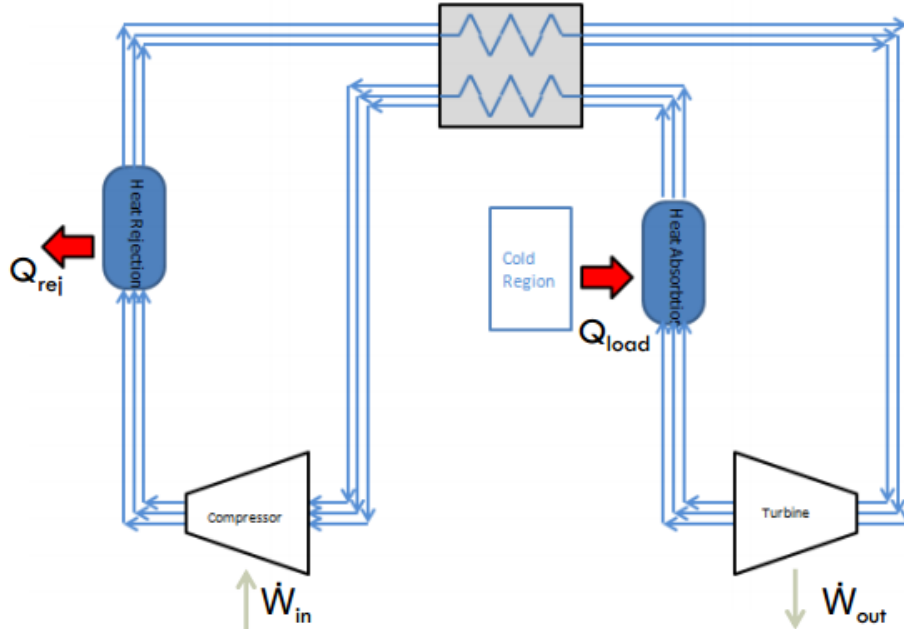


Figure 3.21 – Closed Circuit Reverse Turbo Brayton Cycle

The model defined above is the general representation of the Reverse Turbo-Brayton Cycle. In this model, the blue arrows represent the direction of the flow. For the cycle, the fluid flows through the compressor where it is adiabatically compressed. Next, it flows through the heat rejection element where heat is removed isobarically. Following heat rejection, the fluid moves through the recuperator (depicted by the topmost box in the figure above), which transfers heat to the colder line. Afterwards, the flow is adiabatically expanded which decreases the temperature to cryogenic levels which then proceeds through the heat absorption section and absorbs the heat of the superconducting components. From this model, it is determined that the system can be represented as five elements, as seen in the figure below.

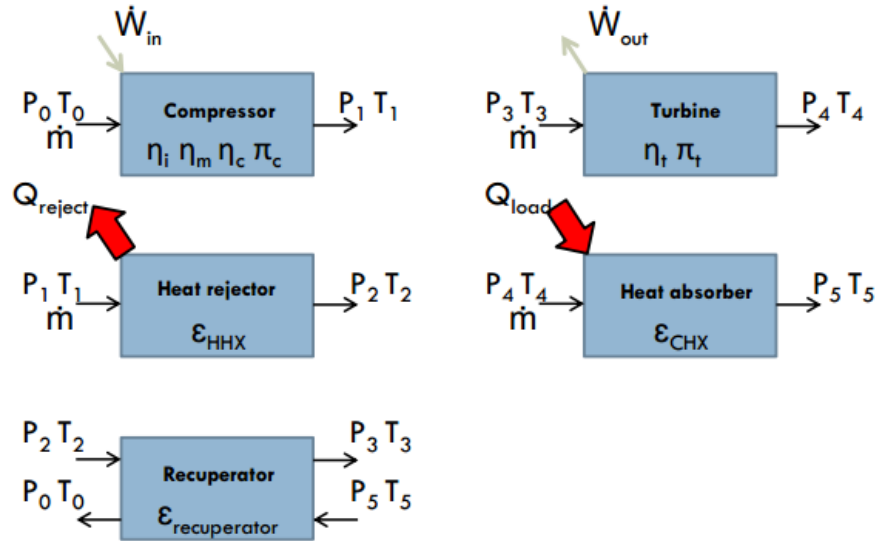


Figure 3.22 – Reverse Turbo Brayton Diagram (from Creare Contract #NAS5-31281)

The model was broken down into the elements above, because this form can be most easily translated into the language of NPSS. As seen in the figure above, the major inputs of the system are temperature, pressure, heat absorbed (Q_{load}) and performance and efficiency factors. The major outputs were work in and out of the system and heat rejection (Q_{reject}).

Next, it was determined that the thermodynamic size is a strong function of massflow. The massflow is sized in order to pump a given amount of heat load away from the superconducting components. This was translated to an independent/dependent relationship of massflow to the desired cryogenic temperature. Along with this, in order to complete the cycle an independent/dependent relation was defined between the turbine pressure ratio and the difference of pressures between the end and beginning of the cycle (before compressor, after turbine).

With the cycle successfully defined, implementation within NPSS began. From the figure above, the model would use a compressor, turbine, three heat exchangers, three flowstarts, three flowends, as well as multiple ducts and shaft elements. For the first iteration, a simple model was created which did not use the recuperator. This was done initially to assess potential difficulties that may be associated with developing a non-turbojet model in the NPSS framework. Following the successful implementation, the recuperator was added. Due to the nature of how NPSS calculates each block in the model file sequentially, the flow was broken after the recuperator adding an additional flowstart and flowend. Schematically this final model can be seen in the figure below. The flow broken is represented by FlowStart4 and FlowEnd4, which initially was connected as one line. ‘Breaking’ the model in this manner and enforcing continuity between FlowEnd4 and FlowStart4 via the NPSS solver helps to remove circular

pathways. NPSS tends to have numerical issues with circular pathways; therefore, this method is applied to increase numerical stability.

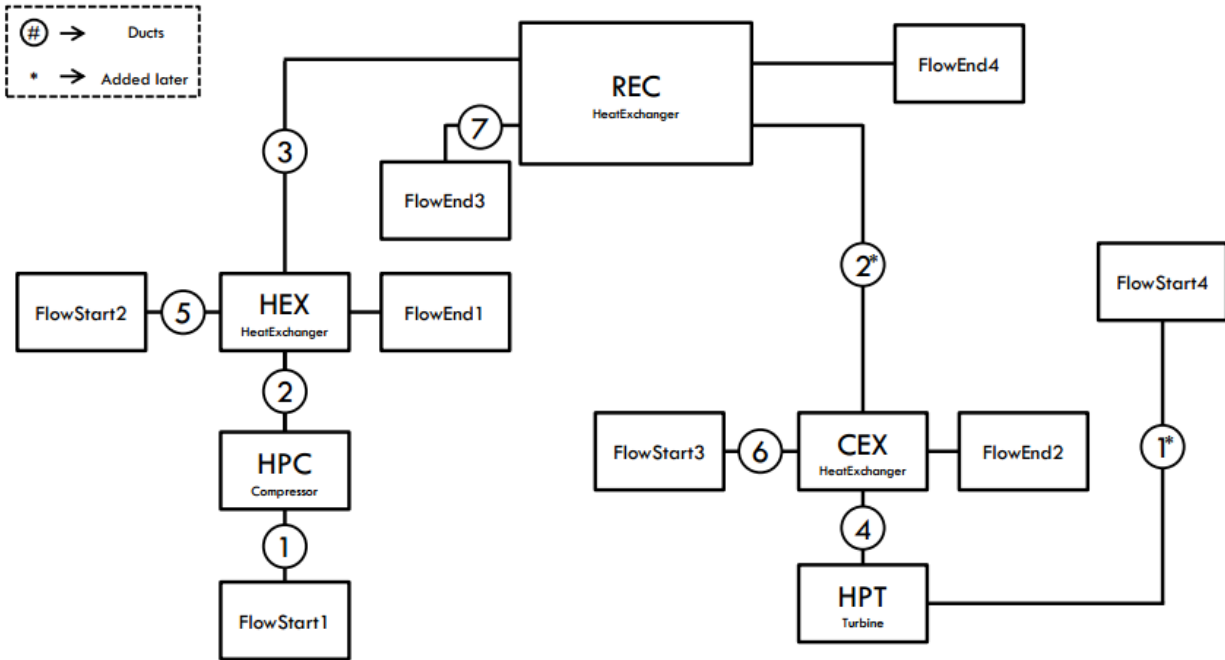


Figure 3.23 – NPSS Block Schematic of Reverse Turbo Brayton Cycle

In addition to the model above, Load elements were added to the shaft ports of HPC and HPT representing the compressor and turbine respectively. This was done to separate the compressor from the turbine because a cryocooler is not a power producing device. To complete the disconnect between the compressor and turbine, the independents and dependents from autoSolverSetup() needed to be modified. Along with this modification, other independent and dependent elements were needed to account for the extra flowstarts. The list of independents and dependents can be seen in Table 3.13.

Table 3.13 – NPSS Model Independents and Dependents

Independent	Dependents
Compressor Load	Compressor Shaft Speed
Turbine Load	Turbine Shaft Speed
Massflow into FlowStart 4	Massflow Balance between FlowStart FlowEnd 4
Temperature into FlowStart 4	Temperature Balance between FlowStart FlowEnd 4
Pressure into FlowStar 4	Pressure Balance between FlowStart FlowEnd 4
Turbine Pressure Ratio	Pressure Balance between FlowStart 1 FlowEnd 3
Internal Massflow	Desired Cryogenic Temperature
Massflow across Heat Rejection (HEX)	Heat Balance across the system
Massflow across Heat Absorption (CEX)	Desired cold side ambient temperature

The model described above was initially built using the NPSS thermodynamic package “GasTbls”. However, in order to define a realistic model, other fluids were required.

From the earlier survey, it was found that the fluids used in most cryogenic systems were Hydrogen, Helium, Nitrogen, Neon, and Methane. Since none of these tables exist within NPSS, Fluid Property Tables or FPTs were created. First, thermodynamic properties for each of the fluids were obtained from the National Institute of Standards and Technology (NIST) website. The website contained various thermodynamic data such as enthalpy, entropy, heat capacity, density, and all other relevant thermodynamic properties necessary to construct FPT tables. Using examples provided in NPSS and the Rocket Supplement included with NPSS, the structure of FPTs were created for each of the fluids. The result was five tables each containing over 150,000 points of data for interpolation and extrapolation. The ranges of these tables depended on the fluid; however these tables represent a temperature range of 100R -2,000R where some had somewhat smaller ranges. Finally, the range of pressures extended from 1 PSI to 10,000 PSI.

With the completion of the FPT, the thermodynamic package being was switched over for validation. However, this resulted in difficulties. While the model was converging with GasTbls, it was not converging with FPTs. First it was assumed the FPT tables were incorrect or too large. Even when the ranges of the tables were reduced and the intervals between each point were also reduced, NPSS still would not converge. After much testing and recreation of the tables, a bug was found within the version of NPSS being used. For some of the NPSS elements, specifically the turbine and compressor, there are functions used to determine the thermodynamic properties at a given station for a fluid. These functions are setTotalTP, setTotalh_P, and setTotalSP. Each of these functions require two inputs to define the conditions at a station, temperature and pressure for setTotalTP, enthalpy and pressure for setTotalh_P, and entropy and pressure for setTotalSP. Specifically, within the compressor and turbine elements, the code was failing with the setTotalSP function.

Further testing outside the NPSS model showed that not only the custom built tables were failing, but also the example cases provided with NPSS were also failing. In order to bypass this issue, a work around was created using the Secant Solver function. The specific code can be seen in the figure below

```
real gs_Tt;
SecantSolver setTotalFix{
    setTotalFix.setMaxIters(20);
    setTotalFix.setPerturb(0.01);
}
gs_Tt = Fl_Otemp.Tt;
setTotalFix.initialize(gs_Tt);
do {
    real error;
    Fl_Otemp.setTotalTP(gs_Tt,PtOut);
    error = Fl_Otemp.S-Sout;
    gs_Tt = setTotalFix.iterate(error);
    //cout<<gs_Tt<<endl;
} while (!(setTotalFix.isConverged()) &&!(setTotalFix.errorType));
Fl_Otemp.setTotalTP(gs_Tt,PtOut);
```

Figure 3.24 – setTotalSP workaround using Secant Solver

The code works by comparing the known entropy S_{out} and the computed entropy $Fl_Otemp.S$. For each iteration, the $Otemp$ entropy is computed using `setTotalTP` and the loop continues until convergence is found. Simply it works by taking the known pressure, and the known entropy, and iterates on temperature until a temperature and pressure is found which would relate to the known entropy.

When these changes were added to the Compressor and Turbine element, the model began converging and validation could proceed.

3.1.4.4 Results: Validation

Validation was performed using two different cryocooler models. The first model used came from a study titled “Preliminary Design for a Reverse Brayton Cycle Cryogenic Cooler” (34); this model used Neon as the working fluid. The second model was a study titled “Second-Law Analysis of a Hybrid Reverse Brayton Stirling Cryocooler” (35), which the working fluid used was Helium.

For the first validation, the model was a single stage Reverse Turbo Brayton cryocooler. The original model was developed by Create Inc. The purpose of the model was to cryogenically cool sensing components on the Hubble Space Telescope. While the purpose was utilized for space, the thermodynamic cycle used for either Aircraft or Spacecraft would be the same.

For the validation, either the parameters were directly given in the paper, or information was calculated from the flowstation data. Major inputs as well as model comparison can be seen in the table and figure below.

Table 3.14 – Comparison NPSS inputs to Source Inputs First Validation

Type	NPSS Value	Source Value
Fluid	Neon	Neon
Input Pressure (PSI)	15.87	15.872
Input Temperature (R)	527.0	527.0
Pressure Ratio	1.602	1.602
Compressor Polytropic Efficiency	0.73	0.73
Heat Rejector Effectiveness	0.95	0.95
Recuperator Effectiveness	0.994	0.993
Turbine Adiabatic Efficiency	0.602	0.602
Heat Absorption (BTU/S)	0.0052	0.0052
High Pressure Line Drop (dPqP1)	0.0058	0.0058
Low Pressure Line Drop (dPqP2)	0.0093	0.0093

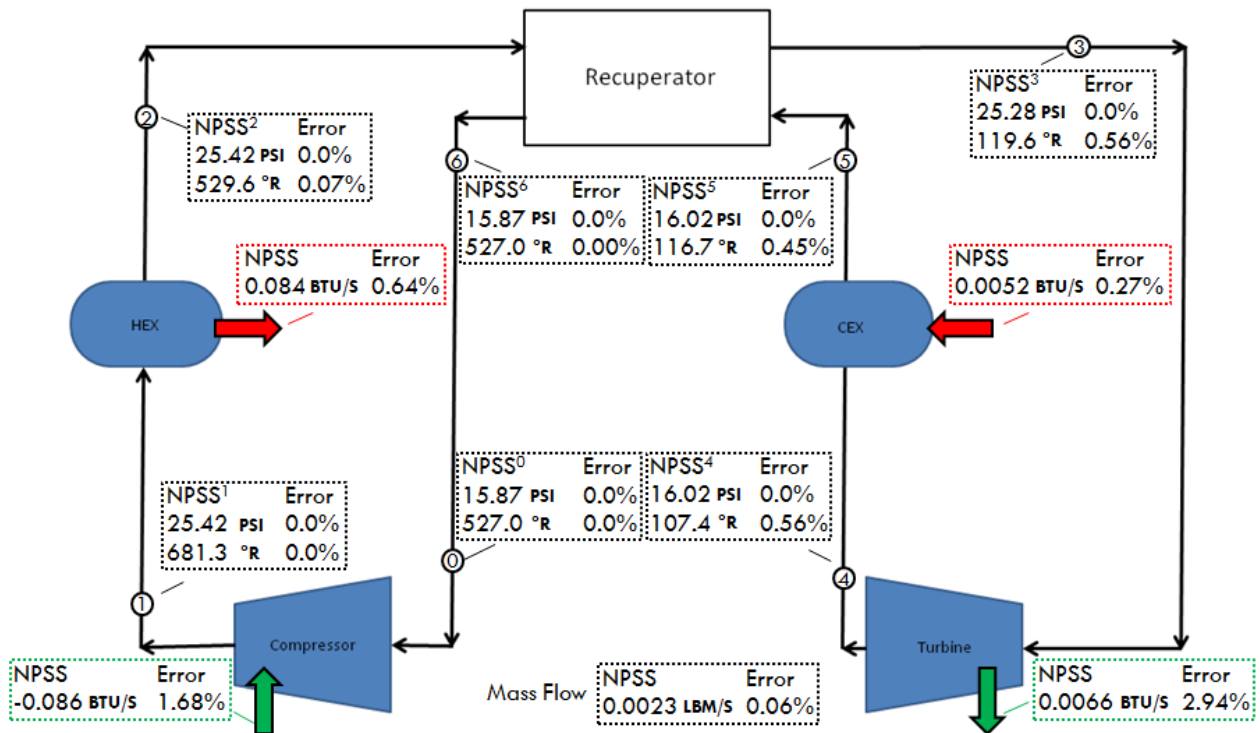


Figure 3.25 – NPSS Model Comparison to Actual Data First Validation

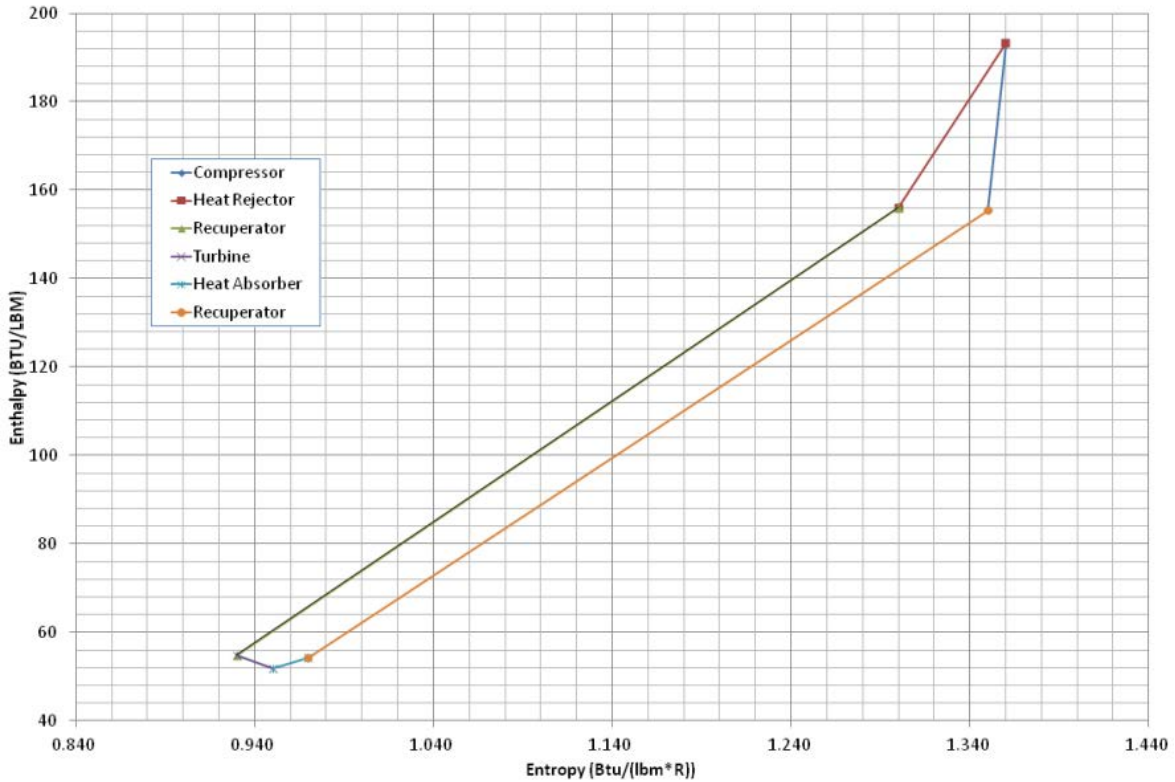


Figure 3.26 – First Validation H-S Diagram

The resulting validation data resulted in a close match between the model and the actual data. Most of the points resulted in an error of <1% and the highest error was the work out of the turbine at around 3%.

The next validation was done with a hybrid Reverse Brayton Stirling cryocooler which uses helium as the working fluid. This model was developed by the Air Force Research Laboratory AFRL and Raytheon Space and Airborne Systems. The purpose of the model was to cool infrared sensors for space applications. While the paper uses a Stirling cycle, it uses it as a precooler which was used for validation. Similarly to the previous model, most of the efficiency information was given. However, only a T-S diagram was provided. In order to determine the flowstation data, the T-S diagram was digitized and temperature was obtained. The general inputs can be seen in the Table below.

Table 3.15 – Comparison NPSS inputs to Source Inputs Second Validation

Type	NPSS Value	Source Value
Fluid	Helium	Helium
Input Pressure (PSI)	15.87	----
Input Temperature (R)	44.55	44.55
Pressure Ratio	1.485	1.5
Compressor Polytropic Efficiency	0.395	0.4
Heat Rejector Effectiveness	0.99	0.99
Recuperator Effectiveness	0.984	0.986
Turbine Adiabatic Efficiency	0.495	0.5
Heat Absorption (BTU/S)	2.84 E-05	2.84 E-05
Recuperator Pressure Drop	0.02	0.02
HEX Pressure Drop	0.01	0.01
Scaled Factor	50000	----

While validating this model, it was found that NPSS did not perform well when using extremely small values of flow. While the previous validation also used small values for massflow, the helium model used significantly smaller values which were 100 times smaller. To bypass this, the system’s mass flow and heat load was scaled by 50,000 in order to help reduce the relative error. The result from the process will not affect the outputs as long as everything is consistently scaled. After the analysis is ran, dividing the result with the scaling factor again will produce the desired results. The second validation including the scaling factor can be seen in the Figure 3.27.

*Heat, Power, and Mass Flow include the scaling factor

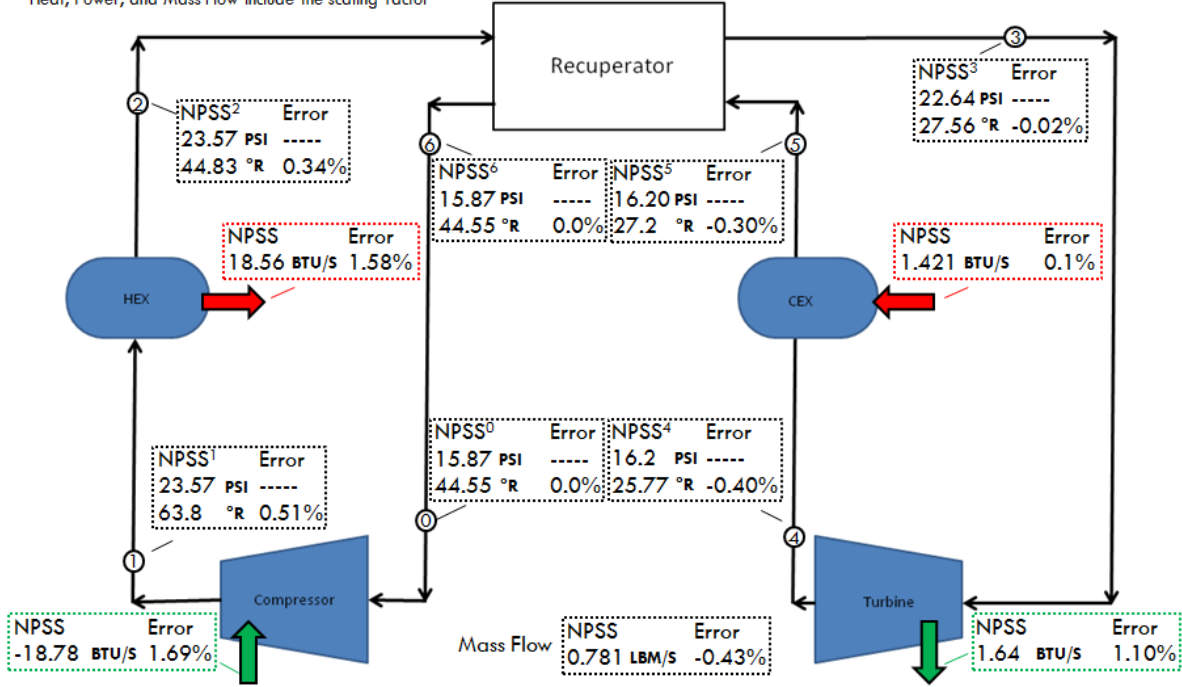


Figure 3.27 – NPSS Model Comparison to Actual Data Second Validation

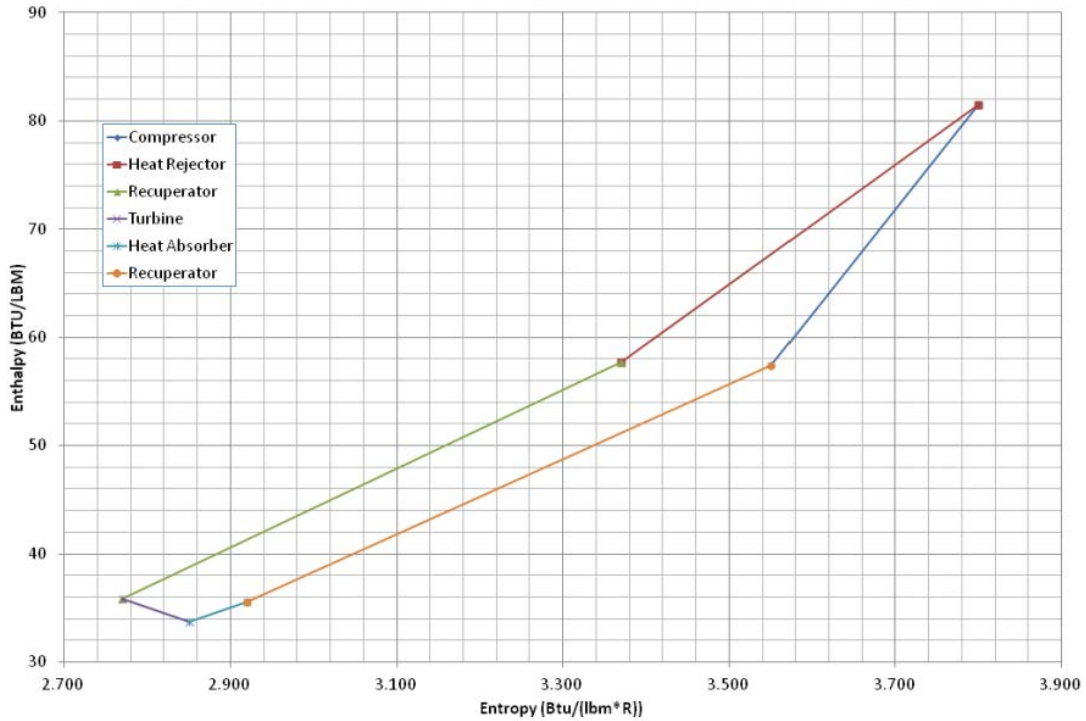


Figure 3.28 – Second Validation H-S Diagram

3.1.4.5 Results: Off Design Analysis

Primarily, the previous sections dealt with sizing a system thermodynamically. Once it is sized, it is important next to assess how a system would behave under off design conditions. Before developing the Off Design for NPSS, it was determined that a cryocooler would experience three differing conditions during operation. The ambient temperature will vary, the required temperature of the cold side could change, and the cooling load could change.

To control the ambient conditions, massflow of the HEX and CEX will become independents. Internal massflow will be used to match the varying cooling load. This leads to a new solver setup which can be seen in the table below.

Table 3.16 – NPSS Off Design Dependent and Independent Setup

Independent	Dependents
Compressor R Line	Compressor Error Term
Compressor Load	Compressor Shaft Speed
Turbine Load	Turbine Shaft Speed
Massflow into FlowStart 4	Massflow Balance between FlowStart FlowEnd 4
Temperature into FlowStart 4	Temperature Balance between FlowStart FlowEnd 4
Pressure into FlowStar 4	Pressure Balance between FlowStart FlowEnd 4
Turbine Pressure Ratio	Pressure Balance between FlowStart 1 FlowEnd 3
Internal Massflow	Desired Cryogenic Temperature
Massflow across Heat Rejection (HEX)	Heat Balance across the system
Massflow across Heat Absorption (CEX)	Desired cold side ambient temperature

Following the successful validation of the model, off design testing began. Using the Off Design solver setup described previously, the model was tested by keeping the massflow across the heat exchanger constant for three conditions. Along with the three conditions, the cooling load was varied. Results from this analysis can be seen in the figures below.

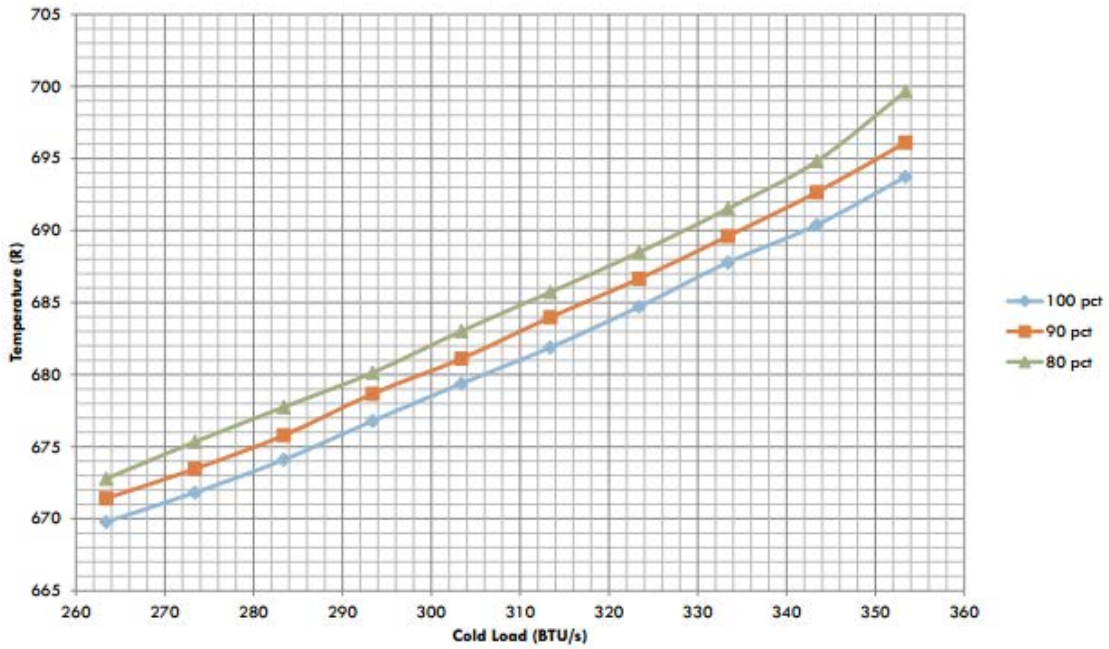


Figure 3.29 – Rejection Temperature

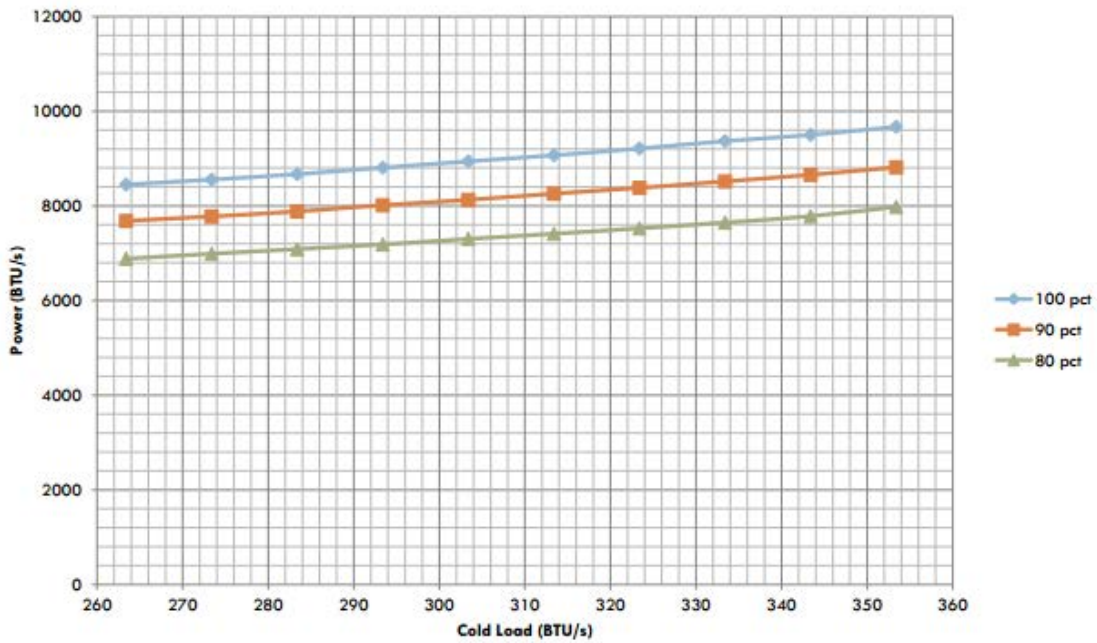


Figure 3.30 – Heat Rejection Load

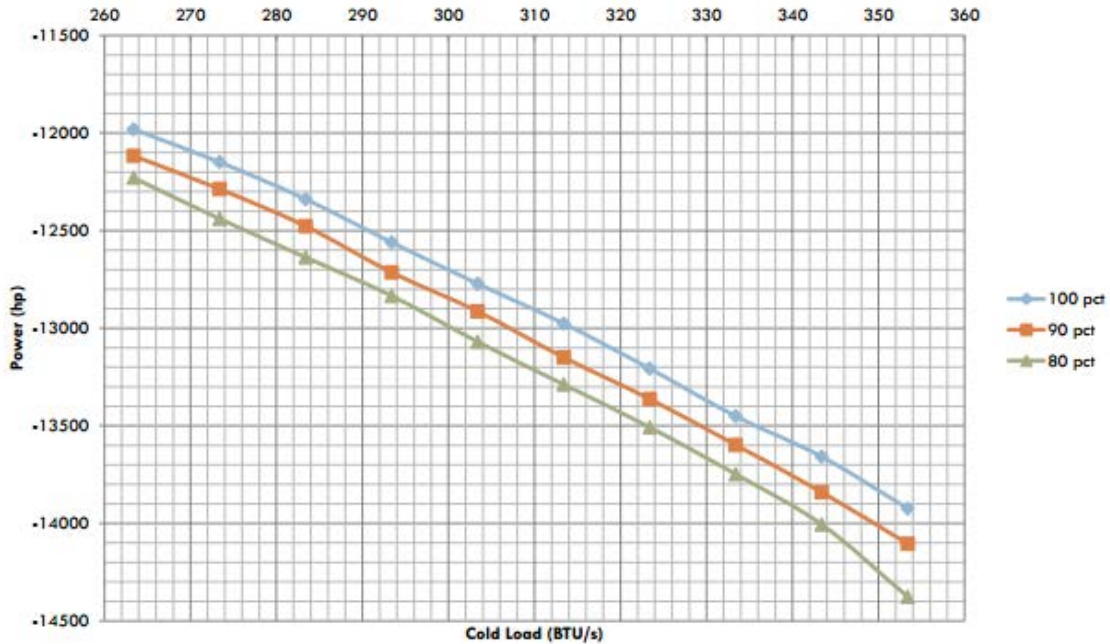


Figure 3.31 – HPC Power

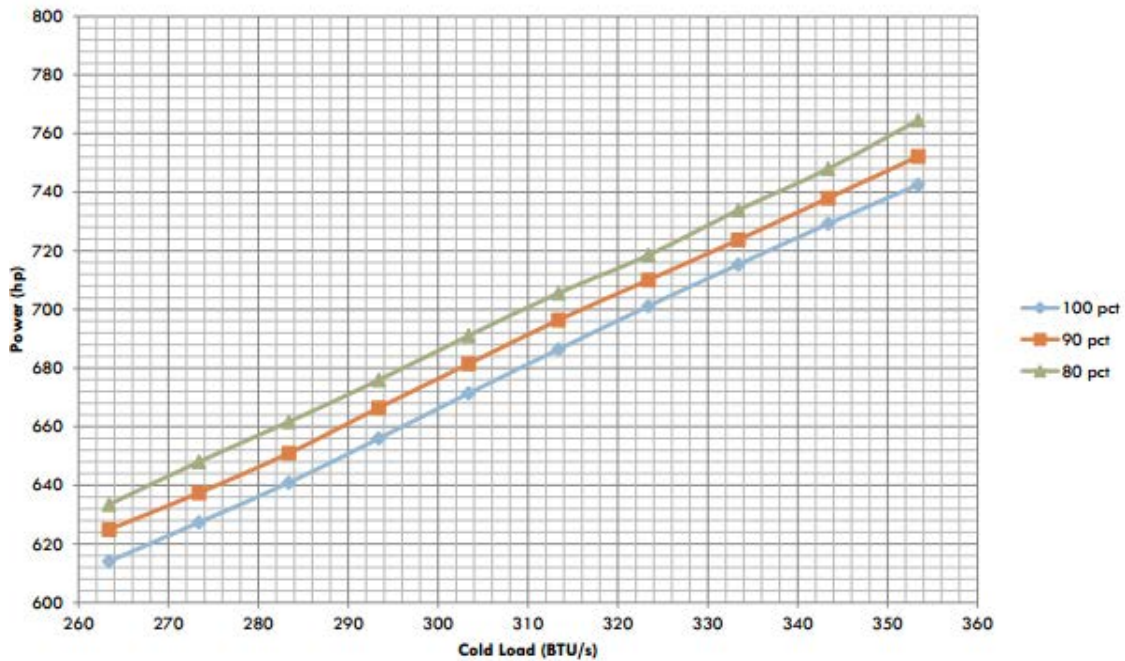


Figure 3.32 – HPT Power

For the heat rejection temperature, it shows that as the cooling load is increased the resulting temperature increases. Also, as the heat flow is varied the line shifts upward, suggesting that less massflow forces the system to work harder to reject the inefficiencies from the compressor. Similarly for the HPC power which is the compressor, as the cooling load increases, the amount of work into the system increases. With the compressor, changing the massflow

causes the line to shift down which means the amount of work required increases. The turbine shows the same trend as the compressor. The results of the off design analysis shows that either increasing the cooling load on the CEX or decreasing the massflow across the HEX forces the system to work harder in order to maintain the cycle.

The full off design assessment can be seen in the trends below. Each trend line represents a different ambient massflow across the HEX. Blue line is the design condition, red line is massflow reduced by 10%, and the green line is massflow reduced by 20%.

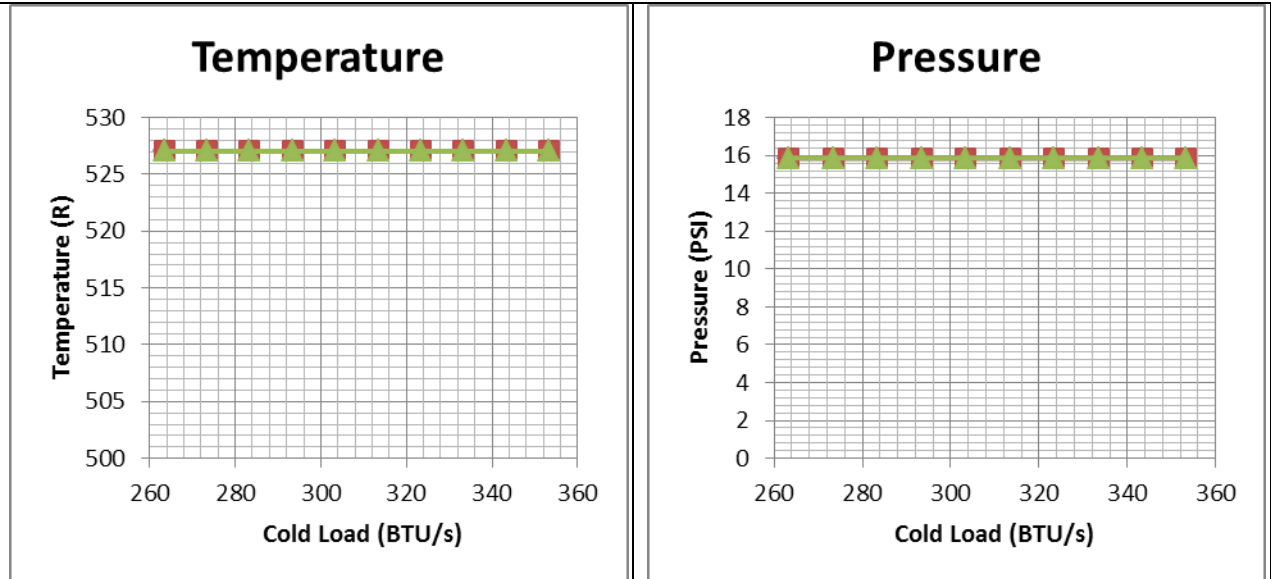


Figure 3.33 – FS_2 Temperature

Figure 3.34 – FS_2 Pressure

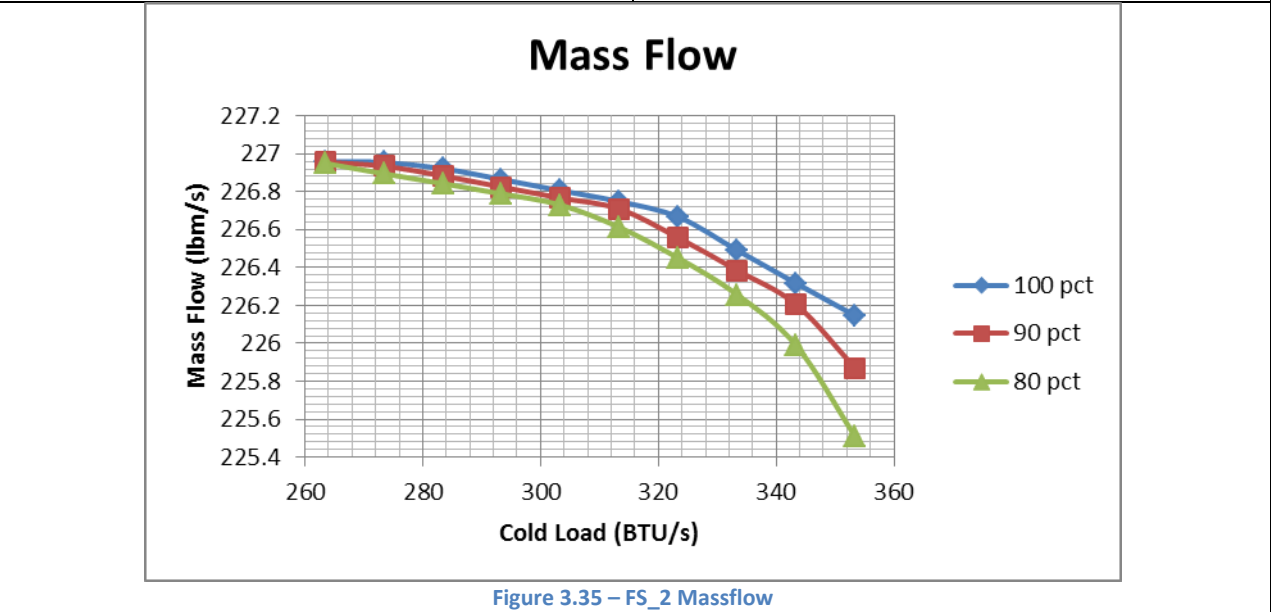


Figure 3.35 – FS_2 Massflow

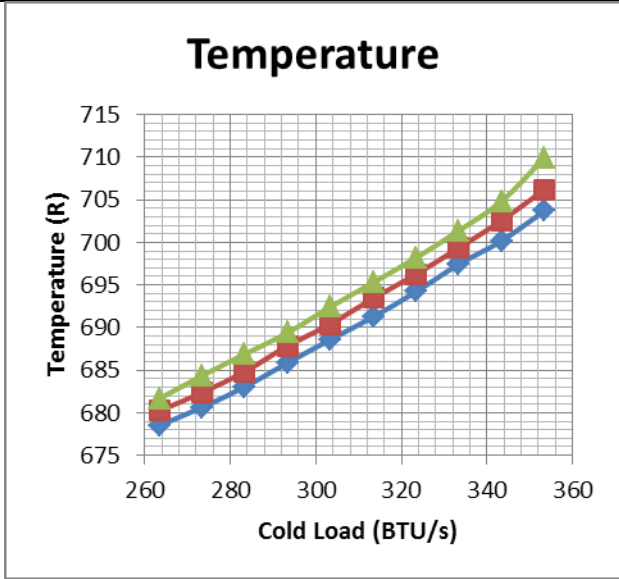


Figure 3.36 – FS_3 Temperature

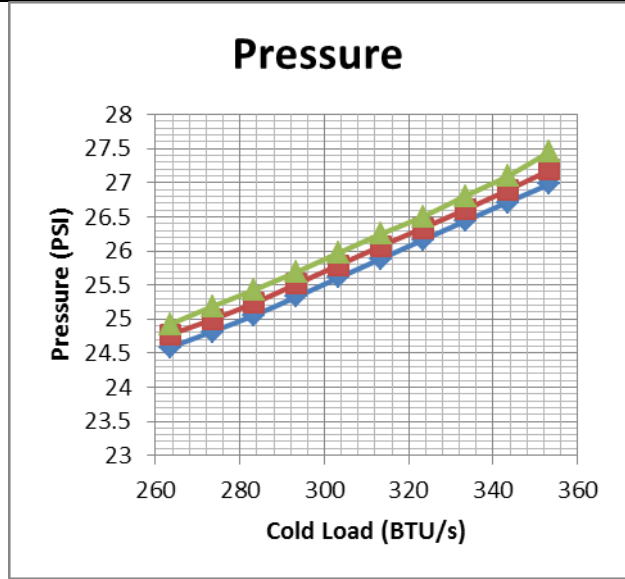


Figure 3.37 – FS_3 Pressure

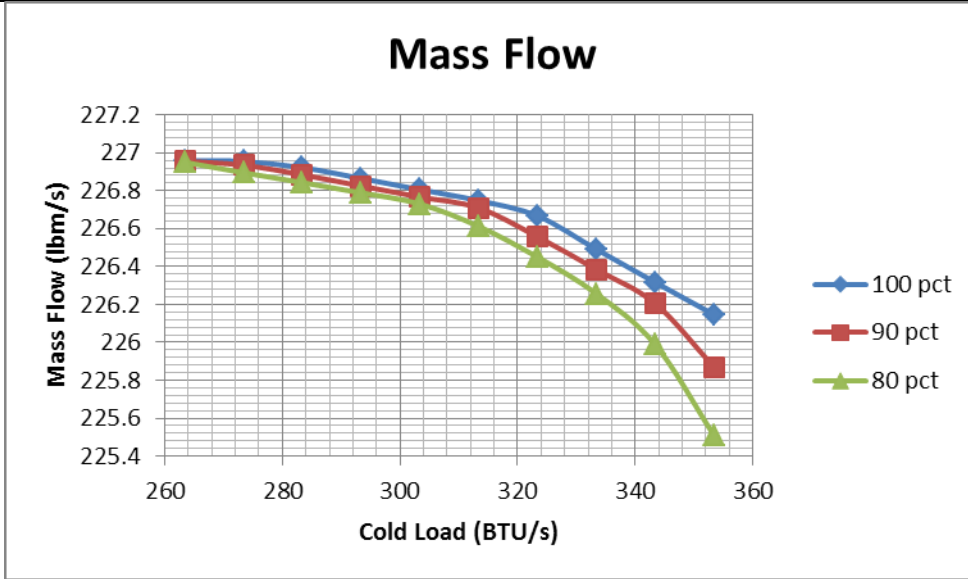


Figure 3.38 – FS_3 Massflow

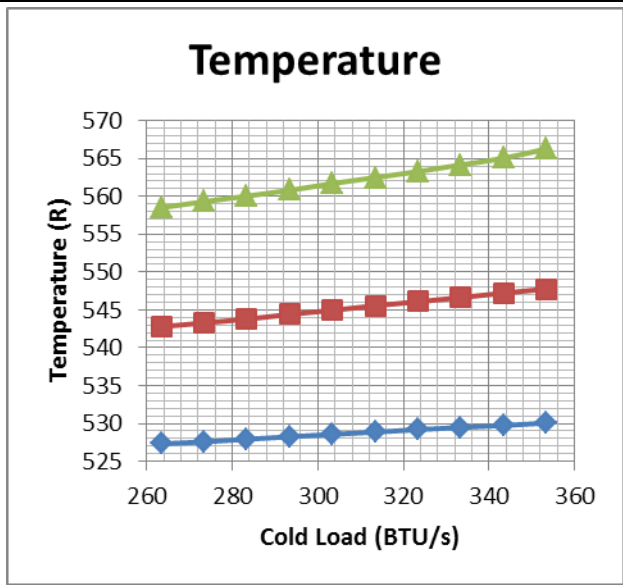


Figure 3.39 – FS_5 Temperature

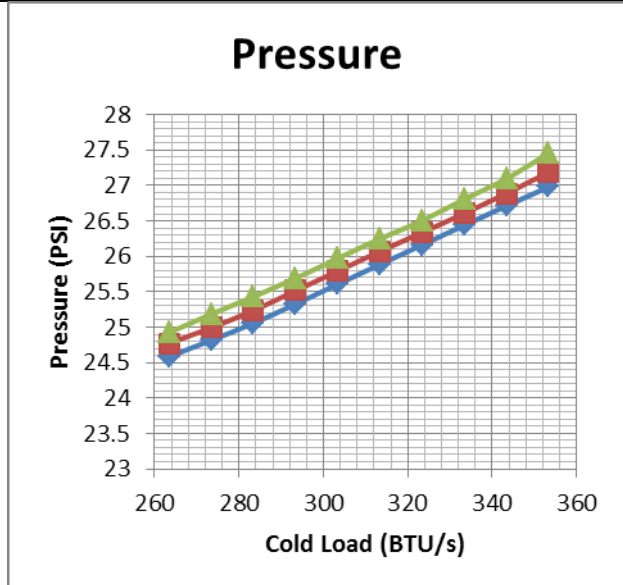


Figure 3.40 – FS_5 Pressure

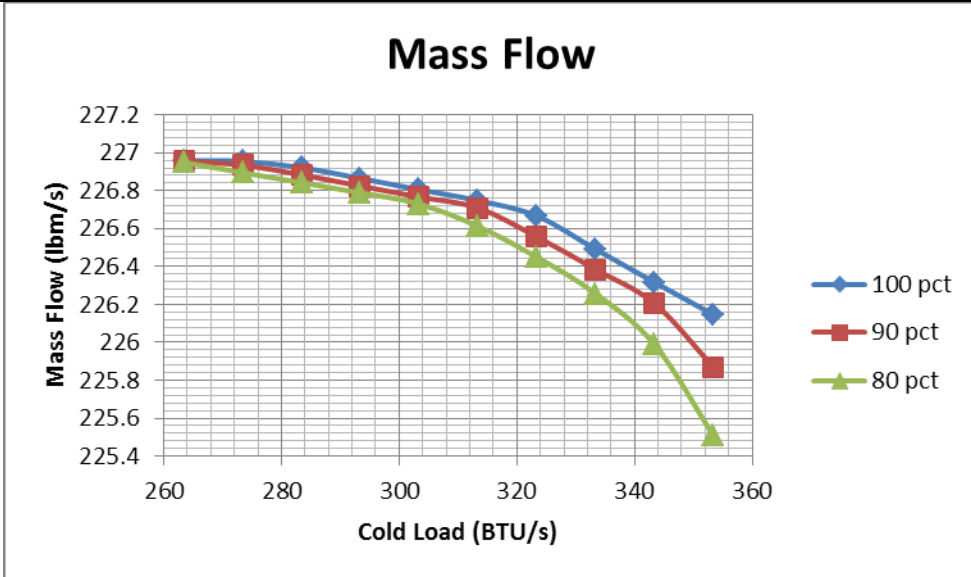


Figure 3.41 – FS_5 Massflow

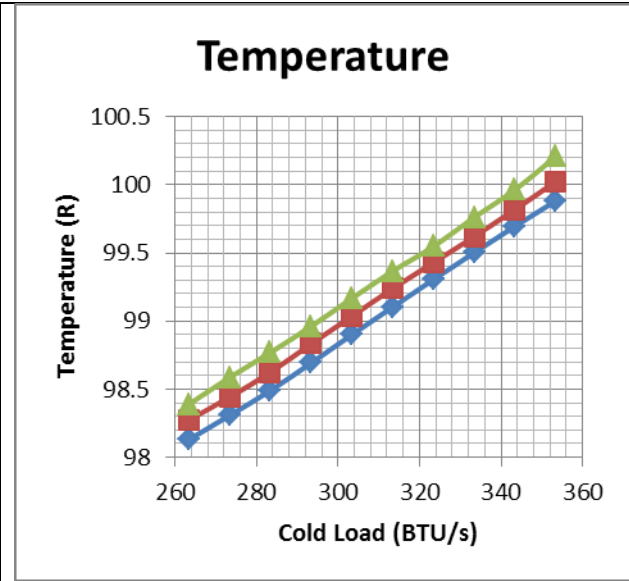


Figure 3.42 – FS_6 Temperature

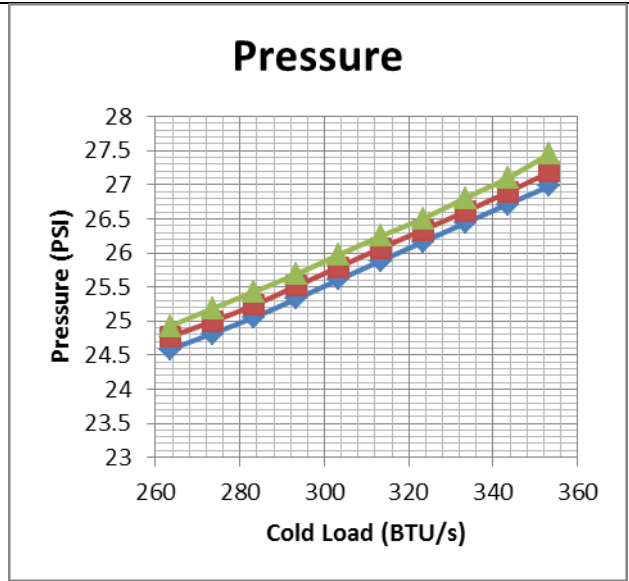


Figure 3.43 – FS_6 Pressure

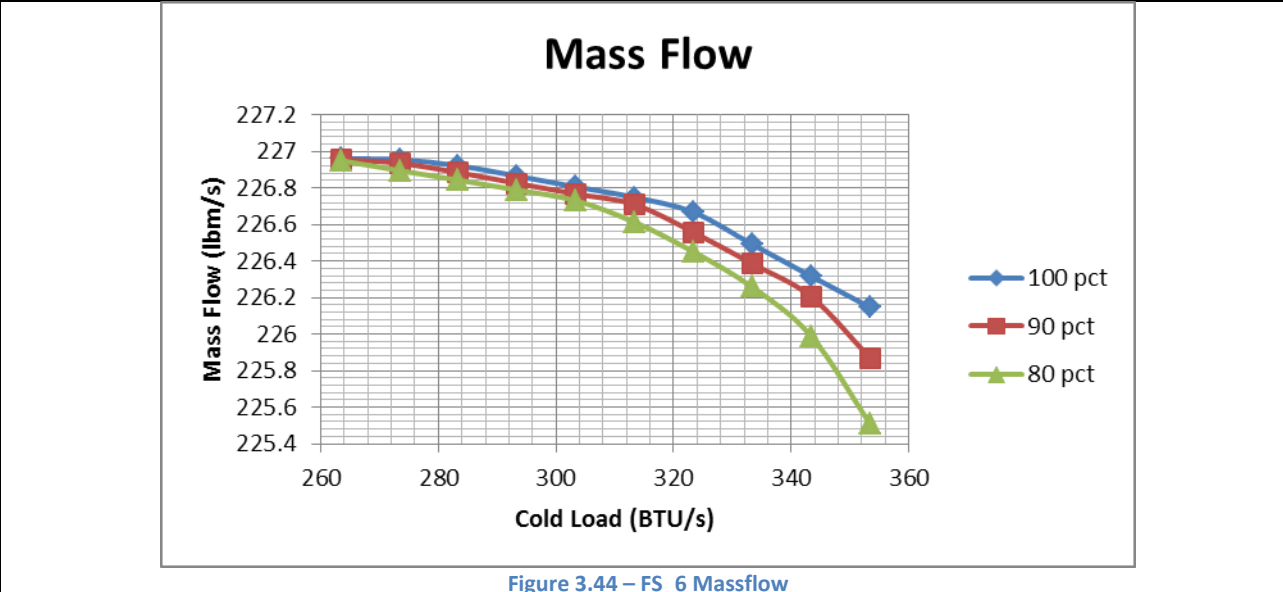


Figure 3.44 – FS_6 Massflow

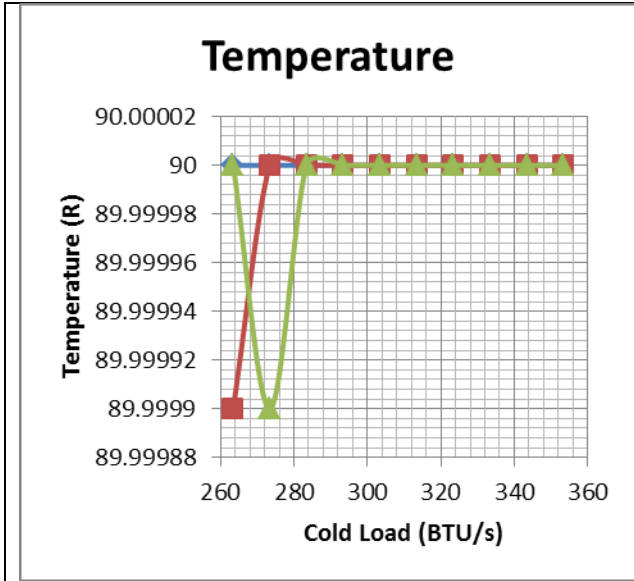


Figure 3.45 – FS_7 Temperature

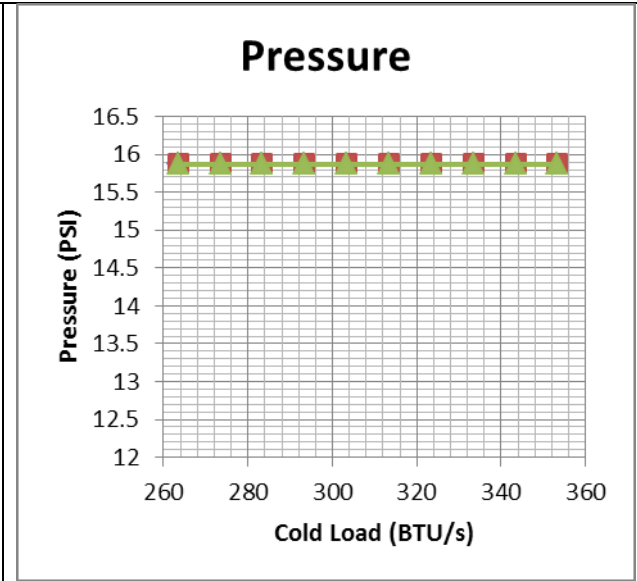


Figure 3.46 – FS_7 Pressure

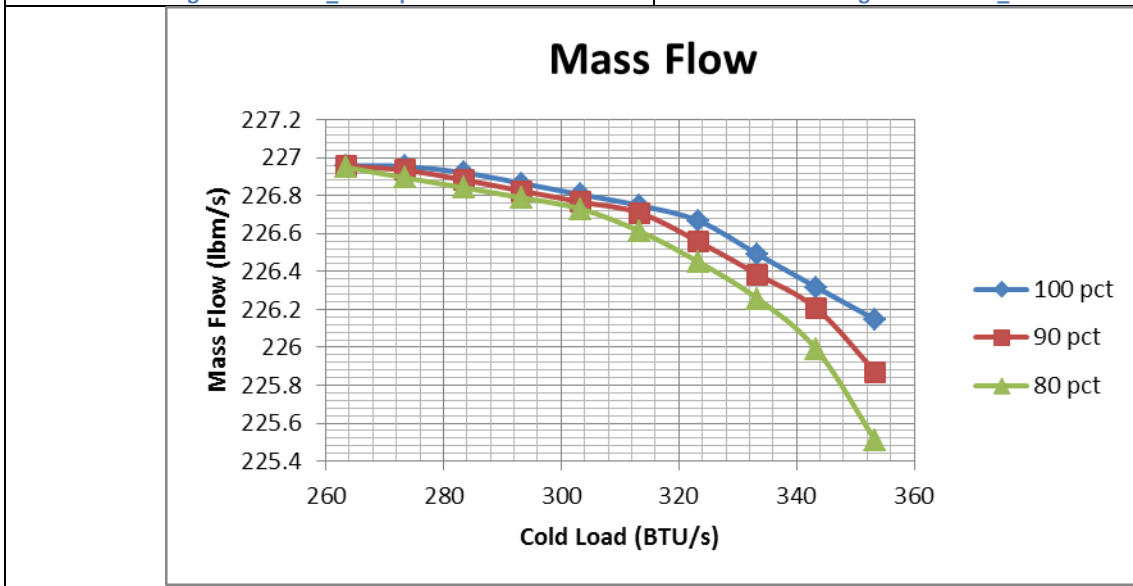


Figure 3.47 – FS_7 Massflow

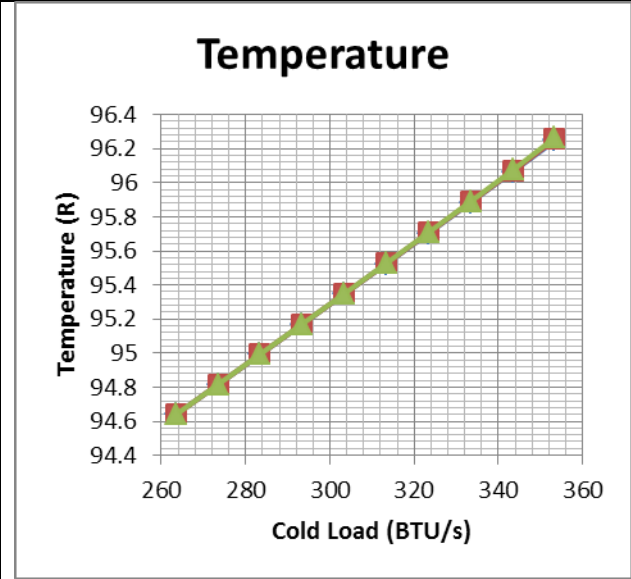


Figure 3.48 – RC_4 Temperature

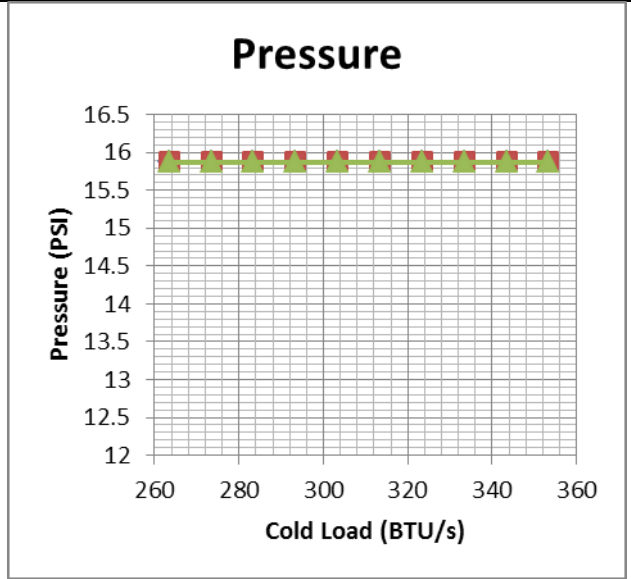


Figure 3.49 – RC_4 Pressure

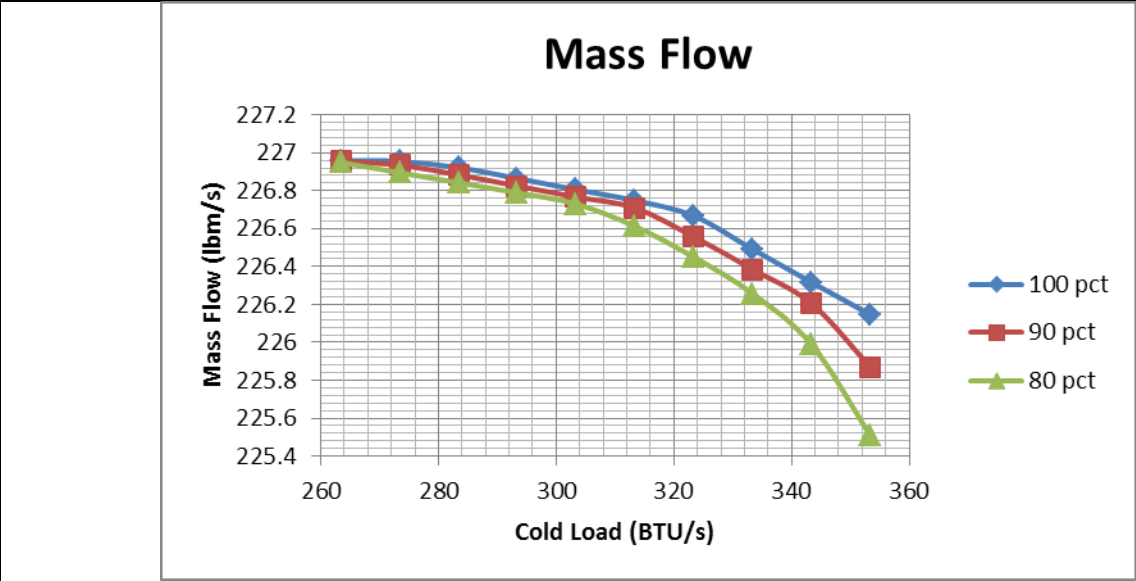


Figure 3.50 – RC_4 Massflow

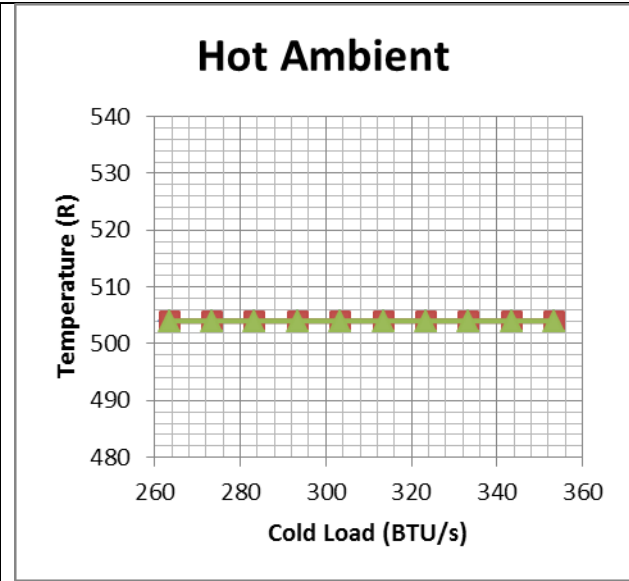


Figure 3.51 – HX_1 at HEX

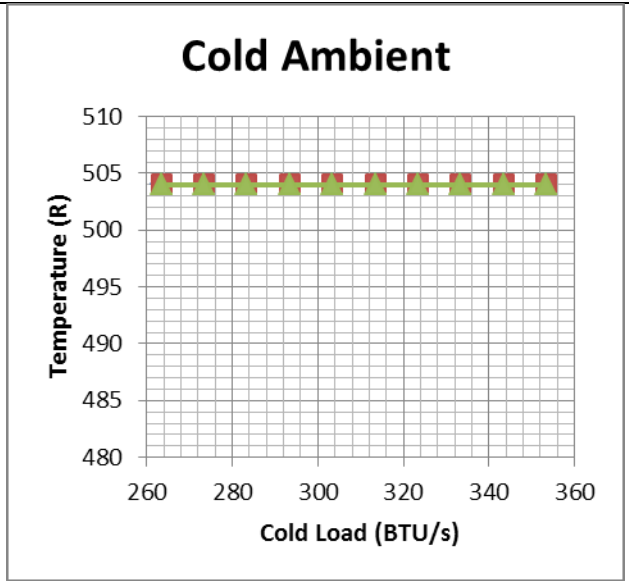


Figure 3.52 – CX_1 at CEX

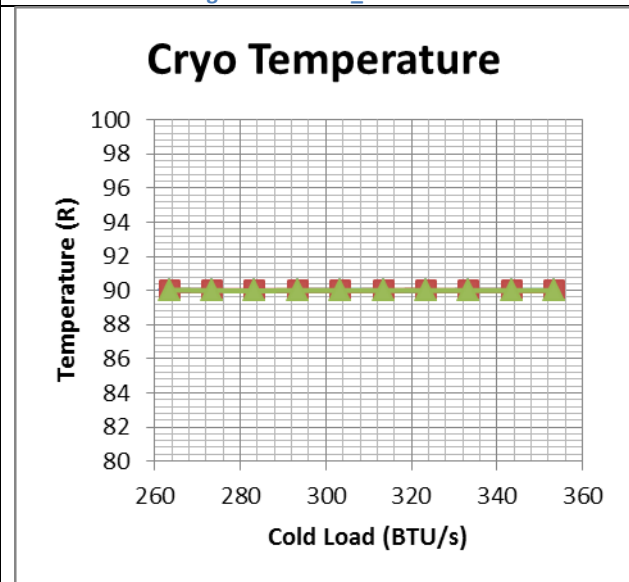


Figure 3.53 – CX_3 Heat Absorption

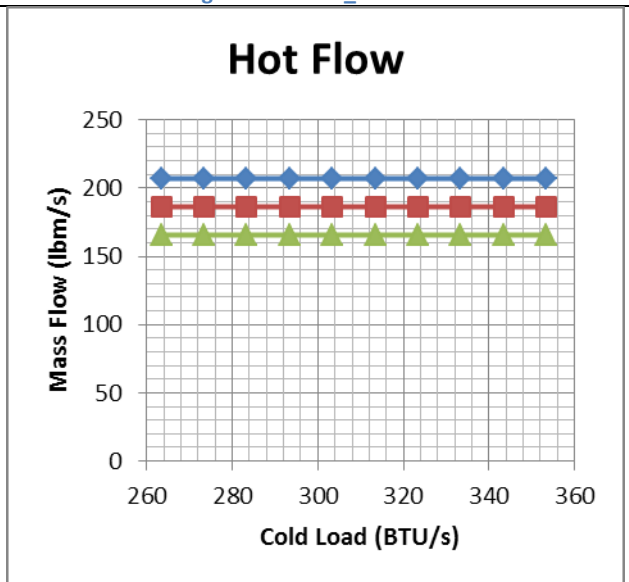


Figure 3.54 – HX_1 Across HEX

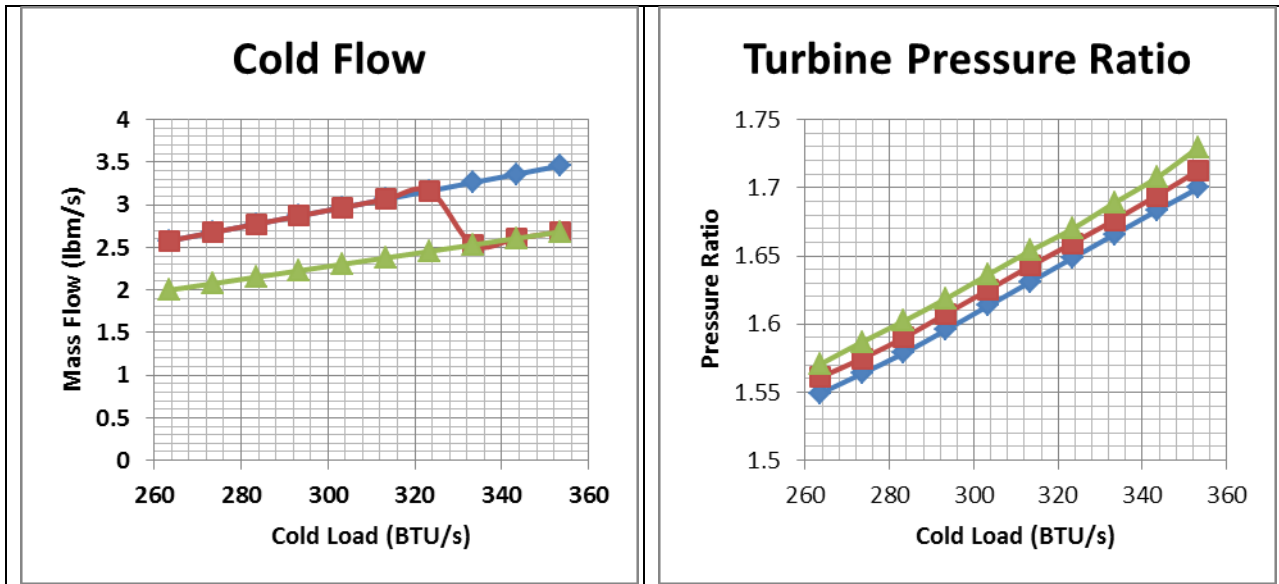


Figure 3.55 – CX_1 Across CEX

Figure 3.56 – Turbine Pressure Ratio

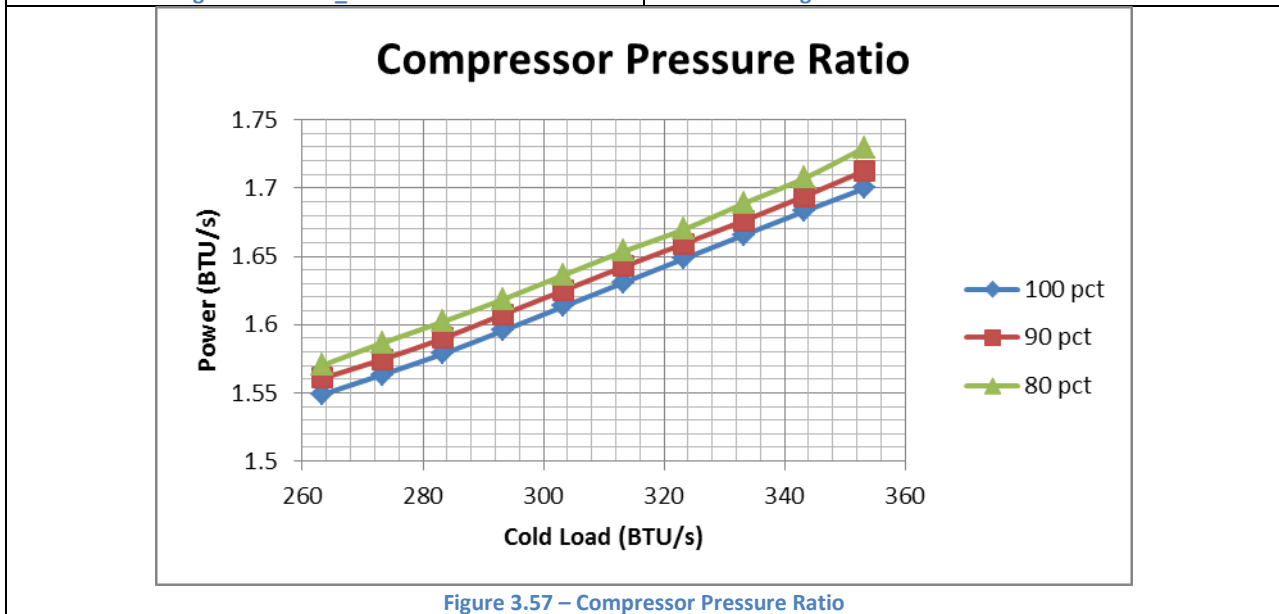


Figure 3.57 – Compressor Pressure Ratio

3.1.5 Generating High Speed Propeller Performance Map

3.1.5.1 Introduction

There is an increase of interest in civilian aircraft designs propelled by open rotors due to the increase in fuel prices as there was in 1980s (36). Open rotors have less fuel consumption compared to modern civilian jet engines. However, highly swept propellers are necessary to operate a typical jet engine powered civilian aircraft cruise Mach numbers. Although there were several projects (37; 38) which built prototypes in 1970s and 1980s, there is significantly less information on highly swept propellers compared to typical propellers. Therefore, higher order analysis capabilities are required to estimate open rotor performance at the conceptual and preliminary design phases.

Higher order analyses are computationally expensive and sometimes they are not available in the conceptual and preliminary design phases. Therefore, an approach for estimating open rotor performance with acceptable computational expense and accuracy is necessary for the conceptual and preliminary design.

To provide a method with acceptable computational expense and accuracy, this study aimed at generating a parametric propeller performance prediction based on empirical data on highly swept propellers. For this purpose, two attempts were made. The first one was repopulating the parametric propeller performance prediction charts for typical, low-speed propellers with highly swept propeller data. The first method is based on a NACA report (39). The second attempt was aimed at adjusting a family of propeller performance maps which were created for propellers designed in the same time frame with the highly swept propellers. The second method is based on a Hamilton-Standard (HS) report (40).

First, the validation process used for evaluating the methods is introduced. Then, the NACA method and how it was adjusted are explained. Later, the validation test results for this approach are presented. After covering the NACA method, the HS method is introduced and the validation test results for the HS method are discussed. Finally, the reason why the HS method was not updated with the highly swept propeller data as a third attempt is discussed.

3.1.5.2 Method Validation Process

As previously mentioned, two methods were tried to create an empirical parametric advanced propeller performance map, namely NACA and HS methods. In this section the validation process devised for these methods is explained. The following sections go over how these methods work, how they are applied, and their validation results in detail.

3.1.5.2.1 Validation Data and Range of Interest

Since the final goal of this research study is to develop an accurate and parametric method using empirical data to predict advanced counter-rotating propeller performance, F7A7 performance data (38) was chosen for validation. The validation data in terms of design and operational variables are given in Table 3.17.

Table 3.17 – F7A7 Design and Operational Variable Values

Design or Operational Variable	Value
Counter Rotating	Yes
Number of Rows	2
Number of Blades per Row	8
Blade Activity Factor (AF)	150
Integrated Design Lift Coefficient (CLi)	0.4
Mach Number	0.24 – 0.80
Pitch Angle (β)	37.9 – 63
Advance Ratio (J)	0.85 – 4.1

The C_{PQA} vs. advance ratio map for F7A7 is shown in Figure 3.58.

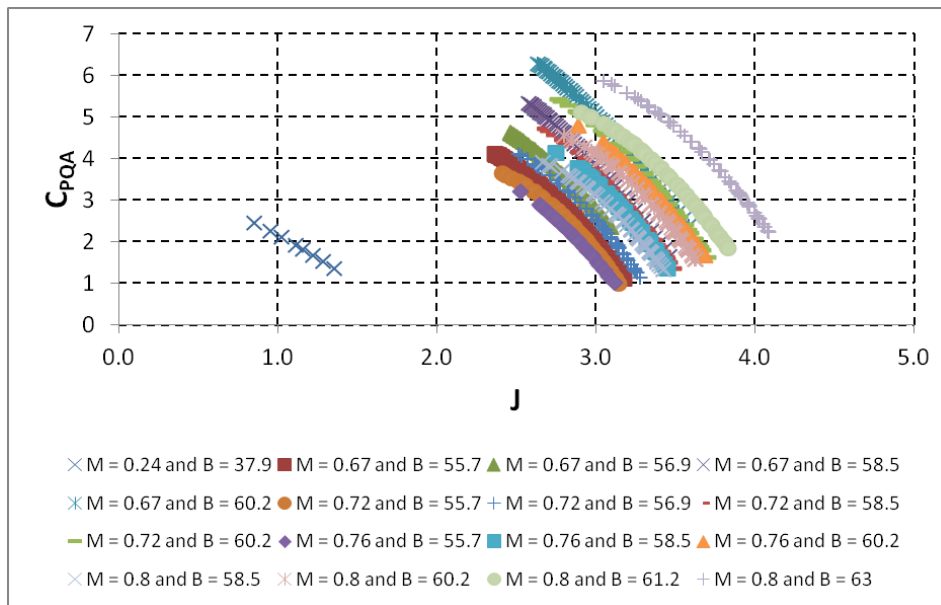


Figure 3.58 – F7A7 C_{PQA} vs. Advance Ratio Map

Figure 3.59 shows the other aspect of performance, namely efficiency.

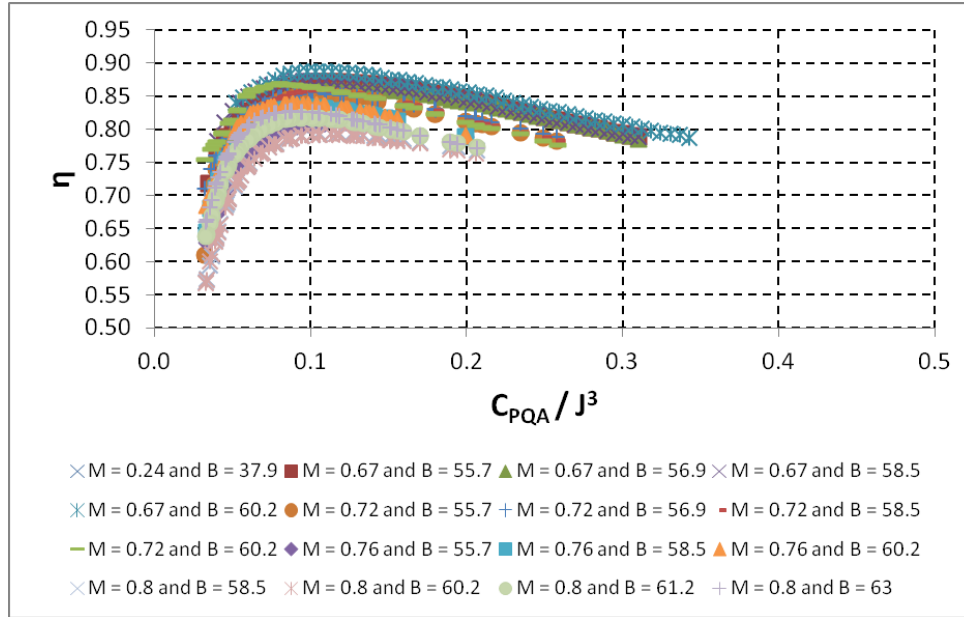


Figure 3.59 – F7A7 Efficiency vs. C_{PQA} / J^3 Map

An ideal parametric performance prediction method should predict all of the validation data with acceptable accuracy. However, acceptable accuracy in a certain portion of the validation data is more important than other portions. For high speed propellers, this more important portion of the data corresponds to the advance ratio range between 2 and 3 which correspond to cruise conditions. This portion covers most of the operational envelope, such as cruise and the efficiency which is highest in this region. In other words, since the efficiency peaks in this region, most of the operation must be in this region for economic viability.

After Figure 3.58 and Figure 3.59 which show the performance in the whole data range, it is necessary to zoom in on the region in which the advance ratio is between 2 and 3 to observe the behavior of the validation data in the most important portion. Figure 3.60 presents the C_{PQA} vs. advance ratio behavior.

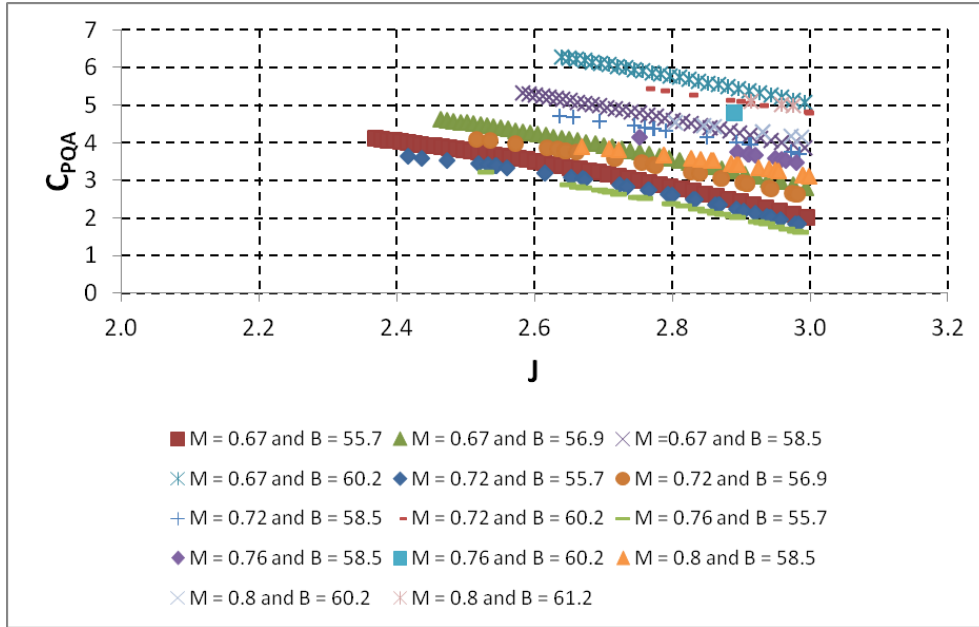


Figure 3.60 – F7A7 C_{PQA} vs. Advance Ratio for $2 \leq J \leq 3$

Initially, Figure 3.60 shows that two pitch angle values, namely 37.9° and 63° do not have any points where the advance ratio is between 2 and 3. As it is shown in Figure 3.58, the curves shift upper right as the pitch angle value increases. Furthermore, the curves shift lower left as the Mach number increases at constant pitch angle value. However, all of the pitch angle values in Figure 3.60 except 61.2° have several curves because of experiments conducted at several Mach numbers. Figure 3.60 shows C_{PQA} whereas Figure 3.61 shows efficiency.

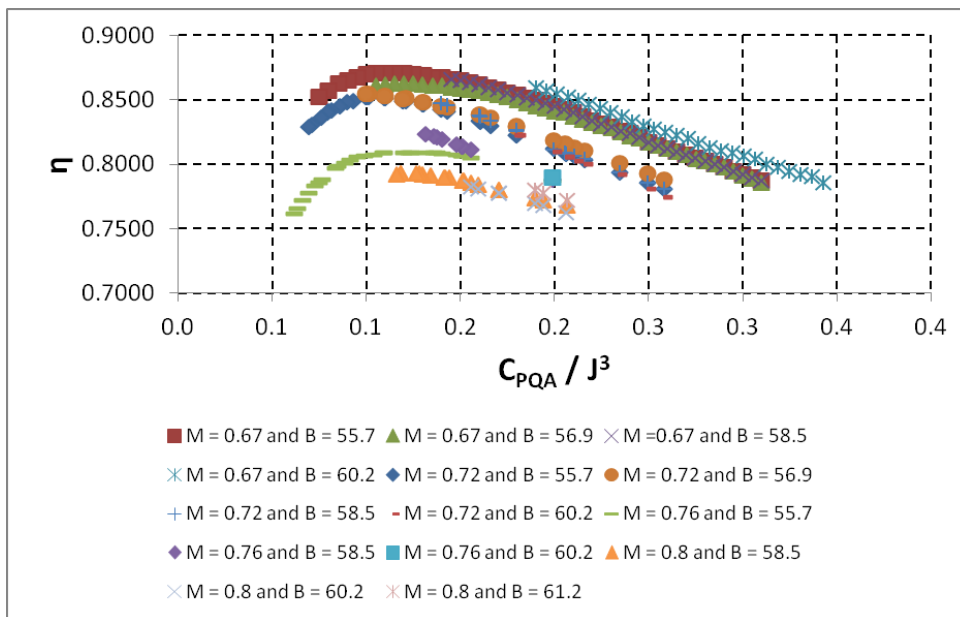


Figure 3.61 – F7A7 Efficiency vs. C_{PQA} / J^3 for $2 \leq J \leq 3$

3.1.5.2.1.1 Relation between C_P and C_{PQA}

For the reader's reference, it is necessary to derive the relation between C_{PQA} and C_P . Generally, propeller performance is shown in terms of C_P or power coefficient. However, here C_{PQA} is used to follow the convention in the source document (38). The relation between C_P and C_{PQA} can be derived as follows and is given in Equation 3.66.

$$C_P = \frac{P}{\rho(nD)^3 D^2} \text{ and } C_{PQA} = \frac{P}{\rho(nD)^3 A}$$

$$\text{whereas } A = \frac{\pi D^2}{4} \text{ then}$$

$$C_{PQA} = \frac{4}{\pi} \cdot C_P$$

Equation 3.66 Relation between C_{PQA} and C_P

Generally, methods for predicting propeller performance parametrically use power coefficient instead of C_{PQA} . The result of the prediction method is corrected based on the relation in Equation 3.66 before the validation test.

3.1.5.2.2 Acceptable Level of Error for the Validation Test

All models have errors when compared with the actual data. However, models which have acceptable level of error for the purpose in mind are useful. The problem is how to determine the acceptable level of error for the given task. Determining the acceptable error is a heuristic process.

In this study the goal is to model the on-design and off-design performance of an advanced propeller parametrically and accurately. Although there is not a standard or recommended practice about the acceptable error for the goal of this study, a recommend practice for a more challenging application can be used to err on the side of caution. For this purpose, a recommended practice for gas turbine engine real-time steady state modeling (41) can be used. The acceptable error for real-time gas turbine engine steady state model is $\pm 2\%$.

3.1.5.3 NACA Method for Parametric Propeller Performance Estimation

The NACA method (39) depends on correcting the ideal propeller efficiency computed using the actuator disk theorem for blade number adjustment, compressibility effects, and counter-rotation if applicable. This approach is for constant speed propellers. Therefore, the propeller operation is always at peak efficiency conditions by changing the pitch angle appropriately. The constant speed operation concept is shown in Figure 3.62. The NACA method predicts only the efficiency since the pitch angle is not handled explicitly to predict the power coefficient (C_P). The main formulation of the approach is given in Equation 3.67.

$$\eta = \eta_i \eta_o \text{ where } \eta_i = \eta'_i + \Delta\eta_i + 0.6 \frac{E_r}{P}$$

Equation 3.67 NACA Propeller Efficiency Prediction Model

η_i is the adjusted induced efficiency and η'_i is the ideal efficiency computed from the actuator disk theorem. On the other hand, $\Delta\eta_i$ is the adjustment for the number of blades and blade activity factor, in other words how the blade thickness is distributed along the blade radius. Because actuator disk theorem does not account for the effect of the blades, the efficiency prediction has to be adjusted for that effect. η_o is the variation in peak efficiency with Mach number, in other words compressibility correction. Finally, E_r / P is the fractional energy loss due to slipstream rotation. Based on experience (39) 60% of the slipstream energy loss can be recovered with counter-rotation.

NACA approach does not account for the blade camber effect, in other words the integrated design lift coefficient (C_{Li}). Integrated design lift coefficient and activity factor are the most important propeller design variables. Since NACA method does not take into account the effect of the integrated design lift coefficient, the validation process was adjusted to observe if the integrated design lift coefficient could be neglected as NACA method suggests.

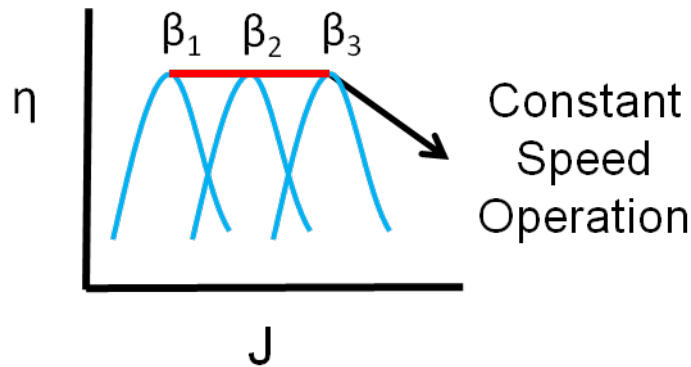


Figure 3.62 – Constant Speed Propeller Operation

After the brief introduction of the NACA method, it is necessary to introduce how each effect is accounted for in greater detail. Before covering the effects and corrections one by one, the method to calculate ideal efficiency based on actuator disk theory will be reiterated for reader's reference. Then, the correction for the blade number and AF is discussed. Later, the variation of peak profile efficiency with Mach number is covered. After that, the counter-rotation effect is accounted for and presented. After discussing the corrections, modifications to the NACA method are discussed. Finally, the validation results for the adjusted NACA method are provided.

3.1.5.3.1 Ideal Propeller Efficiency based on Actuator Disk Theorem

For the reference of the reader, the ideal efficiency (42) of a propeller based on the actuator disk theorem is given in Equation 3.68.

$$\frac{\eta'_i}{(1 - \eta'_i)^{1/3}} = \left(\frac{\pi}{3}\right)^{1/3} \left(\frac{J}{C_P^{1/3}}\right)$$

Equation 3.68 Actuator Disk Theory Ideal Efficiency

The equation above is an implicit nonlinear equation. Therefore, nonlinear Richardson iteration with over-relaxation was used to ensure numerical solution stability at every operating condition.

3.1.5.3.2 Blade Geometry Correction

As it can be seen in Equation 3.68, the actuator disk theorem does not account for the blade number and geometry. Therefore, corrections are necessary. For this purpose NACA method has the chart given in Figure 3.63.

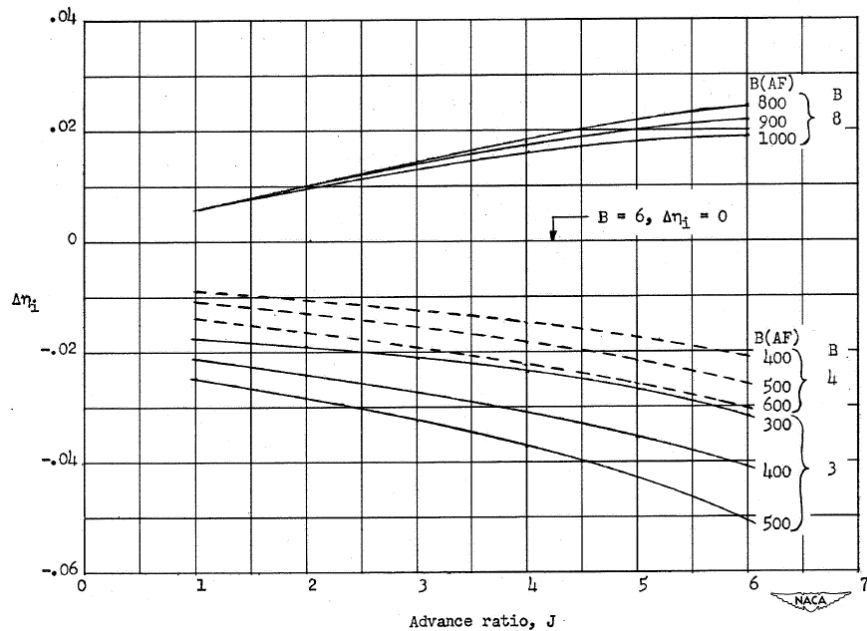


Figure 3.63 – NACA Method Correction for Blade Number and Geometry (39)

Figure 3.63 shows how the geometry correction changes as a function of advance ratio and total activity factor (blade number multiplied by the blade activity factor). Although this correction is for blade geometry, it doesn't account for the camber effect as mentioned before. The six bladed propeller is set as the baseline and the other blade numbers are drawn with respect to the six bladed propeller. The range of blade activity factor in this figure is between

100 and 125 for an eight bladed propeller. If Figure 3.63 is used as is, the predictions for the validation data is extrapolated. Furthermore, each line in this figure is for constant speed operation at the design speed. Values read from this chart are added to the ideal propeller efficiency as the blade geometry correction.

3.1.5.3.3 Compressibility Correction

After the blade geometry effects are accounted for, it is necessary to consider compressibility effects on the propeller performance at high Mach numbers. For that purpose the NACA method uses another chart which shows how the peak efficiency varies with the Mach number. This chart is provided in Figure 3.64.

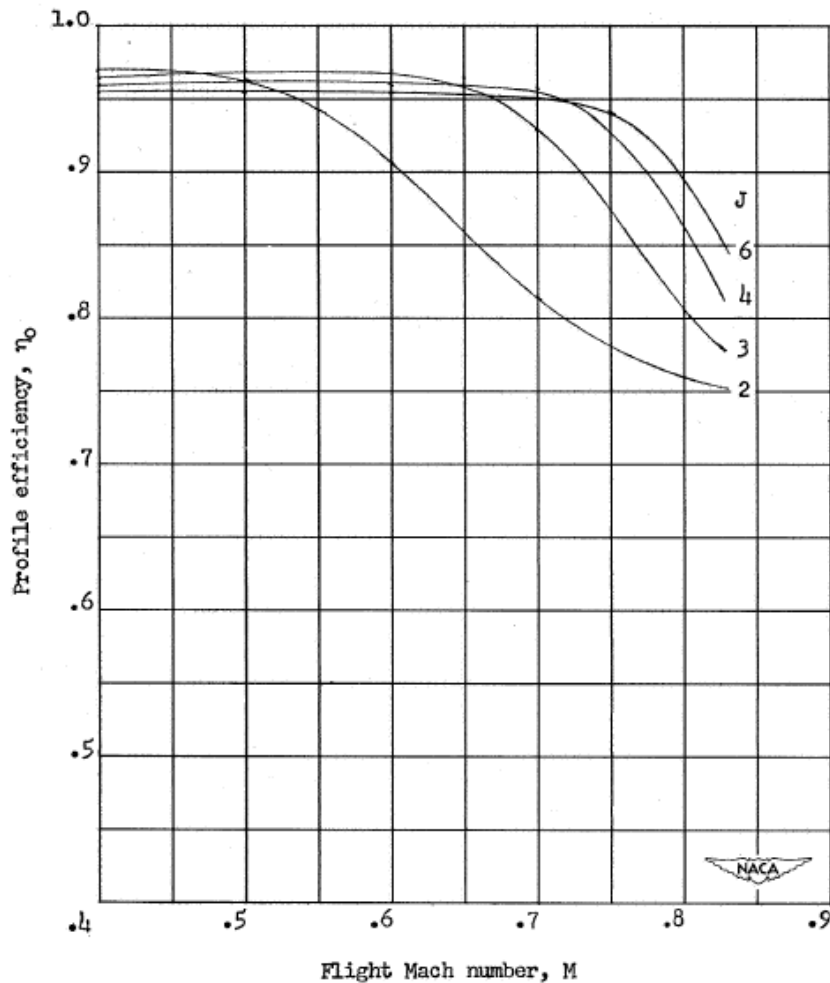


Figure 3.64 – NACA Method Compressibility Correction (39)

In Figure 3.64 the variation in the peak efficiency is a function of Mach number and advance ratio. Constant advance ratio curves are loci of peak efficiencies as a function of the Mach

number. The correction from Figure 3.64 is used as a multiplier on the ideal efficiency corrected for blade geometry and counter-rotation.

3.1.5.3.4 Counter-Rotation Effect

The last effect to account for is the counter-rotation effect. The NACA method captures this effect with another provided chart. As mentioned before, the counter-rotation effect is captured by estimating the amount of recovered energy loss due to slipstream rotation. Figure 3.65 shows how the fractional energy loss due to slipstream rotation changes as a function of total activity factor and advance ratio.

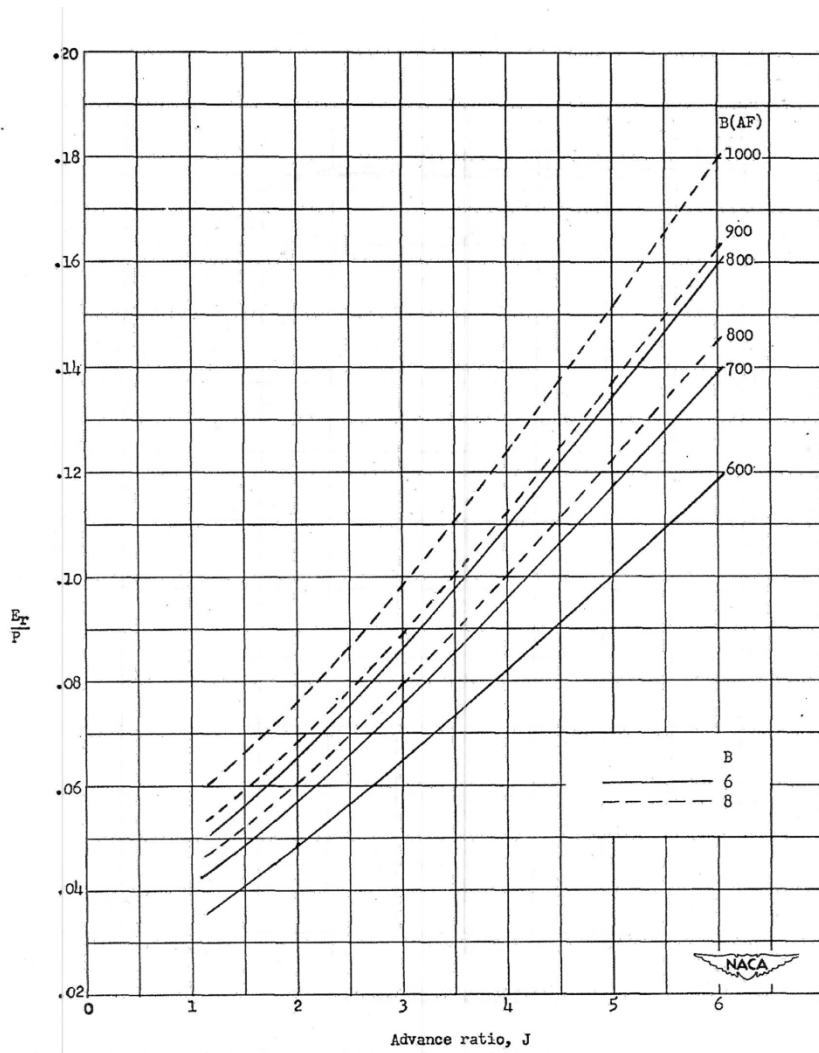


Figure 3.65 – NACA Method Counter-Rotation Correction (39)

Figure 3.65 is for six and eight bladed propellers and the blade activity factor range is again between 100 and 125. Therefore, if this chart is used as is, the predictions for the validation data are extrapolations. The values read from this chart is multiplied by 0.6 (39) and added to the propeller efficiency.

The original NACA method was developed in 1940s and 1950s. However, F7A7 used for the validation test was designed in 1980s. Therefore, the charts in the original NACA method must be updated to predict the performance changes due to the significantly different designs with acceptable accuracy. The data necessary to repopulate the NACA charts were gathered from the reports of Advanced Turboprop Project (ATP) (37). In ATP different highly swept propellers were designed and tested from 1970s to 1980s. After covering all of the corrections in the original NACA method, the NACA method adjustments to account for ATP data is discussed next.

3.1.5.3.5 The Adjusted NACA Method

As previously mentioned, the original NACA charts must be repopulated with more modern data to reproduce high speed propeller performance. For that purpose data from the ATP were used. In ATP several highly swept propellers were designed, built, and tested. These propellers (37; 43; 44) were SR-1, SR-2, SR-3, SR-5, SR-6, SR-7L and SR-7A. SR-2 (45) was an unswept propeller. Therefore, the data for SR-2 were discarded. Performance data for SR-5 and SR-6 were not found during the literature review. SR-7A (44) is a 2/9 scale model of SR-7L built for acoustics test with very limited performance data in the literature. Therefore, data for SR-7A were also discarded.

The data for the remaining propellers, namely SR-1 (45; 46), SR-3 (47; 48; 49), and SR-7L (43; 50; 51; 52) were stored for updating the NACA charts. When all of the NACA charts are considered, the available data can only be used to repopulate the blade geometry correction and the compressibility correction charts. In other words, the counter-rotation chart is used as is for the adjusted NACA and HS methods although it must be extrapolated. Finally, NACA approach does not account for blade camber effects as mentioned several times before.

Before using all of the data for populating the charts, it was necessary to test the accuracy of neglecting the integrated design lift coefficient effect on the performance. If this assumption is incorrect, then the method fails the validation test before any further investigation. Therefore, two data sets, namely SR-1 and SR-3 were selected. Because SR-1 and SR-3 have one row of blades, the accuracy of the assumption can be tested without introducing the extrapolation error for the counter-rotation. Only SR-1 data were used to repopulate the charts and SR-3 chart were used for validation of the assumption.

3.1.5.3.6 Updating Compressibility Correction

As was shown in Equation 3.67, the compressibility correction is used as a multiplier on the ideal efficiency after being corrected for blade geometry and counter-rotation. Therefore, the compressibility correction has a significant effect on the accuracy. As a result, it is updated first. The blade geometry correction is updated later based on difference between the SR-1 data and the efficiency prediction only corrected for compressibility effects.

To generate the compressibility effect curves, the peak efficiencies for all Mach number and pitch angle combinations were used. These points are given in Figure 3.66 and Figure 3.67. These figures show that efficiency goes down as the Mach number increases as expected. Also, higher Mach number values correspond to higher pitch angle and advance ratio values. At these points the compressibility correction was determined to minimize the difference between experimental SR-1 efficiency and the ideal efficiency.

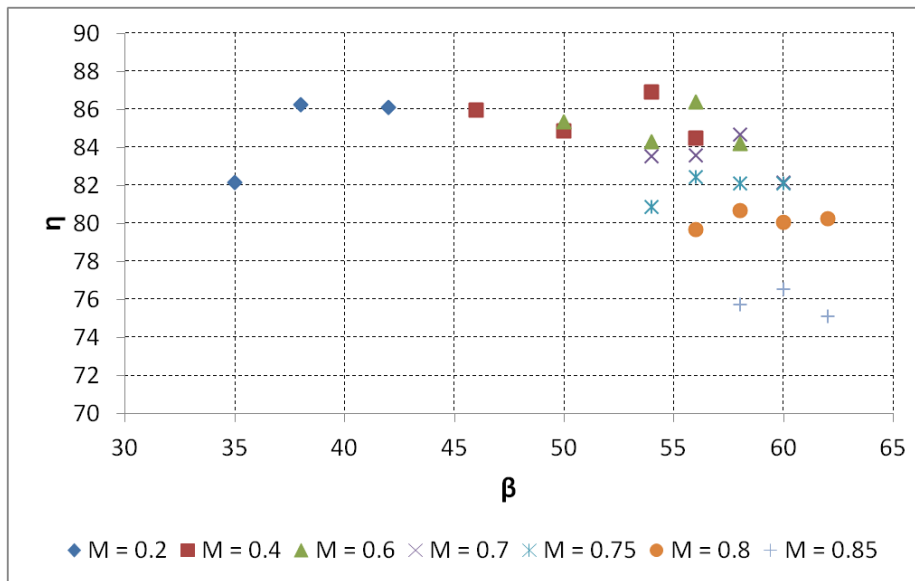


Figure 3.66 – SR-1 Peak Efficiency Points based on Pitch Angle

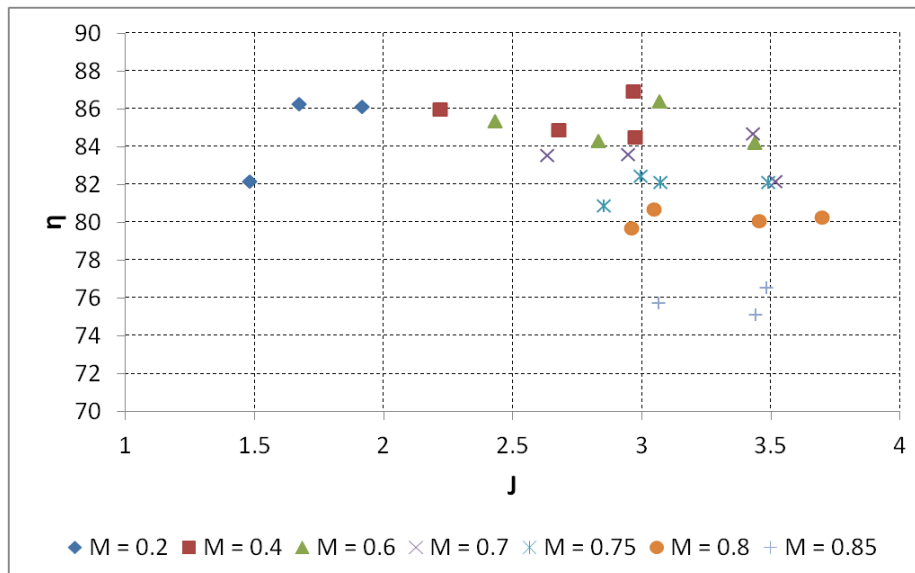


Figure 3.67 – SR-1 Peak Efficiency Points based on Advance Ratio

In Figure 3.67 it can be seen that there are few points in the low advance ratio values. Thus, generating the compressibility correction curves for relatively low advance ratio values were

harder compared to relatively higher advance ratio values. Using close data points the compressibility correction curves were created to minimize the difference between the ideal efficiency and the measured efficiency. The generated compressibility correction curves are shown in Figure 3.68.

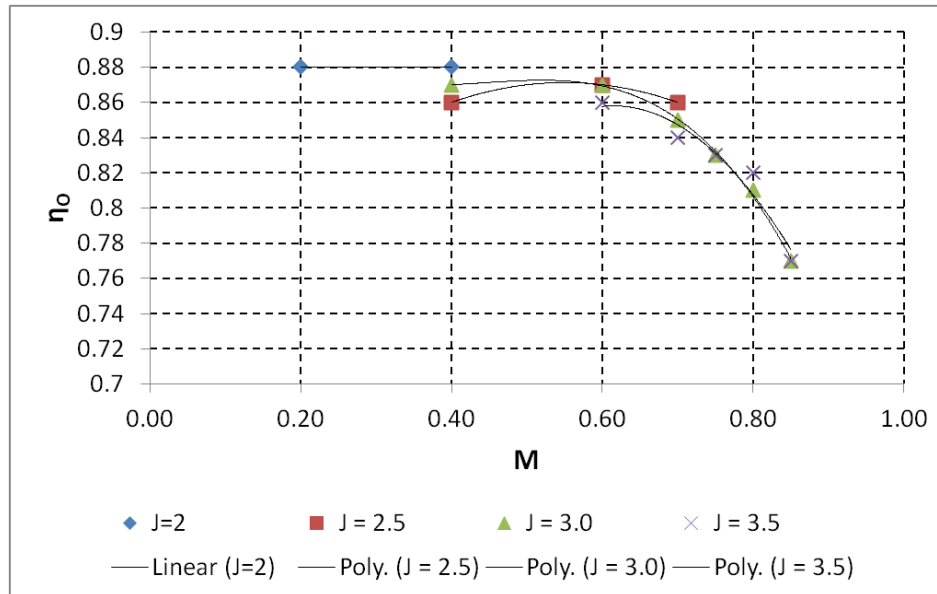


Figure 3.68 – Repopulated Compressibility Correction Chart based on SR-1 Data

The compressibility correction is a function of the Mach number and advance ratio. As Figure 3.68 shows, the compressibility curves cover the advance ratio region between 2 and 3.5. Therefore, the compressibility correction can be used for the advance ratio values between two and three which constitutes the most important operational range as discussed before. However, curves for advance ratios lower than 2 and larger than 3.5 were not available.

3.1.5.3.7 Blade Geometry Correction

As was explained in the section about the original NACA method blade geometry correction, the blade geometry correction is plotted for a constant rotational speed for a given blade number and activity factor. Typically, the performance map data does not include the rotational speed. As mentioned before, a typical propeller performance map has Mach number, pitch angle, advance ratio, power coefficient, and efficiency. From these values the rotational speed must be derived to determine the blade geometry correction curve.

3.1.5.3.7.1 Creating the Blade Geometry Correction Curve

Since SR-1 data were used to create the adjusted NACA method and SR-3 data were used to validate it, the counter-rotation effect can be neglected. Therefore, the NACA efficiency prediction model takes the form given in Equation 3.69 for the blade geometry correction.

$$\eta = (\eta'_i + \Delta\eta_i)\eta_o \text{ then } \Delta\eta_i = (\eta - \eta'_i\eta_o)/\eta_o$$

Equation 3.69 Blade Geometry Correction Model

For the points at which the corrected rotational speed is about 1225 RPM, the blade geometry correction is computed using Equation 3.69. The first step of the computations was determining the compressibility correction for each of these points based on the chart provided before. Then, the ideal efficiency corrected for compressibility was subtracted from the measured efficiency at each of these points to get the blade geometry correction. The blade geometry correction is given in Figure 3.69.

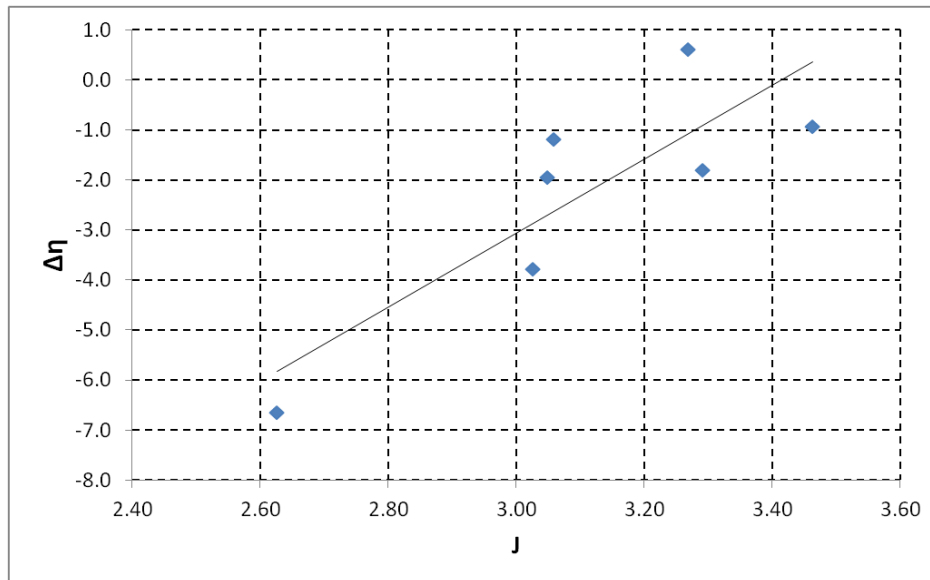


Figure 3.69 – Blade Geometry Correction based on SR-1 Data

After discussing how each of the corrections were updated based on SR-1 data for the adjusted NACA method, the results of the validation test based on SR-3 data is presented in the next section.

3.1.5.3.8 The Adjusted NACA Method Validation Test Results

For the adjusted NACA method validation test, SR-3 data between advance ratio values of two and three were used. For the sake of brevity, the results only at three Mach numbers are reported. These Mach numbers are 0.2, 0.6, and 0.75. The efficiency predicted at these Mach numbers as a function of pitch angle and advance ratio is compared with measured efficiencies. The predicted efficiency at Mach 0.2 and its percent error are given in Figure 3.70 and Figure 3.71.

Figure 3.70 shows that the adjusted NACA method fails to capture the trend in the SR-3 data and the error increases as the advance ratio increases. The increase in the error as the advance ratio increases is given in Figure 3.71. The percent error values are far from being acceptable.

At this point it is trivial that the adjusted NACA method failed the validation test. However, for the sake of completeness, the results at the other Mach numbers are also presented.

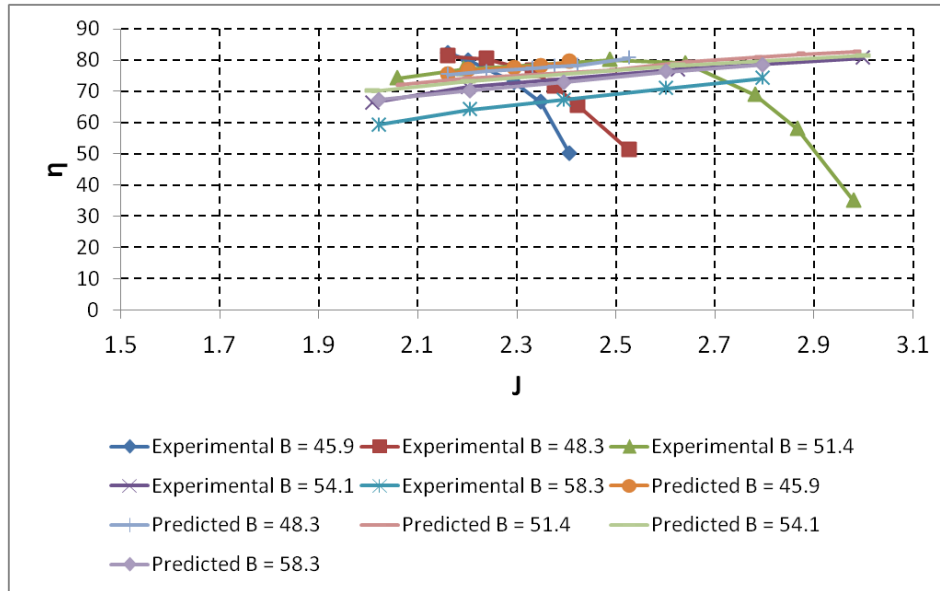


Figure 3.70 – Validation Test Efficiency vs. Advance Ratio for the Adjusted NACA Method at Mach 0.2

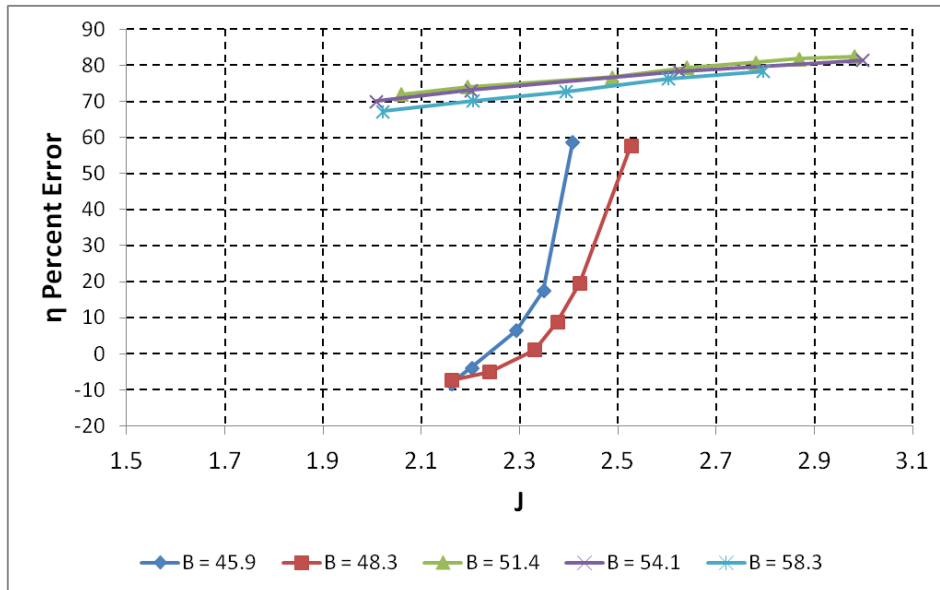


Figure 3.71 – Validation Test Efficiency Error for the Adjusted NACA Method at M=0.2

After Mach 0.2, the next Mach number is 0.6. The validation test results for this Mach number are given in Figure 3.72 and Figure 3.73. Figure 3.72 shows that the adjusted NACA method fails to capture the trends in most of the pitch angle values except 60.5°. This situation is similar to Mach 0.2. The divergence in error for 51.5° and unacceptable level of errors are given in Figure 3.73.

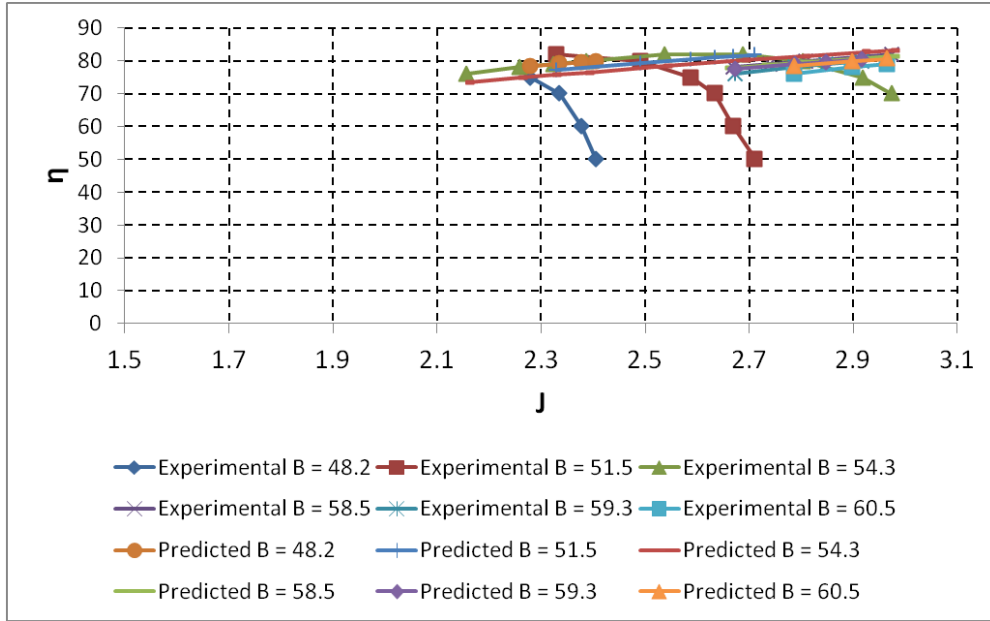


Figure 3.72 – Validation Test Efficiency vs. Advance Ratio for the Adjusted NACA Method at M=0.6

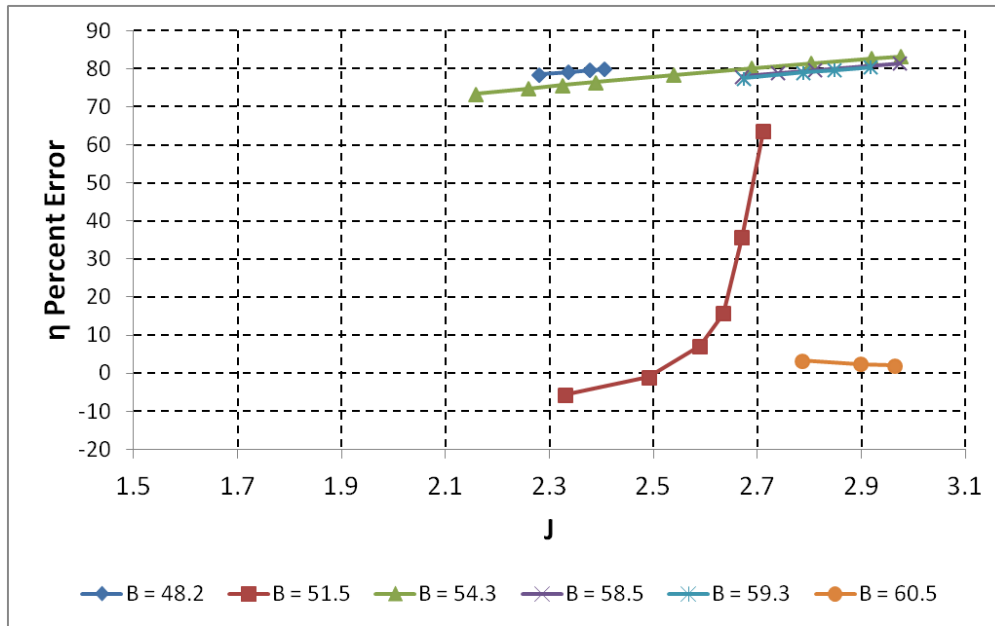


Figure 3.73 – Validation Test Efficiency Percent Error for the Adjusted NACA Method at M=0.6

The final Mach number for the validation test is 0.75. The results for this Mach number are shown in Figure 3.74 and Figure 3.75. Compared to the previous two cases, Figure 3.74 shows that the adjusted NACA method captured the trends in SR-3 data for Mach 0.75. Furthermore, it looks like the predicted efficiencies are off by a constant. The percent error values in Figure 3.75 also suggest that the accuracy was very close to $\pm 2\%$ limit and the prediction are almost off

by a constant. Moreover, the error does not diverge. Although the percent error is the best among the test results, predictions at Mach 0.75 are still unacceptable.

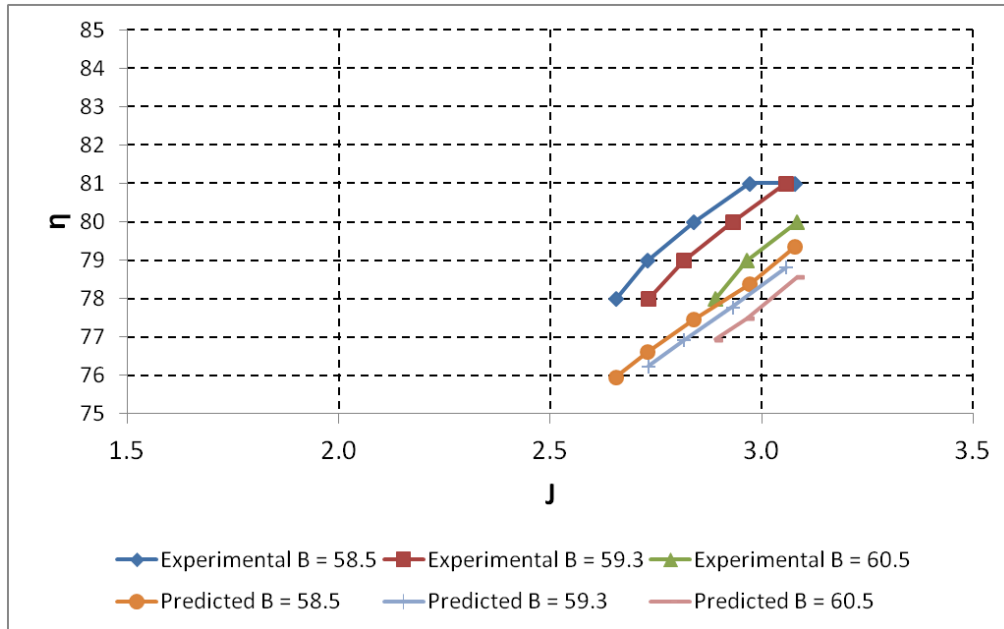


Figure 3.74 – Validation Test Efficiency vs. Advance Ratio for the Adjusted NACA Method at M=0.75

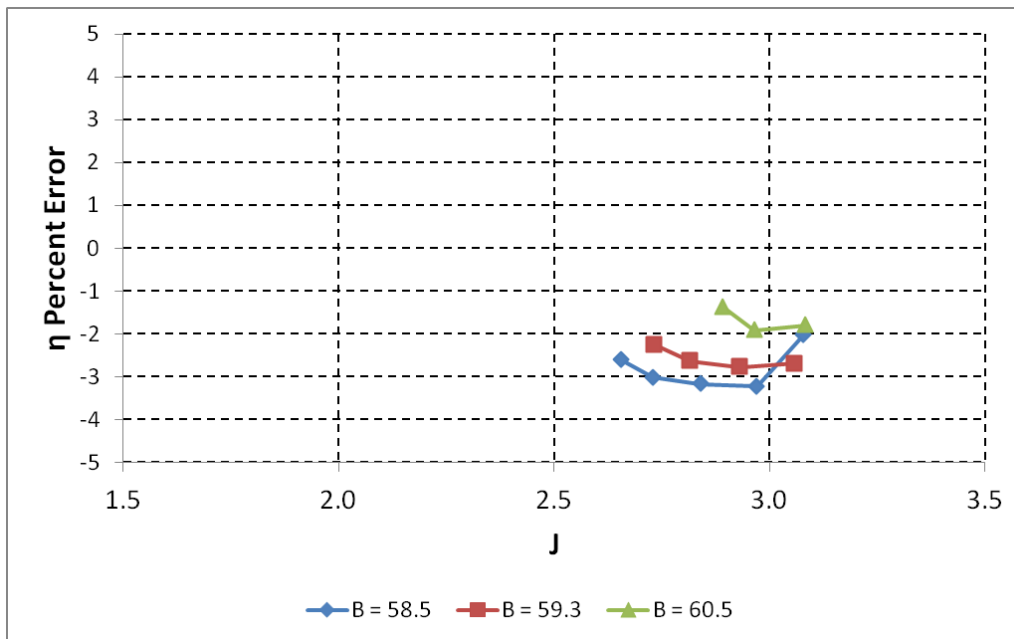


Figure 3.75 – Validation Test Efficiency Percent Error for the Adjusted NACA Method at M=0.75

Overall, it can be concluded that the adjusted NACA method failed the validation test although it managed to capture some of the trends at certain conditions.

3.1.5.4 Hamilton – Standard Method for Parametric Propeller Performance Estimation

The Hamilton – Standard (HS) method (40) is based on a collection of propeller performance maps for ranges of number of blades, activity factor (AF) and integrated design lift coefficient (C_{Li}). These maps are for high Mach number turboprops designed in the 1960s and early 1970s. The performance of a given propeller design is predicted using linear interpolation or extrapolation of the data available in the collection of propeller performance maps. The available ranges for the design variables are given in Table 3.18.

Table 3.18 – Hamilton – Standard Performance Maps Design Variable Ranges

Design Variable	Range
Number of Blades	3 and 4
Blade Activity Factor (AF)	80 – 220
Integrated Design Lift Coefficient (C_{Li})	0.150 – 0.700

As Table 3.18 shows the propeller performance maps available in HS method cover the validation data in terms of blade activity factor and integrated design lift coefficient. However, the HS method does not cover the validation data in terms of the number of blades and counter-rotation. Finally, HS method provides correction for compressibility effects.

3.1.5.4.1 Hamilton – Standard Method Steps

Each map in the HS method is for a given number of blades, blade activity factor, and integrated design lift coefficient. There are series of maps with different integrated design lift coefficients for a given blade number and blade activity factor. For each blade number there are a series of map groups with different blade activity factors. For the reader’s reference, one performance map for a propeller with a blade number of four, a blade activity factor of 140, and an integrated design lift coefficient of 0.3 is reproduced in Figure 3.76

Figure 3.76 shows a typical propeller performance map used in this method. The maps used for the application of this method are given in the appendices. The axes are power coefficient (CP) and advance ratio (J). Constant pitch angle curves and isoefficiency curves are plotted. From this map for given advance ratio and pitch angle values, it is possible to obtain the corresponding power coefficient and efficiency values.

When the given design is not one of the maps in the collection, linear interpolation or extrapolation is used to predict performance. This is done by interpolating on integrated design lift coefficient and activity factor for a given number of blades.

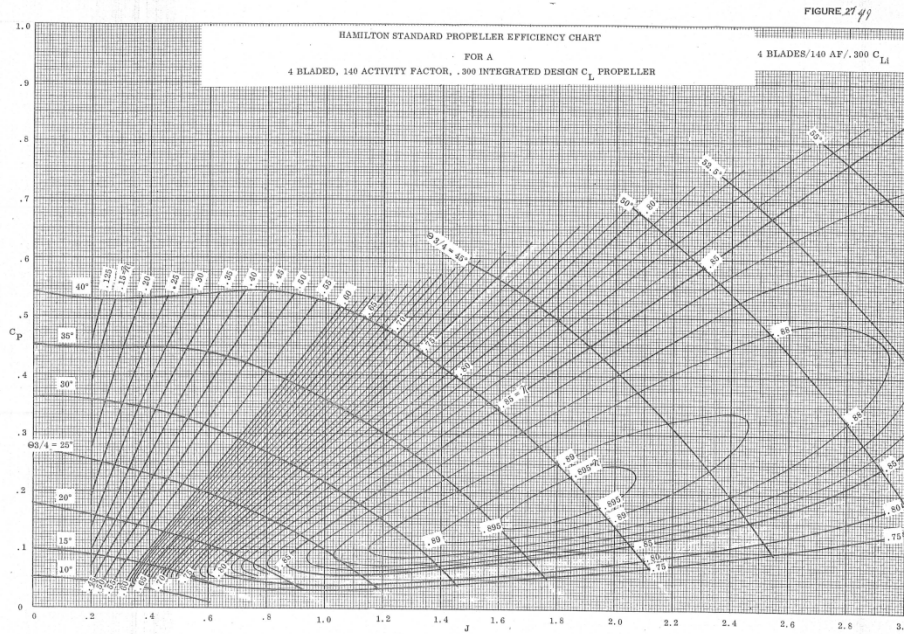


Figure 3.76 – Sample Hamilton – Standard Performance Map (40)

3.1.5.4.2 Adjusted Hamilton – Standard Method

As mentioned before, the original Hamilton – Standard method is for three and four blades, and single row propellers whereas the purpose of this study is to predict the performance of a counter-rotating propeller with eight blades per row. The difference between the number of blades per row and number of rows affect the power consumption of the propeller. On the other hand, having multiple rows affect the propulsive efficiency of the propeller. These effects must be accounted for accurate performance predictions.

In this subsection of the report each of these effects are accounted for is discussed. First, the difference in the number of blades and rows is addressed and explained. Second, the compressibility effects are discussed. Third and last, the effect of the counter-rotation on efficiency is captured is presented.

3.1.5.4.2.1 Power Coefficient Corrections

The original HS method is for three and four blades whereas F7A7 has eight blades in each row. This difference in blade number causes a change in power coefficient for the same operating conditions as expected. Although there are nonlinear effects on power consumption due to the interaction between blades when the number of blades increases, the only possible way of accounting for this effect in an empirical approach is to multiply the power coefficient by the ratio of the blade numbers. For instance, if the maps for four blades are used, then the power coefficient values are multiplied by two to match the eight bladed case.

In summary, only maps for four bladed propellers in the original HS method were used instead of the three bladed ones because F7A7 has eight blades in each row. Moreover, the power coefficient values in these maps were multiplied by two to account for the difference in the number of blades per row. Then, they were multiplied by two to capture the difference in the number of rows. Finally, they were multiplied by $(4 / \pi)$ to convert power coefficient values into C_{PQA} values.

3.1.5.4.2.2 Compressibility Corrections

The original HS method has correction for compressibility effects. This correction was used exactly in the adjusted HS method for this study. The correction is based on Mach number and the Mach number correction for the effect of blade camber. Figure 3.77 shows the general compressibility correction.

The general compressibility correction is a multiplier for the efficiency value read from the maps as given in Equation 3.70. It is a function of the effective Mach number and advance ratio. Effective Mach number is the flight Mach number corrected for the blade camber. Figure 3.78 gives the Mach number correction for the blade camber.

The blade camber correction for the Mach number is added to the flight Mach number. The camber correction is a function of the integrated design lift coefficient. As the integrated design lift coefficient increases (camber increases), the compressibility loss increases.

$$\eta_{Corrected} = \eta_{Map} \times F_t$$

Equation 3.70 Hamilton – Standard Compressibility Correction

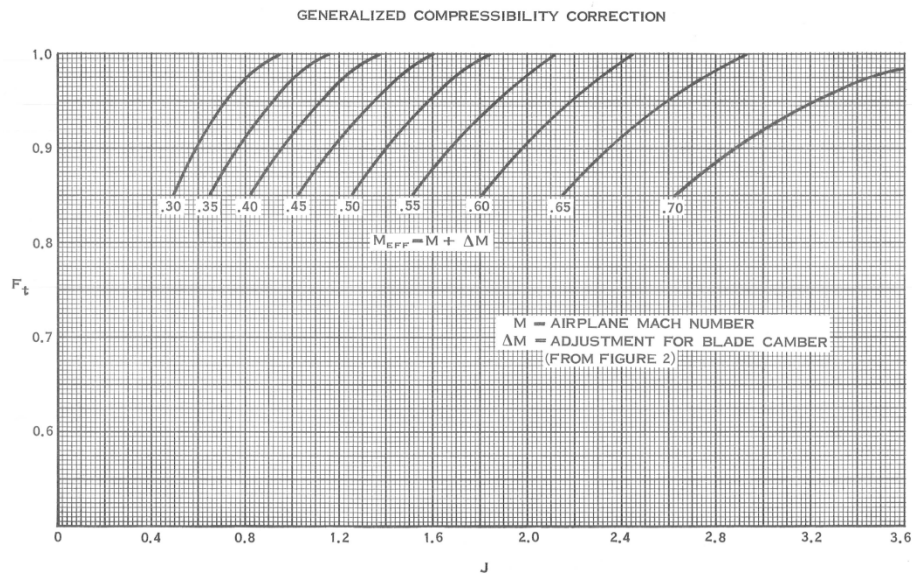


Figure 3.77 – Hamilton – Standard General Compressibility Correction (40)

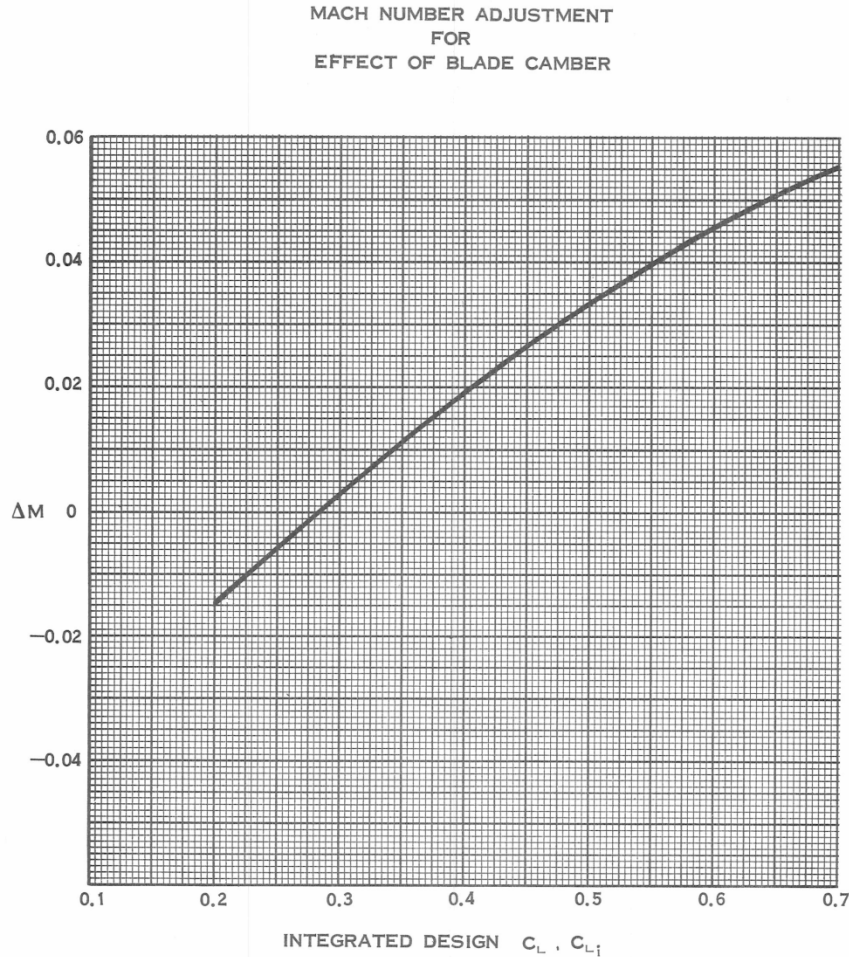


Figure 3.78 – Hamilton – Standard Mach Number Adjustment for Blade Camber (40)

3.1.5.4.2.3 Counter-Rotation Effect

Counter-rotation effects in the HS method were included using the same approach as the NACA method (39). The effects of counter-rotation were modeled as recovery of the fractional energy loss due to rotation of slipstream. A fraction of the energy loss was added to the compressibility corrected efficiency. Experience showed that 60% of the loss can be recovered (39). Because the fractional energy loss chart for NACA method was used here, the chart was extrapolated linearly due to blade activity factor values as was the case for NACA method. The chart was provided in the NACA section of this report. When all of the effects are accounted for, the efficiency prediction can be formulated as in Equation 3.71.

$$\eta = \eta_{Corrected} + 0.6 \cdot \frac{E_r}{P} = \eta_{Map} \cdot F_t + 0.6 \cdot \frac{E_r}{P}$$

Equation 3.71 Adjusted Hamilton – Standard Method Efficiency Prediction Model

3.1.5.4.2.4 Adjusted Linear Interpolation and Extrapolation Scheme

In the original HS method values from the closest four maps were interpolated or extrapolated for each given pitch angle and advance ratio. Instead of repeating this process for every pitch angle and advance ratio combination in the validation data, the common pitch angle and advance ratio combinations among the closest four maps were interpolated once to generate the estimated performance maps for F7A7. Pitch angle and advance ratio combinations in the estimated performance maps were chosen based on the most constraining map. In other words, if the combination does not exist in all of the maps, then that combination was not used for interpolation. The interpolation was based on F7A7 blade activity factor and integrated design lift coefficient. The design variables of the four propeller maps chosen for interpolation are given in Table 3.19.

Table 3.19 – Hamilton – Standard Performance Maps Selected for F7A7 Performance Estimation

Blade Number	Blade Activity Factor	Integrated Design Lift Coefficient
4	140	0.3
4	140	0.5
4	180	0.3
4	180	0.5

These maps were chosen because their design variables envelop F7A7 design variables, namely blade activity factor of 150 and integrated design lift coefficient of 0.4. Before the interpolation their power coefficient values were corrected for blade number and number of rows as explained in the power coefficient correction subsection. The interpolated C_{PQA} vs. advance ratio map for F7A7 is shown in Figure 3.79.

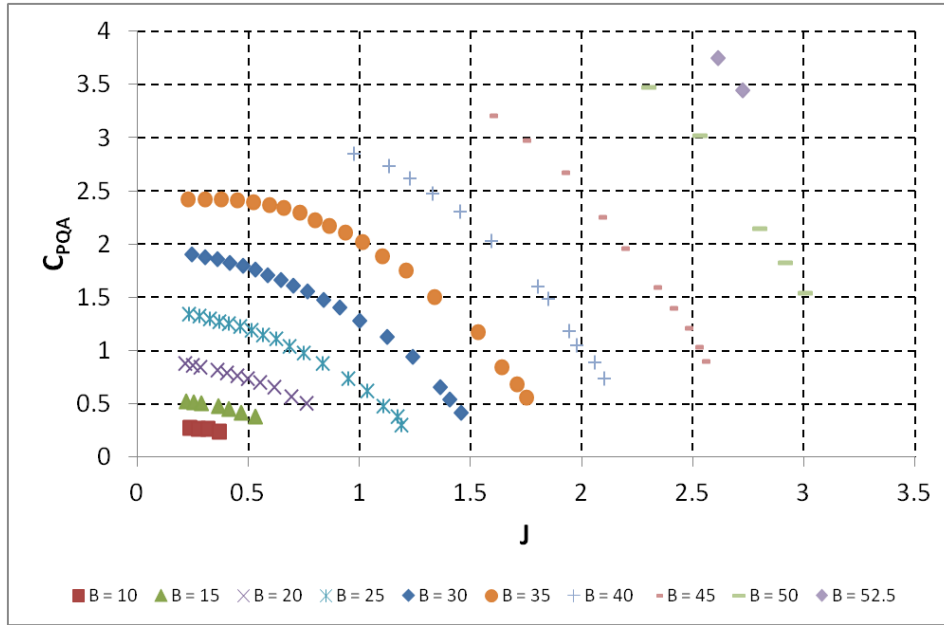


Figure 3.79 – Interpolated C_{pQA} vs. Advance Ratio Map for F7A7

Figure 3.79 shows the estimated C_{pQA} behavior for a counter-rotating propeller with eight bladed two rows. When the pitch angle values in the interpolated performance map are compared with the pitch angle values in the validation data, most of the validation data is outside the interpolated map in terms of the pitch angle values. Thus, error due to extrapolation is introduced in the estimation. The other performance map, efficiency vs. advance ratio is given in Figure 3.80.

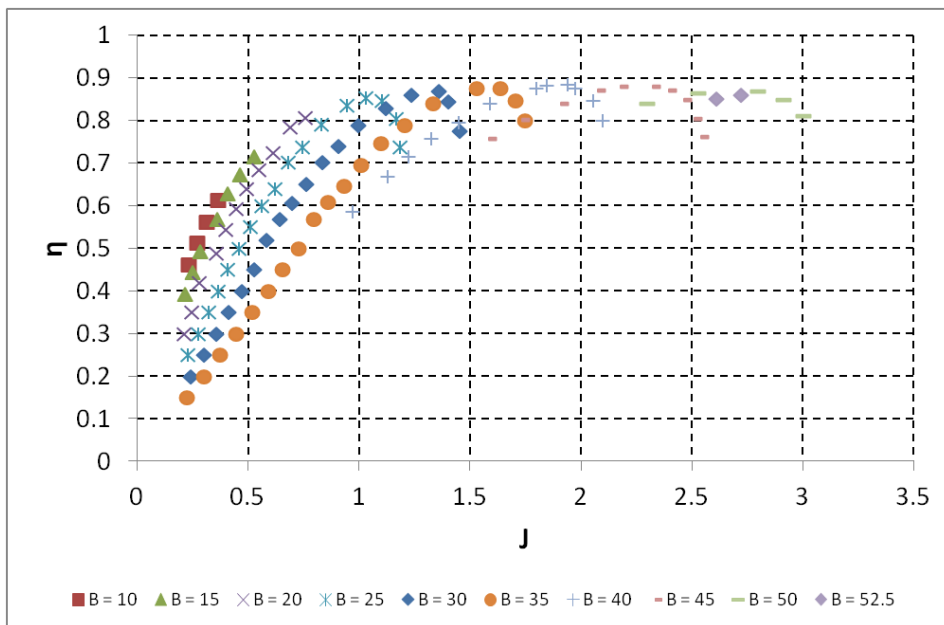


Figure 3.80 – Interpolated Efficiency vs. Advance Ratio Map for F7A7

3.1.5.4.3 Validation Test of the Hamilton – Standard Method

After interpolating the performance maps for F7A7 performance estimation, the next step was the validation test. For the validation test, F7A7 data presented in the method validation process section were used. For each pitch angle and advance ratio combination in the validation data, the interpolated maps were used to estimate the C_{PQA} and efficiency at each of these conditions. The outputs of the maps were corrected for compressibility effects and counter-rotation. This process is illustrated schematically in Figure 3.81.

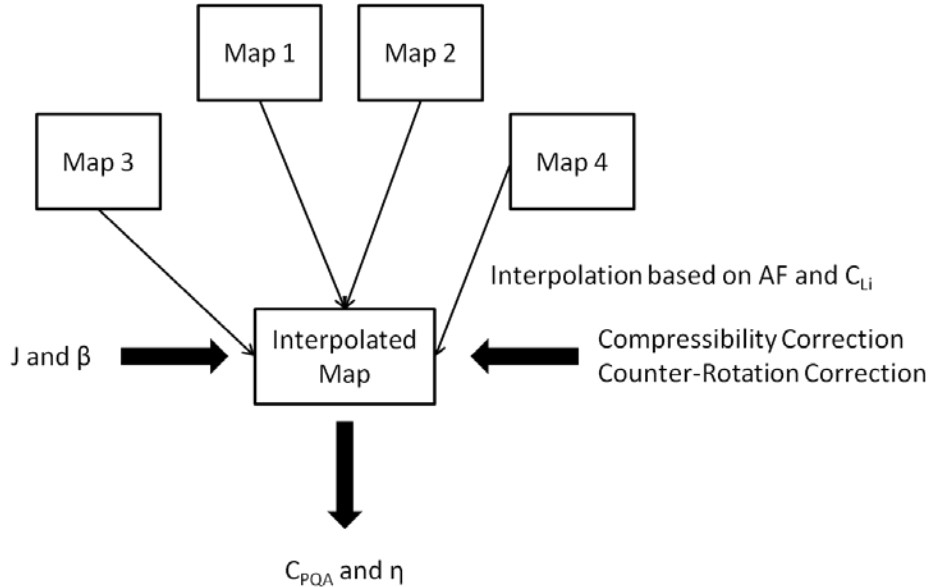


Figure 3.81 – Output Generation Steps for the Validation Test

The corrected outputs, namely C_{PQA} and efficiency were compared with the validation data for each pitch angle and advance ratio combination in the validation data. The results are presented in terms of absolute and relative errors. The results are presented for each pitch angle value to divide the results into easily understandable portions. The first set of results is for a pitch angle of 55.7° and they are given in Figure 3.82, Figure 3.83, Figure 3.84, and Figure 3.85.

Figure 3.82 shows that at a pitch angle of 55.7° , the performance estimation map does not capture the trend in the validation data but as Figure 3.83 shows, percent error at each of these points is almost in a $\pm 10\%$ band and obviously that is above the validation test passing criterion of $\pm 2\%$. At this point it was concluded that the adjusted HS approach could not pass the validation test because it had to meet the accuracy requirement at each point. Furthermore, the pitch angle of 55.7 is the pitch angle which requires the smallest extrapolation from the estimation map. Therefore, if the estimation map has unacceptable error at this level of extrapolation, then the error in the rest of the data will probably fail the test. However, for the

sake of completeness, the error in the rest of the validation data was computed and they are presented in this report.

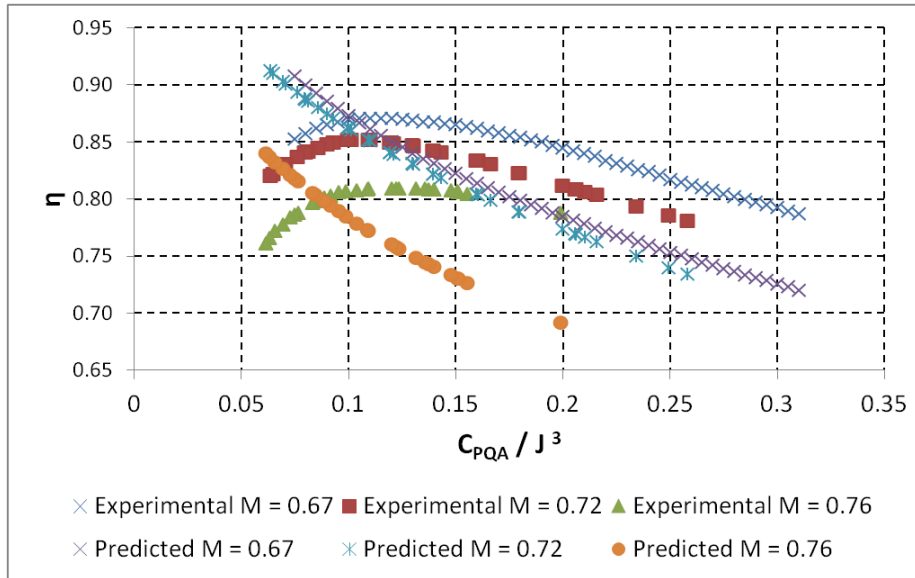


Figure 3.82 – Efficiency vs. C_{PQA} / J^3 Validation Test at a Pitch Angle of 55.7°

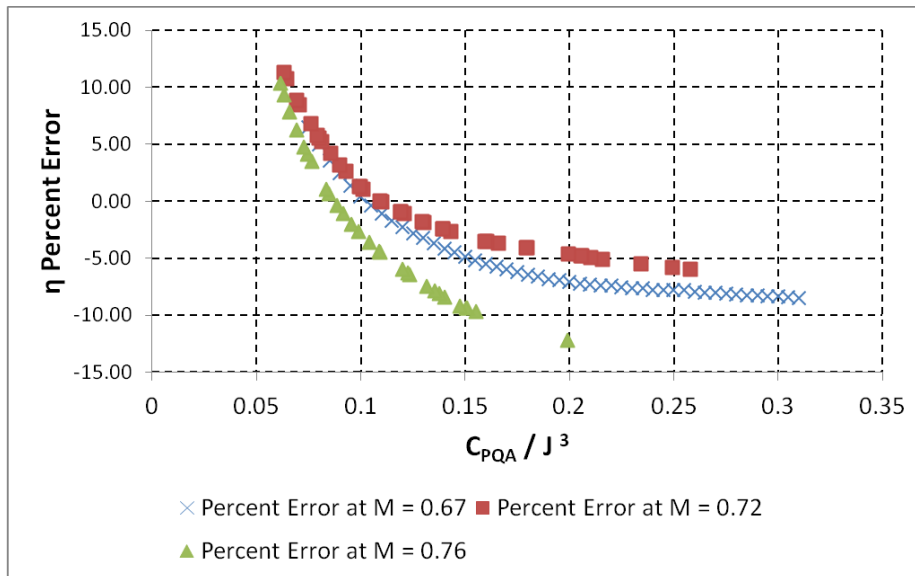


Figure 3.83 – Validation Test Efficiency Percent Error at a Pitch Angle of 55.7°

After analyzing the error in the efficiency prediction, the error in C_{PQA} prediction must be observed. Figure 3.84 shows that the estimation map captured the trend in the validation data to a certain extent but the errors between the predictions and the actual data increase as the advance ratio increases. Figure 3.85 shows this divergence in the errors explicitly. The error in C_{PQA} prediction reaches almost 90% and the amount of divergence increases as the Mach number increases. This amount of difference is not surprising given the very crude assumptions

made to account for the differences between the prediction data and the validation data in terms of the number of blades and the number of rows. C_{PQA} is overestimated throughout the whole validation data for 55.7° . Obviously, the adjusted HS method is better at predicting the efficiency than predicting C_{PQA} .

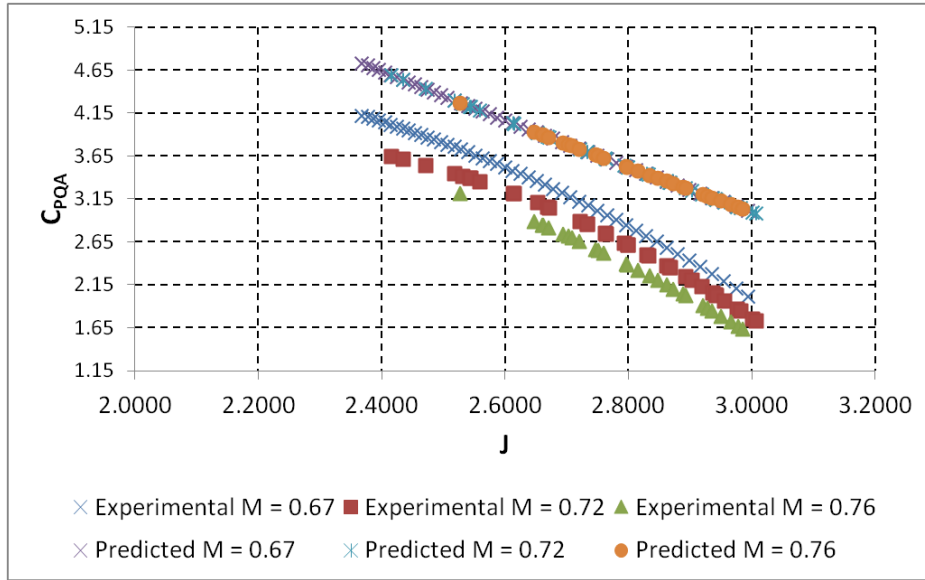


Figure 3.84 – C_{PQA} vs. J Validation Test at a Pitch Angle of 55.7°

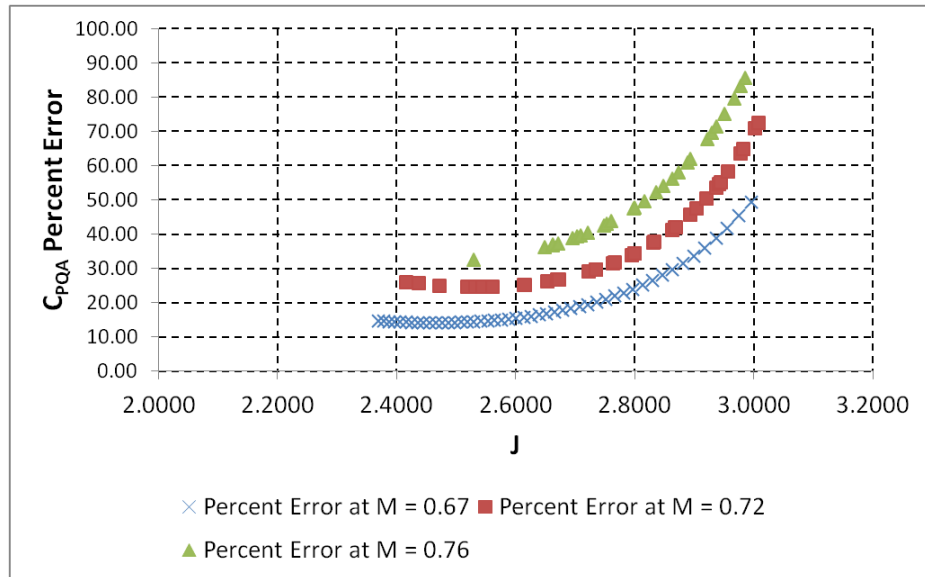


Figure 3.85 – Validation Test C_{PQA} Percent Error at a Pitch Angle of 55.7°

After covering the accuracy of the prediction map at a pitch angle of 55.7° , the results at the next pitch angle value, namely 56.9° are given in Figure 3.86, Figure 3.87, Figure 3.88, and Figure 3.89. Figure 3.86 shows the predicted efficiency trend against the validation data trend whereas Figure 3.87 shows the relative error of the predicted efficiency. In terms of efficiency

results for a pitch angle of 56.9° look similar to those of 55.7°. The prediction fails to capture the trend but the relative error is limited between -6% and 12%. It is not surprising to see similar trends between predictions for two close pitch angle values. Although 56.9° requires further extrapolation than 55.7°, the relative error is contained within a narrower band. Next the prediction results for C_{PQA} at a pitch angle of 56.9° are discussed.

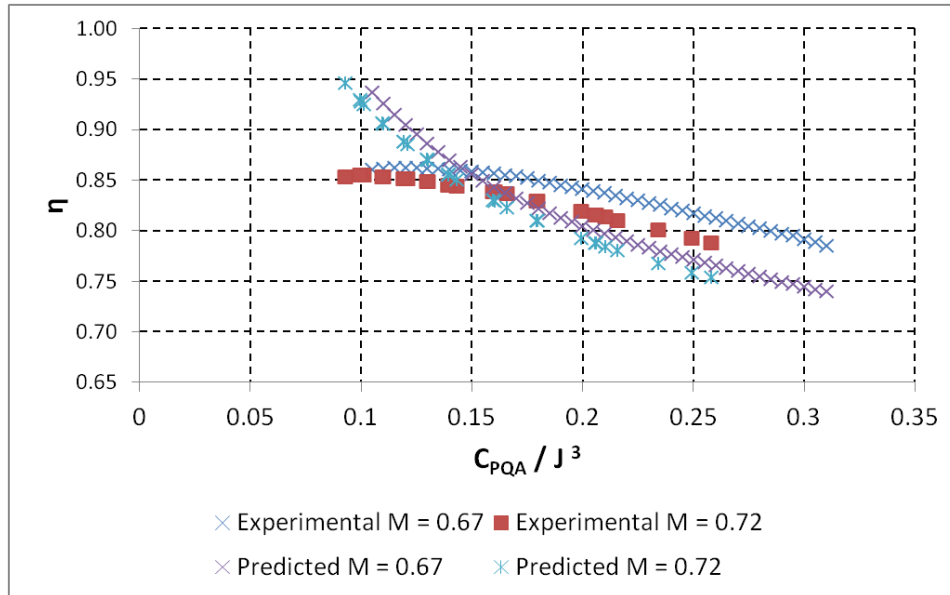


Figure 3.86 – Efficiency vs. C_{PQA} / J^3 Validation Test at a Pitch Angle of 56.9°

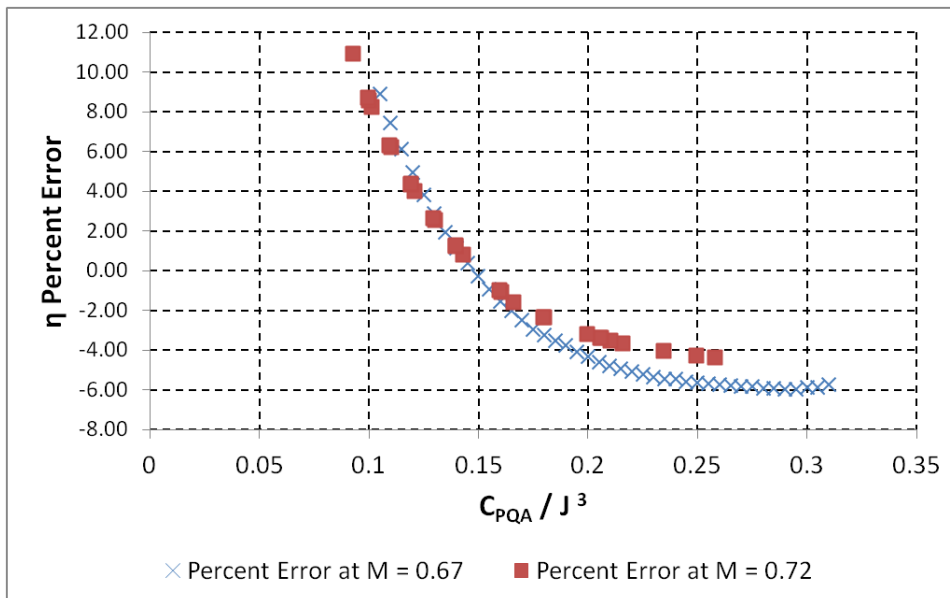


Figure 3.87 – Validation Test Efficiency Percent Error at a Pitch Angle of 56.9°

Figure 3.88 compares the predicted trend for C_{PQA} against the validation data trend and Figure 3.89 shows the relative error in the predicted C_{PQA} . As it was the case for efficiency, C_{PQA} results

at 56.9° look similar to those of 55.7°. The predicted trend is offset from the validation data by almost a constant for the most of the data range. As the advance ratio increases, the difference between prediction and validation data increases. This divergence is shown in Figure 3.89. As it turns out, the relative error in C_{PQA} at 56.9° is not as large as 55.7° case although 56.9° requires further extrapolation. However, C_{PQA} was constantly overestimated as it was in the case of 55.7° and the divergence increases as the Mach number increases.

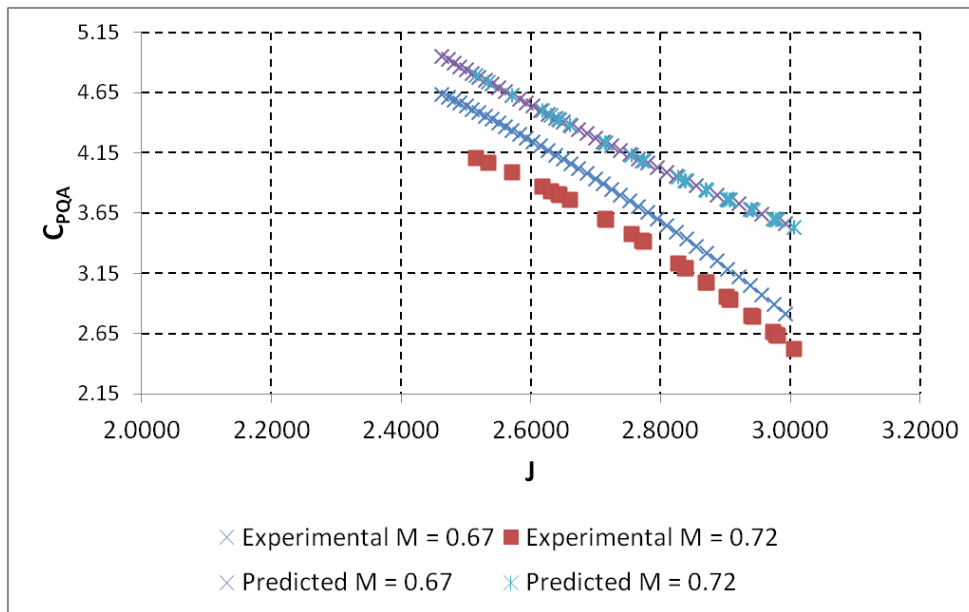


Figure 3.88 – C_{PQA} vs. Advance Ratio Validation Test at a Pitch Angle of 56.9°

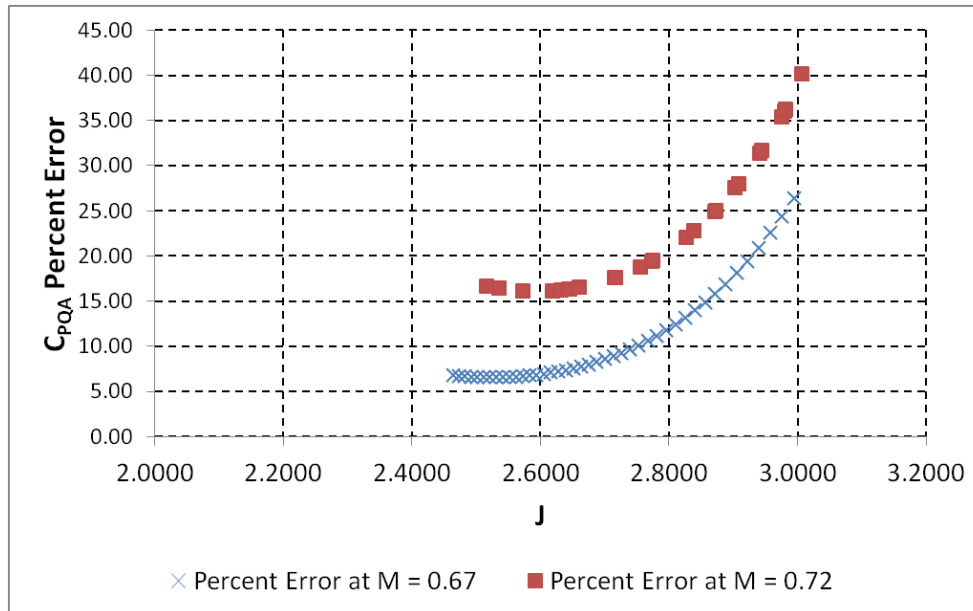


Figure 3.89 – Validation Test C_{PQA} Percent Error at a Pitch Angle of 56.9°

After covering the validation test results for the first two pitch angle settings, the results for the third pitch angle value, namely 58.5° is shown in Figure 3.90, Figure 3.91, Figure 3.92, and Figure 3.93. The order of the figures is the same with previous two cases. Figure 3.90 is for efficiency prediction absolute error comparison at 58.5° and Figure 3.91 is for the relative error of the efficiency prediction. Similar to the previous cases, the prediction fails to capture the validation data trend and the relative error is between almost $\pm 15\%$. The width of the relative error band increased compared to the previous two cases due to further extrapolation probably.

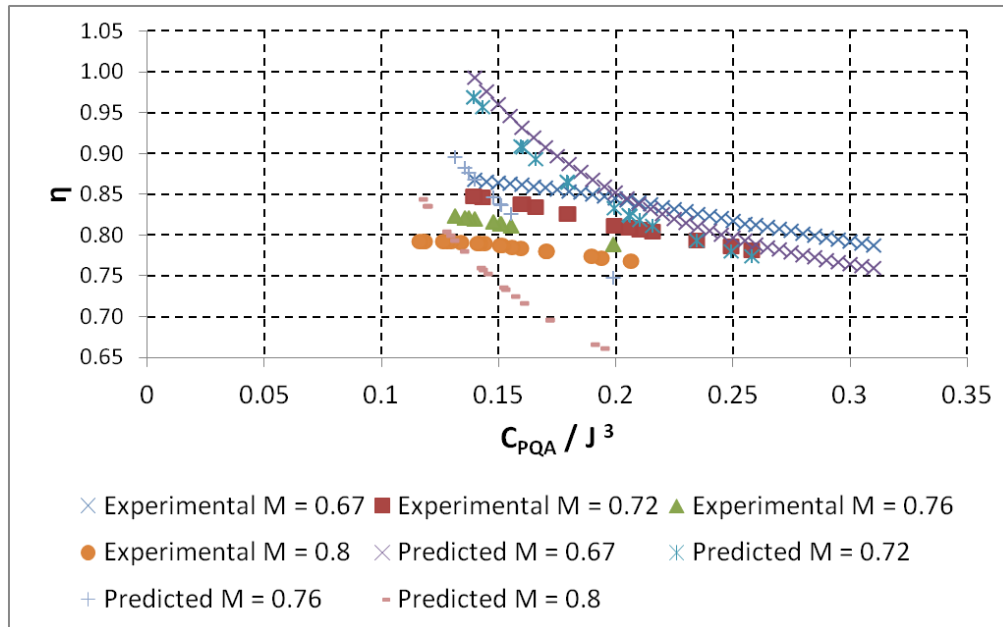


Figure 3.90 – Efficiency vs. C_{pQA} / J^3 Validation Test at a Pitch Angle of 58.5°

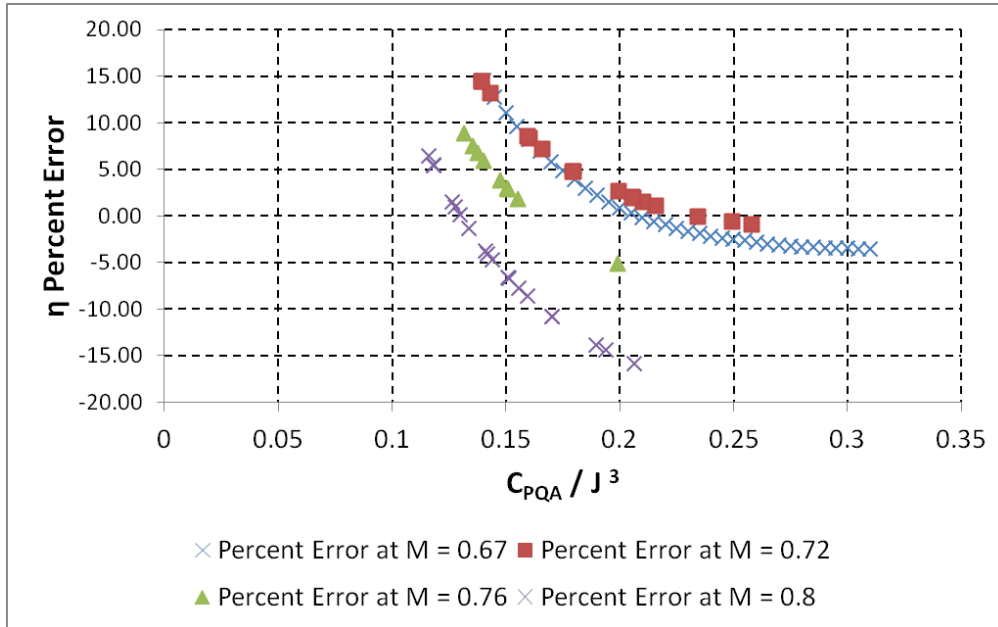


Figure 3.91 – Validation Test Efficiency Percent Error at a Pitch Angle of 58.5°

Figure 3.92 shows that the predicted C_{PQA} trend captures some of the validation data at 58.5°. However, the difference between the prediction and the validation data increases as the advance ratio increases. Since the predicted trend captures some of the data, not all of the validation data is overestimated at 58.5° for the first time as shown in Figure 3.93. As expected, the diverging trend in the relative error is also shown in Figure 3.93 and the divergence increases as the Mach number increases.

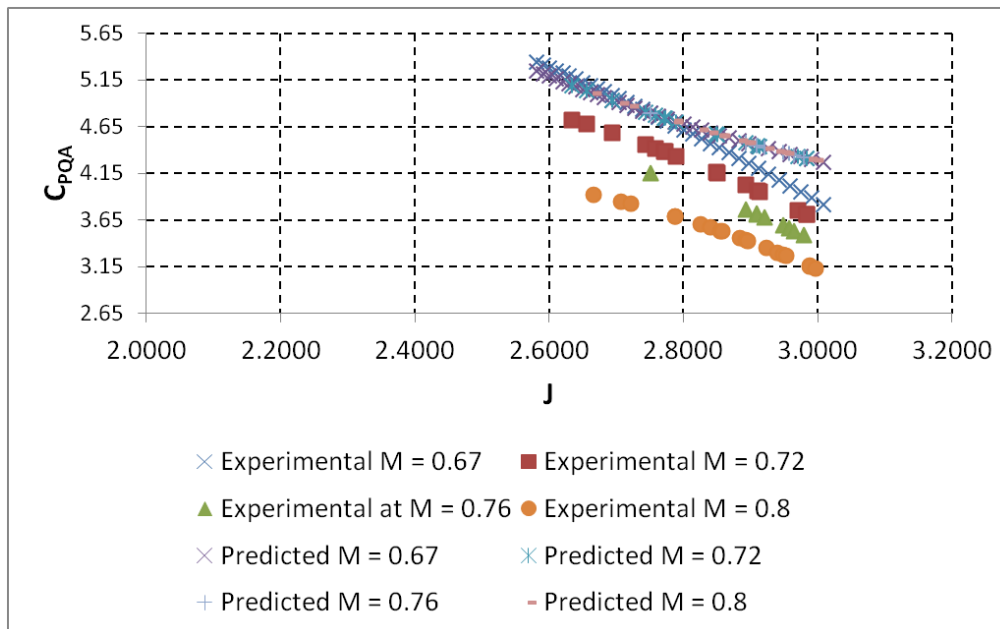


Figure 3.92 – C_{PQA} vs. Advance Ratio Validation Test at a Pitch Angle of 58.5°

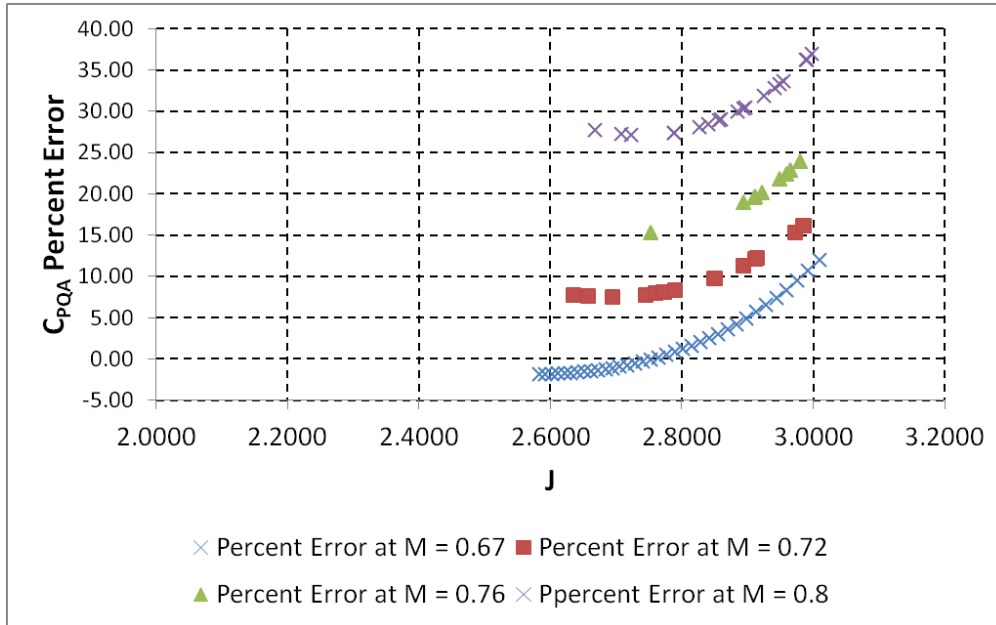


Figure 3.93 – Validation Test C_{pQA} Percent Error at a Pitch Angle of 58.5°

For the validation test results of 60.2°, Figure 3.94, Figure 3.95, Figure 3.96, and Figure 3.97 are provided. Figure 3.94 shows that the predicted efficiency trend is not same with the validation data. The relative error is larger than the previous cases as a result of further extrapolation. The relative error is between -10% and 25% as given in Figure 3.95. For the first time the predicted efficiency is more than one at three points in Figure 3.94. This unreasonable and unrealistic result is a result of slopes in the prediction data and the distance of the extrapolated point.

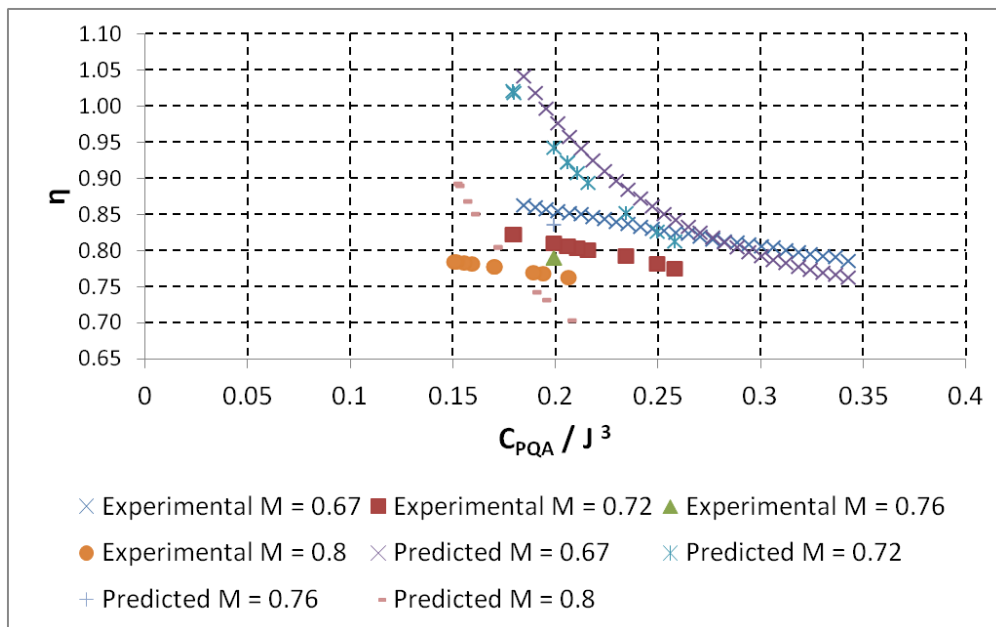


Figure 3.94 – Efficiency vs. C_{pQA} / J^3 Validation Test at a Pitch Angle of 60.2°

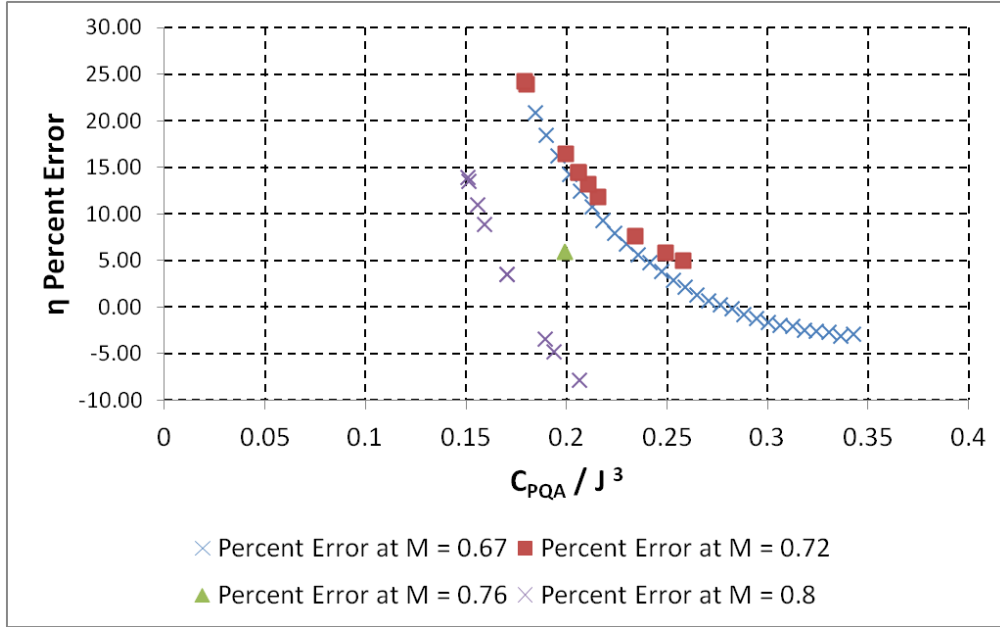


Figure 3.95 – Validation Test Efficiency Percent Error at a Pitch Angle of 60.2°

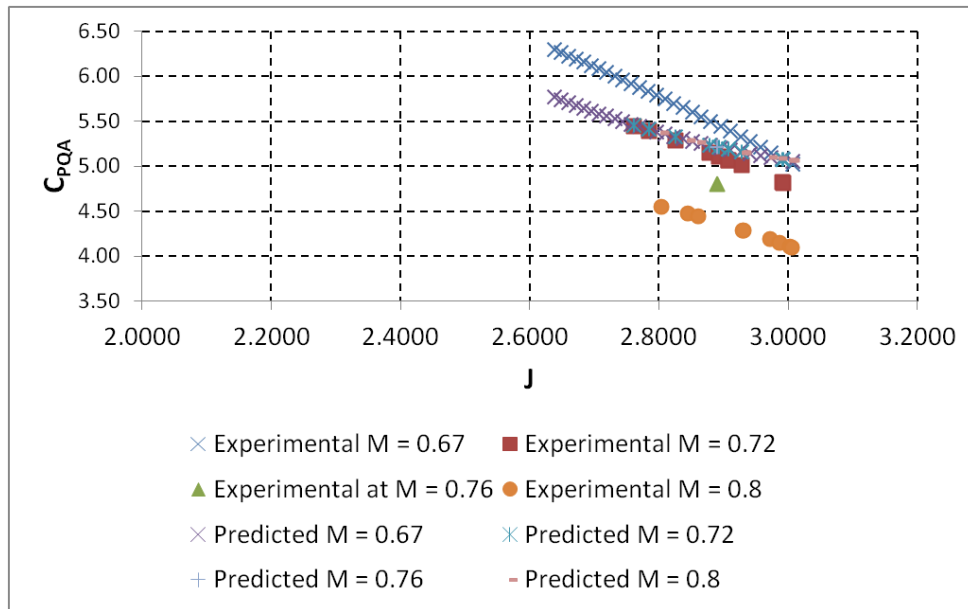


Figure 3.96 – C_{PQA} vs. Advance Ratio Validation Test at a Pitch Angle of 60.2°

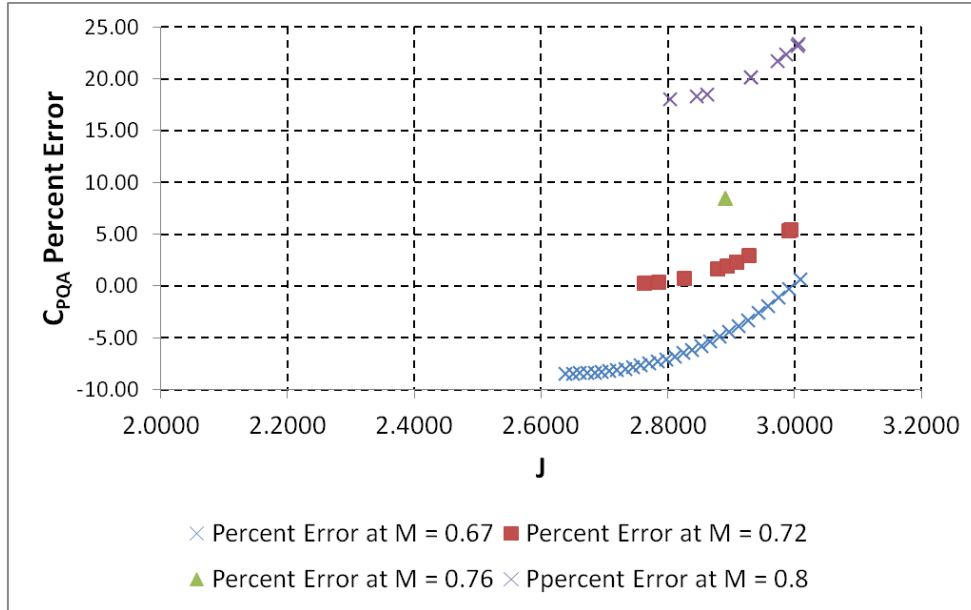


Figure 3.97 – Validation Test C_{pQA} Percent Error at a Pitch Angle of 60.2°

Figure 3.96 and Figure 3.97 are for the C_{pQA} validation test results at 60.2° . Figure 3.96 shows that the predicted C_{pQA} trend crosses through the validation data for the first time. However, the relative error is not acceptable as in all of the cases so far. The relative error is between -10% and 25% and the error increases as the Mach number increases according to Figure 3.97. There is still a diverging trend in the relative error as the advance ratio increases.

There is only one more pitch angle value left in the validation data range of interest. The validation test results at 61.2° are presented in Figure 3.98, Figure 3.99, Figure 3.100, and Figure 3.101. Pitch angle setting of 61.2° has only three points in the validation data range of interest. Compared to the other settings, this setting has the smallest number of points. Figure 3.98 shows that all of the points are overestimated but the amount of overestimation is less than 10% as given in Figure 3.99.

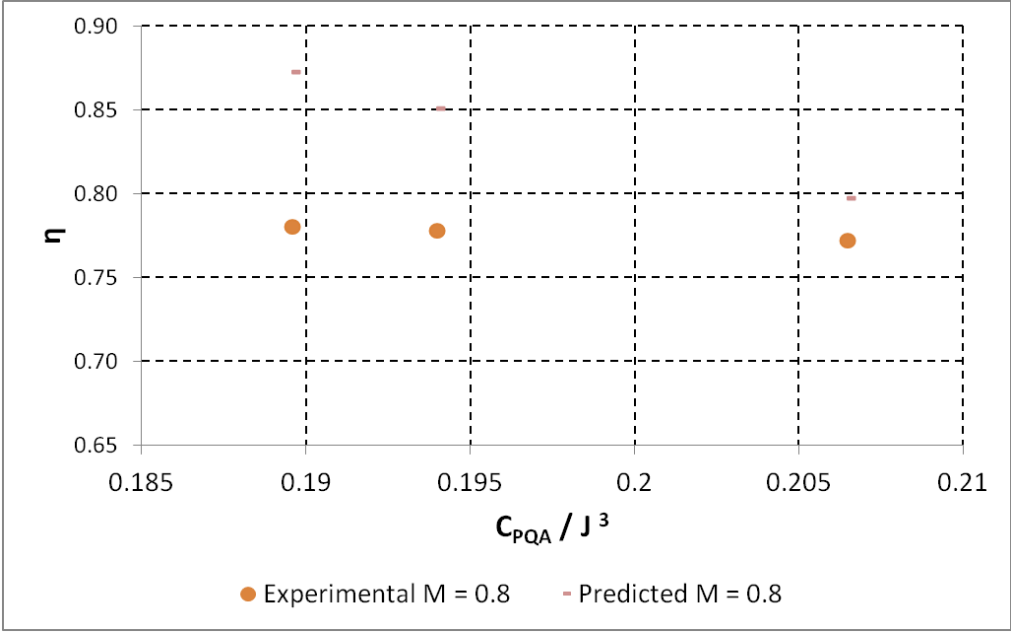


Figure 3.98 – Efficiency vs. C_{pQA} / J^3 Validation Test at a Pitch Angle of 61.2°

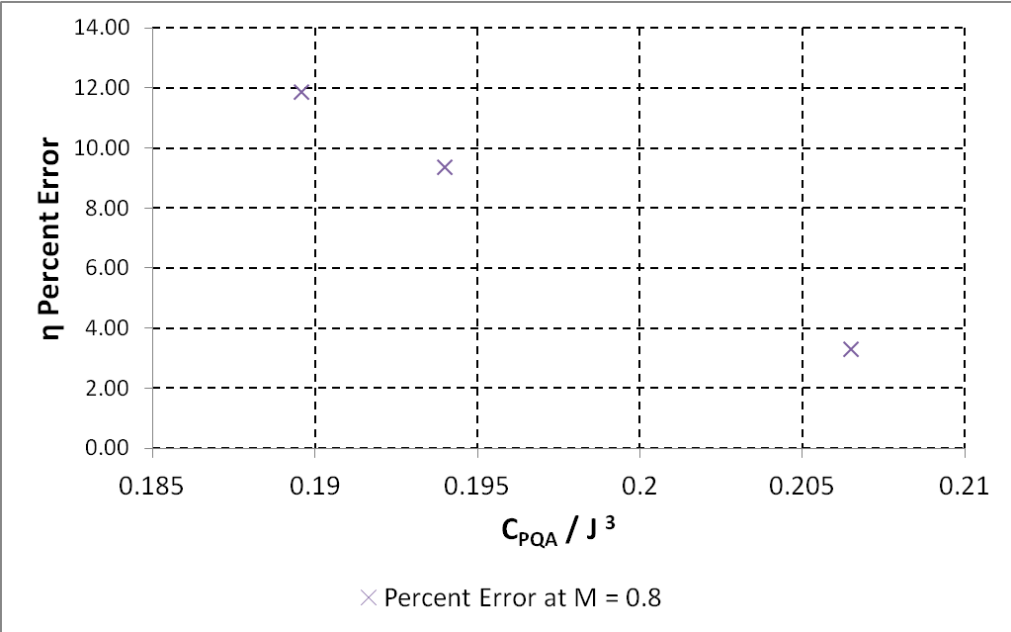


Figure 3.99 – Validation Test Efficiency Percent Error at a Pitch Angle of 61.2°

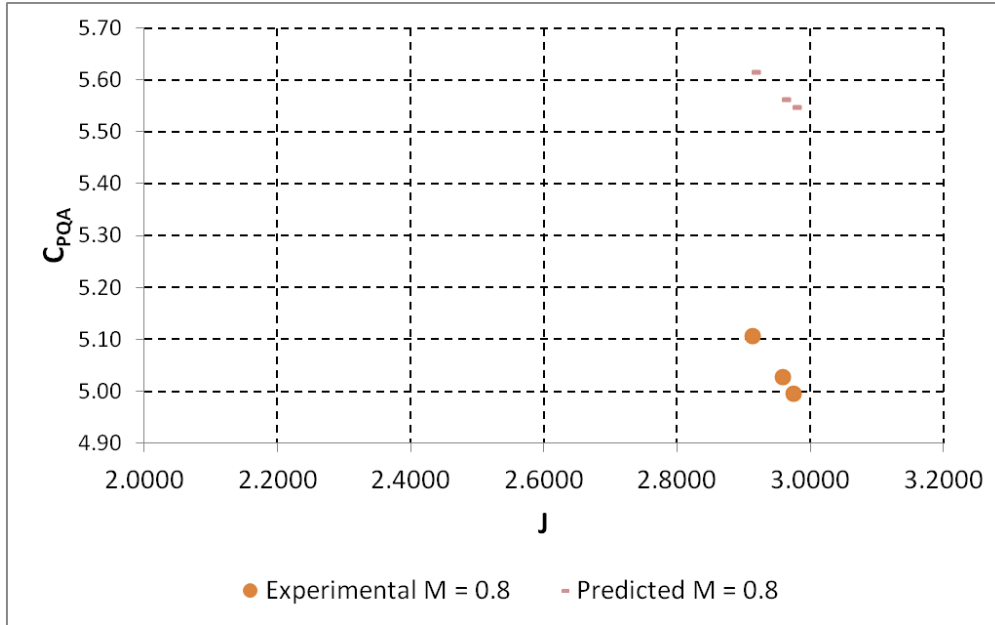


Figure 3.100 – C_{pQA} vs. Advance Ratio Validation Test at a Pitch Angle of 61.2°

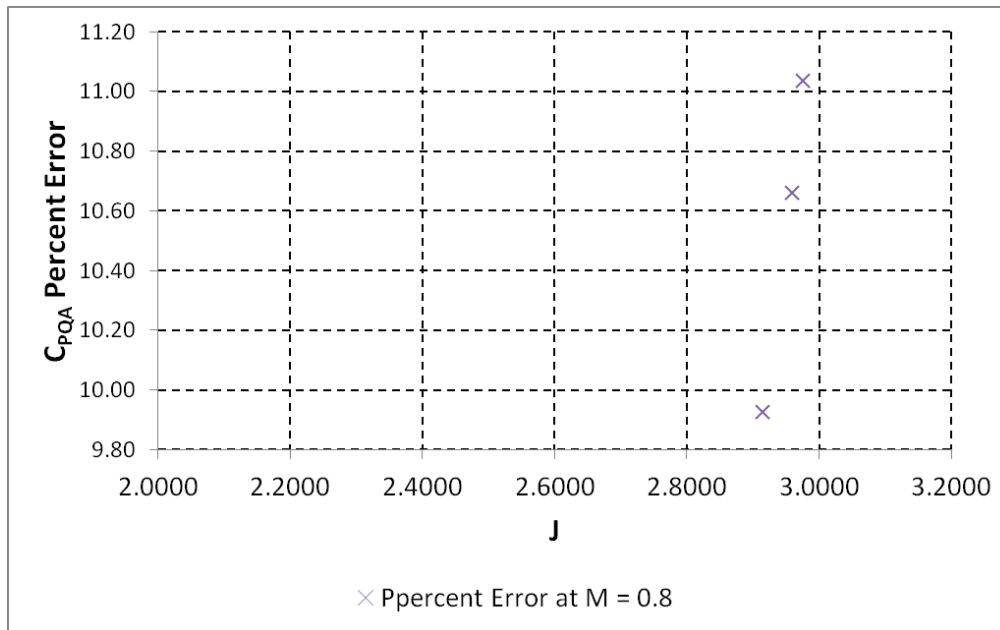


Figure 3.101 – Validation Test C_{pQA} Percent Efficiency at a Pitch Angle of 61.2°

Figure 3.100 and Figure 3.101 show the validation test results for C_{pQA} at 61.2°. In Figure 3.100 the predicted trend overestimates almost by a constant relative error. The relative error is about 10% for all of the three points in Figure 3.101.

After reviewing the HS method performance predictions for the validation data, it was obvious that the method failed the validation test. Efficiency prediction was significantly better than C_{pQA} prediction although both of them failed the validation test.

One of the main contributors to the error was the generation difference between the prediction data used and the validation data. In other words, the prediction data used were for the turboprops in 1960s whereas the validation data used were for an open rotor designed in 1990s. The open rotor blades are swept more than turboprop blades. The difference in sweep affects the efficiency and power consumption behavior.

The last main contributor was the counter-rotation effect. The prediction data had only one row of blades whereas the validation data had two. Accounting for the effect of this difference on the power consumption is not available. Therefore, the power consumption for one row was multiplied by two as another crude assumption. Moreover, the NACA chart used to predict the effect of counter-rotation on efficiency was extrapolated due to larger blade AF values. Therefore, error due to extrapolation was introduced.

3.2 Hybrid Electric Sizing Studies

Once the basic building blocks for modeling hybrid electric propulsion systems has been created in NPSS, they can be used to construct a hybrid electric NPSS engine model similar to the hFan architecture developed by GE. While many specific modeling details of the hFan are proprietary, there is enough data published in this report, to create a public domain model and use it to conduct trade studies. Since the hFan architecture contains additional degrees of freedom (electric power and core power settings) it is first necessary to define the modeling assumptions and methodology, described in section 3.2.1. After that, comparisons to public domain GE engine performance data are made to verify functionality of the GE hybrid electric model. Finally, a study is conducted using cryogenic and non-cryogenic components to assess the engine cycle trades associated with the hybrid electric engine architecture. Additional degrees of freedom also present themselves during the sizing process. The trade study will address the impact of sizing the engine with and without the electric motor ‘turned on’. In order to give context to the trade study, vehicle trade factors for drag, fuel burn, energy usage, and weight are used as provided by Boeing for the SUGAR Volt configuration.

3.2.1 Modeling Methodology

This research seeks to create a public domain representation of the GE hFan engine architecture shown in Figure 3.102. While technologically advanced compared to today’s turbofans, the underlying architecture is fundamentally similar. It is a two-shaft, high bypass, separate flow turbofan designed for podded applications. However, the hybrid electric portion manifests itself through an electric motor embedded in the tailcone of the engine. This motor is coupled to the low pressure spool and provides the ability to drive the fan either in addition to, or in lieu of the core.

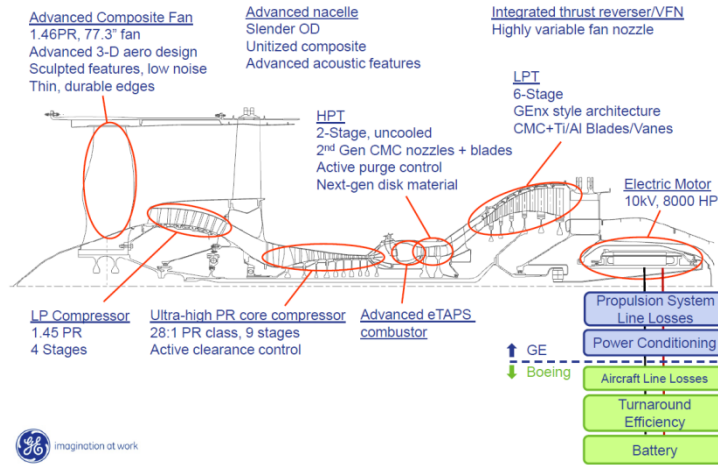


Figure 3.102 – Hybrid Electric Engine Architecture (53)

The electric motor is a switched reluctance motor (SRM) design that allows for robust operation in the event of a failure of one or more of the motors phases. Conventionally, SRM designs may suffer from so-called torque stutter (17). This occurs when the magnetic fields align between the rotor and stator resulting in a momentary a period of no torque until the shaft inertia carries the motor poles out of alignment; however, this is not an issue for such a large machine with the inertia of the fan and low pressure compressor pulling the motor. Furthermore, by using a switched reluctance machine the motor can be switched off simply by de-energizing the stator poles. This allows flexible operation and use of the turbofan in either all fuel, all electric, or hybrid modes depending on the needs of the mission.

The electric motor is connected to an inverter that converts power from DC to AC. Behind that is a transmission line that connects the motor to a series of batteries that are charged before flight. While inflight charging is certainly possible, this study does not include any provisions for that capability. The following sections will describe modeling aspects of the integrated system.

3.2.2 Gas Turbine Modeling Considerations

In order to understand modeling considerations associated with the operation of a hybrid electric system, it is first necessary to establish and extend standard definitions used in aircraft engine power management. First, the establishment of a power code for the electric system must be defined, similar to the power code system for a conventional propulsor. Table 3.20 lists the standard power rating codes for non-augmented turbofan applications (54). It is up to the OEM to determine the exact operational constraints associated with each rating code. Often lifing considerations are associated with each power code and there may be other certification constraints associated with assignment of engine operational state to a power code. For example, there are FAA requirements regarding engine acceleration time from flight idle to maximum power in the event of a go-around.

Table 3.20 – Conventional Power Code Definitions

Power Code	Definition
50	Maximum Takeoff
45	Maximum Continuous
40	Maximum Climb
35	Maximum Cruise
22-35	Intermediate Rated Power
21	Flight Idle
20	Ground Idle

In a practical modeling sense the above rating codes can be simulated through the use of NPSS independent and dependent variables and constraints, shown in Table 3.21. Essentially, given a power code for a sized engine, NPSS will vary the independent until the dependent condition is satisfied, or a constraint is activated. Note that only the commonly active constraint is shown in Table 3.21; however, the engine model used in this, and most applications, includes physical shaft speed constraints, compressor exit temperature constraints, minimum nozzle pressure ratio constraints, and others necessary to keep the engine operable. Note that power code 20 is removed, since in a steady state simulation there is not a reasonable method to predict the difference between ground and flight idle.

Table 3.21 – Conventional NPSS Power Management Scheme

Power Code	Definition	NPSS Independent	NPSS Dependent	Constraint(s)
50	Maximum Takeoff	Burner FAR	100% Corrected Fan Speed	T4.1 Limit
45	Maximum Continuous	Burner FAR	T4.1 Limit – Margin1	Fan Corrected Speed
40	Maximum Climb	Burner FAR	T4.1 Limit – Margin2	Fan Corrected Speed
35	Maximum Cruise	Burner FAR	T4.1 Limit – Margin3	Fan Corrected Speed
22-35	Intermediate Rated Power	Burner FAR	Thrust (% of PC 35)	Fan Corrected Speed
21	Flight Idle	Burner FAR	Thrust (5% of PC 50)	Minimum Burner FAR

While Table 3.21 is fairly straightforward, it is constructed with the mindset that the engine core creates all necessary power for thrust, evidenced, by the burner fuel-to-air (FAR) ratio being the only independent in the solver. For the hybrid electric system being modeled, an

additional term is defined in agreement with the GE defined terminology: the electric power code (EPC). The EPC NPSS implementation is shown in Table 3.22 along with additional constraints that must be added to the solver in addition to those shown in Table 3.21. Since this is a new definition it merits further discussion. For a given operating state (altitude and Mach), a turbofan will produce a certain amount of thrust for a specified power code. Also associated with this state will be a shaft speeds and combustor operating temperatures. While not entirely accurate of reality or NPSS, it is suitable for the purposes of discussion to assume that the fan produces all of the thrust. In order to simplify the power management structure, it is further defined that for a given power code, the thrust level will be held constant regardless of the amount of electric power sent to the motor. In other words EPC=50 and EPC=0 will both provide the same net thrust at PC=45. Defining EPC in this manner allows it to be orthogonal to the PC definition. In essence, PC sets thrust, and EPC sets the amount of electric power (torque) applied to the low pressure shaft. While this is certainly not the only way to define EPC, it is perhaps the easiest to understand.

Table 3.22 – Electric Power Code Definitions

EPC	Definition	NPSS Independent	NPSS Dependent	Constraint(s)
50	Maximum Motor Power	Motor Torque	Minimum Burner FAR (core idle)	Rated Motor Power
0-50	Intermediate Motor Power	Motor Torque	Intermediate Motor Power (% of Rated)	None
0	Motor Off	Motor Torque	Minimum Motor Power	None

In the absence of other operability constraints, which will be discussed later, one primary limiter in maximum allowable motor power is the core idle limit. As more motor power/torque is applied for a given PC, the NPSS solver will reduce burner FAR, and thereby core power output, to maintain thrust. Eventually, the core will drop below acceptable stability limits and could blowout. While this may eventually be allowable in the presence of an electrical drive system, it is assumed in this analysis that the core must remain lit at all times. Therefore, EPC 50 is defined as the motor power required to achieve minimum burner FAR for a given PC, or the maximum rated motor power, whichever happens earlier. EPC 0 through 50 is then defined as a percent of the EPC = 50 power. The general power management algorithm is as follows:

1. Specify Mach, altitude, PC, and EPC
2. Temporarily set EPC to 0
3. Run engine to PC according to Table 3.21
4. Save off thrust
5. Vary motor torque to hit core idle condition, save power

6. Apply motor torque consistent with Table 3.22 and (5), then run model to hold thrust at (4)
7. Repeat for flight envelope

Of course, this simplistic explanation while accurate leaves out real operability features that constrain hybrid electric operation. One primary limiter on application of electrical power to the shaft is the resulting flow mismatch between the high and low pressure spools. Since thrust is fixed for a specified PC it can be assumed that fan speed, flow, and pressure ratio all remain relatively constant. As motor torque is increased, the core no longer needs to produce as much high temperature and pressure gas to drive the low pressure turbine. From an engine and NPSS solver perspective, the burner FAR will be reduced to compensate for additional power being supplied by the motor. Correspondingly, the high pressure shaft speed will decrease as applied motor power increases and core power is decreased. Since, for a two-spool architecture, the low pressure compressor and fan are on the same shaft the amount of flow being sent to the high pressure compressor (HPC) will remain high, even as high pressure spool speed decreases. This flow mis-match between the HPC and low pressure compressor (LPC) results in reduced margin and ultimately surge of the LPC. To alleviate this, an operability bleed must be placed aft of the LPC to control surge. The operability bleed is controlled via a discrete state variable (DSV) in NPSS that opens the bleed valve whenever the LPC stall margin falls below a specified margin. In addition to the operability bleed, variable area fan nozzle logic is defined that varies the bypass nozzle area to maintain peak fan efficiency along the operating envelope unless constrained by a minimum stall margin constraint. Variable area core nozzle logic is implemented; however, it was found to be difficult to achieve consistent convergence with NPSS when the engine included a variable area core nozzle, variable area bypass nozzle, and operability bleed aft of the LPC. The reason for this is that NPSS converges the system through a Newton-Raphson solver. When there are collinear dependents, which are metrics that are affected equally by more than one independent, the solver is singular and cannot converge. For example, core nozzle area and the operability bleed flow can both be used to control LPC stall margin; however, the solver can only vary one at a time. In a final design the two variables would be scheduled (i.e., set from lookup tables) to provide maximum operability and performance; however, since the objective of the integrated NPSS model is to perform parametric studies, the solver must be used to dynamically set operability features so that the engine can adapt to different cycle designs without extensive user adjustment. In order to accomplish this goal the parametric sizing comparisons between the cryogenic and conventionally driven system were performed without a variable area core nozzle.

Weight estimation of the engine was performed using the flow scaling method defined in (55) with parameters tuned to match available GE hFan baseline data. Engine parametric size and efficiency effects were also used using the methods described in (55).

3.2.3 Verification of the NPSS Hybrid Electric Model to GE Public Domain Data

In order to validate the performance trends of the Georgia Tech NPSS model, a comparison was performed with the GE hFan model developed in year 2 of the SUGAR project. The NPSS model was calibrated to match the engine TSFC and performance information presented in (1). The calibrated engine cycle is shown in Table 3.23. Cruise is defined as Mach 0.7 at 40,000 feet ISA.

Table 3.23 – Georgia Tech hFan Calibration Point

Cycle Parameter	Value
FPR at cruise	1.45
BPR at cruise	11.4
LPCPR at cruise	1.45
HPCPR at cruise	28
T41max	3500 deg R
T41 at top of climb	2500 deg R
Cooling	Uncooled advanced CMC
HP Shaft HPX	256 HP
LP Shaft HPX	150 HP
Maximum Motor Power	8000 HP

The GE generated powerhook, recreated in Figure 3.103, was used as a basis for comparison.

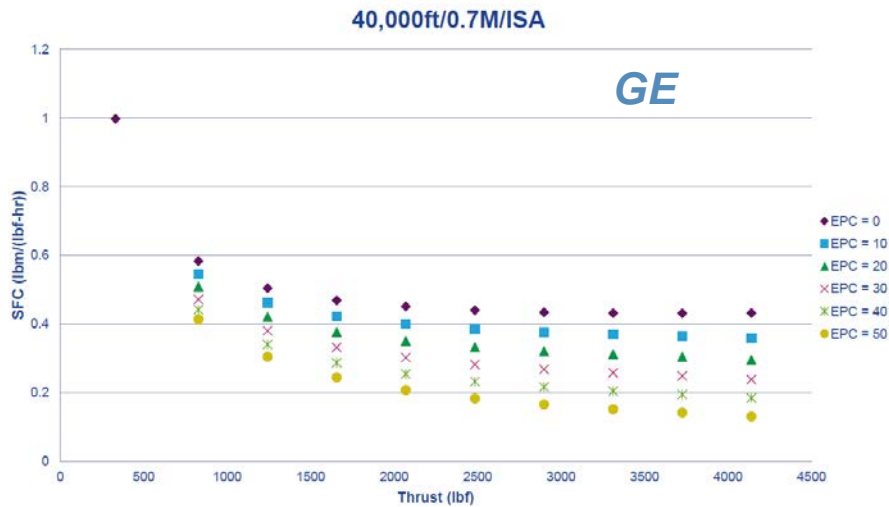


Figure 3.103 – GE hFan Powerhook

The output from the Georgia Tech model, using the operability features described in Section 3.2.1 and detailed motor and inverter elements described in Sections 3.1.1.6 and 3.1.1.7 is shown in Figure 3.104. The trends are similar in both magnitude and shape suggesting the Georgia Tech model is appropriate for use in parametric studies.

40,000 ft / Mach 0.7 / ISA

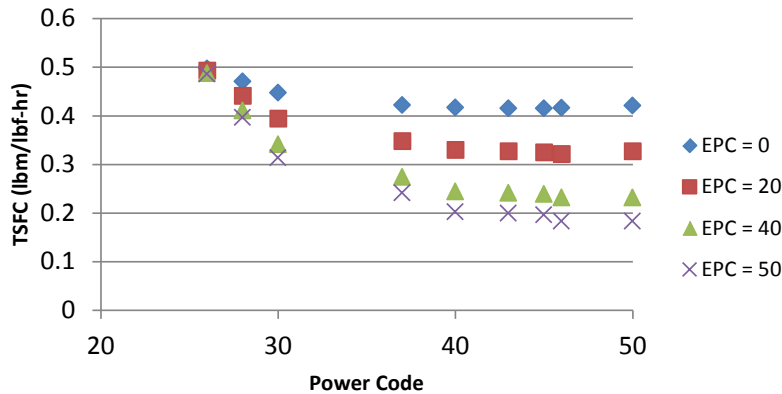


Figure 3.104 – Georgia Tech Hybrid Electric Trends

It is also useful to look at the Georgia Tech hybrid electric performance averaged across all flight Mach numbers and altitudes, shown in Figure 3.105.

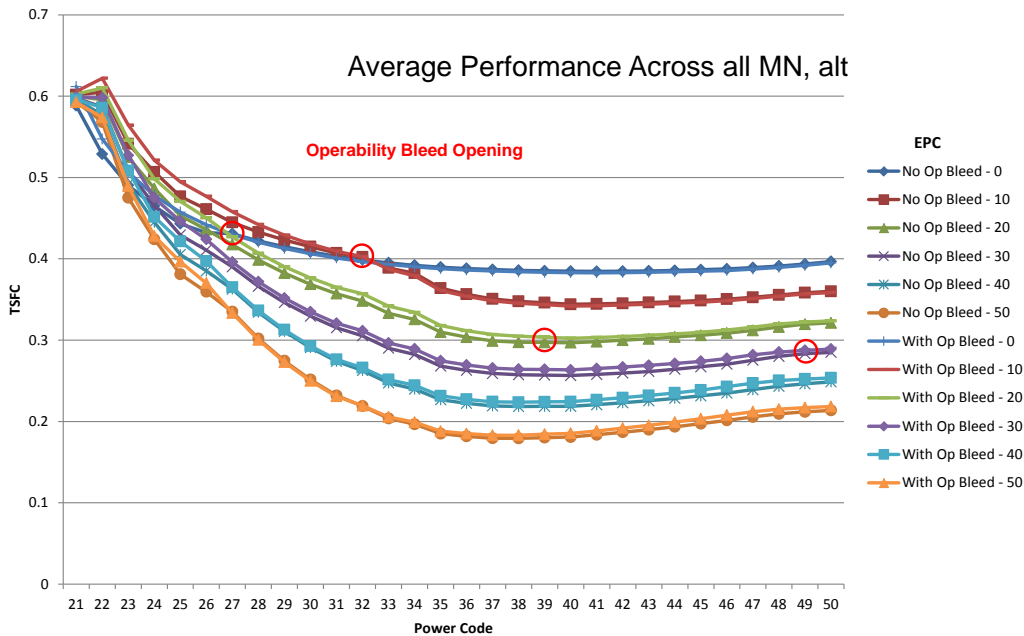


Figure 3.105 – Georgia Tech Average Performance

Marked in Figure 3.105 are several red circles that show the point at which the operability bleed opens. For each EPC from 0 to 50, there are two similar colored lines for each EPC setting. The lighter shaded one represents the engine cycle with the operability bleed logic turned on, whereas the darker line represents the NPSS results with the operability logic completely disabled. (e.g., the LPC is allowed to surge in a numerical sense). The overall trends are still in good agreement with the GE generated data with the core idle limit constraining electric motor

power addition at lower power codes. Furthermore, the operability bleed opens earlier as electric power is increased. While Figure 3.105 is only indicative of average performance, it verifies the desired functionality within the engine model.

3.2.4 Hybrid Electric Engine Sizing Studies

Once the baseline parametric NPSS hybrid electric model is created, it can be used to perform a series of studies to examine the coupling between the engine thermodynamic cycle, electrical system including the motor, and the aircraft. Both a cryogenic and conventional motor and inverter setup are examined. The effect of sizing the engine with and without the electric motor is also investigated for both the cryo and non-cryo applications. The study uses the following assumptions for power system specific weights, listed in Table 3.24 and based on (56). The vehicle trade factors in Table 3.24 were provided by Boeing for the 750 Balanced configuration of the SUGAR Volt and show the percent fuel burn change for the noted engine trade factor. The Energy percent change is calculated relative to the baseline configuration using a 1,380 hp motor. Engines results are compared relative to a common baseline to assess which cycle is optimal; however, this does not provide an absolute level of fuel burn reduction which requires cycling the detailed vehicle sizing; this was outside the scope of this study.

Table 3.24 – NPSS Hybrid Electric Weight Assumptions

	Cryo	NonCryo
Motor Power Density (hp/lb)	13	3
Inverter Power Density (hp/lb)	15	10
Transmission Weight (lbm)	20	20
Cryo Cooler Weight (lbm/hp-input)	5	NA
Cryo COP (Percent Carnot)	0.3	
Battery Energy Density (Wh/kg)	750	
Weight Trade Factor (per 1000 lbm)	0.86	
Drag Trade Factor (per 1" fan diameter)	0.09	
SFC (per %)	1.01	
Energy (per %)	0.31	

Component efficiencies for the engine and electrical system are calculated using the methods described in previous sections. The first set of studies focused on varying fan pressure ratio varied from 1.35 to 1.55 with overall pressure ratio held constant at 58. This was accomplished by varying the low pressure compressor pressure ratio and holding the high pressure compressor pressure ratio at 28. T41 was not changed and extraction ratio was held at 1.15. Unless otherwise stated, all results are shown for the mid-cruise condition.

3.2.4.1 Non-cryogenic Results – Sized With Motor

First, the engine was sized with full electric horsepower addition from the motor. In other words, the fan was sized by top of climb requirements provided by Boeing for the 750 Wh/kg balanced scenario at maximum core power output and full electric motor power addition. Figure 3.106 shows the trade factor results for this scenario for varying levels.

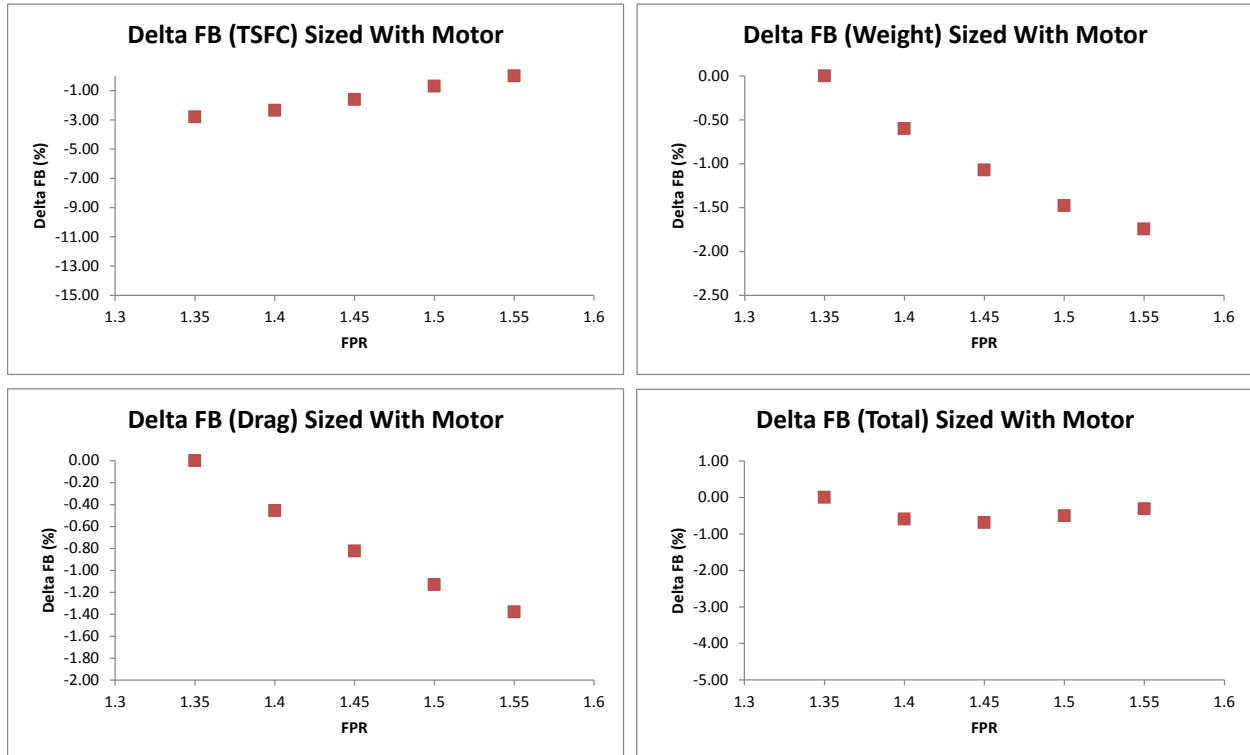


Figure 3.106 – Motor Sized Non-Cryogenic Fan Sizing Breakdown

Starting at the upper left of Figure 3.106, the results are shown with varying FPR. Since extraction ratio (Pt19/Pt9) is held constant, lowering FPR leads to increased BPR, resulting in decreased TSFC. Sizing the fan with the electric horsepower does carry a penalty in all fuel mode which will be fully examined later.

On a fuel efficiency basis alone, one would choose the highest BPR (lowest FPR) cycle with the highest electric motor available; however, as the BPR increases, so does the weight of the engine, shown in the upper right portion of Figure 3.106. The primary driver of weight is bypass ratio, evidenced by the steep slope of fuel burn change with FPR. Moving to the lower right of Figure 3.106, bypass ratio is the primary driver on engine diameter and size; increasing bypass ratio leads to larger engine diameters.

Finally, adding the individual fuel burn sensitivities from Figure 3.106 yields the overall fuel burn and cycle trade, shown in the lower right. The minimum fuel burn occurs near a FPR of 1.42 corresponding to a BPR of approximately 15.

3.2.4.1 Cryogenic Results

The cryogenically driven system results are similar in nature to the non-cryogenic ones; therefore, an in-depth investigation will be avoided; however, the benefit to the cycle is apparent, as shown in Figure 3.107. Again, the deltas are relative to the same points as shown in Figure 3.106 to facilitate comparison between the cryogenic and non-cryogenic systems.

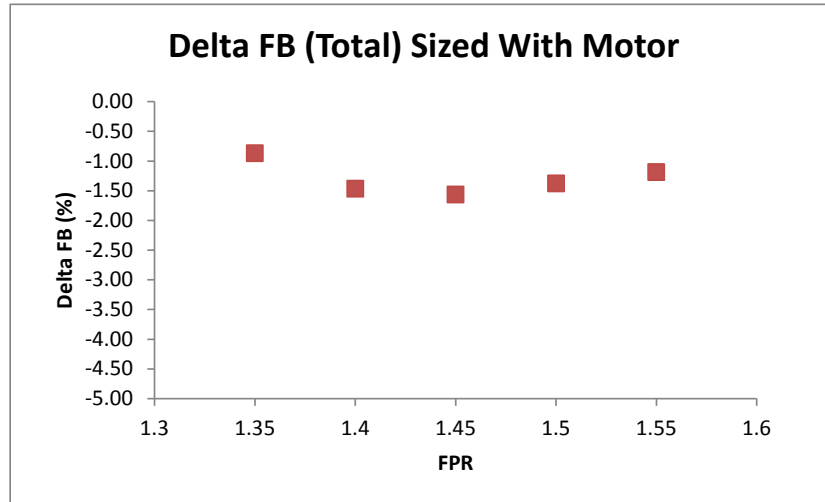


Figure 3.107 – Cryogenic Cycle Trades

Figure 3.108, shows the breakdowns between the various trades underlying Figure 3.107. Of note is that the increased efficiency of the cryogenic components results in the elimination of approximately 3% of the energy usage relative to conventional components. This trades as just over 0.5% vehicle fuel burn, shown in the lower right of Figure 3.108. However, this efficiency increase is offset somewhat by the need to power the cryocooler and carry the heavier cooling equipment.

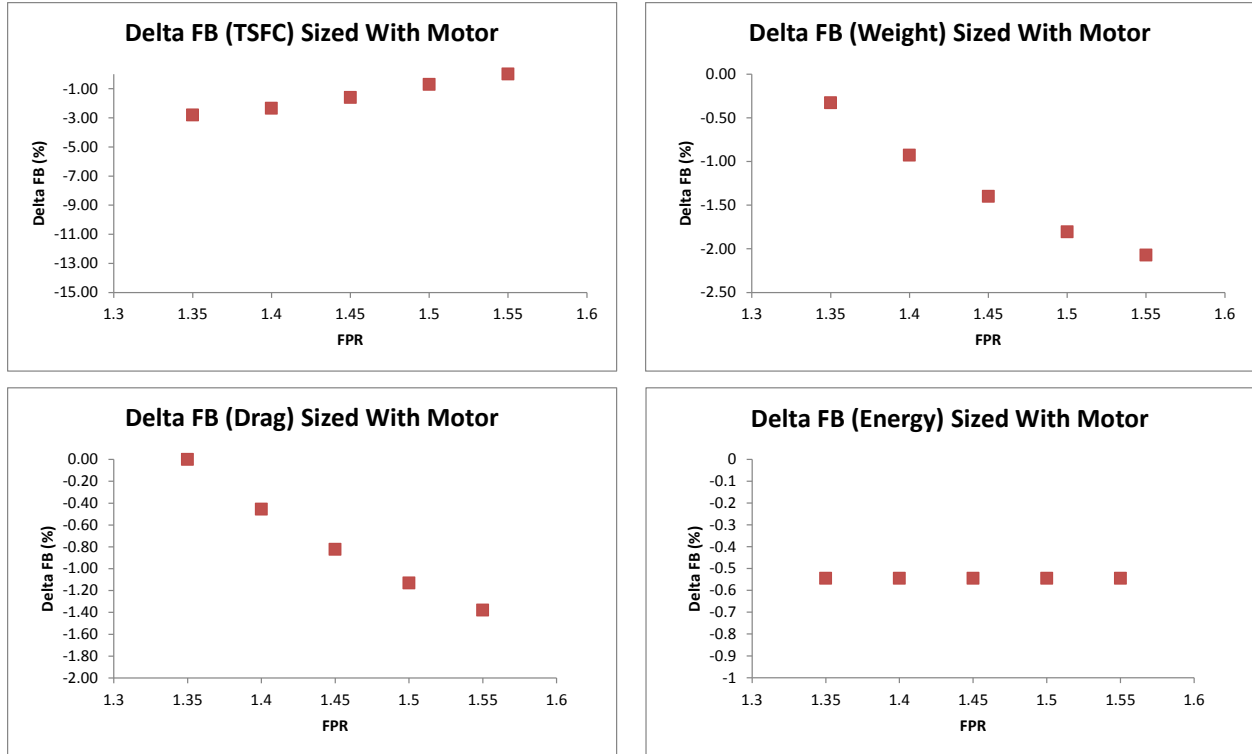


Figure 3.108 – Cryogenic System Sizing

The cryogenic system provides a 1.5% decrease in fuel burn for the motor-sized case.

3.2.4.2 Engine Sizing Method Trades

In order to provide a clearer picture of the trades associated with sizing the hybrid engine and the differences between cryogenic and conventional electric systems, four sets of data have been overlaid in Figure 3.109. The engine has been sized with and without the motor turned on at the sizing condition (top of climb). Evaluations have been made for both the cryogenic and conventional systems. Since extraction ratio is held constant, lowering FPR leads to a rise in bypass ratio. A few observations are immediately apparent. First, there is little variation in the slopes of the four engines with varying fan pressure ratio which means switching to a cryogenic system has little impact on the choice of FPR. Second, sizing with the motor turned on results in a 2% fuel burn reduction for the conventional motor system and a 1% reduction in fuel burn for the cryogenic variant.

The first observation is more easily explained. From an engine viewpoint the electric system manifests itself as a torque applied to the low pressure shaft. The engine cycle is invariant to where the power to drive the motor comes from, or how efficient the electric systems are. As FPR (and therefore BPR) is varied, the electric system remains the same size for a given motor horsepower. These two effects mean that electric system differences in weight and efficiency manifest themselves through the vehicle level trades, as shown in Table 3.24.

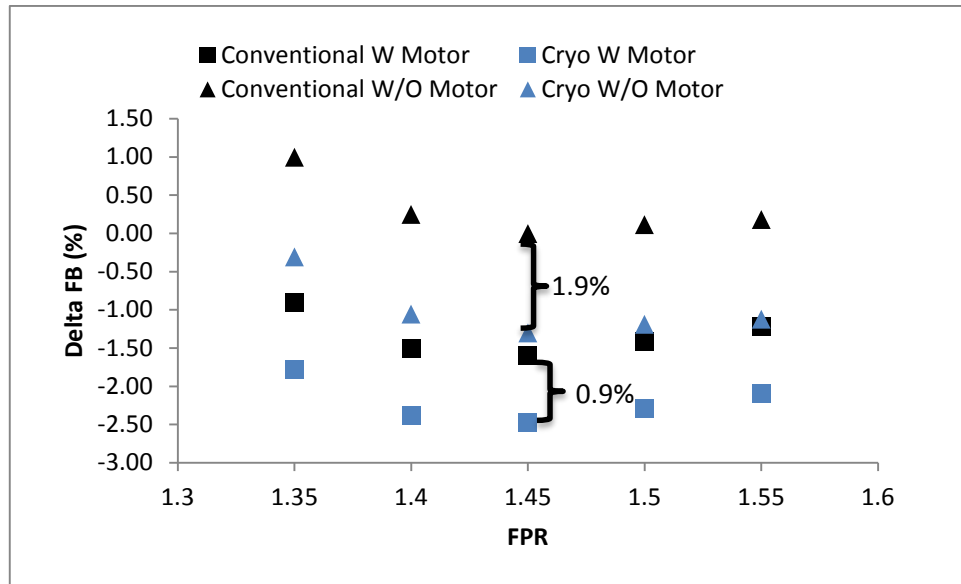


Figure 3.109 – FPR Electric and Sizing Trades

The second trend showing decreased TSFC with increasing motor power merits a more in depth explanation. Table 3.25 a more detailed listing of relevant cycle parameters for the conventional system at FPR 1.45 from Figure 3.109. Only the conventional electric system is shown for simplicity of discussion. The trends and underlying explanation is valid for the cryogenic system too. Since the engine is being sized to a constant top of climb thrust, the addition of 1,380 hp of motor power during sizing means a smaller engine core is required to provide fan power.

Table 3.25 – Core Sensitivity to Sizing With Motor (60 OPR, 2500R T41, FPR 1.45)

Parameter	Conv-W	Conv-W/O
BPR (design)	13.3	10.6
Cruise TSFC (lbm/lbf-hr)	0.340	0.345
Corrected Core Size (lbm/s)	43.8	47.8
Cruise Core Flow (% max)	79.4	77.6
OPR (cruise)	39.46	33.2
T41 (deg R, cruise)	2265	2130

As a result the bypass ratio of the engine increases, leading to a decrease in TSFC. This explains the benefit of sizing the core with the motor turned on; however, there are other benefits. In Table 3.25, the corrected core size indicates the corrected weight flow entering the high pressure compressor at the top of climb condition. Both top of climb conditions have a 2500 degree Rankine T4.1. In the case of the motor turned on during sizing, *Conv-W*, the flow is smaller since the power needed to drive the fan is being partially supplied by the electric motor. In the engine sized without the motor, *Conv-W/O*, the core is larger since it must supply

all of the fan power. The difference in core size has a large effect on part-power operation (cruise). Since the *Conv-W* core is smaller, it can run closer to its full power, peak efficiency point at cruise when the motor power is turned on. This leads to higher OPR and higher component efficiency. Conversely, the *Conv-W/O* engine reacts differently at part-power. Since the core was sized without motor power it must be operated at a lower power setting at cruise. This results in lower percentage flow and lower OPR, leading to a less thermally efficient core at cruise which lowers the TSFC benefit of electric operation. As a side note, the smaller core, while more efficient, does have a higher T41 by almost 130 degrees. This is a maintenance and operational cost that cannot be neglected; however, full assessment of this impact is outside the scope of this study.

There are negative consequences to sizing the core with the motor turned on; however, to fully understand these issues, the overall pressure ratio, T41 space must also be explored. The results of varying T41 between 2,500 and 3,000 degrees Rankine and OPR from 50 to 65, both at the top of climb sizing point, are shown in Figure 3.110. Sensitivities were run at a FPR of 1.45, since it corresponds to the optimum FPR from Figure 3.109.

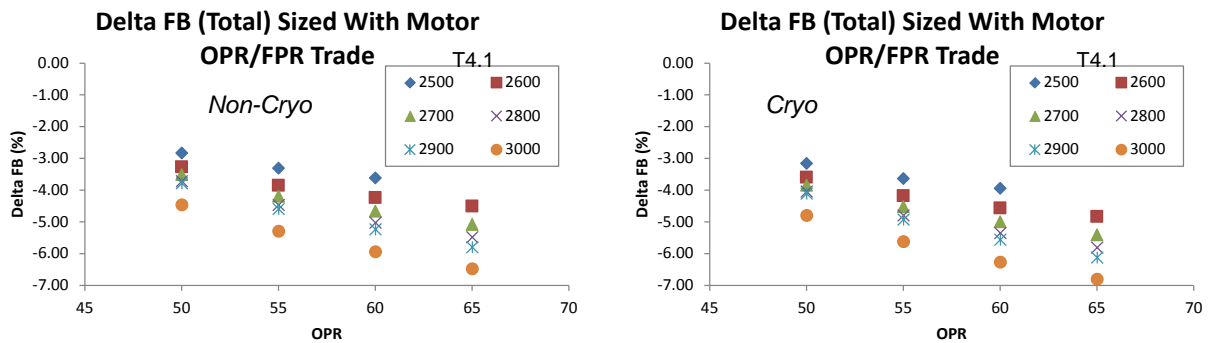


Figure 3.110 – OPR / T41 Trade Space

As was the case for the FPR trade, there is no discernable effect of optimal cycle selection as a function of the electrical system. The cryogenic system is about 1% better depending on cycle, as is the case in the FPR trade space. In order to better understand the results the T41/OPR trade space is reduced to four runs. OPR sweeps are generated for 2,500 and 3,000 degrees T4.1 while sizing the engine with and without the electric motor, designated as W and W/O respectively. The results are shown in Figure 3.111. Some of the trends are familiar, the blue dots, indicating the 2,500 degree T41, show an optimum OPR of approximately 60. The higher T41 of 3,000 degrees leads to an optimum OPR of ~80 if the trends are extrapolated. Conventional sizing trends dictate higher T41 is needed to maximize core specific power and minimize weight as OPR is increased. This trend is independent of whether or not electric motor power is applied during sizing, suggesting that the core may be designed and optimized in isolation of hybrid electric propulsion. Since the electric motor off-design performance is

primarily driven by flow capacity through the core, it could be possible to design a core for a non-hybrid-electric engine and then adapt it to a hybrid electric configuration by changing its flow capacity via the HPT stage one nozzle area.

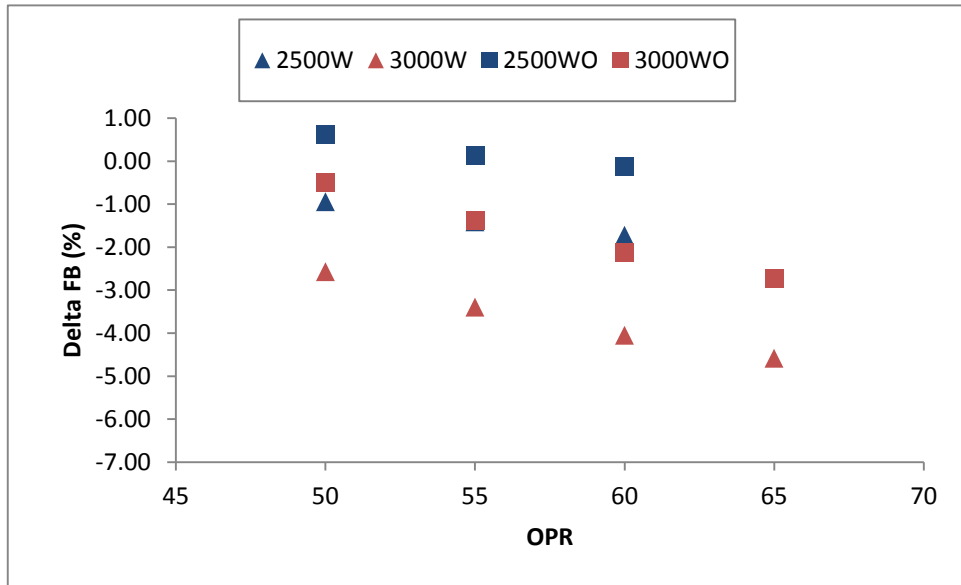


Figure 3.111 – OPR/T41 Electric and Sizing Trades

Also apparent in Figure 3.111 is that sizing with the motor turned on is approximately equivalent to 500 degrees of firing temperature. This is most evident at the 55 OPR point where the red and blue markers overlap, but is also present throughout the space. This suggests that while the smaller core sized with the motor tends to burn hotter in cruise, it may still burn cooler than the equivalent higher T4 design point. At this point it is worth recalling that these results are all for the case of a highly advanced, uncooled turbine. Additional cooling required at higher temperatures may offset the effects from higher T4, meaning sizing with the electric motor may look even more favorable.

Finally, there are negative consequences of sizing the core with the electric motor included. Table 3.26 shows data extracted for the 50 and 60 OPR points shown in Figure 3.111. Recall, the results shown up to this point show fuel burn benefits assuming the electric motor is operating at cruise; however, this will not always be the case. In Table 3.26, the Cruise Penalty column shows the fuel burn detriment of running the engine sized with the motor in all fuel mode. In other words, since the core is small, it must operate in an overspeed condition to drive the fan. For this study, the amount of overspeed varies according to the cycle, but is approximately 102% corrected speed at the cruise condition and 108% at the top of climb condition. While including the motor power when sizing the core leads to up to a 1.6% fuel burn benefit when flying in all electric mode, the downside is up to a two percent increase in fuel burn when flying

in all electric mode. The top of climb fuel consumption is increased up to 6% when flying in all fuel mode.

Table 3.26 – All Fuel Penalties for Smaller Core

OPR	Design T41	Cruise Penalty (All Fuel)	Cruise Benefit (All Electric)
50	2500 R	1.6%	1.56%
	3000 R	1.3%	2.07%
60	2500 R	1.6%	1.6%
	3000 R	1.1%	1.96%

3.2.4.3 Hybrid Electric Trade Study Conclusions and Recommendations

The parametric investigation into the cycle design space of the hybrid electric turbofan configuration has revealed many interesting results. First, the impacts of electric system efficiency and weight manifest themselves at the aircraft level since they are independent of the engine cycle. As a result the engine cycle can be selected without regards to the electrical system setup. Further studies should be examined with varying motor sizes to verify this trend, but is expected to remain consistent with the results presented here. As a result the differences between cryogenic and conventional electric systems are relatively small. The differences are expected to be larger for larger electric motors since they will contribute to a larger amount of vehicle weight.

Second, the impact of the sizing method of the core on fuel burn has been investigated. Sizing the core with the electric motor turned on leads to a smaller core that is more efficient at cruise since it can operate closer to its design point. Unfortunately, this leads to a fuel burn penalty when operating in all fuel mode since the core must overspeed in order to provide cruise and top of climb thrust. While this study examined sizing the core with all or none of the electric power available, further design iterations should focus on determining the optimum intermediate values of electric power applied during sizing. This should be optimized in consideration with the entire vehicle sizing process.

It was also found that smaller high temperature cores are less sensitive to the effects of core sizing method since the flow lapse is smaller and more energy comes from combustion than mass flow. This leads to the conclusion that advanced materials and cooling techniques will remain important with hybrid electric architectures.

Finally, this engine trade study was performed for a fixed motor size and optimized for a single aircraft mission. Since the amount of electric power available on board the aircraft will be a function of flight length, a full optimization over all mission lengths is suggested for future studies. It may be worth taking a fuel burn penalty in all fuel mode, which would be required for longer stage lengths, if the fuel savings on more numerous short range missions proves beneficial from a fleet perspective. Performing such a study requires a wholly integrated engine and airframe sizing tool of which this parametric NPSS tool suite is an important step.

4.0 Summary

4.1 Performance and Sizing Analysis

The SUGAR Volt aircraft was analyzed and the battery and electrical energy usage were optimized to minimize fuel burn and manage battery energy. Two distinct versions of the aircraft were developed:

A “Balanced” aircraft sized the electric motor and batteries to be used relatively evenly over most of the 900 nm mission. This aircraft was approximately 140,000 lb TOGW, used a 1750 HP electric motor, and assumed 750 Wh/kg batteries. This aircraft reduced fuel burn by 60% & energy use by 54% (Goal 60% reduction from the SUGAR Free current technology baseline).

A “Core shutdown” version sized the electric motor for cruise on 100% electric power for at least part of the cruise leg and used more batteries. The TOGW was allowed to grow up to 190,000 lb TOGW. The aircraft used a larger 7150 HP electric motor. This aircraft was able to reduce fuel burn by 64% & energy use by 46% (Goal 60% reduction).

4.2 Emissions Analysis

Landing and takeoff emissions analysis conducted by GE resulted in levels 89%-93% below CAEP/6 (Goal 80% reduction). Compared to the reference CFM-56 engine, cruise NO_x was reduced 74% (Goal 80% reduction) for 1750 HP “Balanced” aircraft and eliminated for 7150 HP “Core shutdown” aircraft for part of the cruise segment. For the “Core shutdown” aircraft with the 900 nm range mission, approximately 50% of the cruise leg can be flow with electric power and no emissions. The SUGAR Volt maintains a total lifecycle emissions advantage (CO₂ and NO_x) if charging electricity is from a clean source.

4.3 Noise analysis

The more detailed noise analysis resulted in quieter aircraft (24 to 31 dB below stage 4) than the less detailed assessment in Phase I. The engine noise was dominated by the fan and jet sources, so reducing the core noise from more electric use resulted in only a small benefit compared to a conventional propulsion system. Although a range of additional airframe noise reduction technologies were identified, the aircraft was not able to achieve the NASA noise goal of 52 dB below stage 4.

4.4 Energy cost analysis

The SUGAR High aircraft was shown to reduce fuel and energy cost by 54% and total cost by 29% relative to SUGAR Free Baseline. The SUGAR Volt showed an additional 6-14% reduced direct energy cost (fuel + electricity) relative to SUGAR High, depending on the future energy

cost scenario selected. However, including costs for increased aircraft weight and complexity reveals little change in SUGAR Volt total cost relative to SUGAR High.

4.5 Technology Plans and Roadmaps

Technology plans and roadmaps for hybrid electric engines and batteries were updated.

4.6 Hybrid Electric Propulsion Modeling Environment

Highly detailed propulsion component models were developed as NPSS elements. These elements were integrated into a hybrid electric modeling environment and exercised on sample engine trade studies.

4.7 Conclusions

The SUGAR Volt, with hybrid electric propulsion, produces significant additional emissions and fuel burn reductions beyond those levels achieved by SUGAR High.

Total energy usage is not decreased with hybrid electric propulsion, but reduced energy cost can be achieved for some energy cost scenarios.

The SUGAR study has identified technologies to reduce noise, but was not able to define a path to meeting the NASA noise goals.

4.8 Recommendations

- 1) Define in detail the next technical maturation steps for the hybrid electric engine technology. Determine what can be done on a modest initial budget.
- 2) Understand shared technologies with HEDP (Hybrid Electric Distributed Propulsion).
- 3) Conduct a battery/electric system integration study to address integration issues (including inlets and exhausts for air batteries and fuel cells).
- 4) Perform an installation study with a lower fan pressure ratio engine and other airframe and engine technologies for improved acoustics. Determine how close to the noise goal is achievable. Consider revising the noise goal.
- 5) Consider support of small aircraft hybrid electric demonstrations. Understand the tradeoffs of cost and technical risk reduction value and learning.

References

1. **Bradley, Marty K. and Droney, Christopher K.** *Subsonic Ultra Green Aircraft Research: Phase I Final Report*. s.l. : NASA, 2011. CR-2011-216847.
2. **Bradley, Marty and Droney, Christopher K.** *SUGAR Phase II: N+4 Advanced Cocnept Development*. s.l. : NASA, 2012.
3. **Bonet, John.** *Environmentally Responsible Aviation (ERA) Project - N+2 Advanced Vehicle Concepts Study and Conceptual Design of Subscale Test Vehicle (STV)*. s.l. : NASA, 2011. CR-2011-216519.
4. *Progress Toward the N+2 Noise Goal: HWB Propulsion Airframe Aeroacoustics Boeing/NASA Low Speed Aeroacoustics Facility Experiment and System Noise Assessment*. **Thomas, R. H. and Burley, C. L.** Atlanta, Georgia : NASA Fundamental Aeronautics Program, 2009. Vol. Third Annual Meeting.
5. **Guo, Y. P.** *Aircraft Slat Noise Modeling and Prediction*. s.l. : AIAA, 2010. AIAA 2010-3837.
6. —. *Aircraft Flap Side Edge Noise Modeling and Prediction*. s.l. : AIAA, 2011.
7. —. An Improved Landing Gear Noise Prediction Scheme. 2006. NASA/CR NAS1-NNL04AA11B Task NNL06AB63T.
8. **Roskam, Jan.** *Airplane Design, Part VIII: Airplane Cost Estimation: Design, Development, Manufacturing and Operating*. s.l. : DAR Corporation, 2002.
9. **Masson, P and Ishmael, S A.** NASA Glenn Superconducting Machine Sizing Model and Design Tool Development. Oct 21, 2009.
10. **Hitachi.** IGBT Module MBN2400E17D. [Online] [Cited: August 30, 2013.] <http://www.hitachi.co.jp/products/power/pse/images/pdf/igbt/MBN2400E17D.pdf>.
11. *Cryogenic Power Converter Module Performannce*. **Hennesy, M. J., et al., et al.** 2006. International Cryogenic Materials Conference.
12. *Selecting film bus link capacitors for high performance inverter applications*. **Salcone, M. and Bond, J.** Miami : s.n., 2009. Electric Machines and Drives Conference.
13. *Efficiency consideration of DC link soft-switching inverters for motor drive applications*. **Lai, J. S., Young, R. W. and McKeever, J. W.** Taipei : s.n., 1994. IEEE Power Electronics Specialists Conference.

14. *12 - kV p-Channel IGBTs With Low On-Resistance in 4H-SiC*. **Zhang, Qingchun, et al., et al.** 9, 2008, IEEE Electron Device Letters, Vol. 29, pp. 1027 - 1029.
15. *12.9 kV SiC PiN diodes with low on-state drops and high carrier lifetimes*. **Sundaresan, Siddarth, et al., et al.** 2012, Materials Science Forum, Vols. 717-720, pp. 949-952.
16. **Thor Power**. Power Factor vs. Output Power. [Online] 2010. [Cited: September 3, 2013.] <http://www.thor-power.com/technique/power-factor-vs-output-power/>.
17. **Krishnan, R.** *Switched Reluctance Motor Drives*. Boca Raton : CRC, 2001.
18. **Hall, Edilberto and Ramamurthy, Juan.** *Design of a Switched Reluctance Motor Drive For Electric Propulsion*. Fayetteville : University of Arkansas, 1998. Grant No. N000014-98-1-0617; Proj No. 98PR05665-00.
19. **Ban, Drago.** *State of the Art and Tendency For Increased Power Efficiency of Electric Machines and Drives*. Croatia : University of Zagreb, 2009.
20. **Vranick, James.** *Prediction of Windage Power Loss in Alternators*. 1968. NASA TN D-4849.
21. *Losses in High Speed Permanent Magnet Machines Used in Microturbine Applications*. **Huynh, C, Zheng, L and Acharya, D.** March, s.l. : Journal of Engineering for Gas Turbines and Power, 2009, Vol. 131.
22. **DiRenzo, Michael.** *Switched Reluctance Motor Control - Basic Operation and Example Using the TMS320F240*. s.l. : Texas Instruments, 2000. Application Report No. SPRA420A.
23. *Modeling of Overpotentials in an Anode-Supported Planar SOFC Using a Detailed Simulation Model*. **Henning, Severson and Mohsen, Assadi.** s.l. : Journal of Fuel Cell Science and Technology, Oct 2011, Vol. 8.
24. *Development of a Solid-oxide Fuel Cell/Gas Turbine Hybrid System Model for Aerospace Applications*. **Freeh, Joshua E, Pratt, Joseph and Brouwer, Jacob.** [ed.] ASME. s.l. : Proceedings of ASME Turbo Expo, 2004.
25. *Solid Oxide Fuel Cell/Gas Turbine Hybrid Cycle Technology for Auxiliary Aerospace Power*. **Freeh, Joshua E, Steffen, Christopher and Larosiliere, Louis.** s.l. : ASME, 2005, Proceedings of ASME Turbo Expo 2005.
26. **Joshua, Freeh E, Steffen, Christopher and Larosiliere, Louis.** *Off-Design Performance Analysis of a Solid-Oxide Fuel Cell/Gas Turbine Hybrid for Auxiliary Aerospace Power*. s.l. : NASA/TM-2005-213805.

27. **Tornabene, Robert.** *Development of Parametric Mass and Volume Models for an Aerospace SOFC/Gas Turbine Hybrid System.* s.l. : NASA/TM-2005-213819.
28. **Mak, Audie and Meier, John.** *Fuel Cell Auxiliary Power Study, Volume 1: RASER Task Order 5.* s.l. : NASA/CR-2007-214461/VOL1.
29. **Larminie, James and Dicks, Andrew.** *Fuel Cell Systems Explained.* New York : Wiley and Sons, Inc., 2000.
30. **Gordon, S and McBride, B J.** *Computer Program for Calculation of Complex Chemical Equilibrium Compositions , and Applications.* s.l. : NASA RP-1311, 1994/1996. Parts I and II.
31. **O'Hayre, Ryan.** *Fuel Cell Fundamentals.* Hoboken : John Wiley & Sons, Inc., 2009.
32. **Li, Xianguo.** *Principles of Fuel Cells.* New York : Taylor & Francis, 2006.
33. **Vincent, et al., et al.** *Modern Batteries: An Introduction to Electrochemical Power Sources.* Baltimore : Edward Arnold, 1984.
34. **Swift, Walter.** *Preliminary Design for a Reverse Brayton Cycle Cryogenic Cooler: Phase I Final Report.* Hanover, NH : Creare Inc., Creare Inc., December 10, 1993. Contract #NAS5-31281.
35. *Second-Law Analysis of a Hybrid Reverse Brayton Stirling Cryocooler.* **Nieuwkoop, A, et al., et al.** [ed.] S D Miller and R J Ross Jr. Boulder : Co, 2009. International Cryocooler Conference. Vol. Cryocoolers 15.
36. **Blythe, A.** Potential Application of Advanced Propulsion Systems to Civil Aircraft. *Journal of Aircraft.* 1988, Vol. 25, 2.
37. **Hager, R. D. and Vrabel, D.** *Advanced Turboprop Project.* s.l. : NASA, 1990. SP-495.
38. **Hogg, G. E.** *Experimental Performance and Acoustic Investigation of Modern, Counterrotating Blade Concepts.* s.l. : NASA, 1990. CR-185158.
39. **Gilman, J.** *Propeller Performance Charts for Transport Airplanes.* s.l. : NACA, 1953. TN-2966.
40. **Hamilton - Standard.** *Generalized Method of Propeller Performance Estimation.* s.l. : Hamilton - Standard, 1963. PDB6101.
41. **SAE.** *Real-Time Modeling Methods for Gas Turbine Engine Performance.* s.l. : SAE, 2008. AIR4548a.
42. **Perkins, C. D. and Hage, R. E.** *Aircraft Performance Stability, and Control.* s.l. : Wiley, 1949.

43. **De George, C. L.** *Large-Scale Advanced Prop-Fan (LAP) Final Report.* s.l. : NASA, 1988. CR-182112.
44. **Dittmar, J. H. and Stang, D. B.** *Cruise Noise of the 2/9th Scale Model of the Large-Scale Advanced Propfan (LAP) Propeller, SR-7A.* s.l. : NASA, 1987. TM-100175.
45. **Mikkelson, D. C., et al., et al.** *Design and Performance of Energy Efficient Propellers for Mach 0.8 Cruise.* s.l. : NASA, 1977. TM X-73612.
46. **Black, D. M., Menthe, R. W. and Wainauski, H. S.** *Aerodynamic Design and Performance Testing of an Advanced 30 Swept, Eight Bladed Propeller at Mach Numbers from 0.2 to 0.85.* s.l. : NASA, 1978. CR-3047.
47. **Jeracki, R. J., Mikkelson, D. C. and Blaha, B. J.** *Wind Tunnel Performance of Four Energy Efficient Propellers Designed for Mach 0.8 Cruise.* s.l. : NASA, 1979. TM-79124.
48. **Stefko, G. L. and Jeracki, R. J.** *Wind Tunnel Results of Advanced High-Speed Propellers at Take-off, Climb, and Landing Mach Numbers.* s.l. : NASA, 1989. TM-87030.
49. **Rohrbach, C., et al., et al.** *Evaluation of Wind Tunnel Performance Testings of an Advanced 45 Swept Eight-Bladed Propeller at Mach Numbers from 0.45 to 0.85.* s.l. : NASA, 1982. CR-3505.
50. **De George, C. L., Turnberg, J. E. and Wainuski, H. S.** *Large Scale Advanced Prop-Fan (LAP) Static Rotor Test Report.* s.l. : NASA, 1987. CR-180848.
51. **Campbell, W. A., Arseneaux, P. J. and Wainauski, H. S.** *Large Scale Advanced Prop-Fan (LAP) High Speed Wind Tunnel Test Report.* s.l. : NASA, 1988. CR-182125.
52. **Parzych, D., Shenkman, A. and Cohen, S.** *Large Scale Advanced Propfan (LAP) Performance, Acoustic, and Weight Estimation.* s.l. : NASA, 1985. CR-174782.
53. **Bradley, M., et al.,.** *Boeing N+3 SUGAR Year 2 Review.* Hampton, VA : s.n., 2013. Presentation.
54. *Gas Turbine Engine Steady-State and Transient Performance Presentation for Digital Computer Programs.* 1997. AS681H.
55. **Welge, R., et al.** *N+2 Supersonic Concept Development and Systems Integration.* 2010. NASA/CR-2010-216842.
56. **Brown, G.,.** *Efficient Flight-Weight Electric Systems.* 2012. Technical Conference: NASA Fundamental Aeronautics Program, Cleveland.

Subsonic Ultra Green Aircraft Research – Phase II

Volume II – Appendix A – Georgia Tech Propeller Performance Maps and Reference Sheets

Contract Number: NNL08AA16B
Task Order: NNL11AA00T

6/30/2014

Prepared by:
GEORGIA INSTITUTE OF TECHNOLOGY

Prepared for:
Erik Olson
NASA Langley Research Center

Propeller Performance Maps

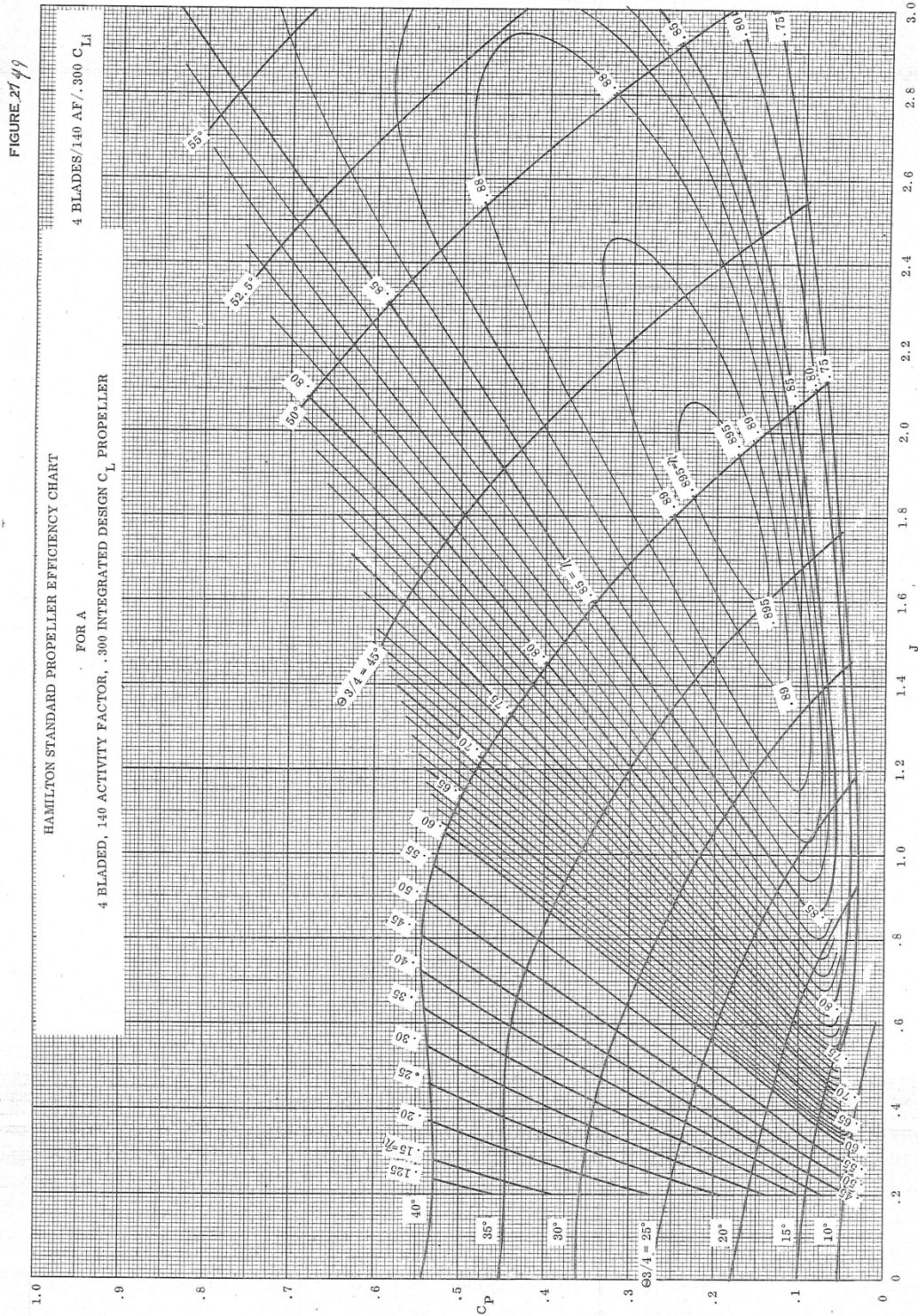


Figure 1 Hamilton - Standard Propeller Performance Map for 4 Blades, AF 140, and C_{Li} 0.3

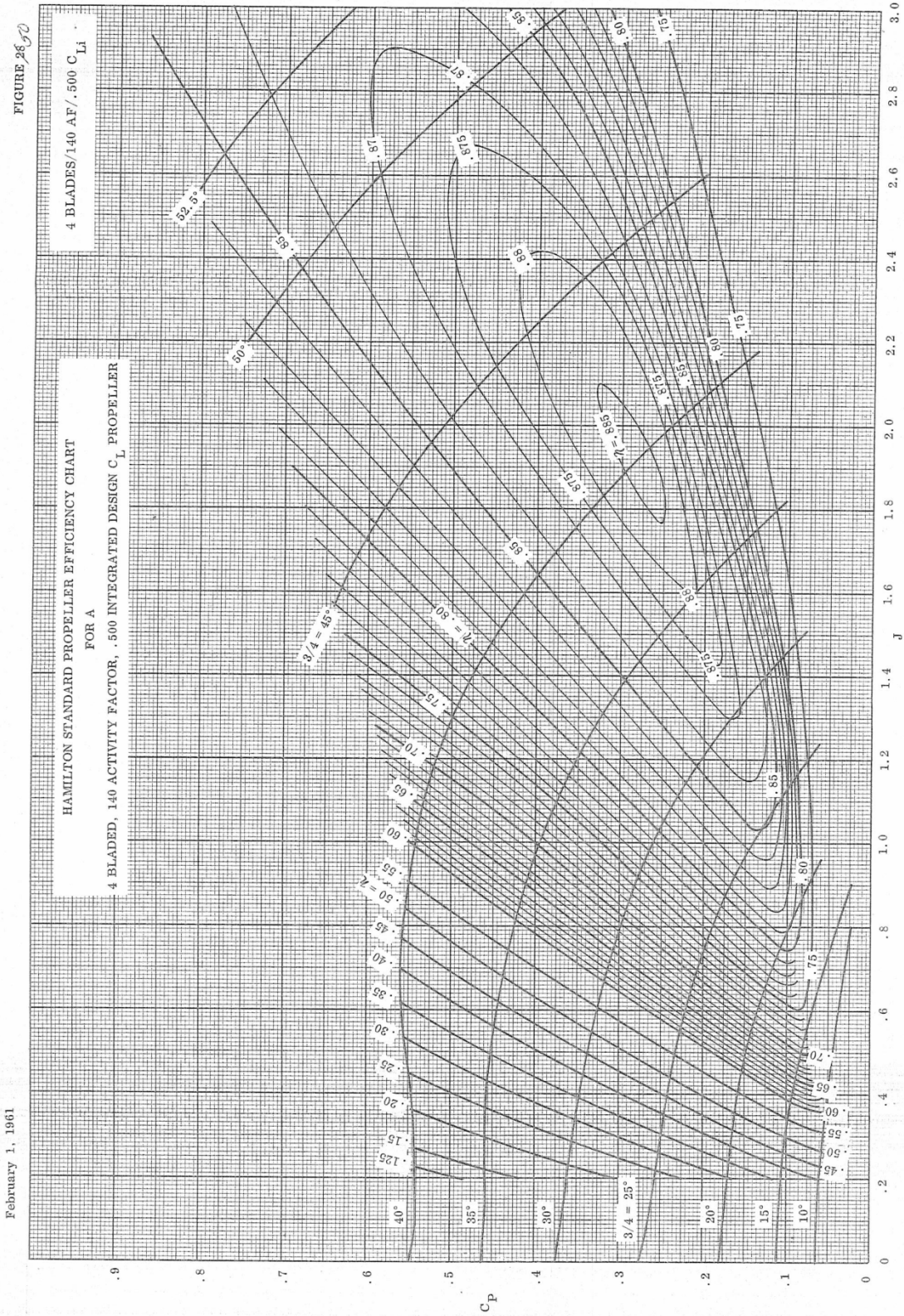


Figure 2 Hamilton – Standard Propeller Performance Map for 4 Blades, AF 150, and C_{Li} 0.5

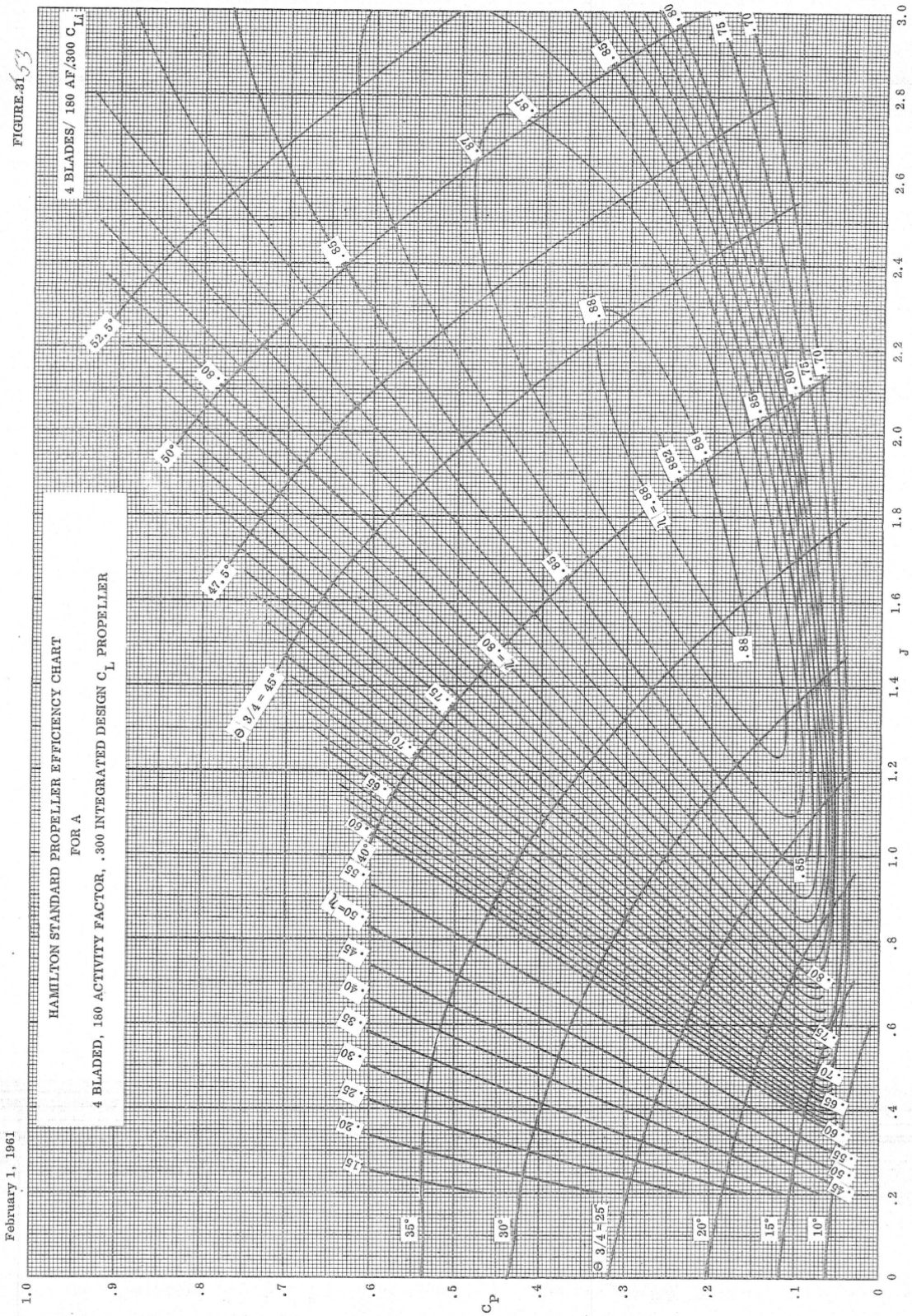


Figure 3 Hamilton - Standard Propeller Performance Map for 4 Blades, AF 180, and C_{Li} 0.3

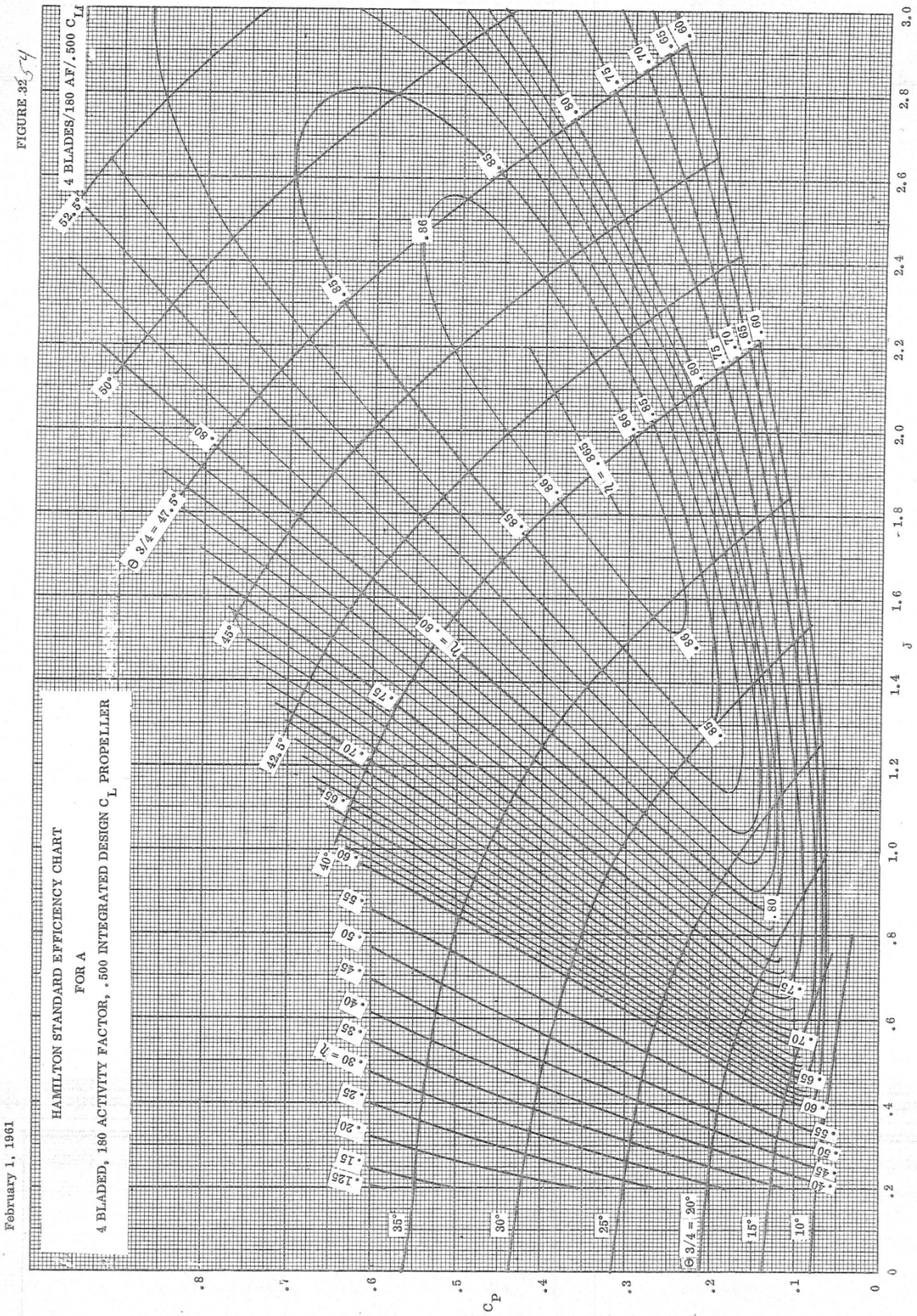


Figure 4 Hamilton - Standard Propeller Performance Map for 4 Blades, AF 180, and C_{Li} 0.5

NPSS Element Reference Sheets

Battery



Socket Name: S_weight
 Socket Type: BATTERY_WEIGHT
 Returns: StackWeight, StackVol

Socket Name: S_heat
 Socket Type: BATTERY_HEAT
 Returns:

Socket Name: TB_current
 Socket Type: Function
 Returns:

Battery calculates the size, layout, weight, and volume of a battery stack and evaluates the performance of a stack given the layout and a current load.

Variables

Variable	Description	Default	Units	IO Status
Capacity				
CapDis	Percent of battery charge left as reserves	0	none	input
CapDisBattDesPower	Nominal capacity of one cell	0	none	input
CapDisLimit	Total current draw during design power load	0	none	input
CurrBatt	Current drawn from each cell			output
Current	Current drawn from the stack	0	none	input
DesPower	Design power load	0	none	input
dischargeInterval	Time interval for performance analysis			
ExpZoneAmp	Voltage lost over exponential zone of discharge curve	0	none	input
ExpZoneTimeConst	Time constant for exponential zone of discharge curve	0	none	input
FlightTime	Duration of the period when batter will be operating	0	none	input
k_1	Technology factor for	1	none	input
k_2	Technology factor for	1	none	input
k_3	Technology factor for	1	none	input
k_4	Technology factor for	1	none	input
k_5	Technology factor for	1	none	input
Ncells	Number of cells in sized battery stack	1	none	output
NewStateOfCharge	State of charge of the battery after			output
NoLoadVoltage	No-load constant voltage of battery	0	none	input
Nparallel	Number of cells in parallel in sized battery stack	1	none	output
Nseries	Number of cells in series in sized battery stack	1	none	output

PolarizationVoltage	Voltage lost due to polarization in discharge curve	0	none	input
Qgen	Heat generated by battery			output
Resistance	Internal resistance of individual cell	0	none	input
StackWeight	Weight of sized battery stack	0	none	output
StackVol	Volume of sized battery stack	0	none	output
StateOfCharge	Initial charge remaining in battery			
TimeDesPower	Time of design power load	0	none	input
timeStep	Interval for trapezoidal integration of load profile			
Voltage	Stack voltage			output
VoltageBatt	Cell voltage			output

Option Variables

Name	Description	Variables IOStatus Affected	Default	Allowed Values
switchDes	Design/Offdesign switch	Ncells, Nseries, Nparallel, Current	DESIGN	DESIGN, OFFDESIGN

Functions

Prototype	Description
void calculate()	None
void variableChanged(string name, any oldVal)	None

Ports and Internal Stations

Port/Station	Type	Description
OUTPUT	DataOutputPort	Electric signal from battery

Independents

Name	Description	Default	Active When
ind_current	Current draw on the battery	Current	Always

Sockets

Socket	Description	socketType	Sets Values
TB_current	Current load profile table	Function	
S_weight	Stack volume and weight socket	BATTERY_WEIGHT	StackWeight, StackVol

Usage Notes

Battery

- In design mode, the element provides a single-pass sizing calculation using a current load profile and a design power load. The load profile is input as a table and is required to have values for the current until the end of the flight. Extrapolation of values is strongly discouraged. A weight and volume calculation is performed in the BatteryWeight subelement based on the parameters calculated during sizing.

- The energy discharged over the flight is calculated using a trapezoidal numerical integration of the load profile with constant time intervals set by the variable "timeStep." This integration is performed twice, once over the entire flight, and once from the beginning of the flight to the time of the design power load.

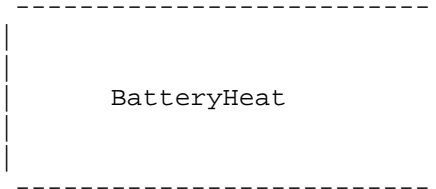
- The number of cells in the stack arranged in parallel is determined by the energy capacity necessary for the flight. The total number of cells is calculated from the design power load. The values are rounded up to the nearest cell. The number of cells in series is calculated based on those two values. The final sized stack is assumed to be a full array. This is achieved through a recalculation of the total number of cells as a product of the number in series with the number in parallel

- $N_{cells} = N_{series} * N_{parallel}$

- In offdesign mode the voltage calculation is performed as a function of the current load and the state of charge of the battery. The calculation determines the voltage output of a single cell, and then the voltage of the entire stack is found based on the input layout.
- Technology factors can be applied to battery performance parameters to accommodate projections of future batteries. Default values of the factors are one, signifying present performance.
- The output port transfers a four-element array of voltage, current, frequency, and phase. Since a battery provide direct current (DC) electricity, the frequency and the phase are both zero (0).

Battery has a baseType of Element.

BatteryHeat



BatteryHeat calculates the heat generated due to the operation of the battery stack.

Variables

Variable	Description	Default	Units	IO Status
Qgen	Heat generated by the battery during operation	0	none	OUTPUT

Functions

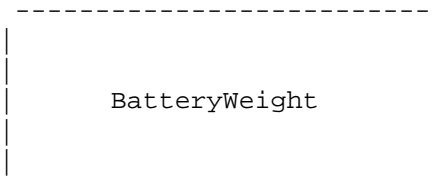
Prototype	Description
void calculate()	None

Usage Notes

BatteryHeat

- Heat is calculated as the power output by a single battery due to internal resistance. This is multiplied by the number of cells to obtain the heat generated by the stack.
- $Q_{gen} = N_{cells} * Curr_{Batt}^2 * Resistance;$

BatteryWeight



BatteryWeight calculates the weight and volume of the battery stack using the specific energy and power density.

Variables

Variable	Description	Default	Units	IO Status
SpecEnergy	Specific energy of battery	0	none	input
PowerDensity	Power density of battery	0	none	input
PowerBattNom	Nominal power of battery	0	none	input
VoltageNominal	Nominal voltage of battery	0	none	input

Functions

Prototype	Description
void calculate()	None

Usage Notes

SOFC_new



Socket Name: S_heat
 Socket Type: SOFC_HEAT
 Returns: qGen, qNet, qNet_total

Socket Name: S_weight
 Socket Type: SOFC_WEIGHT
 Returns: totalWeight, totalVol

Battery calculates the size, layout, weight, and volume of a battery stack and evaluates the performance of a stack given the layout and a current load.

Variables

Variable	Description	Default	NPSS (Actual Units)	Units	IO Status
Capacity	Nominal capacity of a single cell	6.8	none (amp-hr)		

Sockets

Socket	Description	socketType	Sets Values
s_heat	System heat socket	SOFC_HEAT	qGen, qNet, qNet_total
s_weight	System volume and weight socket	SOFC_WEIGHT	totalWeight, totalVol

Usage Notes

SOFC_new

- SOFC_new calculates the performance of a solid oxide fuel cell by determining the ideal voltage of the cell and subtracting electrochemical losses from it. The losses calculated in the model are activation losses, ohmic or resistive losses, and concentration or mass transfer losses.

- The losses are calculated based on either direct inputs or first principles. For direct inputs, exchange current density, area specific resistance, and limiting current density are input as values. If first principles are used, the values are calculated using material properties such as diffusion and resistivity of the fuel cell components. The equations that use first principles can be "turned on" individually based on what properties the user knows.

- For all calculations with partial pressures, the model is currently set to use the partial pressures at the outlet of the electrodes. If the user desires to change this the source code would have to be changed, there is no switch built in.

-The sizing of the fuel cell stack is based on the power output at a design current density. The stack is sized to a design power load at the design point. The sizing not only gives the stack size, but also the fuel and oxidizer flows that match the operating conditions declared by the user.

-For design analysis the model can determine the size of the stack given a power load and an interconnect efficiency, the power output given a stack and efficiency, or an efficiency if the stack size and power required are input.

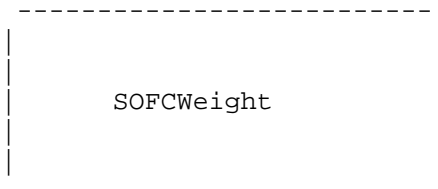
-For off-design, the model can keep a constant stoichiometry, or ratio between the fuel and the air, or constant flows. These flows would need to be determined by the sizing code first.

- The oxygen and hydrogen fuel flows and mole fractions are dependents whenever stoichiometric analysis is performed, both for design and off-design conditions. For constant input flow conditions, the dependents are not included in the solver.

- The SOFC outputs a four element array consisting of voltage, current, frequency and phase to the data output port. The frequency and phase are zero because the fuel cell generates direct current (DC).

SOFC_new has a baseType of Element.

SOFCHeat



SOFCHeat calculates the heat transferred through flows, the heat generated by the fuel cells, and the net heat of the fuel cell system.

Variables

Variable	Description	Default	Units	IO Status
qGen	Heat generated by a single fuel cell	0	none	input
qNet	Heat transferred through anode and cathode flows	0	none	input
qNet_total	Net heat of the fuel cell	0	none	input

Functions

Prototype	Description
void calculate()	None

Usage Notes

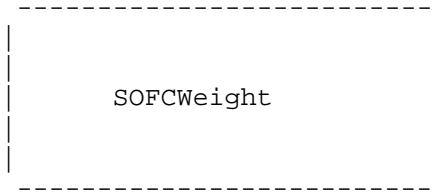
SOFCHeat

-SOFCHeat calculates the heat as the excess energy from the reaction that is not used to produce electricity. The enthalpy of the reaction is used as the total energy available for power production.

-The heat transfer due to the anode and cathode flows is the difference in the enthalpy at the inlet and the enthalpy at the outlet. qNet is the net heat generated for one cell. If qNet is positive, there is excess heat that has not been absorbed by the flows. If it is negative, the flows have absorbed more heat from the cell than the cell has generated.

SOFCHeat has a basetype of Subelement

SOFWeight



SOFWeight calculates the weight and volume of the fuel cell system using densities and geometric values.

Variables

Variable	Description	Default	Units	IO Status
cellArea	Total cell area	0	none	input
cellInstallFactorV	Volumetric installation factor for cells	0	none	input
cellInstallFactorW	Weight installation factor for cells	0	none	input
cellVol	Volume of one cell	0	none	output
cellWeight	Weight of one cell	0		output
numCellPerStack	Number of cells in one stack	1		input
numStack	Number of stacks that make up the total fuel cell system	0		output
rhoAnode	Density of the anode	1		input

rhoCathode	Density of the cathode	1		input
rhoElectrolyte	Density of the electrolyte	1		input
rhoInterconnect	Density of the interconnect	1		input
stackInstallFactorV	Volumetric installation factor for the stack	1		input
stackInstallFactorW	Weight installation factor for the stack	1		input
stackVol	Volume of a stack in the system	0		output
stackWEight	Weight of a stack in the system	0		output
t_Anode	Thickness of the anode	1		input
t_Cathode	Thickness of the cathode	1		input
t_Electrolyte	Thickness of the electrolyte	1		input
t_Interconnect	Thickness of the interconnect	1		input
totalWeight	Weight of the SOFC system	0		output
totalVol	Volume of the SFC system	0		output

Functions

Prototype	Description
void calculate()	None

Usage Notes

SOFCWeight

-SOFCWeight calculates the weight and volume by buiding up a cell using the cell area, the component densities, and the component thicknesses. The cell area is the total cell area, not just the active area used to calculate the current.

-Each cell is assumed to consist of an anode, a cathode, an electrode, and an interconnect. There are installation factors for both weight and volume for other parts not accounted for in the calculation.

-The number of stacks is calculated from the total number of cells determined through the sizing algorithm in the SOFC_new element.

SOFCWeight has a baseType of Subelement.

BatteryWeight

- Weight is calculated as a division of the total energy capacity of the stack by the specific energy. Volume is calculated as the total power of the battery stack divided by the power density. Nominal metrics are used for the calculations since voltage and power can vary.

- StackWeight = Ncells * VoltageNominal * k_2 * CapNominal / SpecEnergy;

- StackVol = Ncells * PowerBattNom / PowerDensity;

BatteryWeight has a baseType of Subelement.

Inverter

Electrical connections are made using Data Ports passing a real[4] array, consisting of:

{Voltage, Current, Frequency, Phase}

Voltage and Current are the magnitudes of the sine waves in an AC system, Phase is the difference in phase between the voltage and current waveforms

DC currents have Frequency = 0 and do not use the value of Phase

Electrical units not defined in NPSS, so most calculations done unitless.

Input = AC Electricity generated (to drive a Motor)

Output = DC required to generate it (Power draw of inverter from Bus)

Sockets:

Socket Name: S_Efficiency

Socket Type: Inverter_Efficiency

Returns: Efficiency

The Inverter element calculates the DC power required to generate the AC waveforms required by the Motor.

Variable	Description	Default	Units (not implemented)	IO Status
Efficiency	Power Out/Power in	1	None	INPUT
OutputVoltage	Amplitude of AC output	120	(Volts)	INPUT
OutputCurrent	Amplitude of AC output current	2	(Amps)	INPUT
InputVoltage	Voltage at DC input	500	(Volts)	INPUT
InputCurrent	DC Input current	.48	(Amps)	OUTPUT
OutputFrequency	Frequency at AC output	60	(Hz)	INPUT
DesignPower	Design Output Power in watts	12000000	(Watts)	INPUT
OutputPower	Output Side Power	12000000	(Watts)	OUTPUT

Option Variables used:

Variable	Description	Variables Affected	Default	Allowed Values
switchDes	Design/Off Design Switch	Efficiency	DESIGN	DESIGN, OFFDESIGN

Functions

Prototype	Description
Void calculate()	None

Ports

Port	Type	Description
INPUT	DataInputPort	Power Requirements from Motor
OUTPUT	DataOutputPort	Power Requirements to Bus

Sockets

Socket	Description	socketType	Sets Values
S_Efficiency	Calculates efficiency from ratio between DesignPower and OutputPower	Inverter_Efficiency	Efficiency

Independents

Name	Description	Variable	Active When
ind_Voltage	Attempts to match voltage to bus voltage through a resistive cable	InputVoltage	always

Usage Notes:

The socket included is currently a table lookup of efficiency based on OutputPower/DesignPower.

The DC input voltage is the bus voltage – the losses in the cable, which are a function of the Input current. The Independent is required to guess what the input voltage is such that the dependent in the bus will find that the bus end of the power cable is at the bus voltage.

Details of Calculate: Read in inputs, set DesignPower=OutputPower if switchDes=Design, calculate efficiency using S_Efficiency, InputPower = OutputPower/Efficiency, format outputs & end.

Rectifier

Electrical connections are made using Data Ports passing a real[4] array, consisting of:

{Voltage, Current, Frequency, Phase}

Voltage and Current are the magnitudes of the sine waves in an AC system, Phase is the difference in phase between the voltage and current waveforms

DC currents have Frequency = 0 and do not use the value of Phase

Electrical units not defined in NPSS, so most calculations done unitless.

Inputs

AC Electricity (from Generator)

DC Electricity (required from Bus)

Sockets:

Socket Name: S_Efficiency

Socket Type: Rectifier_Efficiency

Returns: Efficiency

The Inverter element calculates the DC power required to generate the AC waveforms required by the Motor.

Variable	Description	Default	Units (not implemented)	IO Status
Efficiency	Power Out/Power in	1	None	INPUT

OutputVoltage	Amplitude of DC output	500	(Volts)	INPUT
OutputCurrent	Amplitude of DC output current	.48	(Amps)	INPUT
InputVoltage	Voltage at AC input	120	(Volts)	INPUT
InputCurrent	AC Input current	2	(Amps)	INPUT
InputFrequency	Frequency at AC Input	60	(Hz)	INPUT
DesignPower	Design Output Power in watts	12000000	(Watts)	INPUT
OutputPower	DC Output Power	60	(Watts)	INPUT
InputPower	AC Input Power	60	(Watts)	INPUT

Option Variables used:

Variable	Description	Variables Affected	Default	Allowed Values
switchDes	Design/Off Design Switch	Efficiency	DESIGN	DESIGN, OFFDESIGN

Functions

Prototype	Description
Void calculate()	None

Ports

Port	Type	Description
INPUT	DataInputPort	Power From Generator
OUTPUT	DataInputPort	Power Requirements to Bus

Sockets

Socket	Description	socketType	Sets Values
S_Efficiency	Calculates efficiency from ratio between DesignPower and OutputPower	Rectifier_Efficiency	Efficiency

Dependents

Name	Description	Eq_lhs	Eq_rhs	Active When
dep_Power	Makes sure that generator power*efficiency = power to bus	InputPower*Efficiency	OutputPower	always

Usage Notes:

The Dependent is the one ensuring that the Generator power corresponds to the Motor power and the system efficiency.

Details of Calculate: Read in inputs, set DesignPower=OutputPower if switchDes=Design, calculate efficiency using S_Efficiency. Dependent takes care of the rest.

The socket included is currently a table lookup of efficiency based on OutputPower/DesignPower.

DCTransformer

Electrical connections are made using Data Ports passing a real[4] array, consisting of:
 {Voltage, Current, Frequency, Phase}

Voltage and Current are the magnitudes of the sine waves in an AC system, Phase is the difference in phase between the voltage and current waveforms

DC currents have Frequency = 0 and do not use the value of Phase

Electrical units not defined in NPSS, so most calculations done unitless.

Inputs = DC Electricity (from Battery)

DC Electricity (required from Bus)

Sockets:

Socket Name: S_Efficiency

Socket Type: DCTransformer_Efficiency

Returns: Efficiency

The DC Transformer element compares the power draw from the battery and the power required by the bus

Variable	Description	Default	Units (not implemented)	IO Status
Efficiency	Power Out/Power in	1	None	INPUT
OutputVoltage	Amplitude of DC output	500	(Volts)	INPUT
OutputCurrent	Amplitude of DC output current	.48	(Amps)	INPUT
InputVoltage	Voltage at AC input	120	(Volts)	INPUT
InputCurrent	AC Input current	2	(Amps)	INPUT
DesignPower	Design Output Power in watts	12000000	(Watts)	INPUT
OutputPower	DC Output Power	60	(Watts)	INPUT
InputPower	AC Input Power	60	(Watts)	INPUT

Option Variables used:

Variable	Description	Variables Affected	Default	Allowed Values
----------	-------------	--------------------	---------	----------------

switchDes	Design/Off Design Switch	–	Efficiency	DESIGN	DESIGN, OFFDESIGN
-----------	-----------------------------	---	------------	--------	----------------------

Functions

Prototype	Description
Void calculate()	None

Ports

Port	Type	Description
INPUT	DataInputPort	Power From Generator
OUTPUT	DataInputPort	Power Requirements to Bus

Sockets

Socket	Description	socketType	Sets Values
S_Efficiency	Calculates efficiency from ratio between DesignPower and OutputPower	DCTransformer_Efficiency	Efficiency

Dependents

Name	Description	Eq_lhs	Eq_rhs	Active When
dep_Power	Makes sure that battery power*efficiency = power to bus	InputPower*Efficiency	OutputPower	always

Usage Notes:

The Dependent is the one ensuring that the Battery power corresponds to the Motor power and the system efficiency.

Details of Calculate: Read in inputs, set DesignPower=OutputPower if switchDes=Design, calculate efficiency using S_Efficiency. Dependent takes care of the rest.

The socket included is currently a table lookup of efficiency based on OutputPower/DesignPower.

PowerCable

Electrical connections are made using Data Ports passing a real[4] array, consisting of:

{Voltage, Current, Frequency, Phase}

Voltage and Current are the magnitudes of the sine waves in an AC system, Phase is the difference in phase between the voltage and current waveforms

DC currents have Frequency = 0 and do not use the value of Phase

Electrical units not defined in NPSS, so most calculations done unitless.

Inputs = Electricity

Output = Electricity

The Power Cable models a DC power cable with a specified resistance

Variable	Description	Default	Units (not implemented)	IO Status
Resistance	Resistance of cable	0	(Ohms)	INPUT
OutputVoltage	Amplitude of DC output	500	(Volts)	OUTPUT
OutputCurrent	Amplitude of DC output current	2	(Amps)	INPUT
InputVoltage	Voltage at AC input	500	(Volts)	INPUT
InputCurrent	AC Input current	2	(Amps)	INPUT

Functions

Prototype	Description
Void calculate()	None

Ports

Port	Type	Description
INPUT	DataInputPort	Power From Generator
OUTPUT	DataOutputPort	Power Requirements to Bus

Calculate: Process Inputs from DataInputPort, $OutputVoltage = InputVoltage - Current * Resistance$, Load outputs into DataOutputPort.

Bus

Electrical connections are made using Data Ports passing a real[4] array, consisting of:
 {Voltage, Current, Frequency, Phase}

Voltage and Current are the magnitudes of the sine waves in an AC system, Phase is the difference in phase between the voltage and current waveforms

DC currents have Frequency = 0 and do not use the value of Phase

Electrical units not defined in NPSS, so most calculations done unitless.

Inputs = DC power draws (from Inverters or other power loads)

Output = DC power demands to power sources.

The Bus receives all the power loads of the system and distributes their power draw between all the power sources.

Variable	Description	Default	Units (not implemented)	IO Status
Voltage	Target Voltage of Bus	10000	(Volts)	INPUT
NetCurrent	Net Current into bus from inputs	[15]	(Volts)	INPUT
PowerSourceSplit	Division of power loads between	[]	None	INPUT

	power sources			
--	---------------	--	--	--

Functions

Prototype	Description
Void calculate()	None
void postcreate(string name)	Processes DataInputPorts, DataOutputPorts, and Dependents declared in the .mdl file

Ports

Port	Type	Description
dataInputPortList[]	String array of pointers to DataInputPort objects	Power Demanded by each load
dataOutputPortList[]	String array of pointers to DataOutputPort objects	Power Required from each source

Dependents

Name	Description	Eq_lhs	Eq_rhs	Active When
dependentList[] (string array of pointers to the dependents)	Makes sure that each load is receiving the bus voltage at its DC input	InputVoltage[i]	Voltage	always

Usage Notes:

The DataInputPorts, DataOutputPorts, and Dependents must be declared in the .mdl file. The Dependents eq_lhs and eq_rhs are handled in the postcreate() function but there must be as many dependents as datainputports. In addition the division of power between the sources is even unless PowerSourceSplit[] has as many entries as there are DataOutputPorts and has at least one non-zero element. The split is normalized to ensure that the total current into and out of the bus sums to zero.

Details of Calculate: Read in inputs, sum currents into NetCurrent, normalize PowerSourceSplit and check to see if it is the same length as DataOutputPortList and nonzero, then divide power into each of the outputs.

Motor

Inputs = Shaft Speed and Torque

Outputs = AC Electricity required to turn motor

Calculates the performance of a conventional motor with specified Kv, R, and L

Variable	Description	Default	Units (not implemented)	IO Status
Resistance	Resistance of Stator	0	(ohms)	INPUT

Inductance	Motor Inductance	0	(Henrys)	INPUT
Current	AC input current magnitude	2	(Amps)	OUTPUT
Voltage	AC voltage across motor	500	(Volts)	OUTPUT
Phase	Phase offset between Current & Voltage	0	(Radians)	OUTPUT
Frequency	Frequency at AC Input	60	(Hz)	OUTPUT
Torque	Output Torque	1000	(ft-lb)	INPUT
Speed	Output Shaft Mechanical speed	50	(rad/s)	INPUT
Kv	Speed/Volt	60	((rad/s)/volt)	INPUT
PolePairs	Number of Pole Pairs in the motor	4	None	INPUT

Functions

Prototype	Description
Void calculate()	None

Ports

Port	Type	Description
Sh_O	ShaftOutputPort	Shaft Port Connection
ElectricOutput	DataOutputPort	Power Requirements to Inverter

Independents

Name	Description	Variable	Active When
ind_Torque	Matches torque required to spin shaft	Torque	Should have autoSetup=true for solver to work

Usage Notes:

Uses Kv and a calculated Kt to generate ideal motor, to which resistive and inductive losses are then added

Details of Calculate: Read in inputs, calculate Kt from Kv, Frequency from PolePairs and ShaftSpeed, Current from Kt&torque, ideal voltage from Kv and speed, resistive and inductive behavior from frequency and current, and the output voltage as the sum of the ideal, resistor and inductor voltages. Calculate phase difference from inductor voltage and output the electricity.

Generator

Electrical connections are made using Data Ports passing a real[4] array, consisting of:
 {Voltage, Current, Frequency, Phase}

Voltage and Current are the magnitudes of the sine waves in an AC system, Phase is the difference in phase between the voltage and current waveforms

DC currents have Frequency = 0 and do not use the value of Phase

Electrical units not defined in NPSS, so most calculations done unitless.

Outputs = AC Electricity to system

Calculates the performance of a conventional generator with specified Kv, R, and L

Variable	Description	Default	Units (not implemented)	IO Status
Resistance	Resistance of Stator	0	(ohms)	INPUT
Inductance	Generator Inductance	0	(Henrys)	INPUT
Current	AC input current magnitude	2	(Amps)	OUTPUT
Voltage	AC voltage across motor	500	(Volts)	OUTPUT
Phase	Phase offset between Current & Voltage	0	(Radians)	OUTPUT
Frequency	Frequency at AC Input	60	(Hz)	OUTPUT
Torque	Output Torque	1000	(ft-lb)	INPUT
Speed	Output Shaft Mechanical speed	50	(rad/s)	INPUT
Kv	Speed/Volt	60	((rad/s)/volt)	INPUT
PolePairs	Number of Pole Pairs in the Generator	4	None	INPUT

Functions

Prototype	Description
Void calculate()	None

Ports

Port	Type	Description
ElectricOutput	DataOutputPort	Power Requirements to Inverter

Independents

Name	Description	Variable	Active When
ind_Torque	Determines how much power generator is producing	Torque	Should have autoSetup=true for

			solver to work
--	--	--	----------------

Usage Notes:

Uses Kv and a calculated Kt to generate ideal generator, to which resistive and inductive losses are then added. Currently doesn't include a shaft, eventually a shaft would be added which could be attached to a gas turbine.

Details of Calculate: Read in inputs, calculate Kt from Kv, Frequency from PolePairs and ShaftSpeed, Current from Kt&torque, ideal voltage from Kv and speed, resistive and inductive behavior from frequency and current, and the output voltage as the difference of the ideal, resistor and inductor voltages. Calculate phase difference from inductor voltage and outputs the electricity.

HTSMotor

Electrical connections are made using Data Ports passing a real[4] array, consisting of:

{Voltage, Current, Frequency, Phase}

Voltage and Current are the magnitudes of the sine waves in an AC system, Phase is the difference in phase between the voltage and current waveforms

DC currents have Frequency = 0 and do not use the value of Phase

Electrical units not defined in NPSS, so most calculations done unitless.

Inputs = Shaft Speed and Torque

Outputs = AC Electricity required to turn motor

Calculates the performance of a HTS superconducting motor.

Variable	Description	Default	Units (not implemented)	IO Status
MachinePower	Nominal power of motor	10728.1767 (80)	(HP) (MW)	INPUT
MachineSpeed	Speed of motor	13000	(RPM)	INPUT
MachineShapeFactor	Ratio of length to radius	5	None	INPUT
NPolePairs	Number of pole pairs in the motor	500	(Volts)	INPUT
StatAveRad	Radius of the stator	.3937 (.12)	(feet) (meters)	INPUT
StatElecLoad	Current loading of stator	152400 (500000)	(Amps/ft) (Amps/m)	INPUT
StatOpFac	Stator operating factor	.6	(none)	INPUT
StatorACLossDim	Reference distance for AC losses	.0007874 (.00002)	(feet) (meters)	INPUT
HTSTemp	Temperature of	36	(Degrees Rankine)	INPUT

	superconductor	20	(Kelvin)	
BkFeFDensity	Magnetic field strength within the back iron	1.9	Tesla	INPUT
CryoWallThick	Wall thickness of cryocooler	.1575 (.004)	(inches) (meters)	INPUT
EMShieldTh	Thickness of EM shield	.0787 (002)	(inches) (meters)	INPUT
MachineLosses	Thermal and EM losses within motor	29.22 (21.79)	(Hp) (kW)	Output
ElectricPower	Total electric power drawn	10750	(Hp)	Output
Weight	Mass of HTS motor	670 304	(lbm) (kg)	Output
OffDesignPower	Current power setting of motor	10728.1767 (80)	(HP) (MW)	OUTPUT
OffDesignSpeed	Current speed that motor is running at	13000	(RPM)	OUTPUT
OffDesignTorque	Current torque of motor	38000	(ft-lb)	INPUT
Current	stator current magnitude 3 phase	200	Amps	OUTPUT
Voltage	Stator phase to phase voltage	220	Volts	OUTPUT

Functions

Prototype	Description
Void calculate()	None

Ports

Port	Type	Description
Sh_O	ShaftOutputPort	Shaft Port Connection
ElectricOutput	DataOutputPort	Power Requirements to Inverter

Independents

Name	Description	Variable	Active When
ind_desPower	Sizes motor to match required power	MachinePower	When switchdes = "DESIGN"

Usage Notes:

Based on Masson Motor Model

Details of Calculate: Finds geometry of motor and does physics based modeling of magnetic fields from there.

HTSGenerator

Electrical connections are made using Data Ports passing a real[4] array, consisting of:

{Voltage, Current, Frequency, Phase}

Voltage and Current are the magnitudes of the sine waves in an AC system, Phase is the difference in phase between the voltage and current waveforms

DC currents have Frequency = 0 and do not use the value of Phase

Electrical units not defined in NPSS, so most calculations done unitless.

Inputs = Shaft Speed and Torque

Outputs = AC Electricity out

Calculates the performance of a HTS superconducting generator

Variable	Description	Default	Units (not implemented)	IO Status
MachinePower	Nominal power of motor	10728.1767 (80)	(HP) (MW)	INPUT
MachineSpeed	Speed of motor	13000	(RPM)	INPUT
MachineShapeFactor	Ratio of length to radius	5	None	INPUT
NPolePairs	Number of pole pairs in the motor	500	(Volts)	INPUT
StatAveRad	Radius of the stator	.3937 (.12)	(feet) (meters)	INPUT
StatElecLoad	Current loading of stator	152400 (500000)	(Amps/ft) (Amps/m)	INPUT
StatOpFac	Stator operating factor	.6	(none)	INPUT
StatorACLossDim	Reference distance for AC losses	.0007874 (.00002)	(feet) (meters)	INPUT
HTSTemp	Temperature of superconductor	36 20	(Degrees Rankine) (Kelvin)	INPUT
BkFeFDensity	Magnetic field strength within the back iron	1.9	Tesla	INPUT
CryoWallThick	Wall thickness of cryocooler	.1575 (.004)	(inches) (meters)	INPUT
EMShieldTh	Thickness of EM shield	.0787 (002)	(inches) (meters)	INPUT
MachineLosses	Thermal and EM losses within motor	29.22 (21.79)	(Hp) (kW)	Output
ElectricPower	Total electric power drawn	10750	(Hp)	Output
Weight	Mass of HTS motor	670 304	(lbm) (kg)	Output

OffDesignPower	Current power setting of motor	10728.1767 (80)	(HP) (MW)	OUTPUT
OffDesignSpeed	Current speed that motor is running at	13000	(RPM)	OUTPUT
OffDesignTorque	Current torque of motor	38000	(ft-lb)	INPUT
Current	stator current magnitude 3 phase	200	Amps	OUTPUT
Voltage	Stator phase to phase voltage	220	Volts	OUTPUT

Functions

Prototype	Description
Void calculate()	None

Ports

Port	Type	Description
Sh_O	ShaftOutputPort	Shaft Port Connection
ElectricOutput	DataOutputPort	Power Requirements to Inverter

Independents

Name	Description	Variable	Active When
ind_desPower	Sizes motor to match required power	MachinePower	When switchdes = "DESIGN"

Usage Notes:

Based on Masson Motor Model

Details of Calculate: Finds geometry of generator and does physics based modeling of magnetic fields from there.

REPORT DOCUMENTATION PAGE

*Form Approved
OMB No. 0704-0188*

The public reporting burden for this collection of information is estimated to average 1 hour per response, including the time for reviewing instructions, searching existing data sources, gathering and maintaining the data needed, and completing and reviewing the collection of information. Send comments regarding this burden estimate or any other aspect of this collection of information, including suggestions for reducing this burden, to Department of Defense, Washington Headquarters Services, Directorate for Information Operations and Reports (0704-0188), 1215 Jefferson Davis Highway, Suite 1204, Arlington, VA 22202-4302. Respondents should be aware that notwithstanding any other provision of law, no person shall be subject to any penalty for failing to comply with a collection of information if it does not display a currently valid OMB control number.
PLEASE DO NOT RETURN YOUR FORM TO THE ABOVE ADDRESS.

1. REPORT DATE (DD-MM-YYYY) 01-04-2015		2. REPORT TYPE Contractor Report		3. DATES COVERED (From - To) February 2012 - June 2014	
4. TITLE AND SUBTITLE Subsonic Ultra Green Aircraft Research: Phase II – Volume II – Hybrid Electric Design Exploration				5a. CONTRACT NUMBER NNL08AA16B	
				5b. GRANT NUMBER	
				5c. PROGRAM ELEMENT NUMBER	
6. AUTHOR(S) Bradley, Marty K.; Droney, Christopher K.				5d. PROJECT NUMBER	
				5e. TASK NUMBER NNL11AA00T	
				5f. WORK UNIT NUMBER 081876.01.07.02	
7. PERFORMING ORGANIZATION NAME(S) AND ADDRESS(ES) The Boeing Company 5301 Bolsa Ave, MC H017-D334 Huntington Beach, California 92647-2099				8. PERFORMING ORGANIZATION REPORT NUMBER	
9. SPONSORING/MONITORING AGENCY NAME(S) AND ADDRESS(ES) National Aeronautics and Space Administration Washington, DC 20546-0001				10. SPONSOR/MONITOR'S ACRONYM(S) NASA	
				11. SPONSOR/MONITOR'S REPORT NUMBER(S) NASA/CR-2015-218704/Volume II	
12. DISTRIBUTION/AVAILABILITY STATEMENT Unclassified - Unlimited Subject Category 05 Availability: NASA STI Program (757) 864-9658					
13. SUPPLEMENTARY NOTES Final Report Langley Technical Monitor: Erik D. Olson					
14. ABSTRACT This report summarizes the hybrid electric concept design, analysis, and modeling work accomplished by the Boeing Subsonic Ultra Green Aircraft Research (SUGAR) team, consisting of Boeing Research and Technology, Boeing Commercial Airplanes, General Electric, and Georgia Tech. Performance and sizing tasks were conducted for hybrid electric versions of a conventional tube-and-wing aircraft and a hybrid wing body. The high wing Truss Braced Wing (TBW) SUGAR Volt was updated based on results from the TBW work (documented separately) and new engine performance models. Energy cost and acoustic analyses were conducted and technology roadmaps were updated for hybrid electric and battery technology. NOx emissions were calculated for landing and takeoff (LTO) and cruise. NPSS models were developed for hybrid electric components and tested using an integrated analysis of superconducting and non-superconducting hybrid electric engines. The hybrid electric SUGAR Volt was shown to produce significant emissions and fuel burn reductions beyond those achieved by the conventionally powered SUGAR High and was able to meet the NASA goals for fuel burn. Total energy utilization was not decreased but reduced energy cost can be achieved for some scenarios. The team was not able to identify a technology development path to meet NASA's noise goals.					
15. SUBJECT TERMS Acoustics; Aircraft performance; Batteries; Cryogenics; Emissions; Fuel burn; Fuel cells; Generator; Truss-braced wing; Unducted fan					
16. SECURITY CLASSIFICATION OF:			17. LIMITATION OF ABSTRACT	18. NUMBER OF PAGES	19a. NAME OF RESPONSIBLE PERSON
a. REPORT	b. ABSTRACT	c. THIS PAGE			STI Help Desk (email: help@sti.nasa.gov)
U	U	U	UU	233	19b. TELEPHONE NUMBER (Include area code) (443) 757-5802